

**Development of Lightweight High Stiffness
Alloys assisted by Integrated
Computational Materials Engineering
(ICME)**



**University of
Sheffield**

Panagiotis Pavlos Stavroulakis

Department of Materials Science and Engineering

University of Sheffield

This thesis is submitted as a requirement for the degree of

Doctor of Philosophy

Submitted August 2023

Abstract

The reduction of greenhouse gas emissions (GGE) is one of the more prominent challenges of the automotive industry. This is achieved through the utilisation of lightweight automotive components without compromising their structural integrity. Multicomponent alloys (MCAs) have the potential to address this challenge owing to their chemical flexibility. Nevertheless, navigating the vast compositional space of MCAs can be difficult. In this work a novel computational methodology for predicting the elastic properties of any single phase or multiphase alloy is presented. When applied to the equiatomic AlTiVCr and AlTiVCr-Si_{7.2} alloys it is discovered that both possess elastic properties far surpassing those of even the more advanced high modulus steels. Nevertheless, both alloys exhibited extensive cracking during manufacturing. This was originally thought to derive from the presence of the ordered B2 phase at equilibrium manifesting through an order-disorder transformation. Water quenching (WQ) trials post heat treatment unveiled that the order-disorder (B2-BCC) transformation could be partially inhibited, resulting in the manifestation of a dualphase BCC-B2 microstructure. Nevertheless, no improvements in ductility were observed between the single phase B2 and the dualphase BCC-B2 alloys due to the presence of profound cracking in the WQ condition. It was revealed that the reason behind the crack formation lied in their abnormally low thermal conductivity, inducing thermal shock upon exposure to rapid thermal cycles. Compositional modification ensued, aimed at destabilising the B2 in favour of the BCC phase by reducing the aluminium (Al) content of the alloys. Indeed, in the case of the Al_{11.1}TiVCr alloy, WQ produced a single phase BCC microstructure while both the Al_{11.1}TiVCr and Al_{16.7}TiVCr alloys exhibited a dualphase BCC-B2 microstructure after furnace cooling from the heat treatment temperature. Interestingly, the reduction in Al also led to a significant drop in both the density and the Young's modulus of the tested alloys. Therefore, the manifestation of elevated elastic properties in single phase Al-rich alloys was attributed to the Al addition modifying the bonding type of the alloys from metallic to partially covalent. These findings lay the foundations for manipulating the elastic properties of Al-containing MCAs, while the associated methodologies guided the discovery of candidate alloys for lightweight high stiffness applications.

Acknowledgements

“In September 2018 my journey as a PhD researcher began. Endeavouring across Europe to the United Kingdom I set out to explore a novel category of materials, namely high entropy alloys. The will to do “good science” and my aspirations brought me to the University of Sheffield and Sheffield itself, which became my home for the past four and a half years. But who would have considered the impact these years would end up having. During this time, many people entered but also left my life. There were times when I found myself alone on my little balcony on Upper Allen Street pondering upon my decisions and whether it was all going to be worth it in the end. Times when quitting seemed like the sensible option. Times when pushing through seemed improbable, if not impossible. Even so, rays of light shun through my cloudy sky and showed me the way forward. All these people who believed I could even when I thought I could not, ended up making me believe as well. This thesis, my PhD in its entirety devoted to you. For without you, my dreams would not have become a reality. Thank you.”

I would like to start by expressing my sincerest gratitude to my supervisors Prof. Russell Goodall and Dr. Colin Freeman. You have always been there for me, offering guidance and support regarding both professional and personal matters and I wish all students would have the opportunity to collaborate with such wonderful people as yourselves. I will always be wondering how you managed so many things Russell, from family, to work, research and being able to devote time to your students even for things most other people would find negligible. You were always there. And you Colin. You taught me what a good work environment truly looked like and the importance of mental health. Thank you for checking up on me that one time when things were quite grim. And thank you for the 9 am chats, I will truly miss being around for these. I would also like to thank my industrial sponsor Volkswagen and my industrial supervisors Dr –Ing. Oliver N  th, Dr –Ing. Ralf Rablbauer, Dr. –Ing. Robert Thomas and Dr –Ing. Oliver Schauerte. I still remember our first meeting in Wolfsburg in 2018 when I was inquiring about material specifications for designing the project and Dr –Ing. Schauerte just told me to “do science”. And science I did. Oliver and Ralf, thank you for your continued interest and really helping provide a steer for the project. I cherish the time we spent together during my placement in VW, especially the post-lunch coffee breaks with Ralf. I really miss those. Finally, Robert thank you for making my time in Berlin and VW a lifetime experience. It truly felt like home. I will also remember to add more salt to the Moussaka next time. Auf wiedersehen!

At this point I would like to sincerely thank members of staff and technicians who aided with all the work starting with Dr. Lisa Hollands and Mr. Neil Hind in the Quarrell lab who helped me design and carry out the heat treatments explored within my project. I would also like to thank Dr. Yunus Azakli who supported me greatly in all aspects of arc and induction melting. Many thanks to Dr. Claire Utton for all her support regarding the CALPHAD work, encapsulated within this PhD. I also thank Dr. Stavrina Dimosthenous for her support and guidance regarding DFT calculations and their analysis. A massive thank you to Dr. Dhinisa Patel for extensively supporting the project in aspects relating to material design and XRD and to Dr. Robert Moorhead for his guidance regarding the XRD and indentation work. Lastly, I would like to express my gratitude to Dr. John Nutter of the University of Sheffield and Dr. Alexander Carruthers of the University of Manchester for carrying out the TEM work relating to my PhD and their assistance with the subsequent data analysis. From the VW side I would also like to thank Mr. Martin Stanke and Ms. Melanie Lenz for their technical assistance during my placement. Lastly, I would like to kindly thank ELKEME S. A. and specifically the general manager Mr. Kimon Daniilidis for allowing me to carry out experimental work in their laboratories during November 2020 when research work could not be carried out in-house. Furthermore, I would like to thank Dr. Athanasios Vazdirvanidis, Dr. Sofia Papadopoulou, Ms. Eugenia Spyropoulou and Mr. Andreas Rikos for the technical assistance during my time in ELKEME S. A. I would like to extend my thanks to Prof. Dr -Ing. Spyros Papaefthymiou and PhD candidate Mr. Spyridon Chaskis of the National Technical University of Athens for setting up a fruitful research collaboration from 2019 to 2022 regarding high entropy alloys. This work was supported by the University of Sheffield and ELKEME S. A. Naturally, I would also like give kudos to my MSc thesis students, Mr. Ioannis Daskalopoulos, Mr. Dimitrios Kiousis and Ms. Stavroula Maritsa to whom I wish professional and interpersonal excellence. The Advanced Metallic Systems Centre for Doctoral Training is what made this PhD possible. I am entirely indebted to the academic staff and members for giving me this opportunity and to my cohort members with whom I have made beautiful memories from my time in Sheffield.

On a more personal level there are multiple individuals I would like to acknowledge for helping me get to where I am today. I believe the seeds of engineering were planted in me when I was still young, watching my father's architectural work in his office or when he would bring me along to construction sites. Dr. Athanasios Vazdirvanidis, Dr. Anagnostis Toulfatzis and Dr. George Pantazopoulos took me in as a student during my undergraduate internship and transformed me into a professional by the end of my degree. I sincerely believe that working

alongside them back then is what truly lay the foundations that enabled me to pursue and eventually attain my PhD. I would also like to acknowledge the continuous support of my friends throughout this journey who have consistently pushed me to bring my A-game to the table. Moving towards the end I also express an overwhelming gratitude to my family for continuously believing in me and my capabilities and for always being there for me. And lastly, thank you Barbara for the peace and happiness you brought into my life and for supporting my dreams. Thank you to everyone who has been on this journey with me. It has been quite the ride. I could not have done it without you, and I am grateful for all the memories we made along the way.

~ Cheers!



Crookes Valley Park, Sheffield, Feb 2021

I would like to acknowledge EPSRC grant (EP/L016273) Centre for Doctoral Training in Advanced Metallic Systems and Volkswagen Group for supporting this research. Via our membership of the UK's HEC Materials Chemistry Consortium, which is funded by EPSRC (EP/L000202, EP/R029431, EP/T022213), this work used the ARCHER2 UK National Supercomputing Service (<http://www.archer2.ac.uk>).

With shortness of breath, I'll explain the infinite.

How rare and beautiful it truly is that we exist

Στη γιαγιά μου.

Publications

Journal Papers

Stavroulakis, P., Freeman, C. L., Patel, D., Utton, C. and Goodall, R., Successful prediction of the elastic properties of multiphase high entropy alloys in the AlTiVCr-Si system through a novel computational approach. *Materialia*, 2022. 21: p. 101365.

Daskalopoulos, I., Chaskis, S., Bouzouni, M., Stavroulakis, P., Goodall, R. and Papaefthymiou, S., Microstructural Characterization of AlCrTiV – Si High Entropy Alloy for advanced applications. *MATEC Web of Conferences*, 2021. 349: p. 02003.

Chaskis, S., Kiouisis, D., Stavroulakis, P., Goodall, R. and Papaefthymiou, S., Examination of Fracture Mechanisms in two Al – Ti – V – Cr – (Si) High Entropy Alloys. *MATEC Web of Conferences*, 2021. 349: p. 02002.

Diploma Theses

Daskalopoulos, I., Study of thermal processes and microstructural characterization of the AlCrTiV-Si high-entropy alloy. 2020. <http://dx.doi.org/10.26240/heal.ntua.19460>.

Kiouisis, D., Αξιολόγηση της δυνατότητας παρασκευής κράματος μέσης εντροπίας TiAlCrV με μεθόδους προσθετικής κατασκευής (Additive Manufacturing). 2021. <http://dx.doi.org/10.26240/heal.ntua.21006>.

Conference Attendance

2023

7th International Conference of Engineering Against Failure (Spetses, Greece) – Presentation

TMS 2023 (San Diego, CA, USA) - Presentation

2022

8th Conference of the Hellenic Metallurgical Society (Patras, Greece) - Presentation

First UK Workshop on High-Entropy Materials (Manchester, UK) – Elevator Pitch

13th Annual International Student Conference in Metallic Materials (Dublin, Ireland) - Presentation

2021

Euromat 2021 - Online Presentation

2020

National Student Conference Advanced Metallic Systems – Presentation

2019

Hands-On DFT and Beyond (Barcelona, Spain) - Attendance

CASTEP Training Workshop 2019 (Oxford, UK) - Attendance

National Student Conference Advanced Metallic Systems – Poster

CASTEP Users Workshop (Birmingham, UK) - Attendance

Prizes

First UK Workshop on High-Entropy Materials 2022 - QinetiQ Early Career Researcher Award

National Student Conference Advanced Metallic Systems 2020 - Best Oral Presentation

Table of Contents

1. Introduction.....	1
1.1 Aims and Objectives	3
1.2 Thesis Overview	3
2. Literature Review	5
2.1 High Entropy Alloys (HEAs).....	5
2.1.1 High Entropy alloys behaviour understanding	7
2.1.2 Empirical Solid Solubility Rules and Phase Formation Criteria	9
2.1.3 Applications of High Entropy Alloys	13
2.1.4 Body Centred Cubic (BCC) High Entropy Alloys	14
2.1.5 From High Entropy alloys to Multicomponent alloys (MCAs).....	16
2.2 Body Centred Cubic Multicomponent alloys	17
2.2.1 Challenges of BCC MCAs and their resolution.....	17
2.2.2 Development of novel BCC MCAs – Refractory high entropy superalloys (RSAs)	21
2.2.3 Development of high specific stiffness RMCAs	23
2.2.4 AlTiVCr-based RMCAs	24
2.3 Computational design of Multicomponent alloys.....	28
2.3.1 Calculation of Phase Diagrams (CALPHAD)	29
2.3.2 Density Functional Theory	31
2.3.3 Machine Learning	34
2.4 Trends in RMCA research	36
2.5 Mechanisms and Phenomena.....	38
2.5.1 Elastic Properties	38
2.5.2 Order-Disorder Transformations	40
2.5.3 Ductile to Brittle Transition Temperature (DBTT)	46
2.5.4 Ostwald Ripening.....	47

2.5.5 Thermal Shock.....	48
2.6 Conclusions.....	50
3. Materials and Methods.....	52
3.1 Computational Methods.....	52
3.1.1 Calculation of Phase Diagrams (CALPHAD)	52
3.1.2 Density Functional Theory (DFT)	54
3.1.3 Homogenisation Modelling - Finite Element Modelling (FEM)	61
3.1.4 pyMPEALab Toolkit.....	62
3.2 Experimental Methods	63
3.2.1 Cold Crucible Vacuum Arc Melting (VAM).....	63
3.2.2 Heat Treatments	66
3.2.3 Metallographic Preparation.....	66
3.2.8 X-Ray Diffraction (XRD)	70
3.2.11 Compression Testing.....	72
3.2.12 Inert Gas Fusion Analysis (IGFA)	73
4. Computational Prediction of Elastic Properties in the AlTiVCr-Si system through ICME.....	74
4.1 Aim.....	76
4.2 Computational and Experimental Methods.....	76
4.2.1 Computational Methods	76
4.2.2 Experimental Methods	78
4.3 Results and Discussion.....	81
4.3.1 Modelling Predictions	81
4.3.2 Experimental Verification and Analysis	86
4.4 Conclusions	102
5. Assessment of the Fracture Mechanisms in AlTiVCr-based and AlTiVCr-Si_{7.2} alloys	
104	
5.1 Aim	105

5.2 Computational and Experimental Methods	107
5.2.1 Computational Methods.....	107
5.2.2 Experimental Methods	107
5.2.2.3 Vickers Hardness (HV) Testing.....	108
5.3 Results and Discussion	110
5.3.2 The addition of Mn towards the improvement of the Fracture Behaviour	115
5.4 Conclusions.....	129
6. Compositionally Invariant Phase Transformation Control in the AlTiVCr alloy	131
6.1 Aim.....	131
6.2 Experimental Methods	132
6.2.1 X-ray Diffraction Analysis.....	132
6.2.2 Focused Ion Beam (FIB) SEM and Transmission Electron Microscopy (TEM) .	134
6.2.2 Mechanical Testing	134
6.2.4 Inert Gas Fusion Analysis (IGFA).....	135
6.3 Results and Discussion	136
6.3.1 Microstructural Characterisation.....	136
6.3.2 Mechanical Properties.....	151
6.3.3 Oxygen Content Measurements (IGFA).....	154
6.4 Conclusions.....	155
7. Design of Novel Single phase BCC AlTiVCr-based alloys through ICME	157
7.1 Aim.....	157
7.2 Computational and Experimental Methods.....	158
7.2.1 Computational Methods.....	159
7.2.2 Experimental Methods	161
7.3 Results and Discussion	165
7.3.1 Computational Predictions	165
7.3.2 Experimental Assessment of Novel Compositions.....	177

7.4 Implications.....	210
7.5 Conclusions.....	214
8. Conclusions.....	216
9. Future Work.....	220
9.1 Manufacturing.....	220
9.2 From alloys to intermetallics	223
9.3 Dataset completion.....	223
10. Appendix.....	225
11. References.....	233

1. Introduction

Metallic materials have always been a pillar of our civilisation, even from the ancient times. The use of copper (Cu) was prevalent even dating back to the Neolithic period (10,000 – 2,200 BC), predominantly for cosmetics, eventually transitioning over to bronze. Bronze among many things was also used as a trading commodity in the form of coins alongside silver (Ag) and gold (Au) [1]. Eventually, the use of iron started to dominate that of other available metals for most applications due to its higher strength [2]. Although the original interest pertained to the utilisation of metallic elements, the concept of alloying eventually surfaced, particularly through the understanding of the role of carbon in iron, thus producing steel. During the 20th century the abstract nature of alloying shifted towards a more scientific paradigm. Advances in microscopy allowed for the establishment of correlations between the microstructure and the observable properties of an alloy [3]. Alloying can enable the manifestation of desirable properties in metallic systems. For example, diffusionless transformations in steels depend on the presence of carbon while carbides themselves can produce significant strengthening effects [4]. Further alloying additions such as chromium (Cr) enable the formation of a protective Cr₂O₃ layer on the surface of the steel providing anti-corrosive properties [5]. In aluminium (Al) alloys the introduction of Cu as a microalloying element enabled the formation of Al-Cu secondary phase particles (SPPs) capable of producing a notable strengthening effect [6]. In the case of Ti alloys, the joint introduction of Al and V enabled the formation of a dualphase $\alpha + \beta$ (HCP – BCC) microstructure characterised by a combination of strength, ductility and fatigue resistance depending on the processing [7]. Nevertheless, all of the aforementioned alloys tend to utilise a primary alloying element, namely Fe, Al and Ti respectively, while the secondary alloying additions remain at relatively low concentrations. An exception to this would be copper – zinc (Zn) and copper – tin (Sn) alloys, otherwise known as brasses and bronzes respectively. Both of these systems contain elevated amounts of both Cu and Zn or Sn. This design approach enables a good combination of strength, machinability and corrosion performance in such alloys depending on their chemical composition and microalloying additions [8]. There is also the case of nickel (Ni) base superalloys which are characterised by a wide range of properties depending on their chemical composition. They tend to incorporate alloying elements such as Cr, Fe, Al, but also less common ones such as cobalt (Co), hafnium (Hf), rhenium (Re) and many more, each time tailored to the application they need to address. Apart from making their metallurgy particularly complex, these alloying additions can have notable effects on the mechanical properties of Ni-base superalloys, including creep or fatigue

resistance alongside good corrosion performance. Typically, while Ni still remains as the primary element, other alloying elements are also notable elevated in terms of their concentrations [9]. Nonetheless, it can be argued that most modern alloys are characterised by one, two, or in extremely rare case three principal alloying elements. This was predominantly deliberate as in alloys comprised from an increasing number of alloying elements navigating their compositional landscape can be challenging. As a matter of fact, considering metastable conditions and the associated microstructures and constituent phases the complexity of thermodynamic description increases dramatically. Therefore, alloy design approaches have been thus far limited to incrementally improving well-studied compositions. Nevertheless, as new engineering challenges emerge, the development of novel alloys and even alloy design approaches in their entirety may become an inevitability. Naturally, there are beacons of innovation lying in simpler systems such as binary alloys through the discovery of superconductors and quasicrystals. Nevertheless, one may argue that these inceptions pale in comparison to the progress made in other fields of materials science [3].

One of the more dominant global engineering challenges of transportation sector is the reduction of greenhouse gases emissions (GGE). As the EU-wide targets for 2030 require a reduction of at least 40% GGE compared to their 1990 levels, a 32% share for renewable energy and an over 32.5% improvement in energy efficiency [10, 11], it is paramount that the automotive sector adapts to these demands. Automotive manufacturers have used multiple approaches towards achieving higher fuel efficiency and complying with the GGE emission targets. Nevertheless, the more efficient means of attaining such a goal is currently through weight reduction of the structural parts of a vehicle. However, existing lightweight materials tend to either not satisfy the relevant structural demands or impose an elevated manufacturing cost. In the automotive sector specifically, these efforts have been targeted towards the replacement of steel, as the dominant structural material, with primarily aluminium alloys or composite materials [12]. To date though, through the introduction of 3rd generation advanced high strength steels (AHSS) to the market, steel remains the preferred material for such applications [13]. Therefore, the development of novel lightweight materials without compromising structural integrity has become a focal point in the field of alloy design. Multicomponent alloys (MCAs) could prove to be an asset in tackling this challenge due to their compositional flexibility. This allows for the manufacturing of alloys with properties tailor-made for their application. Subsequently, research concerning High Entropy Alloys (HEAs) has seen massive growth in the latest years [14, 15].

1.1 Aims and Objectives

This work concerns the determination of the feasibility of MCAs for application in environments demanding lightweight high stiffness components. Given the vast compositional space of MCAs the use of computational tools will be paramount for identifying potential compositions of interest. Experimental work will be carried out alongside the computational approaches to verify the relevant predictions and proceed with the optimisation of candidate compositions. The relevant objectives are:

1. Devise a methodology for extracting the elastic properties of candidate MCA compositions.
2. Identify a candidate system and highlight potential compositions of interest to be experimentally manufactured, tested, and optimised.
3. Understand the factors influencing the elastic properties in the tested MCA systems.
4. Explore the wider processability of candidate alloys by developing material and processing routes to allow sufficient ductility.

1.2 Thesis Overview

In total, this thesis consists of nine chapters including the current introductory chapter. The contents of each chapter are summarised here:

Chapter 2 provides the overview of the state of the art concerning the development of MCAs, starting with the inception of the concept of High Entropy Alloys (HEAs) and the transition from HEAs to MCAs with a particular focus on body centred cubic (BCC) MCAs. Additional information will be lay out regarding the computational design of MCAs alongside the current general trends in the field. Lastly, certain mechanisms and phenomena pivotal for the context of the thesis will be highlighted and explained.

Chapter 3 focuses on the experimental and computational methodologies used for this work regarding the alloy discovery, design and selection process, and the associated characterisation and mechanical testing techniques required for unveiling properties of interest.

Chapter 4 presents the development of a methodology for predicting the elastic properties of any single phase or multiphase MCA with a focus on the equiatomic AlTiVCr and AlTiVCr-Si_{7.2} systems which were found to exhibit particularly elevated elastic properties.

Chapter 5 explores the challenges associated with the successful manufacturing of AlTiVCr-based alloys and providing insight on the pathways available for tackling the lack of ductility they exhibit.

Chapter 6 proposes, applies, and confirms a methodology for suppressing a phase transformation thought to be the culprit for the lack of ductility. Nevertheless, it is discovered that the manufacturing challenges would actually be associated with other, inherent properties of the material.

Chapter 7 presents an investigation of a wide compositional field through the use of computational methods. Potential AlTiVCr-based compositions are identified and are experimentally tested. This reveals an interesting phenomenon which seems to dictate the manifestation of elevated elastic properties and at the same time phase stability in the present system.

Chapter 8 is a summary of the findings of the thesis, highlighting the most important points.

Chapter 9 proposes future work based on the concepts, ideas and findings made within the context of this thesis.

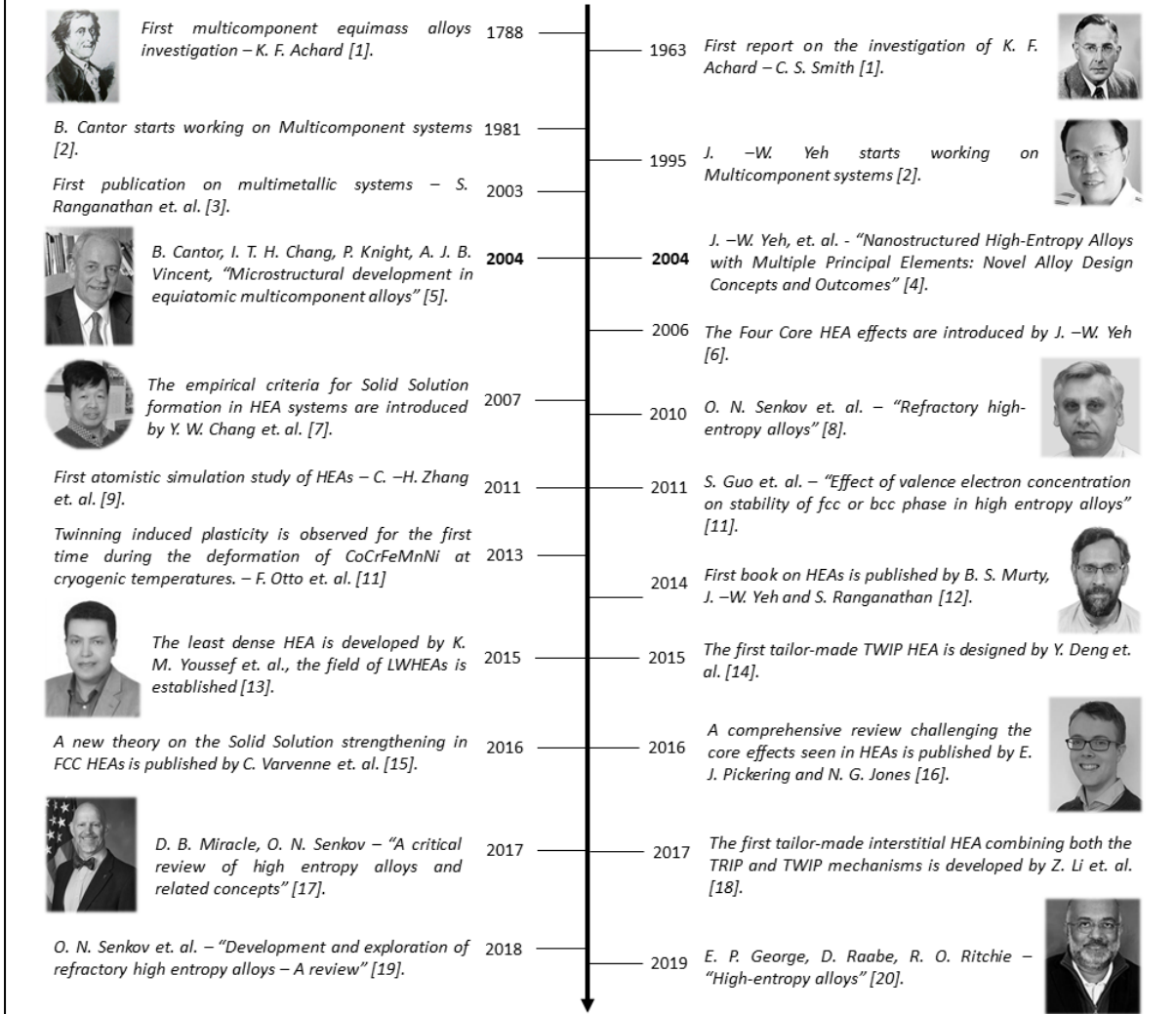
2. Literature Review

2.1 High Entropy Alloys (HEAs)

High Entropy Alloys (HEAs) are a novel class of metallic materials first explored by Cantor and Yeh separately in the early 2000s (Figure 1). Their motivation was to explore the central region of multicomponent alloy phase space, emphasising the achievement of a single phase solid solution. These alloys were comprised of five or more alloying elements at concentrations between 5-35 at. %, originally in equiatomic combinations, and were demonstrated in some cases to form single phase FCC solid solutions. The most famous and well-studied alloy of this category would be equiatomic CrMnFeCoNi otherwise known as the “Cantor” alloy. Their single phase nature enabled the manifestation of exceptional mechanical and anti-corrosive properties, even at elevated temperatures [15, 16]. These observations were subsequently based upon four principal effects reportedly present in HEAs [17-22]:

- A high configurational entropy owing to their multicomponent nature, which plays a dominant role on the systems’ Gibb’s free energy; thus, favouring the formation of a solid-solution over intermetallic phases. Therefore, the number of phases typically observed in HEAs is far less than the maximum number allowed according to Gibb’s phase rule [23].
- Highly distorted lattices due to the size difference between the different alloying elements introduced in an HEA, allowing for exceptional solid-solution strengthening [23].
- Sluggish diffusion kinetics since the mobility of alloying elements through a multi-component single-phase matrix is severely hindered. Hence, the nucleation and growth of additional phases is delayed. This enables a greater degree of control during thermomechanical treatments and the achievement of improved mechanical properties [23].
- A “cocktail effect” arising from the complexity of HEA compositions which results in properties that differ significantly from those of the forming elements, and are not predicted by the rule of mixtures [23].

High Entropy Alloy Development Timeline



References *Images were labeled for reuse or extracted from academic's individual webpages.

[1] C. S. Smith, "Four outstanding researchers in metallurgical history". American society for testing and materials, Baltimore, MD, (1963).

[2] B. S. Murty, J. -W. Yeh, S. Ranganathan, P. P. Bhattacharjee, "High-Entropy Alloys". Elsevier, (2019).

[3] S. Ranganathan, "Alloyed pleasures: multimetallic cocktails". *Curr. Sci.*, **85**, (2003), 1404-1406.

[4] J. -W. Yeh, S. -K. Chen, J. -Y. Gan, T. -S. Chin, T. -T. Shun, C. -H. Tsau, S. -Y. Chang, "Nanostructured High-Entropy Alloys with Multiple Principal Elements: Novel Alloy Design Concepts and Outcomes". *Adv. Eng. Mat.*, **6**(5), (2004), 299-303.

[5] B. Cantor, I. T. H. Chang, P. Knight, A. J. B. Vincent, "Microstructural development in equiatomic multicomponent alloys". *Mat. Sci. Eng. A*, **375-377**, (2004), 213-218.

[6] J. -W. Yeh, "Recent progress in high-entropy alloys". *Ann. Chimie Sci. Materiaux*, **31**, (2007), 633-648.

[7] Y. W. Chang, N. J. Kim, C. S. Lee, "Solid solution formation criteria for high entropy alloys". *Mat. Sci. For.*, **561-565**, (2007), 1337-1339.

[8] O. N. Senkov, G. B. Wilks, D. B. Miracle, C. P. Chuang, P. K. Liaw, "Refractory high-entropy alloys". *Intermetallics*, **18**(9), (2010), 1758-1765.

[9] C. -H. Zhang, M. -H. Lin, B. Wu et al., "Explore the possibility of forming fcc high entropy alloys in equal-atomic system CoFeMnNiM and CoFeMnNiSmM". *J. Sh. J. Uni. (Science)*, **16**, (2011), AN: 173.

[10] S. Guo, C. Ng, J. Lu, C. T. Liu, "Effect of valence electron concentration on stability of fcc or bcc phase in high entropy alloys". *J. App. Phys*, **109**, (2011), AN: 103505.

[11] F. Otto, A. Dlouhý, Ch. Somsen, H. Bei, G. Eggler, E. P. George, "The influences of temperature and microstructure on the tensile properties of a CoCrFeMnNi high-entropy alloy". *Acta Mat.*, **61**(15), (2013), 5743-5755.

[12] B. S. Murty, J. -W. Yeh, S. Ranganathan, "High-Entropy Alloys". Elsevier, (2014).

[13] K. M. Youssef, A. J. Zaddach, C. Niu, D. L. Irving, C. C. Koch, "A novel low-density, high hardness, high-entropy alloy with close-packed single-phase nanocrystalline structures". *Mat. Res. Lett.*, **3**(2), (2015), 95-99.

[14] Y. Deng, C. C. Tasan, K. G. Pradeep, H. Springer, A. Kostka, D. Raabe, "Design of a twinning-induced plasticity high entropy alloy". *Acta Mat.*, **94**, (2015), 124-133.

[15] C. Varvenne, G. P. M. Leyson, M. Ghazisaeidi, W. A. Curtin, "Solute strengthening in random alloys". *Acta. Mat.* **124**, (2017), 660-683.

[16] E. J. Pickering, N. G. Jones, "High-entropy alloys: a critical assessment of their founding principles and future prospects". *Int. Mat. Rev.*, **61**(3), (2016), 183-202.

[17] D. B. Miracle, O. N. Senkov, "A critical review of high entropy alloys and related concepts". *Acta Mat.*, **122**, (2017), 448-511.

[18] Z. Li, C. C. Tasan, H. Springer, B. Gault, D. Raabe, "Interstitial atoms enable joint twinning and transformation induced plasticity in strong and ductile high-entropy alloys". *Sci. Rep.*, **7**, (2017), AN: 40704.

[19] O. N. Senkov, D. B. Miracle, K. J. Chaput, J. -P. Couzinie, "Development and exploration of refractory high entropy alloys - A review". *J. Mat. Res.*, **33**(19), (2018), 3092-3128.

[20] E. P. George, D. Raabe, R. O. Ritchie, "High-entropy alloys". *Nat. Rev. Mat.*, **4**, (2019), 515-534.

Figure 2.1. A timeline concerning the development of the High Entropy Alloy field.

Subsequently, these unique properties of HEAs led to a significant increase in interest surrounding such alloys due to their vast potential for application in various fields. However, as research in the field progressed, doubts were raised concerning the evidence of those original core effects [15]. It was demonstrated that in most HEAs systems secondary phases would form after prolonged heat-treatments even in the originally documented single-phase HEAs [24]. It was also identified that in the cases where indeed the HEA would form a stable single-phase solid solution, this could be attributed to a lower enthalpy term relating to the formation of secondary phases [25]. Additionally, the formation of secondary phase particles (SPPs) was observed in several as cast HEAs even in the cases of subjected to rapid cooling [26]. Furthermore, computational and experimental assessments of HEAs demonstrated a level of lattice strain similar to that encountered in binary alloys. This implies that the magnitude of those lattice strain-induced effects could have originally been overestimated. While it was thought that the difference between the lattice parameter of HEAs compared to their alloying constituents would result in highly strained structures the opposite may in fact be the case. The dilated structures characterising HEAs may in fact exhibit reduced local strains given that the dilation itself takes place to minimize the internal strain energy. Nevertheless, relevant experimental studies focusing on the assessment of the local lattice strains remain scarce. As such, additional dedicated studies need to be carried out to shed light regarding the true magnitude of this effect in HEAs [23, 27-29]. Regardless, the seeds for an innovative and flexible alloy design approach had been planted, allowing for the development of novel composition straying from the original single-phase solid solution concept.

2.1.1 High Entropy alloys behaviour understanding

Given the property flexibility that HEAs originally displayed, a deeper understanding of the mechanisms involved became of paramount importance to effectively design novel compositions. Generally, HEAs that tend to crystallise in highly symmetric structures have been the focus of investigations [30]. Further research on the Cantor alloy has demonstrated the manifestation of elevated mechanical properties at lower temperatures with a lower strength-temperature dependence for the higher temperature range [27]. It was additionally seen that subjecting the alloy to stresses near the fracture stress at room temperature would result in twinning behaviour. However, when the same experiment was repeated under cryogenic conditions, twinning behaviour was observed significantly earlier resulting in exceptional toughness [31]. This case is the opposite of most materials where exposure to lower temperatures results in more brittle behaviour. In turn, this led to investigations regarding the

critical resolved shear stress (CRSS) dependence of the Cantor alloy on the deformation temperature. It was observed that the CRSS values during testing at cryogenic temperatures were significantly higher than those observed under ambient testing conditions [32]. This led to the development of new theories regarding solid solution strengthening evident in FCC HEAs as such a level of solution strengthening would not be expected in cases where the atomic radii of the alloying elements do not differ more than 1% [33, 34]. As for BCC alloys, one of the more interesting categories would be the case of Refractory HEAs (RHEAs) otherwise named Senkov alloys, with the most prominent one being the TiZrHfNbTa alloy [34, 35]. This displays a single BCC phase with relative dendritic segregation upon manufacturing, and was originally one of the few RHEAs which showed a degree of ductile tensile behaviour at room temperature. However, it later became apparent that the alloy was in fact metastable and would decompose in two BCC phases upon cold rolling and subsequent annealing at 800°C [36]. Future studies would further demonstrate additional variations of such transformations for different thermomechanical treatment conditions resulting in the embrittlement of the alloy in most cases [37, 38]. It thus became clear that the focal point of HEA research had originally been their initial manufacturing and the verification of their single-phase nature in their as cast condition and very few investigations were initially made regarding the heat-treatments of said HEAs or the in-depth characterisation of the phases. Subsequently, one of the current main points of interest regarding HEA research is the investigation of their thermomechanical processing (TMP) routes in respect to phase formation and the improvement of their mechanical properties [14].

Before discussing TMP of HEAs the effects of various alloying additions need to be introduced given that their behaviour can be quite different compared to that encountered in conventional compositions. One such alloying addition is aluminium (Al), which plays a pivotal role regarding phase stability. More specifically, it has been shown that in FCC HEAs a progressive increase of Al leads to the formation of a BCC phase [39-43]. This tuning is achieved through the manipulation of the valence electron concentration (VEC) or due to a notable atomic size difference, which will be discussed in a following chapter. In refractory BCC HEAs however, the addition of Al leads to the formation of the ordered B2 phase, thus compromising the ductility of these systems [40-42, 44]. This contrasts with the typical role of Al in conventional systems as an FCC stabiliser [43]. Furthermore, in stark contrast to conventional systems Al does not typically form intermetallic phases in HEAs, except in cases where particularly elevated concentrations of Al would be encountered [45]. Therefore, it becomes apparent that

otherwise typical alloying presumptions may not necessarily apply when designing multicomponent systems. Nevertheless, in terms of the mechanical properties most alloying elements were seen to behave in the expected manner in accordance with the solid solubility rules in cases where HEAs would end up forming solid solutions [46-48]. Additionally, in cases where secondary phases may form, their effects usually match those encountered in conventional alloys. For example, the formation of sigma (σ) and Laves phases leads to an increase in hardness and a reduction in ductility, while the use of atom types with appropriate differences in atom size leads to a progressive increase in strength [41]. As for other strengthening mechanisms (e.g. precipitation hardening) these too can manifest given proper alloying design as will later be discussed with the more general field of Multicomponent Alloys (MCAs). It can be concluded however that particular attention needs to be paid to the rules dictating phase formation in both HEAs and MCAs. At the same time, it would seem that the principles upon which HEAs were founded, particularly in regard to their single phase nature, were exaggerations of the originally observed phenomena. As such, they have been referenced here to provide a historical background concerning the inception of the field of HEAs rather than to be seen as “ground truths” characterising the properties of said alloys.

2.1.2 Empirical Solid Solubility Rules and Phase Formation Criteria

Before proceeding any further with the evolution of HEAs it is important to underline certain principles that have been developed for predicting solid solution (SS) formation in these systems. Achieving single phase microstructures is a critical design factor in HEAs that will also play a pivotal role in this research when designing Multicomponent Alloys (MCAs).

From a thermodynamic standpoint, the stability of an alloy can be described through the Gibbs free energy term as seen in Eq. 2.1 [49]:

$$\Delta G_{mix} = \Delta H_{mix} - T\Delta S_{mix} \quad \text{Equation 2.1}$$

where ΔG_{mix} the Gibbs free energy, ΔH_{mix} the enthalpy of mixing, T the temperature in Kelvin and ΔS_{mix} the entropy of mixing of a particular alloying system.

As previously mentioned, HEAs generally tend to have a higher entropy of mixing, otherwise known as configurational entropy, compared to conventional alloying systems; an effect which, although overestimated, is still present in these systems [15]. The configurational entropy (ΔS_{conf}) is defined according to Eq. 2.2 [49]:

$$\Delta S_{conf} = -k \ln w = R \ln n \quad \text{Equation 2.2}$$

where ΔS_{conf} the configurational entropy, k the Boltzmann's constant, w the number of ways of mixing, R the ideal gas constant (8.314 J/kmole), n the number of alloying elements.

It can be observed that the configurational entropy increases proportionally to the number of alloying elements for a given alloy. Therefore, if this were the only factor, one would expect that HEAs with the greatest number of alloying elements would be the more thermodynamically stable ones. Nevertheless, research has shown that alloys characterised by a high configurational entropy could still decompose into multiple phases, while all single phase HEAs were shown to have a high configurational entropy. This means that configurational entropy is not a useful predictor regarding solid solution formation in HEAs [25]. This also shows that the enthalpic term in Eq. 2.1 should also be playing an important, if not dominant, role regarding phase formation in HEAs, especially at lower temperatures where the contribution of the entropic term is reduced [15, 26, 50]. Therefore, additional descriptors of SS formation in HEA systems would need to be employed to enable sensible predictions to be made.

Apart from ΔH_{mix} and ΔS_{conf} , a set of empirical rules was proposed by Singh and Subramaniam [51], Guo et al. [52] and Zhang et al. [53] to predict solid solution formation in multicomponent systems. In total they identified four parameters, namely the atomic size difference (δ), the melt-interaction parameter more commonly known as the omega (Ω) parameter, electronegativity difference ($\Delta\chi$) and the valence electron concentration (VEC), expanding upon the Hume-Rothery rules for solid solubility [54]. The atomic size difference (δ) is related to the size of the solute atoms of a solid solution and their concentration in said solid solution, according to Eq. 2.3 [53]:

$$\delta = \sqrt{\sum_{i=1}^N C_i \left(1 - \frac{r_i}{r_{mean}}\right)^2}, r_{mean} = \sum_{i=1}^n C_i r_i \quad \text{Equation 2.3}$$

where δ the atomic size difference, N the number of solute atoms, c the atomic percentage of a solute, r the atomic radius of each solute and r_{mean} the average atomic radius of all solute atoms calculated in respect to their concentrations in the solid solution.

The omega parameter (Ω) definition is rather arbitrary and does not, strictly speaking, correspond to a physical parameter in itself, rather a combination of the melting point T_m , configurational entropy ΔS_{conf} and the enthalpy of mixing ΔH_{mix} as seen in Eq 2.4 [51]:

$$\Omega = \frac{T_m \Delta S_{conf}}{|\Delta H_{mix}|}, T_m = \sum_{i=1}^N c_i (T_m)_i \quad \text{Equation 2.4}$$

where the omega parameter Ω , mean melting point of all solute atoms T_m , the configurational entropy ΔS_{conf} and the enthalpy of mixing ΔH_{mix} .

The electronegativity difference ($\Delta\chi$) is directly related to the electronegativity of each constituent alloying element (Eq. 2.5) [51]:

$$\Delta\chi = \left[\sum_{i=1}^N c_i (\chi_i - \chi_{mean})^2 \right]^{1/2}, \chi_{mean} = \sum_{i=1}^N c_i \chi_i \quad \text{Equation 2.5}$$

where $\Delta\chi$ the electronegativity difference, χ_i the Pauling electronegativity of each constituent alloying element and χ_{mean} the average electronegativity of all solute atoms calculated in respect to their concentrations in the solid solution.

The valence electron concentration (VEC) is the number of valence electrons per formula unit and is derived by averaging out the VEC of all solute elements while considering their concentration in the solid solution as per Eq. 2.6 [52]:

$$VEC = \sum_{i=1}^N c_i VEC_i \quad \text{Equation 2.6}$$

where VEC the valence electron concentration of either each alloying element VEC_i or the solid solution itself VEC .

In contrast to the other parameters, VEC is used to predict the crystal structure of the solid solution rather than its direct formation. In cases where $VEC \leq 6.87$ the solid solution is expected to adopt a BCC crystal structure, while for $7.84 \leq VEC$, an FCC crystal structure is expected instead. Naturally VEC values between 6.87 and 8.0 hint at the formation of a dualphase BCC-FCC structure instead, and the formation of a single solid solution would be unexpected in this range [55].

Should the designed alloys satisfy all the relevant requirements for solid solution formation as described by the requirements expressed in Table 2.1 by considering the limitations set by the empirical rules, the formation of a single solid solution may be probable. Nevertheless, in practice these rules may only act as rough indicators and should not be considered “ground truths” as they have been shown to incorrectly predict the phase structure of several MCAs; however, the empirical rules are a quick method for evaluating a wide range of compositions.

In the context of this thesis and the surrounding work, the empirical parameter which would prove to be the most vital for predicting the formation of solid solutions would be Ω . As seen in chapters involving novel alloy design, the Ω parameter would agree with both computational predictions and the experimental findings in all cases where its value would not lie between 1.0 and 1.1 where a degree of uncertainty was observed.

Table 2.1 Empirical parameters for the prediction of solid solution formation in multicomponent systems.

Parameter	Conditions for solid solution formation
Enthalpy of mixing (ΔH_{mix})	$-15\text{kJ/mol} \leq \Delta H_{\text{mix}} \leq 5\text{kJ/mol}$ [55]
Configurational entropy (ΔS_{conf})	$13.38 \leq \Delta S_{\text{conf}}$ [55]
Melt-interaction parameter (Ω)	$1.1 \leq \Omega$ [56]
Atomic size difference (δ)	$\delta \leq 6.6$ [55]
Electronegativity difference ($\Delta\chi$)	As close to 0 as possible. [51]

The field of HEAs is incomparably vast in relation to any other explored alloying system due to the many possible compositional arrangements, and there are many challenging aspects to their design and manufacturing. It is crucial that additional systems of this type are investigated and the phenomena behind their complex behaviours are properly understood. Currently, HEAs are characterised by elevated mechanical properties at a range of temperatures and in some cases by unexpected properties altogether. Still, there are aspects of their design relating to their ductility and oxidation resistance that leave more to be desired. In addition, more complex alloys in terms of both their composition and microstructural features are expected to be uncovered, such as the case of interstitial HEAs (iHEAs) [57, 58]. These alloys have only very recently been first investigated and are documented to possess improved strength and ductility owing to their interstitial additions. It is also important to identify possible applications where the unexpected properties of certain HEAs may be used [49]. Consequently, advanced and precise computational screening tools are required to guide relevant HEA design accordingly, such as quantum-mechanical calculations through *Ab-initio* or refined DFT.

2.1.3 Applications of High Entropy Alloys

Although HEAs have displayed significant potential they have yet to be integrated into commercial product lines and as such their scope of current application remains rather limited. Nevertheless, their concept has introduced a new field in alloy design, encompassing a wide range of applications. It is hoped that in the future HEAs may substitute conventional materials in challenging applications demanding advanced or tailor-made properties. HEA research in general has moved to address engineering challenges in applications demanding a wide range of properties (Table 2.2) [49].

Table 2.2 Table displaying the desirable HEA properties for each field of application or application demand [49].

Material Property	Demand of Applications
Strength and toughness	Elevated mechanical properties (e.g., automotive)
Wear resistance	Adhesion, abrasion, erosion resistance (e.g., tooling)
High temperature resistance	Softening, oxidation, hot corrosion, thermal shock, thermal fatigue, creep resistance (e.g., gas turbines)
Chemical resistance	Resistance to general, pitting and stress corrosion cracking (e.g., naval)
Radiation damage resistance	Structural applications in nuclear reactors
Light weight	Energy saving and efficiency application (e.g., automotive)
Magnetism	Soft or hard magnetic properties and higher Curie points (e.g., electric motors)
Electrical resistance	Low TCR in large temperature range, superconductivity (e.g., electrotechnical applications)
Thermal conductivity	Thermal conduction for heat spreaders, thermal barrier applications (e.g., heat exchangers)
Green requirements	Low pollution, lead-free, cadmium-free, recyclable, low energy consumption
Functional properties	Antistick, antibacterial, hydrogen storage, dielectrics, ionic conductivity, catalysts, shape-memory alloys

Apart from exhibiting interesting, even exotic properties, test examples of some engineering components have been manufactured. These include cast bearings, surface hardened tools, coatings for anti-adhesive molds and solar cells, solders for welding hard metals and steels and

thin film resistors. Eutectic HEAs show significant promise for immediate use as cast components for ship propellers, replacing bronze or stainless steel ones (AlCoCrFeNi_{2.1}) [49]. The only fields where HEAs have been successfully introduced to the market to this day consist thermal sprayed coatings for marine structures and brazing filler metals. The company Nanosteel developed the SHS 7570 HEA (Table 2.3) to be used for thermal spray coating the hull of tugboats to act as a protective coating [49].

Table 2.3 Composition of SHS 7570 alloy [49].

Upper compositional limits of SHS 7570 alloy (at. %)							
Fe	Cr	Mo	W	Mn	B	C	Si
36	22	7.2	1.2	1.7	21	7.6	3.3

Brazing filler MCAs have garnered notable research interest over the years [59-63] and have also transitioned into industrial application. Titanium Brazing Inc. have also introduced a series of brazing filler MCAs such as amorphous foils, wires, powders or pastes, heat-resistant filler metals, HEA filler metals, and even low-temperature Al-based filler metals, addressing a range of brazing temperatures between 510-1160°C. All of these alloys have received relevant tradenames.

Multiple patents concerning HEAs have been submitted and even approved. The total number of patents reached about 300 at the end of 2017. Most of these patents were applied for by companies and most are related to the development of thin film coatings, high strength alloys, cemented carbides, cermets and spray deposited hard facing metals. Overall, this shows that although the HEA market is still in its infancy, multiple industries and companies are supportive of the development of HEAs. This new category of materials exhibits a wide variety of properties and as such HEAs may find application in various fields while partially replacing traditional materials or synergistically operating alongside traditional components [49].

2.1.4 Body Centred Cubic (BCC) High Entropy Alloys

Refractory body-centered cubic (BCC) high-entropy alloys (HEAs) are a class of HEAs that started to gain traction in recent years due to their exceptional potential for high-temperature applications. Alloying elements crystallising in the BCC structure are generally characterised by high strength and elevated melting points alongside high-temperature stability, properties which tend to carry over to alloys incorporating them. The concept of body centred cubic (BCC) HEAs or rather viable examples of this concept originated from the work of Senkov et

al. [64]. They noticed a gap in HEA literature where, although there was a particular emphasis placed upon the development of transition metal HEAs including iron (Fe), nickel (Ni), cobalt (Co) and copper (Cu), there was a complete absence of HEAs constituted of refractory elements. Initial attempts to design BCC HEAs were fruitless due to the higher melting points and brittleness of the resulting alloys, the former making their homogenisation and heat treatment in general a challenging task [30, 64]. The breakthrough in this field was made through the design of equiatomic TiZrHfNbTa, otherwise known as the Senkov alloy, in 2011 which exhibited reasonable ductility at room temperature [34]. Not only that, but it was demonstrated that the alloy could be heavily cold rolled (86% thickness reduction) without failing [36], as such enabling the possibility of thermomechanical processing (TMP) towards the optimisation of the grain structure [65]. This result must be underlined as cold rolling an HEA with a BCC crystal structure had not been previously achieved. Nevertheless, a minimal volume fraction of second phase particles (SPPs) was also observed after annealing post cold working. As previously established it was also discovered that the TiZrHfNbTa alloy would decompose into multiple phases. The field of BCC HEAs had nonetheless been established giving birth to multiple different refractory alloy design principles including single phase refractories, multi phase refractories and refractory superalloys RSAs which will be covered in a following chapter. Alloys falling within this category would be characterised by high hardness and relatively low density. Some BCC alloys also displayed high temperature strength surpassing that of Ni-base superalloys while retaining a lower density on par with titanium (Ti) alloys [66-70]. Various investigations also highlighted the potential for lightweight high entropy alloy (LWHEA) design; however, more research is required to confidently pinpoint candidate alloying systems. Lightweight HEAs originated from the concept of RHEAs, aiming to achieve a density reduction while retaining good mechanical performance at elevated temperatures [71]. The first attempts at designing such alloys resulted in refractory compositions with relatively high density in comparison to materials used in lightweight applications [34, 35]. Eventually, this led to the development of alloys exhibiting densities in the region of $3 \text{ g}\cdot\text{cm}^{-3}$ and exceptional hardness; although without a full assessment of their mechanical behaviour or ease of manufacturing [72, 73]. A famous such alloy is the $\text{Al}_{20}\text{Li}_{20}\text{Mg}_{10}\text{Sc}_{20}\text{Ti}_{30}$ LWHEA with a density of $2.67 \text{ g}\cdot\text{cm}^{-3}$ and a single-phase nanocrystalline structure [74]. It is therefore evident that HEAs present a wide range of properties that can potentially be fine-tuned to suit the needs of virtually any application through proper alloy design and manufacturing routes.

Around the time of these breakthroughs in the field of refractory BCC HEAs, the scientific community seemed to be in notable turmoil regarding the progress of HEAs. It had started to become clear that the mechanisms thought to dictate the initially reported “exotic” properties of HEAs were not consistent. A number of HEAs thought to be single phase were found to decompose into multiple phases through heat treatments [20, 75]. This was due to the fact that most alloys discovered and assessed up until this point were investigated in the as-manufactured condition, meaning that the resulting microstructures would refer to a potentially metastable state [76]. Therefore, various research groups across the globe devised different pathways for the development of novel compositions.

2.1.5 From High Entropy alloys to Multicomponent alloys (MCAs)

As a general trend, in the East, emphasis was placed on the identification of single phase systems conforming to the original HEA definition, while in the West the approach of further development of FCC HEAs started to emerge [20, 77]. By understanding and thoroughly investigating the fundamental mechanisms dictating the behaviour of HEAs it became clear that these were perhaps originally misunderstood. Although single phase alloy design could still be interesting, it would be difficult to achieve, challenging to sustain and could even prove to be restrictive when considering the design of alloys tailored to address a wide range of applications. As such, this steered research towards the assessment of multiphase systems. Multiphase microstructures allow for additional metallurgical mechanisms to come into play, therefore providing additional pathways for enhancing the mechanical properties. As such, a new category of alloys emerged titled Multicomponent (MCAs), Multi Principal Element (MPEAs) or Complex Concentrated (CCAs) alloys with the definitions and differences between these naming conventions remaining unclear to this day. In the context of the present thesis the term MCAs will be used to describe the broad type of alloys [78].

Regarding their mechanical properties, apart from solid-solution strengthening, which is the common trait of HEAs, further compositional manipulation would be aimed at enabling complex mechanical behaviour such as the inhibition of dislocation motion, either through the introduction of secondary strengthening phases or the activation of induced plasticity effects such as transformation (TRIP) and twinning (TWIP) induced plasticity [57]. A notable example of these alloys would be the novel grades of compositionally complex steels (CCSs). These are comprised of elevated amounts of manganese (Mn) and Al to enable the manifestation of a lightweight FCC matrix phase alongside the formation of shearable κ -carbides and non-shearable B2 (Ni-Al-based) particles through the introduction of carbon (C) and nickel (Ni)

[79]. Another case of CCS development achieved the design of Fe-Mn-Co-Cr-C alloy combining all the strengthening mechanisms at once. This was achieved by fine-tuning the chemical composition and the processing of the alloy by considering a mechanistic approach instead [57, 58, 80]. This new generation of HEAs would open pathways for exploring a broader landscape, including multiphase microstructures. The field of HEAs and MCAs presented new challenges, such as efficiently exploring the now unbounded hyper-dimensional design space. To address these challenges, the materials science community would need to innovate extensively towards the integration of data-mining techniques with computational and experimental approaches to accelerate materials discovery and innovation [78].

2.2 Body Centred Cubic Multicomponent alloys

It could be argued that the introduction of MCAs would have a somewhat liberating effect on research surrounding BCC HEAs and MCAs given that even the more prominent compositions were found to be unstable post heat treatment. Therefore, the focus shifted from paying attention to the design, manufacturing, and retainment of single phase BCC HEAs towards the property-driven design of potentially multiphase refractory BCC MCAs (RMCAs). This can be directly seen through the immediate adoption of the multi-principal element alloys (MPEAs) and Complex Concentrated Alloys (CCAs) terms by Miracle and Senkov [14] to describe compositions previously termed HEAs although not conforming to the term by definition standards. As the authors very clearly specified in their closing remarks of their work:

“No longer safe along corners and edges of ternary phase diagrams, the materials community is now thrust into an uncharted, hyper-dimensional territory that is difficult to conceive, difficult to visualize, and difficult to explore systematically. The vastness is frightening, and it beckons.”

- D. B. Miracle, O. N. Senkov [14]

2.2.1 Challenges of BCC MCAs and their resolution

Apart from redefining the taxonomy, definitions, classifications and the general nomenclature surrounding MCAs Miracle and Senkov also specified a number of challenges that would have to be resolved for this concept of RMCA design to flourish. At the time of their work only 29 RMCAs had been discovered, making that category of alloys quite immature compared to their FCC counterparts. Emphasis was placed on the control of microstructures in terms of the type, volume fraction, size, and morphology of SPPs or in general second phases in RMCAs. Furthermore, discovering the limits dictating BCC solid solution formation in non-equiatomic

compositions would be paramount for the establishment of multiphase microstructures. These were intended to contain multiple BCC matrices or a BCC matrix alongside SPPs to induce precipitation hardening [14]. At this time the $\text{AlMo}_{10}\text{NbTa}_{10}\text{TiZr}$ exhibiting a dualphase BCC – B2 microstructure had just been discovered and was sparking interest in terms of its potential mechanical properties [81]. Its microstructure was found to contain an ordered B2 matrix with cuboidal BCC plate-like particles dispersed homogeneously within the microstructure. It must be underlined that this microstructure manifested after heat treating at 1400°C for 24h followed by furnace cooling. The review by Miracle and Senkov also highlighted the lack of tensile testing data on RMCAs while the TMP of RMCAs had not been explored at all [14]. This is particularly important given that a severe drawback of RMCAs at that point was their notable lack of ductility. Nevertheless, a pathway for tackling this challenge would soon be facilitated through the work of Soni et al. [82].

The work by Senkov et al. [66] introduced a range of novel RMCAs, some of which exhibited the discrete cuboidal structures previously mentioned. One of these alloys was the $\text{Al}_{11.3}\text{Nb}_{22.3}\text{Ta}_{13.1}\text{Ti}_{27.9}\text{V}_{4.5}\text{Zr}_{20.9}$ which was exclusively characterised by this cuboidal dualphase microstructure which was significantly finer compared to the rest of the compositions investigated within the frame of that work. Compression testing revealed that this alloy entirely lacked room temperature ductility while it was characterised by a notable compressive strength and the highest specific strength compared to the rest of the alloys. The work of Soni et al. [82] aimed to achieve a proof of concept towards the enhancement of the ductility of high strength BCC – B2 dualphase RMCAs by manipulating their microstructure. To do this, they manufactured the $\text{Al}_{11.3}\text{Nb}_{22.3}\text{Ta}_{13.1}\text{Ti}_{27.9}\text{V}_{4.5}\text{Zr}_{20.9}$ alloy, subjected it to homogenisation treatment at 1200°C for 24h followed by furnace cooling which will be considered the reference alloy. The reference alloy was then heat treated at 1400°C for 20 mins followed by water quenching (WQ condition) while it was then aged at 600°C for 120h and subsequently water quenched (aged condition). It was observed that in the reference condition the alloy comprised of a dualphase BCC – B2 microstructure with the B2 phase corresponding to the matrix phase and the discrete plate-like particles to the BCC phase. The B2 phase was enriched in Al and Zr while the BCC in Nb and Ta. On the other hand the alloy in the WQ condition was characterised by a single phase BCC microstructure exhibiting weak B2 superlattice reflections. Atom probe tomography (APT) revealed a minor degree of clustering with certain regions becoming enriched in Al, Zr and Ti and others in Nb and Ta. This suggested that the alloy attained a single BCC crystal structure during the 1400°C heat

treatment with the early stages of compositional partitioning taking place during the quenching process. The aged condition instead exhibits a superalloy-like type of microstructure consisting of a bright continuous BCC matrix phase and homogeneously dispersed B2 SPPs arranged in a pattern. Once again, Al and Zr migrated to the B2 phase while the BCC phase is enriched in the rest of the alloying elements. This would become known as the first recorded case of a mechanism termed as “phase inversion” in RMCAs. In terms of the mechanical properties, the aged condition displayed a good combination of strength and ductility, while the reference condition exhibited peak strength but no ductility and the WQ condition the highest compressive ductility but limited strength in comparison to the aged condition [82].

Further investigation of the aging process in this system uncovered that the alloy was thought to initially decompose from the high temperature BCC phase, ending up producing a dualphase microstructure consisting of continuous B2 channels around cuboidal BCC precipitates. Although there is controversy surrounding the nature of the phase transformations in this system, two mechanisms were proposed in the original work. The high temperature BCC phase would spinodally decompose into two BCC phases with one of the two undergoing a chemical ordering process and attaining a B2 structure instead. On the other hand, it could be that the high temperature BCC phase would transform into a B2 phase through a chemical ordering process. The B2 phase would then spinodally decompose into two B2 phases, one of which would then transform back into a disordered BCC phase due to the ensued compositional changes. It needs to be underlined that, while both scenarios do propose the spinodal decomposition as the primary phase transformation, a miscibility gap is required for spinodal decomposition to manifest. Therefore, while the investigated alloy in the work of Soni did exhibit a miscibility gap, this is not a universally applicable mechanism since the lack of a miscibility gap does not enable phase separation [83, 84].

The chemical composition of both the BCC particles and the B2 channels would stabilise after aging for 5h at 600°C. This would roughly coincide with the point where the maximum hardness would be achieved pointing at a peak aged condition. Upon entering the overaging region the microstructure would evolve where the B2 phase would start becoming isolated into distinct particles and as such the BCC phase would become continuous; thus, phase inversion would be achieved and be associated with a notable drop in hardness. The reasoning behind the phase inversion process would lie in the differences between the elastic moduli of the BCC and B2 phase. Through the progression of the aging treatment, the composition of the BCC and B2 phase would continuously change until stabilising at roughly 5h. During this process, an

elastic inhomogeneity would develop between the BCC and B2, increasing the elastic energy of the system, therefore deeming the microstructure unstable. Subsequently, the morphology of the B2 phase would shift towards the formation of isolated spheroidised particles to minimise both the elastic strain and interfacial energy of the system. In turn, this would favour the coalescence of the nearest BCC particles and, as such, a continuous BCC network would be formed as seen in Fig. 2.2 [84]. This mechanism would spark the development of refractory high entropy superalloys (RSAs) although it would later be discovered that it would not be universally applicable to RSAs.

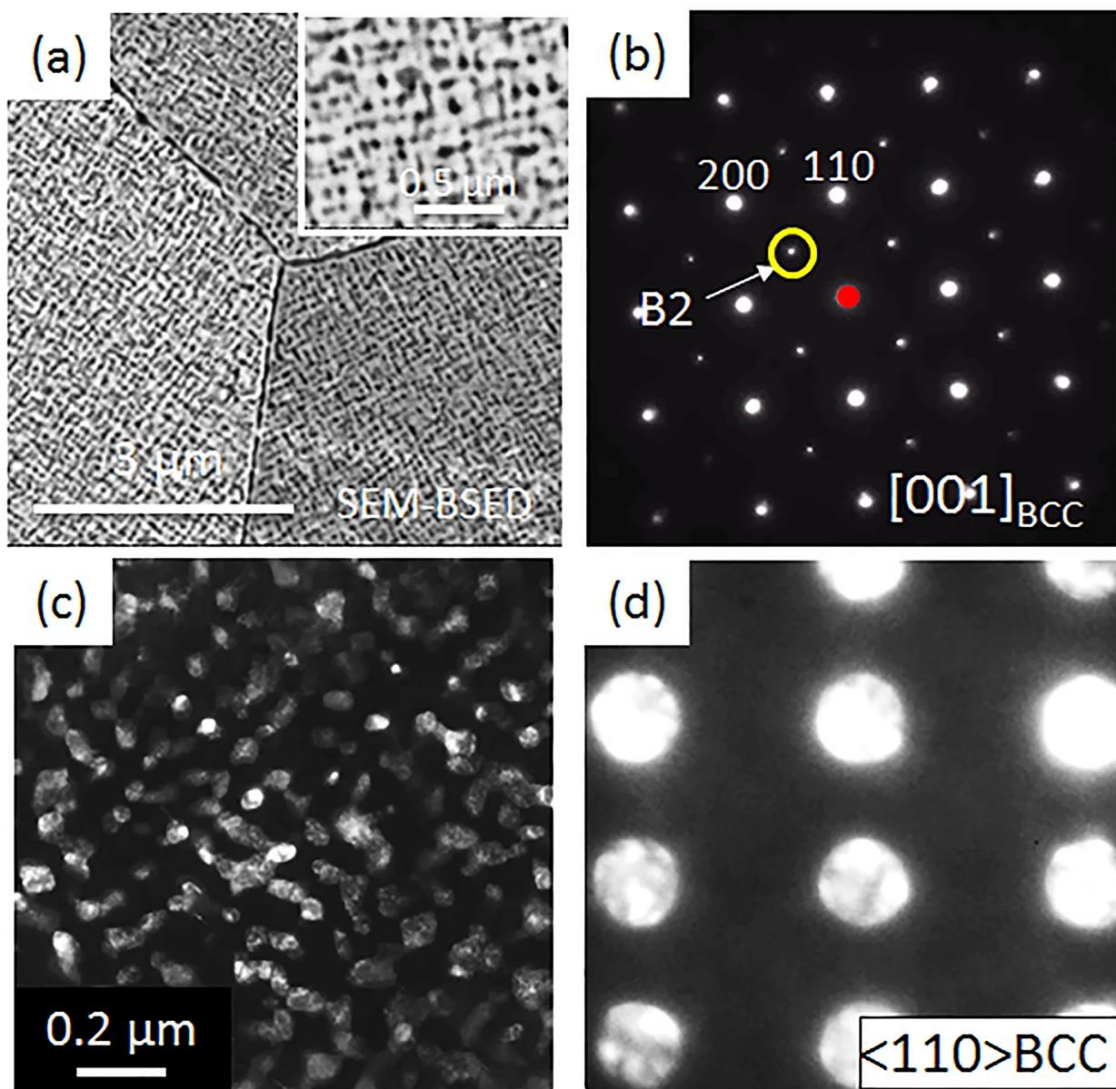


Figure 2.2 Microstructure of the $Al_{11.3}Nb_{22.3}Ta_{13.1}Ti_{27.9}V_{4.5}Zr_{20.9}$ alloy in the aged condition (a) BSE image, (b) diffraction pattern corresponding to the B2 phase, (c) DF TEM image originating from a B2 superlattice spot in the $\langle 001 \rangle$ axis and (d) diffraction pattern corresponding to the BCC phase (reproduced from [82]).

2.2.2 Development of novel BCC MCAs – Refractory high entropy superalloys (RSAs)

The developments in the field of RMCAs to solve the ductility issues this category of alloys exhibited gave rise to a new generation of RMCAs called high entropy superalloys (RSAs) [85]. The concept of RSAs originated from their distinct dualphase BCC(A2)-B2 microstructure which is reminiscent of the γ/γ' type of structures generally encountered in Ni-base superalloys. Given that dislocation mobility in A2 is much improved compared to the ordered B2 it would be possible to enable an adequate compromise between strength and ductility by achieving a proper ratio between the two phases. Nevertheless, the foundations for the design of BCC-base superalloys were laid even before the inception of the concept of HEAs by Naka and Khan in 1997 [86]. In their work, Naka and Khan attempted to utilise an intermetallic phase forming binary systems (e.g. Ni-Al) as the base where, through the addition of BCC transition metals an A2-B2 microstructure would be induced. Eventually, this led to the substitution of Ni with Ti and the design of alloys constituted of 3 to 6 alloying elements, one of which attained a dualphase A2-B2 microstructure. As the field of BCC RHEAs rose to prominence their original research resurfaced and led to the introduction of the concept or RSAs [85].

According to Miracle et al. [85], RSAs are defined as multicomponent alloys containing at least two refractory principal elements that exhibit a dualphase ordered-disorder microstructure similar to the γ/γ' and A2-B2. Furthermore, they need to possess an elevated volume fraction of distinct ordered particles surrounded by continuous channels of a disordered matrix phase, with the two phases being coherent or semi-coherent with one another. This aspect of the definition is however nebulous as the authors later specify that any alloy able to simultaneously display both the A2 and B2 phases could be considered an RSA. Apart from the refractory principal alloying elements (Cr, Hf, Ir, Mo, Nb, Os, Re, Rh, Ru, Ta, V, W and Zr), Ti and Al are also considered principal alloying elements based on the work of Naka and Khan and their general use towards the formation of the ordered phase. RSAs are also permitted to contain elevated amounts of non-refractory elements and any number of minor alloying elements. The main challenge with RSAs is to achieve an inversion of the equilibrium A2 (particles) – B2 (matrix) microstructure to enable the manifestation of adequate room temperature (RT) ductility without compromising the RT and high temperature (HT) mechanical properties, as seen in Fig. 2.3. At the same time, the B2 has been shown to become unstable at lower temperatures during prolonged exposure and as such, identifying systems that satisfy both design criteria can be quite an intensive task [85].

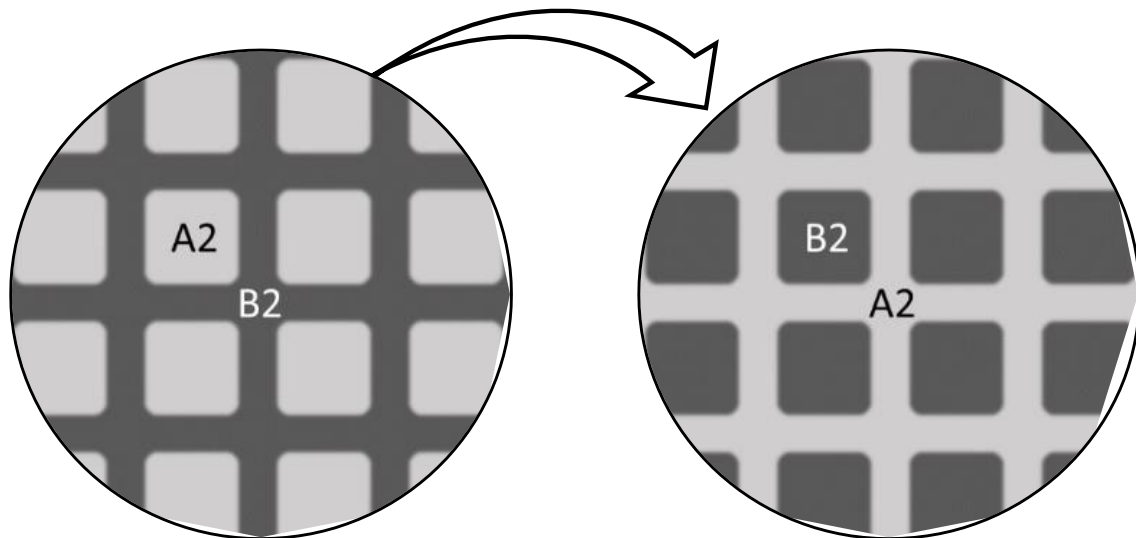


Figure 2.3 Phase inversion in BCC-RSAs moving from a B2 matrix alongside A2 particles at equilibrium to an A2 matrix alongside B2 particles post heat treatment.

According to Miracle et al. [85], one of the key directions for RSAs would be development for high temperature applications, aimed at replacing conventional alloys such as MAR-M247, INCONEL 718 or Haynes 230 while maintaining adequate RT ductility. This however requires a greater degree of optimisation of the microstructures commonly encountered in RSAs. Proper design of RSAs should lead to lower-density alloys with notable RT and HT mechanical properties [85]. Further points of assessment should be creep resistance, which is entirely absent from the literature surrounding RMCAs, and corrosion resistance, which has also not been investigated extensively. Lastly, certain suggested directions were provided regarding the exploration of novel RSA compositions [85]:

1. Exploration of the feasibility of Al substitution with other alloying elements capable of producing B2 phases such as the Nb-Ru and Ru-Zr system.
2. Additional research on the factors that dictate B2 stability and structure.
3. Development of experimental phase diagrams for novel RSA systems.
4. Understanding of the deformation modes that govern refractory B2 phases and systems incorporating them.
5. Achievement of balance between RT and high temperature ductility.

Overall, the creation of a framework for the development of RSAs but also RMCAs in general is paramount to the success of the field. Without clear directives or goals to guide the development of novel compositions, efforts in the field can become disorganised or misguided. Therefore, the contribution of this work was critical. Nevertheless, these also provide directives for the development of novel compositions and the associated goals, meaning that certain

deviations in the name of science would definitely be justified. Although the concept of RSAs and their high temperature properties is exciting for certain fields, others may be more interested in focussing on the potential of their room temperature properties instead.

2.2.3 Development of high specific stiffness RMCAs

High modulus alloys, with their elevated elastic modulus, are prized for their use in applications requiring stiffness, such as structural components and springs or may even find use in bimetallic and composite structures. In the automotive sector specifically, ultrahigh strength steels have seen prominent use for both advancing road safety and achieving weight reduction. The latter predominantly involves gauge reduction, utilising steels capable of striking a balance between mechanical properties and formability. When considering plate bending, stiffness is directly proportional to the Young's modulus and the plate thickness. Therefore, exclusively relying on gauge reduction, while effective for weight savings, diminishes stiffness. For applications like chassis and suspension components, enhancing specific rigidity is crucial for weight reduction. Subsequently, the development of materials exhibiting elevated specific stiffness combined with appropriate mechanical properties and formability is as a key challenge, holding potential to significantly reduce automotive structure weight while enhancing road safety and fuel efficiency [87].

One thing that becomes immediately clear when assessing the literature surrounding RSAs, RMCAs and HEAs in general is that experimental studies concerning their elastic properties are not very numerous [88-94], and is mostly to be found in the supplementary information in most published research. Furthermore, a wide range of experimental techniques has been used to assess these properties, while the associated alloys may have been heat treated or manufactured in different ways. As such, design of RMCAs with a focus on their elastic properties reliant on information from the published data in the field is not a feasible strategy, (the use of computational methods for this will be covered in a following chapter). Therefore, inspiration must be drawn from other fields where the concept of high modulus design is more mature, such as high modulus steels (HMS) otherwise known as high modulus metal matrix composite steels [13].

Attempts to extensively alloy steels with an aim to improve the Young's modulus but retain a low density have proven to be an ineffective strategy [95]. The concept of HMS is based on the incorporation of SPPs ceramic-like phases such as intermetallics, carbides, nitrides, or borides in an advanced high strength (AHSS) steel matrix. The idea is that the AHSS steel

matrix provides a strong and ductile foundation within which the SPPs can be artificially introduced during the manufacturing process (e.g. ex situ production, powder mixing, compaction) [13]. These SPPs, typically TiB_2 , are characterised by significantly elevated elastic properties combined with a lower density compared to the AHSS matrix. Therefore, their incorporation results in a drastic decrease in the density and increase in the stiffness of the HMS, reaching a specific Young's modulus of over $33 \text{ GPa m}^3 \text{ kg}^{-1}$ [96]. The volume fraction of these SPPs may reach 30% which is however the upper limit as a higher volume fraction of SPPs would compromise the ductility of the steel [13, 96]. Currently, the field of HMS is faced with notable challenges regarding the synthesis and downstream production strategies available for the manufacturing of this steel grade [13]. Drawing inspiration from this concept perhaps it would be possible, and simpler, to achieve in the field of RMCAs. This is due to the chemical flexibility associated with RMCA compositions where the formation of significant volume fractions of high modulus SPPs in a multicomponent matrix would have a similar effect. An even better approach however would possibly be the combination of the HMS and RSA concepts where the B2 phase could be optimised to attain elevated elastic properties with the A2 constituting a ductile matrix. Such a concept would have notable strategic advantages, especially regarding the manufacturing of said alloys. Since the formation of the A2 + B2 structures would exclusively be dictated by an optimisation of the composition and heat treatments, the use of sophisticated manufacturing techniques could perhaps be avoided.

2.2.4 AlTiVCr-based RMCAs

The equiatomic AlTiVCr alloy was originally designed and manufactured by Qiu et al. [97] during an endeavour to identify a potent lightweight single-phase HEA system. The alloy was documented to form the ordered $(\text{Ti}, \text{V})_{0.5}(\text{Cr}, \text{Al})_{0.5}$ B2 phase according to atom probe tomography (APT) and nearest neighbour analysis with temperature dependent DFT calculations, while the lattice parameter was measured at 3.06 \AA through a X-ray diffraction (XRD). This phase was also predicted to be more stable than a disordered BCC (A2) solid solution up to 900 K, with a bulk modulus of 151.6 GPa at room temperature according to temperature dependent DFT calculations and was measured to attain a hardness of roughly 500 HV. In another work Qiu et al. also investigated the corrosion properties of the equiatomic alloy, showing the formation of a passivation layer comprised of Al, Cr and V oxides, alongside metallic species capable of potentially providing adequate corrosion resistance [98]. Esmaily et al. carried out an investigation regarding the high temperature oxidation behaviour of the

alloy and discovered that the development of Ti and V containing oxides was instead favoured at temperatures above 700°C. Therefore, the alloy would not form a protective oxide film without additional compositional modifications [99].

In 2019, Huang et al. [100] investigated the AlTiVCr-C/B/Si_x systems, attempting to predict their thermodynamic behaviour through CALPHAD techniques and further increase the hardness of the alloy. Evidently, these modifications enabled the formation of secondary phases in most of the examined chemical compositions. In the case of the AlTiVCr-Si_x system, their TEM study verified the existence of both the secondary Ti₅Si₃ phase and the primary B2 matrix. However, their investigation was only limited to the as cast state of all specimens, meaning that the accuracy of their thermodynamic predictions was not extensively verified. Regardless, their CALPHAD simulations did imply that the B2 to A2 transformation temperature lied in the region of 873 – 1073 K [14, 44, 82-84, 101]. Nevertheless, transmission electron microscopy (TEM) investigations in the present system did not reveal such features. Therefore, the B2 phase in the investigated alloy was expected to be highly stabilised to the point where the cooling rate upon manufacturing was insufficient to sustain the high-temperature A2 phase in a metastable form at room temperature. It could also be thought that there was simply no high-temperature A2 phase to begin with as its existence had not been verified through experimental means. A later study by Cao et al. through DFT showed that from a theoretical standpoint the A2 and B2 phases should have minor energy differences and as such it would be difficult to distinguish between the two [102]. In terms of the ordering of the B2 phase, a computational study by S. Huang et al [103] also suggested that Al and Ti would not prefer to be located on the same sublattice, while the same applied to V and Cr, meaning that the original (Ti, V)_{0.5}(Cr, Al)_{0.5} structure proposed by Qiu would be verified further. It was also noted that significant difference between the elastic properties of the A2 and B2 structures would be expected with the B2 exhibiting a 22.1% increase compared to the A2 as extracted through 0 K DFT calculations. Similarly to the previous studies, it was also predicted that the alloy would undergo an order-disorder transformation but this time the predicted temperature of the transformation lay at 900 M. Sun et al. [104] carried out the first study in this system concerning its high temperature heat treatment behaviour. It was found that heat treating the equiatomic alloy at 1100°C for 5h was sufficient to induce the formation of fine Ti-rich particles alongside elemental segregation. This resulted in the development of Al-Cr-rich and Ti-V-rich zones which agrees with the calculations of previous studies regarding the optimal energy configuration in the equiatomic alloy. It was underlined that compositional segregation was

exclusively observed near to anomalously small grains which may have formed during the precipitation of the Ti-rich particles. The Ti-rich phase would attain an FCC structure resulting in the formation of misfit dislocations due to its lack of coherency with the matrix phase.

The final, but most extensive study explicitly concerning the AlTiVCr system was published by Huang, Miao and Luo in 2022 [105] where, in the pursuit of the stabilisation of the A2 phase, a novel series of Ti-rich non-equiatomic AlTiVCr alloys was introduced (Table 2.4). The alloys were not subjected to any prolonged heat treatments at temperature. Instead, they were heated up slowly to 1200°C over 2h during differential scanning calorimetry (DSC) experiments. It is however not clear whether the transmission electron microscopy (TEM) studies were carried out on the DSC samples post-experiment or in the as cast state. It was observed that increasing the Ti content to 70 at. % was sufficient to not only reduce the order-disorder transformation temperature as measured through (DSC) but also enable the suppression of the order-disorder transformation resulting in a single phase A2 crystal structure. It was also discovered that the AlTi₇₀VCr alloy was characterised by a limited degree of ductility in tension. Nevertheless, none of these series of alloys were subjected to any prolonged heat exposure to assess their thermodynamic stability. Although this finding supports the case regarding the increase of Ti towards the ductilisation of the alloy, it also highlights a potential issue. It had been established thus far that the B2 was the culprit behind the profound lack of ductility in RMCA and RSA systems. Nevertheless, in this particular case where a complete suppression of the B2 formation should have been achieved, the ductility issues still manifest while the improvements seem incremental. This begs the question of whether the limited dislocation mobility in the B2 is the exclusive factor behind the lack of ductility in these systems, or whether additional phenomena that remain currently unaccounted for come into play.

Table 2.4 Tensile and differential scanning calorimetry (DSC) results extracted from study [105].

Alloy Composition	Yield Strength (MPa)	Fracture Strength (MPa)	Elongation %	Transition Temperature (°C)
AlTiVCr	-	36 ± 3.4	-	965.67
AlTi ₄₀ VCr	-	49 ± 2.8	-	983.96
AlTi ₅₅ VCr	-	51 ± 2.5	-	969.63
AlTi ₇₀ VCr	877 ± 5.2	889 ± 8.9	1.1 ± 0.1	900.52

Overall, the AlTiVCr system has various intricacies which, upon proper manipulation, may assist in the discovery of an alloy capable of manifesting useful properties. The most pivotal point of focus will have to be the investigation of its conformation to the RSA concept through proper heat treatment control. This is a crucial step given that no detailed studies have been carried out focussing on this aspect of AlTiVCr-based alloy development. The selection criteria, specific goals and challenges entailed with this system will be lay out in the appropriate research chapters that follow.

2.3 Computational design of Multicomponent alloys

As facilitated previously, the design of MCAs can prove to be a daunting task when exclusively assessed experimentally. Furthermore, navigating such a vast compositional space requires some degree of steering if it is to become successful. Therefore, the use of computational techniques can be paramount towards the efficient and effective design of novel multicomponent compositions. The use of the empirical parameters in tandem with the application of advanced models, calculations and even machine learning approaches proves to be a significant factor pushing the boundaries of MCAs. Multiple approaches have been proposed and are currently utilised towards this goal. These can be applied in various ways depending on the demands of each alloy design project. CALPHAD (calculation of phase diagrams) can be considered one of the more widespread high throughput computational techniques for assessing novel systems in terms of their thermodynamic properties. A close second would be *ab initio* techniques, most often density functional theory (DFT) and, to a much lesser extent, molecular dynamics (MD). DFT is generally used for assessing novel systems in terms of their electronic structure, structural properties, elastic properties and even their thermodynamic properties [106]. In certain cases, DFT can even be used to inform the CALPHAD calculations through the creation of databases or even to design interatomic potentials to be used in MD calculations. The main drawback however of DFT is that it can be particularly slow compared to CALPHAD or MD calculations [30, 107]. Nevertheless, combining DFT with machine learning (ML) approaches can yield impressive results. In a recent study by Takamoto et al., a universal interatomic potential developed by combining neural networks with DFT calculations was presented [108]. This is potentially a true breakthrough in the field of computational materials design as it will enable bigger scale calculations to be carried out using MD without compromising the calculation accuracy.

In the context of this thesis, a combination of empirical parameters, CALPHAD and DFT were used, and as such will be explored in this section to gain some insight regarding these methods. Although not utilised here, ML is also present in the literature, and will also be covered, with a particular focus on database building and the associated challenges.

2.3.1 Calculation of Phase Diagrams (CALPHAD)

The CALPHAD method is one of the more widely used predictive techniques for gaining information regarding the thermodynamic properties of a certain alloy. This is particularly useful in the case of MCAs where the massive number of possible compositions poses a notable challenge in terms of converging towards potential candidate alloys. Nevertheless, the typical manufacturing methods used in MCA research result in the formation of alloys in a paraequilibrium state which may not be directly related to the predictions CALPHAD may yield. This again highlights the need for subsequent heat treatments and processing in order to achieve near-equilibrium conditions during the characterisation and comparison with other modelling and predictive techniques. In turn this also underlines the need for establishing reliable thermodynamic data for all novel systems. In terms of the method itself, CALPHAD relies on the approximation of the Gibbs energy of each constituent phase for a given composition. Depending on the results of this approximation the number and types of phases expected to form at equilibrium are predicted. The calculation also considers the enthalpy, entropy and thermodynamic physical contributions for a given composition. The accuracy of this method entirely depends on the quality of the database used for each calculation and therefore, older databases can become obsolete when assessing novel systems. Certain phases that CALPHAD predicts the formation of could be considered irrelevant in certain cases and removed in published research. These inconsistencies may result in limited predictive capabilities or misleading assumptions or conclusions [109-111]. Focussing on MCA research, brute force CALPHAD does not seem to be the most efficient way to explore such a wide variety of compositions. New high throughput experiments are needed alongside supplementary ab-initio calculation in order to build novel databases upon which CALPHAD relies. At the same time, new pathways need to be developed for navigating this wide compositional field depending on the properties of interest [109]. Therefore, most of the focus has been on the development of these new databases. Given the wide variety of approaches when it comes down to CALPHAD, more emphasis will be put on the utilisation of CALPHAD for deducing the phase stability of the BCC against the B2 in RMCA systems and the tendency for intermetallic phase formation which is one of the more pivotal points of the thesis.

In RMCA and RSA CALPHAD calculations are one of the more critical pieces of information is to gain insight regarding the stability of the B2 against the BCC matrix phase. There are multiple approaches towards extracting this information. High throughput calculations seem to be the more prevalent, where with a given database a compositional surface is explored

recursively and filtered according to the criteria set by the user (Figure 2.4). For example that BCC and B2 phases should be stable at lower temperatures, or that a BCC should be stable at higher temperatures etc [112-116].

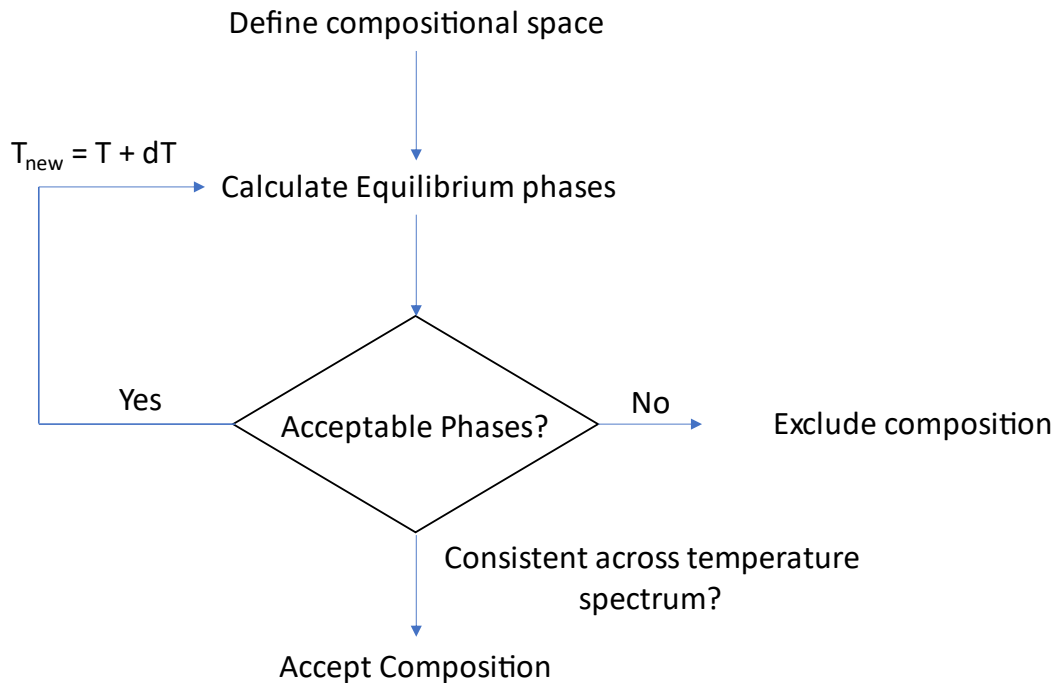


Figure 2.4 High throughput CALPHAD approach flowchart.

As seen in Figure 2.3 the process of excluding or including certain compositions can become as complex or simplistic as the application demands. By setting lenient or strict criteria for phase acceptance one may increase or decrease the number of compositions conforming to the set rules respectively. At the same time, the routines used for the definition of the compositional space may also vary in complexity. For example, in certain cases some pre-processing may have been carried out to pre-emptively restrict the compositional space to be investigated with CALPHAD. The issue remains however that regardless of the approach, high throughput CALPHAD methods still rely heavily on the quality of the databases for their success. As such, their direct utilisation on complex systems may not be the most sensible pathway. Naturally, this process becomes even more convoluted in cases where the calculations need to address the formation of intermetallic phases. That is due to the criteria for their inclusion deeming the compositional space to be explored too vast. Therefore, the need for compositional pre-processing becomes clear.

In terms of CALPHAD databases created with a focus on HEAs, the two most prominent commercially available series are the TCHEA developed by Thermo-Calc Software AB,

Sweden and the PanHEA database from CompuTherm LLC, USA. Both databases however originated from databases specific to Ni-base superalloys, which are not particularly optimised for use in refractory BCC systems [107]. Therefore, researchers often do not employ these specialised databases for calculations concerning RMCA systems, instead opting to utilise databases from the Ti or Ni alloy spectrum. At the same time, custom databases have begun to emerge, aimed at the assessment of particular RMCA systems [117].

CALPHAD has been paramount to the advancement of alloy design and compositional optimisation in various alloying systems over the years. Nevertheless, when assessing the feasibility for the extensive application of CALPHAD in RMCA systems, it becomes clear that the lack of raw data has become a bottleneck. Therefore, the use of additional experimental and computational techniques alongside CALPHAD is required at a pre-processing stage to maximise the method's efficiency. One such practice is the utilisation of the empirical rules set out previously to effectively reduce the number of compositions to be analysed through CALPHAD [107]. Interestingly however, even these tend to produce notable inaccuracies when assessing lightweight RMCA systems [118]. Therefore, more advanced techniques need to be utilised.

2.3.2 Density Functional Theory

In DFT modelling of MCAs, an exact-muffin-tin orbital (EMTO) method is most often used for solving the Kohn-Sham equations while a coherent-potential approximation (CPA) is used to account for chemical inconsistencies in the lattice. This approach significantly simplifies the system meaning key features may be ignored. The use of pure DFT simulations for such a multiphase system would require extreme computational resources, while Molecular Dynamics (MD) simulations, with minimal computational expense would allow for the generation of a representative supercell, but currently require the formulation of an adequate interatomic potential for each alloy case which would make this approach ineffective for alloy screening [42, 47, 103, 107, 119-123]. Finding the right balance between these techniques towards the efficient and effective screening of alloys for particular applications can be key. The underlying principles and concepts of DFT are thoroughly explained in chapter 3. Here, DFT was predominantly used for the calculation of the elastic properties of candidate alloys and to a lesser extent to estimate phase stability.

2.3.2.1 Phase Stability

DFT methods have also been used extensively for the evaluation of the thermodynamic properties of novel compositions with reasonable success. Depending on the type of calculation, it is possible to extract information regarding the entropy, enthalpy, and Gibbs energy, all of which can be used to predict the phase stability in novel compositions [107]. Specifically focussing on the BCC – B2 aspect of the investigation, reports have shown that the B2 phase is characterised by a lower energy than the BCC equivalent in the same system [103, 124]. Nevertheless, in both of these cases the EMTO-CPA method was used with the implications associated with its usage applicable. It should also be brought up that the methods associated with temperature-dependent calculations for the extraction of the thermodynamic properties can be extremely computationally expensive [125-127]. In such cases, the quasi-harmonic Debye-Grüneisen model needs to be considered [128] which is typically carried out through the GIBBS2 code [129, 130]. In the context of this thesis, a more crude but efficient method was used to gain some insight into the thermodynamic properties of alloys of interest which will be discussed in the appropriate methods section.

2.3.2.2 Elastic Properties

Although experimental studies concerning the elastic properties of MCAs are scarce, there is an abundance of computational studies, predominantly utilising both DFT and ML approaches. The first study concerning the investigation of MCAs through DFT was carried out by Tian et al. in 2013 using the EMTO-CPA method to calculate the magnetic properties of the equiatomic CoCrFeNi alloy [131]. Immediately after, the same group published the first DFT study concerning the prediction of elastic properties [132]. Again, they applied the EMTO-CPA method to uncover the properties of the NiCoFeCrAl_x alloy series. It was thus demonstrated that the EMTO-CPA method was an efficient, non-computationally intensive method for gaining insight into the elastic properties of MCAs. In their review, Ikeda, Grabowski and Körmann [106] list all of the reports of ab initio works carried out prior to 2019 concerning the elastic properties of MCAs, which were thirty in total. From these, twenty focused on or included the EMTO-CPA method for supplementary calculations, to illustrate how prominent the method was. Nevertheless, another upcoming concept concerned the special quasirandom structure (SQS) approach employed predominantly through the commercial DFT software VASP. SQS enables the development of a supercell where the different atom types are algorithmically homogeneously distributed. Hence, there are distinct differences in terms of the treatment of the atomic arrangements in MCAs [133]. A study by Zaddach et al. [134]

highlighted certain deviations between EMTO-CPA and VASP-SQS in their assessment of the CoCrFeNi and CoCrFeMnNi systems. More specifically, it was found that while the experimentally measured Young's modulus (E) lay at 171.5 GPa for the NiFeCrCo alloy, the EMTO-CPA predicted an E of 225 GPa while VASP-SQS an E of 195 GPa instead. It was later discovered that these inconsistencies between the two methods could have stemmed from not accounting for magnetic effects [135, 136]. Nevertheless, although convergence was achieved between the two methods, none of these estimates originating either from EMTO-CPA or VASP-SQS were confirmed experimentally within the frame of these studies. Unfortunately, the lack of consistent and comparable experimental data is a true bottleneck in this field. While DFT studies concerning the elastic properties of MCAs from a computational perspective continue to be carried out, their findings cannot be verified. Therefore, while it is possible to gain some insight regarding the behaviour of MCAs, it is unknown whether these reflect the actual physical properties of MCAs until experimental verification ensues.

Overall, most of the focus has been upon MCAs with cubic crystal structure, but hexagonal close packed (HCP) cases such as the TiZrHfTa_{0.8} alloy have also been addressed [137, 138]. The Zener ratio has been used to provide some insight regarding elastic anisotropy, while calculations of the Pugh ratio (B/G where B is the Bulk and G the Shear modulus respectively) is known to enable the prediction of ductile or brittle behaviour [139]. More specifically, in cases where the Pugh ratio lies above 1.75, the alloy would be expected to be characterised by a ductile fracture mechanism [139]. In the case of RMCAs specifically, various systems have been investigated [106, 107, 139]. In certain cases, it was established that the alloying addition with the most drastic effect on the elastic properties would be Al, which was found to notably increase the anisotropy of the elastic properties. One such system would be TiZrNbMoAl_x where increasing the Al content would lead to the progressive increase of the Zener ratio [139]. In the case of 3d transition metal-based MCAs that have been verified to comprise from an FCC solid solution, DFT calculations have also been carried out. It was discovered that many FCC MCAs would be characterised by notable elastic anisotropy, while their respective polycrystalline elastic properties as produced through DFT were particularly close to those approximated using the rule of mixtures [139, 140]. It has been suggested that the selection of a proper methodology, alongside the correct model system and the establishment of well converged theoretical key would be key to the success of the application of DFT for the prediction of elastic properties of novel MCAs [139].

2.3.3 Machine Learning

The compositional space of HEAs and MCAs is extremely vast; to the point where its navigation may sometimes prove to be a daunting task both from an experimental and a computational viewpoint. Nevertheless, the utilisation of machine learning (ML) methodologies towards alloy design may prove to be a valuable asset. ML is based on the use of algorithms drawing information from databases to make predictions regarding certain properties of interest [141, 142]. Assuming the emergence of continuously expanding and reliable databases, ML models can be applied to uncover properties of previously unexplored alloys, predict novel trends, and generally aid in the discovery of compositions tailored to address challenging engineering applications [143, 144]. Of those approaches, artificial neural networks (ANNs) seem to be the most prevalent and have been used extensively in the field of HEAs and MCAs [142, 145, 146]. These methods have been documented to exhibit appropriate predictive capabilities that can aid in the development of novel compositions. They have been used both for the prediction of phase constitution and the mechanical properties of novel alloys, while they have seen some degree of application for the prediction of the elastic properties as well [143, 146-150]. Although the field of ML is bound to become an even more prevalent alloy design route in the future, given that such approaches were not utilised within the frame of this work it is not necessary to go into additional depth regarding the way such techniques operate. However, a crucial aspect of their utilisation must be underlined and accounted for extensively, that being the databases that are used as foundations for the deployment of ML approaches.

These databases tend to either be exclusively computationally or experimentally derived. EMTO-CPA and DFT methodologies are used for the computational prediction of the properties of novel compositions, while most of the experimental data is gathered from published research and compiled into a single database [142-151]. While this may seem like a sensible approach for the rapid creation of databases, it is characterised by a crucial flaw, that being the quality, consistency, and comparability of the data itself. For example, as previously discussed the use of ab-initio methodologies has been shown to exhibit some degree of deviation from the respective experimentally measured material properties. Furthermore, even simply altering the parameters of the models themselves these may yield notably deviating results, for example in cases where insufficient attention has been given to convergence testing. These differences are additionally exacerbated by the use of different modelling methods for the derivation of the same properties. At the same time, experimental studies may also be

inconsistent with one another. This is due to the employment of a wide range of manufacturing methods, different characterisations techniques and, in general, a lack of standardisation in materials testing. Subsequently, when a database is formed containing data produced through incomparable means using it as a basis for the development of ML predictive methods results in notable inconsistencies. Furthermore, given that HEA research has mostly been focusing on the as-manufactured state, the observable microstructural and by extension mechanical properties, refer to a metastable state. This makes direct comparisons between theory and experiment unreliable, compromising the integrity of databases in cases where both experimental and computational data would be used for their creation. Therefore, the need for standardisation in materials testing is of paramount importance, especially towards the assessment of novel systems and the formation of databases. Additional emphasis should be placed on the investigation of the heat treated conditions of novel compositions to approach equilibrium and thus deem comparisons between theory and experiment more reliable.

2.4 Trends in RMCA research

RMCA's have emerged as promising candidates for a wide range of high temperature and high strength structural applications, with the aim of surpassing the capabilities of nickel-based superalloys. These applications encompass critical components within aerospace propulsion systems, land-based gas turbines, nuclear reactors, heat exchanger tubing, and the chemical process industry. Moreover, RMCA's can be considered for diverse applications where conventional refractory metals and alloys are traditionally employed, such as liquid rocket engine nozzles, rotating anodes for X-ray production, and high-temperature heat exchangers. Additionally, RMCA's exhibit potential in environments where high temperature strength is not the primary concern, such as corrosion-resistant settings. The primary focus of current RMCA exploration lies in fulfilling the demanding requirements of gas turbine engine components, including blades, vanes, and disks. These components require a combination of high temperature tensile strength and damage tolerance during assembly and operation. They also require resistance to fatigue, creep, stress-rupture conditions, environmental degradation, thermal conductivity, dimensional tolerances, and long-term microstructural stability, which is a difficult combination of properties to balance out. Other fields of applications that provide opportunities for the utilization of RMCA's with relatively lower risk might be various high-temperature settings with lower stress levels, such as combustors, thermal protection systems, rocket nozzles, temperature sensors, high-temperature heat exchangers, and heat-treating equipment. Nevertheless, several technical challenges must be addressed in the development of RMCA's for high temperature structural applications [152].

These primarily involve evaluating their performance in corrosive environments, enabling room temperature ductility, and optimizing the pathways for alloy discovery and development. Refractory elements and conventional refractory alloys are susceptible to various forms of environmental attack, such as nonprotective oxide formation, volatilization, solid solution embrittlement, and the "pest" attack phenomenon. To enhance environmental resistance, protective coatings and the addition of elements that promote the formation of dense and adherent protective oxides can be employed. Accelerated environmental resistance tests and high throughput computations serve as valuable tools for identifying candidate alloys resistant to degradation. Room temperature ductility is another critical aspect to be addressed, as refractory metals and alloys, including RMCA's, typically exhibit a brittle behaviour at ambient conditions. For RMCA's to be commercially viable, they need to display a ductile to brittle transition temperature (DBTT) below room temperature. Several approaches can aid in

improving room temperature ductility, such as optimizing material parameters like elastic and shear moduli, surface energy, lattice constant, and grain size. Gaining a deeper understanding of the dislocation structures, deformation mechanisms, and strengthening mechanisms within RMCAs may be crucial for enhancing their ductility. The vast array of potential RMCAs presents a significant challenge in terms of alloy discovery and development. Current exploration efforts have yielded only a limited number of alloys, and fully exploring the RMCA system at the current pace would be impossible due to time constraints. To accelerate the exploration and development of RMCAs, novel alloy discovery methods, including high-throughput experiments and computations, are needed [152]. Moreover, advancing the understanding of the metallurgical mechanisms entailed in their mechanical performance such as dislocation behaviour, deformation and strengthening mechanisms will be pivotal in improving room temperature ductility. Accelerated alloy discovery methods, encompassing high throughput experiments and computations, offer a pathway to expedite the exploration and development of RMCAs [152].

2.5 Mechanisms and Phenomena

Given the wide context of this thesis it is important to highlight some key mechanisms and phenomena that particularly stand out and are intricately connected with design criteria, findings or conclusions. Properly explaining these points is vital for understanding the pathways employed when navigating the vast compositional space of MCAs. Certain design criteria or potential challenges are also highlighted when appropriate. Nevertheless, this part of the work focuses on the mechanisms, not the actual techniques employed, which will be analysed extensively in the relevant chapters.

2.5.1 Elastic Properties

The elastic properties of a material refer to its mechanical properties characterising the initial, elastic stage of deformation. Upon deformation, the material structure changes into a state of metastability, giving rise to the development of internal stresses, aimed at returning the material to the equilibrium state. Should the deformation be minimal, the material will return to its undeformed state once the external forces causing the deformation cease. This is defined as elastic deformation and from a materials engineering perspective refers to the region up to low strain (typically 0.2%) upon mechanically deforming the material. The stress tensor describing a case of elastic deformation in an isotropic solid is directly related to the magnitude of B and G . The bulk modulus (B) refers to the strain response of a material to hydrostatic stress with an associated change in volume while retaining the original shape. The shear modulus (G) instead refers to the strain response of a material to shear or torsional stress, involving a change of shape (via change of angles) while preserving volume [153, 154]. For minor deformations the magnitude of the deformation is directly related to the applied stress, per Hooke's law (Eq. 2.7) [154]:

$$\sigma_{ij} = \frac{E}{1+\nu} \left(u_{ij} + \frac{\nu}{1-2\nu} u_{\text{ff}} \delta_{ij} \right), E = \frac{9BG}{(3B+G)}, \nu = \frac{3B-2G}{2(3B+G)} \quad \text{Equation 2.7}$$

where σ_{ij} the applied stress, E the Young's modulus, ν the Poisson's ratio, u_{ij} the stress tensor for a small deformation, δ_{ij} the displacement, B the bulk modulus and G the shear modulus.

As can be seen from Eq. 2.7 the applied stress is directly related to the displacement and Young's modulus, and inversely related to the Poisson's ratio. The Young's modulus (E) is the ratio of the uniaxial stress over the uniaxial strain in the elastic region and can be determined through experimental means from the slope of a stress-strain curve obtained during mechanical testing. The ratio of the transverse compression to the longitudinal extension is instead the Poisson's ratio [154]. In terms of the origins of the magnitudes of the elastic properties, these

are directly related to the atomic bonding. B is related to the external force needed to either compress or stretch the interatomic distances, counteracting the internal forces that aim to establish a balanced interatomic distance. G represents a deformation or bending of atomic bonds and is unaffected by interatomic spacing. Subsequently, E measures a combination of bond bending, as well as extension or compression. K (or E) is essentially linked to the curvature of the bonding energy-atomic volume curves and the bonding energy itself. As such, the interatomic forces and to a lesser extent the crystal structure of a material dictate its elastic properties [153, 154]. Therefore, the only way of affecting the elastic properties of a material is predominantly by directly manipulating the bond strength.

2.5.2 Order-Disorder Transformations

Order-disorder transformations are phase transformations involving a change in the degree of atomic ordering within a material, leading to alterations in its properties and microstructure. More specifically, they involve the transition between ordered and disordered atomic arrangements within a material. These transformations occur due to changes in temperature, pressure, or even the chemical composition [155, 156]. The ordering of atoms can significantly affect the material's mechanical, thermal, and magnetic properties, making order-disorder transformations crucial in tailoring material characteristics for specific applications [156].

One of the challenges associated with order-disorder transformations is the impact on ductility, particularly in ordered phases. Ordered structures often exhibit reduced ductility compared to disordered structures. This reduction in ductility is primarily attributed to the nature of the chemical bond between the atoms of said systems, where the ordered structures would be intermetallic phases. Dislocation motion in B2 systems would be hindered compared to the equivalent BCC ones, due to the size of the dislocation required to match the B2 superlattice being double the length of the BCC one. Assuming that two regular dislocations are propagating through the B2 structure, upon the initial passing of the first one, the material would now contain a disordered line of atoms (effectively a stacking fault in the ordered structure) termed as an antiphase boundary (APB), which would need to be erased through the subsequent passing of the second one. The additional energy requirement for this would be a notable barrier to dislocation motion and would make the B2 notably less ductile than its BCC equivalent [157]. Studies concerning single crystal of β' -brass (B2) in a binary Cu-47.1 at. % Zn alloy clearly demonstrate the move from the usual dislocation motion mechanisms observed in BCC systems towards the APB formation mechanism explained above in the B2 [158, 159]. To overcome the ductility issues in ordered phases, various pathways have been explored. These include compositional adjustments and heat treatments to enhance the material's ability to accommodate plastic deformation. Nevertheless, achieving a balance between desired properties and ductility remains a challenge in ordered alloys [160].

Ordered alloys have gained attention over the years in numerous industrial sectors demanding elevated mechanical performance during high temperature exposure. One such example is the group of alloys based on Titanium Aluminides (Ti-Al). These alloys exhibit excellent high-temperature strength, low density, and good oxidation resistance. However, the widespread use of Titanium Aluminides has been limited due to their brittleness, leading to poor fracture toughness and low impact resistance. These characteristics restrict their application in load-

bearing structural components that require high ductility. Efforts have been made to improve the ductility of Titanium Aluminides through alloying additions, microstructure refinement, and advanced processing techniques. However, the complex interplay between microstructure, composition, and processing parameters poses significant challenges in achieving the desired balance of properties required for practical applications. Order-disorder transformations are also prevalent in RMCAs as previously mentioned. The addition of alloying elements in BCC multicomponent alloys can induce order-disorder transformations, leading to the formation of ordered phases within the microstructure, particularly the B2 similarly to the formation of the γ' in a γ matrix as encountered in superalloys. Although the ordering can enhance certain properties, such as strength, it may also introduce challenges related to reduced ductility and increased brittleness. Researchers are actively exploring strategies to optimise the microstructure and composition of BCC multicomponent alloys to balance the desired properties with improved ductility. By understanding the kinetics and mechanisms of order-disorder transformations, it is possible to tailor the microstructure and properties of these alloys for specific applications. As such, particular attention must be paid to the way order-disorder transformations occur in RMCA systems.

2.5.2.1 Nucleation and Growth

Nucleation and growth theory is a fundamental concept that explains the formation of new phases or microstructures during various transformations, including solidification, solid state phase transformations, and precipitation. Nucleation is the initial step in the formation of a new phase or microstructure. It occurs when a nucleus of critical size is formed from the parent phase. The nucleation process can be either homogeneous or heterogeneous [161, 162].

Homogeneous nucleation occurs when the nucleation sites are uniformly distributed throughout the material, and nucleation happens spontaneously. It is a relatively rare phenomenon and typically requires specific conditions such as high temperatures or supersaturation. During homogeneous nucleation, atoms or molecules in the parent phase come together to form a stable nucleus of the new phase. However, the energy barrier associated with nucleation, due to the relatively large surface area to volume ratio of small size clusters, makes it a thermodynamically unfavourable process, and it often requires the presence of impurities or defects to facilitate nucleation. Heterogeneous nucleation, on the other hand, involves the formation of nuclei on pre-existing surfaces or interfaces. These surfaces can be grain boundaries, dislocations, or foreign particles present in the material. Heterogeneous nucleation is more common than homogeneous nucleation. The presence of nucleation sites reduces the

energy required to form a critical nucleus, making the nucleation process more favourable. Once nucleation occurs, growth follows as the newly formed nuclei increase in size [161-163].

Growth can proceed through either diffusion-controlled or interface-controlled growth. Diffusion-controlled growth occurs when atoms or molecules from the parent phase continuously diffuse and deposit onto the surface of the growing nucleus. This process is influenced by the concentration gradient between the parent phase and the growing phase. As atoms or molecules deposit onto the nucleus, the new phase expands, and the microstructure evolves. Interface-controlled growth occurs when the interface between the parent phase and the growing phase advances, resulting in the transformation of the material. During this process, atoms or molecules at the interface rearrange to form the desired microstructure. The movement of the interface can be driven by various factors, such as temperature, concentration gradient, or applied stress [163, 164].

2.5.2.2 Spinodal Decomposition

Spinodal decomposition is a process that occurs in certain materials when they undergo a phase separation due to thermodynamic instabilities. It is characterised by the formation of a highly interconnected microstructure with compositional fluctuations on a nanometre scale. During this, the alloy experiences a decrease in configurational entropy, leading to a decrease in the overall free energy of the system. Spinodal decomposition typically initiates in homogeneous alloys that are thermodynamically unstable and exhibit a miscibility gap. When such an alloy is slowly cooled from a high temperature single phase region or subjected to a prolonged low temperature heat treatment, the compositional fluctuations within the alloy amplify due to the negative feedback between composition and the free energy of the system. This amplification leads to the formation of two distinct phases with different compositions. The microstructure evolves through the coarsening of these compositional fluctuations, resulting in a network-like structure [165]. This network can span across multiple length scales, resulting in a hierarchical microstructure. Over time, the compositional fluctuations coarsen through diffusion processes, and the network structure evolves. Coarsening occurs as the alloy seeks to minimise its free energy by reducing the interfacial energy associated with the high curvature regions of the network. The resulting microstructures from spinodal decomposition in RMCA and RSA can have significant implications for their properties and performance. The interconnected network can influence mechanical strength, thermal stability, and other material characteristics. Understanding and controlling spinodal decomposition in these systems is crucial for tailoring their properties for specific applications [41, 84, 85, 166].

As previously mentioned, the mechanism through which spinodal decomposition manifests in RSAs is controversial. In the original work by Soni et al. it was not clear whether the high temperature BCC phase would immediately spinodally decompose into two BCC phases upon exposure to lower temperatures, or if the high temperature BCC phase would first undergo an order-disorder transformation into B2 which would then spinodally decompose into two B2 phases. In the first instance one of the two BCC phases would then transform into B2 while in the second one of the two B2 phase would transform into BCC. Therefore the question becomes clear. Does the spinodal decomposition or the order-disorder transformation come first? Thankfully, the work by Whitfield et al. sheds some light on the relevant phase transformation mechanisms encountered in RSAs [44, 84, 166-168].

2.5.2.3 Effect of Al of the Thermodynamic stability of B2

Perhaps the most important factor dictating the thermodynamic stability of the B2 phase in RHEAs, RMCAs and RSAs would be the Al content of the alloy. As previously described, an overwhelming volume fraction of the B2 phase in these systems may compromise their mechanical properties, more specifically their ductility. Favourable energetics of B2 formation may also render the alloy non-heat treatable meaning that the alloy would not be processable. Therefore, it is important to highlight pathways towards the suppression of the order – disorder transformation.

Al as an alloying addition has been found to be vital for achieving a lower density in RMCAs [81]. Nevertheless, it has also been associated with the formation of the ordered B2 superlattice phase [78] and brittle grain boundary phases [83]. Specifically, in terms of the B2 phase the effect of Al would be considered quite abstract. It was observed that the B2 phase would not form in refractory alloys where Al would be absent [168]. On the other hand, increased concentrations of Al would lead to the manifestation of a B2 phase or even the formation of single phase B2 alloys [14]. To pin down the specifics regarding the influence of Al on the B2 formation, Whitfield et al. investigated the ternary Ti-Ta-Zr system where they progressively introduced Al as an alloying element to observe its effects regarding phase formation [167]. From the investigated $Al_x(TiTaZr)_{100-x}$ ($x = 0, 5, 10, 15$ at. %) it was noted that an addition of Al over 10 at. % was necessary to induce the formation of the B2 phase. Interestingly enough, the alloys with 0 and 5 at. % Al were also characterised by a “basketweave” morphology as the BCC/B2 alloys but instead comprised of two BCC phases. Similar work was carried out in the $Al_x(NbTiZr)_{100-x}$ system where the formation of a B2 phase was observed at only 5 at. % Al [169], while an 8 at. % addition of Al was sufficient in the case of the $Al_x(Ti_{40}Zr_{20}Hf_{10}V_{20}Nb_{10})_{100-x}$ system [170], showing that the tendency for B2 formation was also related to the other alloying elements present. This is particularly interesting in the case of the $Al_x(HfNbTiZr)_{100-x}$ alloy where an addition of over 11.1 at. % was necessary for the formation of a B2 phase [171]. At the same time, the $AlMo_{10}NbTa_{10}TiZr$ alloy exhibited the dualphase microstructure post heat treatment and furnace cooling with an Al content of 20 at. %. Therefore it is also clear that apart from Al, other alloying elements also play a role on the energetics dictating BCC/B2 formation [81]. Nevertheless, as previously discussed the B2 phase needs to also be stable enough to allow the formation of the BCC - B2 dualphase microstructures that provide the proper balance between strength and ductility in these systems. Therefore, the aim should not be to completely suppress the BCC – B2 transformation but to

instead lower the tendency of B2 formation to the point where it can be suppressed through water quenching and then induced through a controlled aging treatment.

Another interesting effect related to the Al addition is its effects on the nature of the bond of the alloys where it is introduced. Wang et al. proposed that in cases where an ordered phase would be formed it would actually be an intermediate phase between a typical solid solution and an intermetallic compound [171], attaining a bond type exhibiting characteristics of both a metallic and a covalent bond. This could be attributed to the higher electron density, Fermi level and filled p-orbitals of Al atoms. Upon introducing sufficient amounts of Al into a solid solution comprised of transition metals which have partially filled d-orbitals, pd hybridisation would ensue and partially covalent bonds would form as in the case of intermetallic phases [172-174]. Naturally, this would further support the reason behind the formation of the ordered B2 phase in Al-containing RMCAs. This could have significant implications regarding the manipulation of the elastic properties of RMCAs.

A clear pathway for designing high stiffness low density RMCAs can be established by combining all of the points brought up in previous chapters. The nature of the bond is the primary factor dictating the elastic properties of a certain system. Al seems to be key in not only lowering the density of novel compositions but also indirectly modifying their bonding from metallic to partially covalent. This however, is also associated with the formation of the B2 phase which is characterised by particularly limited dislocation mobility in most systems and as such is directly responsible for the lack of ductility in RMCAs where it is the only phase present. It is also possible to suppress the order-disorder transformation partially or completely through water quenching depending on the Al-content and subsequently the tendency for B2 formation. Nevertheless, it can be assumed that the presence of the B2 phase alone is not indicative of a change in the bond type. Surely, it would be expected that a lack of ordering may have some effect on the elastic properties [103] but overall there should be no direct inverse correlation between the crystal structure and the bond type in quenched microstructures. As such, it may be possible that in cases where the formation of the B2 would be fully suppressed and a BCC solid solution would be formed instead that even the BCC solid solution would be characterised by a partially covalent bond. Subsequently, the improved dislocation mobility in the BCC could be taken advantage of and enable ductile behaviour in partially covalent RMCA systems. Therefore, the key challenge is to control the Al content to the point where water quenching post-heat treatment is sufficient to prevent the formation of the B2, while ensuring that the Al content is retained at a high enough level for the bond-

altering effects to manifest. Naturally, this concept has many potential pitfalls from a high-temperature application perspective. Should the service temperature lie in the A2 + B2 region it would be expected that the single phase BCC structure would decompose into an A2 + B2 or pure B2 structure instead, compromising the ductility of the component. At the same time, should the service temperature lie within the single phase BCC region it could lead to the decomposition of the previously achieved structure during the cooling process, resulting in the formation of an A2 + B2 or even pure B2, thus once again leading to a reduction in ductility. Therefore, the importance of fine tuning alloys utilising such order-disorder transformations to account for the aforementioned points for high-temperature applications cannot be overstated.

2.5.3 Ductile to Brittle Transition Temperature (DBTT)

The ductile to brittle transition temperature (DBTT) is a critical characteristic of metals and alloys that directly affects their suitability for a wide variety of applications. DBTT represents a range of temperatures over which metals and alloys transition from a ductile to a brittle fracture mode. Ductile fracture is characterised by plastic deformation and notable energy absorption before failure, while brittle fracture takes place with minimal plastic deformation and limited to no energy absorption, resulting in sudden and catastrophic failure. At temperatures above their DBTT, materials would exhibit ductile fracture while, as the temperature approaches the DBTT, the material becomes more susceptible to a brittle fracture mode. The DBTT is influenced by several factors such as the chemical composition and the microstructural characteristics. For example, the addition of Ni or Mn to steel can shift the DBTT to lower temperatures, while higher C content pushes the DBTT to higher temperatures. Heat treatment processes, such as annealing or quenching, can affect the DBTT by modifying the material's microstructure and reducing its susceptibility to brittle fracture [4, 175-177].

Clearly, considering the DBTT can be crucial for material selection and design in various industries as it can dictate safe operation of structures and components under low-temperature or impact conditions. For example, the DBTT is a critical factor for the selection of materials used in infrastructure, such as bridges and pressure vessels, in cold environments or regions prone to impact events. Nuclear reactor materials must have a DBTT below the operating temperature to ensure integrity and prevent brittle fracture in case of accidents or transients [178]. Materials used in automotive applications, particularly in regions with cold climates, must exhibit a low DBTT to ensure crashworthiness and passenger safety. Materials used in Arctic and offshore environments must have a low DBTT to resist brittle fracture in extremely low-temperature conditions [179, 180].

2.5.3.1 Effect of Cr

Since chromium (Cr) is one of the more prevalent alloying additions in this thesis it is critical to assess potential pitfalls, its incorporation may entail. Cr has been used extensively in a wide variety of alloys and alloying systems owing to a high melting point, oxidation resistance and notable thermal conductivity. At a certain point research was focussed on the development of Cr-based alloys precisely due to its rich properties. Nevertheless it would not come to pass due to some major drawbacks associated with the incorporation of Cr in significant quantities, mainly embrittlement due to excessive N pickup and predominantly due to a low DBTT [181].

At ambient temperatures Cr exhibits a complete lack of ductility, its DBTT lies at above 150°C for commercial purity material. This is due to the presence of impurities such as N, C, oxygen (O) and sulfur (S) which increase the DBTT of Cr. Therefore, controlling the content of impurities is vital to ensure a lower DBTT and enable ductile behaviour at lower temperatures. Nevertheless, the required impurity content would have to remain at levels below 0.0001 wt. % which is not commercially feasible. Therefore, alternative pathways would have to be explored. The investigation of the effects various alloying elements would have on the DBTT of Cr found that rhenium (Re) could considerably improve the low temperature ductility of Cr. However, the addition of Re would have to be at 20 – 40 at. % which, again, is not commercially feasible due to the price of Re. From the other alloying additions that were investigated, only ruthenium (Ru) showed an effect of similar magnitude to Re, though Fe, cobalt (Co), iridium (Ir) and Mn were also found to positively affect the DBTT and by extension the ease of fabrication. Again, all these additions would have to be introduced at over 20 at. % in their respective binary alloys with Cr, as such making every addition apart from Fe and Mn unrealistic. Therefore, in RMCA's with significantly elevated Cr contents the addition of Fe or Mn would be recommended to offset the potentially negative effect the Cr addition would have on the DBTT of the RMCA [181].

2.5.4 Ostwald Ripening

Ostwald ripening is a phenomenon observed in metals and alloys, which involves the growth or dissolution of particles due to the differences in their size and solubility. It is driven by the minimisation of the total free energy in the system. In the case of alloys, the driving force for Ostwald ripening arises from the difference in the solubilities of particles in the matrix and the presence of diffusion pathways [182, 183]. During Ostwald ripening, smaller particles that have a higher solubility tend to dissolve and release their solute atoms into the matrix. These solute atoms diffuse through the matrix towards larger particles with lower solubility. The solute

atoms then deposit on the surfaces of larger particles, causing their growth. This process continues until the system reaches a state of equilibrium consisting of larger, more stable particles and a reduced number of smaller particles [182, 183]. Heat treatment processes may induce Ostwald ripening in metallic alloys. During the heat treatment, the alloy is exposed to elevated temperatures, allowing for atomic diffusion and redistribution. The diffusion of solute atoms from smaller particles to larger particles is facilitated by the thermal energy provided during heating. Proper control of this phenomenon can lead to improved mechanical properties, such as increased strength and hardness, as particles with the appropriate size act as obstacles to dislocation movement through a combination of Orowan looping and particle shearing, enhancing the alloy's resistance to deformation. This can be done by carefully selecting the temperature, duration, and cooling rate during heat treatment [183-185].

In the context of this thesis Ostwald Ripening would be considered a rather supplementary phenomenon, taking place in alloy cases where multiphase microstructures consisting of a matrix phase and one or more types of intermetallic phases. It was however observed during the heat treatment processes of certain alloys and as such its importance, implications, and the mechanism itself needs to be laid out. It also implies that in cases where it does take place, the alloys involved truly do respond well to heat treatments, acting as an additional insurance in terms of the potential of the specific composition.

2.5.5 Thermal Shock

Thermal shock is a phenomenon that occurs when a material undergoes rapid and extreme temperature changes, leading to structural damage or failure. The extent of this phenomenon is dependent both on the material properties and the manufacturing process. More specifically, materials with a lower thermal conductivity and higher thermal expansion coefficient are more prone to thermal shock due to their inability to rapidly transfer and distribute thermal energy (and the resulting differential expansions and elastic strains) throughout their structure. When a material is exposed to a sudden change in temperature, different regions of the material may expand or contract at different rates. This non-uniform expansion or contraction leads to the development of internal stresses. If these stresses exceed the material's strength, it can lead to the formation of cracks, therefore compromising the structural integrity of a component. Overall, metallic alloys are not as prone to this phenomenon as other materials such as ceramics due to their high thermal conductivity. However, certain alloys are more susceptible to thermal shock than others. Metallic alloys used in aircraft engines, such as nickel-based superalloys, experience rapid temperature changes during takeoff, landing, and high-speed flight, making

them susceptible to thermal shock. Alloys used in glass manufacturing, such as stainless steels and refractory alloys, are exposed to sudden temperature changes in processes like annealing, quenching, and tempering [186]. To define the resilience of a material in terms of thermal shock susceptibility the term thermal shock resistance is introduced which is directly related to the maximum temperature differential which can be sustained by a material of a given thickness (Eq. 2.7 - 2.9) [187-189]:

$$B\Delta T = \frac{\sigma_f}{\alpha E} \quad \text{Equation 2.8}$$

where ΔT the dependence of the maximum temperature jump, on the failure stress σ_f , the thermal expansion coefficient α , the Young's modulus E and the constant B .

$$B = \frac{C}{A}, A = \frac{Bi}{1 + Bi}, C = \begin{cases} 1 \\ 1 - \nu \\ 1 - 2\nu \end{cases} \quad \text{Equation 2.9}$$

where B is a constant dependent on the Biot number Bi and the Poisson's ratio ν for axial, biaxial and triaxial stress constraints respectively.

$$Bi = \frac{h}{k}L \quad \text{Equation 2.10}$$

where Bi is the Biot number as a function of the convective heat transfer coefficient h , the thermal conductivity k and the length of the considered geometry L .

Overall, it can be deduced that a higher Young's modulus and thermal expansion coefficient alongside a lower thermal conductivity greatly exacerbate this phenomenon. The reason why this can become a notable issue during the processing of MCAs is intricately connected to the usual manufacturing paths employed. In the case for example of Vacuum Arc Melting (VAM) the material is subjected to rapid thermal cycles and therefore, should the material have poor thermal shock resistance its production may not be feasible. Similarly, an alloy with poor thermal shock resistance may not respond well to heat treatments utilising rapid heating or cooling cycles such as water quenching.

To mitigate the risk of thermal shock in metallic alloys, several strategies can be employed during alloy design and manufacturing processes [186, 187]:

1. Altering the chemical composition to increase the thermal conductivity and lower the thermal expansion coefficient. Furthermore, design alloys that exhibit a proper balance

between strength and ductility and by extent may provide improved resistance to thermal shock.

2. Employing controlled cooling rates during the manufacturing and heat treatment process can minimize thermal gradients and reduce the risk of thermal shock. Slow and controlled cooling allows the material to adjust to temperature changes more uniformly.

Another potential pathway for the manufacturing of such materials may be through the reduction of their Young's modulus which, unfortunately defeats the purpose of the current thesis. As such, although this phenomenon will be acknowledged in cases where it becomes prevalent it will not be a primary design criterion at this point. Nevertheless, thermal shock can pose a significant concern when moving towards the employment of novel alloys in engineering applications. As such, understanding the correlation between thermal conductivity, thermal expansion coefficient, and the occurrence of thermal shock is crucial in selecting alloys resistant to such stresses.

2.6 Conclusions

MCA's present an exciting opportunity for designing alloys with properties tailored to address a wide range of engineering challenges owing to the flexibility of their chemical composition. Nevertheless, certain aspects of MCA design have not been thoroughly investigated, with clear gaps in the literature being present. As previously established, very limited work has been carried out regarding the design of high stiffness MCAs. Furthermore, the methodologies used for extracting the elastic properties of systems of interest assess each alloy without considering the different phases constituting it. Experimental verification of these properties is also scarce and underreported, which is a significant bottleneck for evaluating the accuracy of the predictive computational techniques and their subsequent development. Computational studies have highlighted the potential of certain RMCAs for high stiffness applications which also exhibit notable properties in fields demanding materials with high temperature strength. Their elastic properties, however, have not been experimentally assessed. RMCAs have also been found lacking in terms of their room temperature ductility, which is a limitation towards their industrial application. Although some pathways for tackling these challenges have been developed, the associated concepts are still in their infancy. Therefore, the following key questions surface that are necessary to answer for expanding the general understanding and state of the art regarding RMCAs and their associated properties, namely:

1. What is the potential of RMCAs for high stiffness applications?

2. How can such RMCA systems be computationally evaluated when considering both their phase constitution and elastic properties?
3. Could the established processes for RSAs for controlling the BCC – B2 transformation be expanded to RMCAs exhibiting potential for high modulus applications without compromising their elastic properties?
4. What are the implications of high stiffness design on the ductility of RMCAs.

3. Materials and Methods

This chapter covers the various experimental and computational methodologies used for the design, manufacturing and testing of the investigated alloys. We start by describing the theory behind CALPHAD, DFT and Homogenisation Modelling (FEM) and then proceed with the experimental methods. While this chapter provides an overview of said techniques and methodologies, specific computational and experimental details will be provided within the individual subsequent research chapters.

3.1 Computational Methods

A wide variety of computational tools have been used individually or synergistically to make predictions regarding the thermodynamic and elastic properties of HEAs. Calculation of Phase Diagrams (CALPHAD) and Density Functional Theory (DFT) approaches have been independently used to guide the experimental design and optimisation of candidate alloys and alloying systems. In addition, a methodology was also developed for calculating the elastic properties of novel multiphase HEAs through a purely computational approach sequentially utilising CALPHAD, DFT and Homogenisation Modelling with Finite Element Modelling (FEM). The development and use of this methodology will be discussed in depth in Chapter 4. Lastly, the Neural Network (NN) package pyMPEA is used to benchmark the experimental results of this work against the relevant predictions regarding phase constitution.

3.1.1 Calculation of Phase Diagrams (CALPHAD)

CALPHAD is a thermodynamic modelling tool used for the prediction of the thermodynamic properties of an alloying system, such as the phase composition. It is based on the use of available thermodynamic databases concerning pure elements, binary and ternary systems to extrapolate the properties of higher order multicomponent systems. We implement this approach through the Thermo-Calc 2 (TC) Software v. 2020-2022_b using multiple databases that are referenced within each relevant research chapter.

The methodology for CALPHAD database development is based on four sequential steps, 1) the gathering of raw data (such as phase equilibria, enthalpies of mixing, formation energies and crystal structures) of pure elements, binary and ternary systems, 2) critical assessment of captured data, 3) optimisation of the model parameters and 4) storage of the optimised model parameters in a database. Once the database building process is complete, the critical assessment and pre-processing is then initiated in a process called Model Selection, involving the calculation of the Gibbs free energy for each of the phases potentially present. The user

may also elect to manually omit certain phases from the calculation; this was however not the case in the present work. The calculation itself entails a parameterisation process depending on the crystal structure of each phase to assign a specific model optimised for each case. The free parameters of the assigned model are then fitted against the input data generated during the data gathering process. Then, the Gibbs energy functions are stored in a database alongside their optimised free parameters to be accessed by TC. The CALPHAD predictions are then validated against experimental results of higher order systems before being released in a commercial TC database [190].

It is important to note that in cases where experimental raw data is unavailable, *ab-initio* or machine learning techniques may be employed instead. Therefore, when entirely novel systems are surveyed such as HEAs, TC and in general CALPHAD-based methods in general may yield inconsistent results. Subsequently, the use of multiple databases and thermodynamic predictors is of paramount importance for gaining proper insight regarding the thermodynamic properties of a novel system.

3.1.2 Density Functional Theory (DFT)

DFT is based on the Hohenberg-Kohn theorem [191] which assumes that the total ground-state energy of a many-body electron system is a direct functional of the electron density according to Equation 3.1.

$$E = \int dr n(r) V_n(r) + \langle \Psi | \hat{T} + \hat{W} | \Psi \rangle, E = F[n] \quad \text{Equation 3.1}$$

where E is total energy, r the position of the electron, $n(r)$ the ground-state density, $V_n(r)$ the external potential, Ψ the many-body wavefunction, \hat{T} the kinetic energy operator and \hat{W} the electron-electron potential energy.

Kohn and Sham approximated this functional by adding the implicit kinetic energy and electron potential terms into their independent electron approximation counterparts and summarising energetic discrepancies within an additional term E_{xc} (Equation 3.2). The first three terms of Eq. 3.2, specifically the external potential, kinetic energy and hartree energy respectively make up the total energy in the independent electron approximation [192].

$$F[n] = \int dr n(r) V_n(r) - \sum_i \int dr \phi_i^*(r) \frac{\nabla^2}{2} \phi_i(r) + \frac{1}{2} \iint dr dr' \frac{n(r)n(r')}{|r-r'|} + E_{xc}[n] \quad \text{Equation 3.2}$$

where the term $\phi_i(r)$ refers to the probability of finding an electron at point r and E_{xc} refers to the exchange-correlation energy.

Furthermore, by utilising the Hohenberg-Kohn variational principle it is possible to determine the ground-state electron density n_0 , leading to Equation 3.3, where $V_{xc}(r)$ is a direct function of the exchange-correlation energy E_{xc} . Subsequently, it is possible to determine the total energy of a many-body electron system by simply approximating E_{xc} [123].

$$\left[-\frac{1}{2} \nabla^2 + V_n(r) + V_H(r) + V_{xc}(r) \right] \phi_i(r) = \varepsilon_i \phi_i(r) \quad \text{Equation 3.3}$$

where $-\frac{1}{2} \nabla^2$ is the kinetic energy, $V_n(r)$ the external nuclear potential, V_H the Hartree potential and V_{xc} the exchange-correlation potential.

3.1.2.1 Cambridge Serial Total Energy Package (CASTEP)

The DFT calculations were performed using the Cambridge Serial Total Energy Package (CASTEP), a first-principles-derived code for electronic structure calculations, capable of approximating the exchange-correlation functional [193]. The software uses a plane-wave-based pseudopotential approach to solve a set of one-electron Kohn-Sham equations [194]. The pseudopotential is an approximation aimed at simplifying the representation of the core and

valence electrons allowing for a significant reduction in computational requirements compared to pure ab-initio techniques [195]. The electron-electron interactions were approximated using the Perdew, Burke Erzenhof (PBE) exchange-correlation functional which is used to calculate the exchange-correlation energy E_{xc} [196]. Ultrasoft pseudopotentials (generated on the fly) were used in all simulations [197]. These operate to simplify the descriptions of tightly bound orbitals from the core region of the atom and thus significantly reduce the cutoff energy required to achieve reasonable calculation accuracy. In turn, the cutoff energy itself is proportional to the number of plane wave functions used as basis functions to represent the wavefunction. Therefore, the higher the cutoff energy the greater the accuracy of the calculation and the computational expenses to describe the additional plane wave functions. The SCF cycle energetic tolerance was defined at 5×10^{-7} eV and a Gaussian smearing scheme [198] with a smearing width of 300 K using 48 additional bands was used to allow for proper K-point distribution. K-points could be considered as the sampling points in the Brillouin zone where the calculation of wavefunctions will ensue. An increase in K-points leads to an increase in sampling points and subsequently to a higher calculation accuracy at the expense of computational resources. It must also be noted that the number of K-points should be inversely proportional to the size of the investigated system. Hence, appropriate adjustments need to be made when upscaling or downscaling the DFT calculations. The geometry optimisation process was executed using the limited-memory Broyden-Fletcher-Goldfarb-Shanno (LBFGS) algorithm [199] which is based on the Newton Raphson approach. Unfortunately, this also deems this method prone to converging to local instead of total minima. Therefore, prior convergence testing is required to ensure appropriate calculation precision. Lastly, symmetry operations were enabled to speed up the calculation, while the supercell was forced to maintain symmetry during optimisation when possible.

3.1.2.2 Convergence Testing

Convergence testing refers to the process identifying an appropriate level of calculation accuracy while maintaining reasonable computational efficiency. Depending on the property of interest that one would be looking to extract from the DFT calculations convergence to the appropriate term is advised. Therefore, calculations aiming at unveiling energetic or crystal properties such as the lattice parameter require convergence testing in respect the final energy of the atomic arrangement. On the other hand, in cases where the elastic properties would need to be calculated convergence testing should be conducted in respect to the final stress of the

atomic arrangement. Calculations exclusively converged to the final energy are not sufficiently accurate for the reliable extraction of the elastic properties.

Before we proceed with laying out the methodology of carrying out convergence testing the concepts of singlepoint and geometry optimisation calculations need to be introduced. A singlepoint calculation refers to the calculation of the final energy of an unoptimised atomic arrangement. A geometry optimisation refers to the process of optimising an atomic arrangement according to a series of energetic and structural tolerances defined by the user and outputs the final energy of the optimised structure. Convergence to the final energy requires singlepoint calculations while convergence to stress requires the use of geometry optimisations while restraining atomic positions and cell size.

To conduct convergence testing, a series of calculations with progressively increasing cutoff energies and K-point spacings are initiated. The property of interest is then plotted against the cutoff energy, K-point spacing set and computational resource usage. It is observed that the property of interest starts to converge around a certain value once a critical cutoff energy and K-point spacing combination is used. From that point on, further increase of both parameters only yields incremental results by comparison. As such, the cutoff energy and K-point spacing combination achieving the best balance between computational resource usage and necessary accuracy should be selected for the calculation of interest. In this work, convergence was achieved in respect to the final stress matrix of all investigated supercells up to 50 MPa per stress component.

3.1.2.3 Calculation of Elastic Properties through DFT

Two methods were employed to extract elastic properties from DFT simulations – The Birch-Murnaghan Isothermal Equation of State and the derivation of the elastic constant matrix. The integrated form of BME can be used for fitting volume – total energy data derived from DFT calculations according to Equation 3.4 [200].

$$E(V) = E_0 + \frac{9V_0B_0}{16} \left\{ \left[\left(\frac{V_0}{V} \right)^{\frac{2}{3}} - 1 \right]^3 B'_0 + \left[\left(\frac{V_0}{V} \right)^{\frac{2}{3}} - 1 \right]^2 \left[6 - 4 \left(\frac{V_0}{V} \right)^{\frac{2}{3}} \right] \right\} \quad \text{Equation 3.4}$$

where V_0 is the relaxation volume, V the post-deformation volume, E_0 the relaxation internal energy, E the strained internal energy and B'_0 the derivative of bulk modulus in respect to pressure.

The implementation consists of the execution of a stress-convergence tested geometry optimisation calculation to obtain the relaxed atomic arrangement and the relevant relaxation energy. This is then followed by subjecting the atomic arrangement to a series of minor deformation intervals using low-tolerance geometry optimisation DFT routines and extracting each strained final energy. The last step entails fitting the obtained values to the BME and obtaining B_0 .

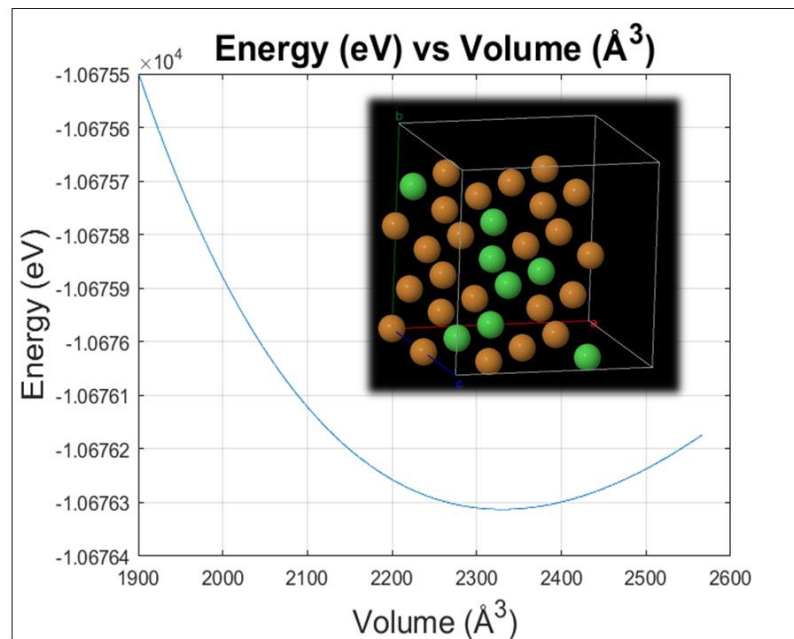


Figure 3.1 Predicted effect of supercell volume (atomic displacement) on the final energy of the atomic configuration.

The first step for calculating the elastic properties is to execute a stress-convergence tested geometry optimisation to obtain the relaxed atomic arrangement. The elastic constants matrix can then be calculated using a stress-strain approach. In this work, secondary low-tolerance geometry optimisation CASTEP routines were used to calculate the components of the 3x3 elastic matrix for strained instances of the relaxed supercell [119]. The components of the calculated stress matrix are hence denoted σ_{ij} , and are related to the 6 independent components of the Green-Lagrange strain tensor, denoted as E_{ij} , through Equation 3.5, where the elastic components are denoted as C_{ij} , according to the Voigt notation. The calculated stresses are then linearly fitted into each row or column of the matrix to obtain the elastic constants.

$$\begin{bmatrix} \sigma_{11} \\ \sigma_{22} \\ \sigma_{33} \\ \sigma_{44} \\ \sigma_{55} \\ \sigma_{66} \end{bmatrix} = \begin{bmatrix} C_{11} & C_{12} & C_{13} & C_{14} & C_{15} & C_{16} \\ C_{21} & C_{22} & C_{23} & C_{24} & C_{25} & C_{26} \\ C_{31} & C_{32} & C_{33} & C_{34} & C_{35} & C_{36} \\ C_{41} & C_{42} & C_{43} & C_{44} & C_{45} & C_{46} \\ C_{51} & C_{52} & C_{53} & C_{45} & C_{55} & C_{56} \\ C_{61} & C_{62} & C_{63} & C_{46} & C_{56} & C_{66} \end{bmatrix} \begin{bmatrix} E_{11} \\ E_{22} \\ E_{33} \\ 2E_{23} \\ 2E_{13} \\ 2E_{12} \end{bmatrix} \quad \text{Equation 3.5}$$

In the cases where cubic symmetry can be applied or approximated if solute content is relatively low, the elasticity matrix can be further simplified due to symmetry operations and is thus preferred for use whenever possible (Equation 3.6) [201].

$$\begin{bmatrix} \sigma_{11} \\ \sigma_{22} \\ \sigma_{33} \\ \sigma_{44} \\ \sigma_{55} \\ \sigma_{66} \end{bmatrix} = \begin{bmatrix} C_{11} & C_{12} & C_{12} & 0 & 0 & 0 \\ C_{21} & C_{22} & C_{12} & 0 & 0 & 0 \\ C_{21} & C_{21} & C_{33} & 0 & 0 & 0 \\ 0 & 0 & 0 & C_{44} & 0 & 0 \\ 0 & 0 & 0 & 0 & C_{55} & 0 \\ 0 & 0 & 0 & 0 & 0 & C_{66} \end{bmatrix} \begin{bmatrix} E_{11} \\ E_{22} \\ E_{33} \\ 2E_{23} \\ 2E_{13} \\ 2E_{12} \end{bmatrix} \quad \text{Equation 3.6}$$

The calculated C_{ij} values are then used to compute the upper and lower boundaries of the bulk modulus B_V , B_R and the shear modulus G_V , G_R to extract the mean moduli B_{VRH} and G_{VRH} [202, 203]. To do this, the compliance matrix was calculated and populated through the manipulation of the elastic matrix constants through the following expressions (Equations 3.7 - 3.14).

$$S_{11} = \frac{C_{11} - C_{13}^2/C_{33}}{C_{11} - C_{12}} S \quad \text{Equation 3.7}$$

$$S_{12} = -\frac{C_{12} - C_{13}^2/C_{33}}{C_{11} - C_{12}} S \quad \text{Equation 3.8}$$

$$S_{13} = -\frac{C_{13}}{C_{33}} S \quad \text{Equation 3.9}$$

$$S_{33} = \frac{C_{11} + C_{12}}{C_{33}} S \quad \text{Equation 3.10}$$

$$S_{44} = \frac{1}{C_{44}} \quad \text{Equation 3.11}$$

$$S_{66} = \frac{1}{C_{66}} \quad \text{Equation 3.12}$$

$$S = \frac{1}{C_{11} + C_{12} - 2C_{13}^2/C_{33}} \quad \text{Equation 3.13}$$

$$\begin{bmatrix} E_{11} \\ E_{22} \\ E_{33} \\ 2E_{23} \\ 2E_{13} \\ 2E_{12} \end{bmatrix} = \begin{bmatrix} S_{11} & S_{12} & S_{13} & 0 & 0 & 0 \\ S_{21} & S_{22} & S_{23} & 0 & 0 & 0 \\ S_{31} & S_{32} & S_{33} & 0 & 0 & 0 \\ 0 & 0 & 0 & S_{44} & 0 & 0 \\ 0 & 0 & 0 & 0 & S_{44} & 0 \\ 0 & 0 & 0 & 0 & 0 & S_{66} \end{bmatrix} \begin{bmatrix} \sigma_{11} \\ \sigma_{22} \\ \sigma_{33} \\ 2\sigma_{23} \\ 2\sigma_{13} \\ 2\sigma_{12} \end{bmatrix} \quad \text{Equation 3.14}$$

This form of the compliance matrix accounts for both a cubic and a hexagonal supercell. For the estimation of the Youngs' modulus E and the Poisson's ration ν , it was assumed that the material was isotropic and were subsequently calculated using Equations 3.15 and 3.16 [122].

$$E = \frac{9B_{VRH}G_{VRH}}{3B_{VRH} + G_{VRH}} \quad \text{Equation 3.15}$$

$$\nu = \frac{3B_{VRH} - 2G_{VRH}}{2(3B_{VRH} + G_{VRH})} \quad \text{Equation 3.16}$$

3.1.2.4 Evaluation of Phase Stability through DFT

It is possible to estimate the stability of an investigated phase by calculating the final energy of a specific configuration and then comparing that term with the final energies of its constituent alloying elements as calculated through DFT according to Equation 3.17.

$$E = E_{conf} - \sum_{i=1}^n N_i E_i \quad \text{Equation 3.17}$$

where E is the net energy of the phase of interest, E_{conf} is the final energy of the optimised structure of the phase of interest, N the number of atoms of a specific alloying element contained within the phase of interest and E_i the final energy per atom of the alloying element as calculated through DFT. If $E \leq 0$ then it is probable that the phase of interest will form, otherwise if $E > 0$ then the phase of interest should not form. Note that the regular DFT simulations in this work relate to an internal energy, U , and not a temperature dependent free energy such as G or A and therefore these stability calculations do not directly include a temperature component.

3.1.3 Homogenisation Modelling - Finite Element Modelling (FEM)

Finite Element Modelling (FEM) is a numerical method for solving differential equations by subdividing a system into finite elements through space discretisation. Thus, each discrete component is described by a set of simpler equations which are summarised into a larger system of equations capable of describing the entire system. The FEM is then capable of approximating a solution through the minimisation of an associated error function [204].

A homogenisation modelling approach expands upon the principles of FEM and can be used to combine the elastic properties of an intermetallic phase with that of a matrix phase in a material. The commercial software ABAQUS along with the Micromechanics plugin can be used for the creation of a Representative Volume Element (RVE) as illustrated in Figure 3.2 and the EasyPBC plugin [205] to perform the homogenisation. The employed homogenisation scheme is a combination of the RVE method and Asymptotic Homogenisation (AH) approaches [206]. The RVE method refers to the use of an RVE upon which the Dirichlet and Neumann boundary conditions are applied, and a strain energy calculation is performed.

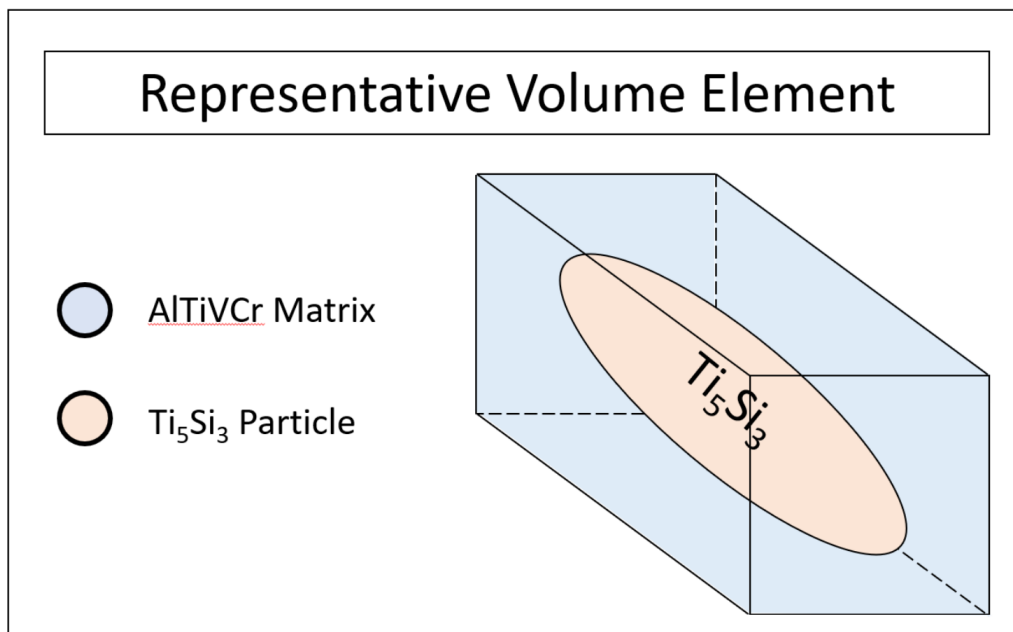


Figure 3.2 Illustration of the representative volume element (RVE) used for the ABAQUS homogenisation scheme through the EasyPBC plugin.

Subsequently, the strain energy of the RVE is matched to the strain energy of the homogeneous material [207]. These boundary conditions produce results that approximately correspond to the upper Voigt and lower Reuss bounds, respectively [208]. The AH method is used to study partial differential equations with rapidly oscillating coefficients and has been demonstrated to accurately predict the effective modulus of 2-D and 3-D periodic materials. The method

employed in EasyPBC bypasses the computational difficulties encountered in the AH method by using the outputs of the FEM of the commercial software to calculate the effective elastic properties resulting in a significant increase in computational efficiency and high accuracy.

3.1.4 pyMPEALab Toolkit

The Python Multi-Principal Element Alloys Lab (pyMPEA) toolkit is based on the use of an artificial neural network for the prediction of the microstructural constituents of multicomponent systems. This is done by using the properties of the alloys as input including the atomic size difference (δ), enthalpy of mixing (ΔH_{mix}), entropy of mixing (ΔS_{mix}), omega (Ω) parameter, electronegativity ($\Delta\chi$) and valence electron concentration (VEC). The outputs of this model describe the most probable phase types to appear in the alloy of interest, specifically a Solid Solution (SS), Intermetallic (IM) and Amorphous (AM) or a combination of the three [209]. pyMPEALab was used as a complementary technique to gain some insight regarding the potential phase constitution of a composition of interest.

3.2 Experimental Methods

Since a wide variety of equipment and practices were used for the experimental aspects of the different stages of the thesis, details are provided here exclusively for operations which have been consistent across the entire thesis work. Specific experimental details are available in research Chapters 4-7.

3.2.1 Cold Crucible Vacuum Arc Melting (VAM)

Cold crucible vacuum arc melting (VAM) is a material manufacturing technique utilising an electron plasma arc for melting raw materials contained within a water-cooled copper (Cu) crucible. This method is capable of rapidly producing small quantities of alloys and is widely used for high-throughput alloy manufacturing. Especially prevalent in the field of HEAs alongside vacuum induction melting (VIM), VAM is the only technique used for alloy manufacturing technique in this work [30, 82, 97, 100, 105, 121, 210].

3.2.1.1 Raw Materials

One of the limitations of VAM is the unsuitability of incorporating elemental powders as raw material feed. As the method itself relies on the use of an inert gas to backfill the chamber of the machine and flush out atmospheric air any powder within the Cu crucible could be agitated and escape into the chamber which could, in turn damage the vacuum and diffusion pumps. As such, the use of raw materials in a comparatively bulk form is preferred. Details concerning the alloying elements used within this work are presented in Table 3.1.

Table 3.1: Details concerning the purity, form and supplier of the raw elemental materials used for VAM.

Element	Purity (wt. %)	Form	Supplier
Aluminium (Al)	>99.99	Sheet, Lumps	NewMet Ltd, UK
Titanium (Ti)	99.9	Rod, Lumps, Wire	NewMet Ltd, UK
Vanadium (V)	99.8	Turnings	NewMet Ltd, UK
Chromium (Cr)	99.86	Lumps	NewMet Ltd, UK
Manganese (Mn)	99.95	Flakes	NewMet Ltd, UK
Silicon (Si)	>99.99	Grains (1 mm)	Advent Research Materials, UK

3.2.1.1 Arc 200 - Arcast Inc.

The Arc 200 cold crucible arc melting furnace allows the user to melt materials up to temperatures of 3000°C and rapidly solidify quantities of metal alloys up to 200 g. In this work alloy quantities in the region of 20 – 100 g have been manufactured with an estimated melting point exceeding 1800°C. A schematic of the machine is illustrated in Fig. 3.1.

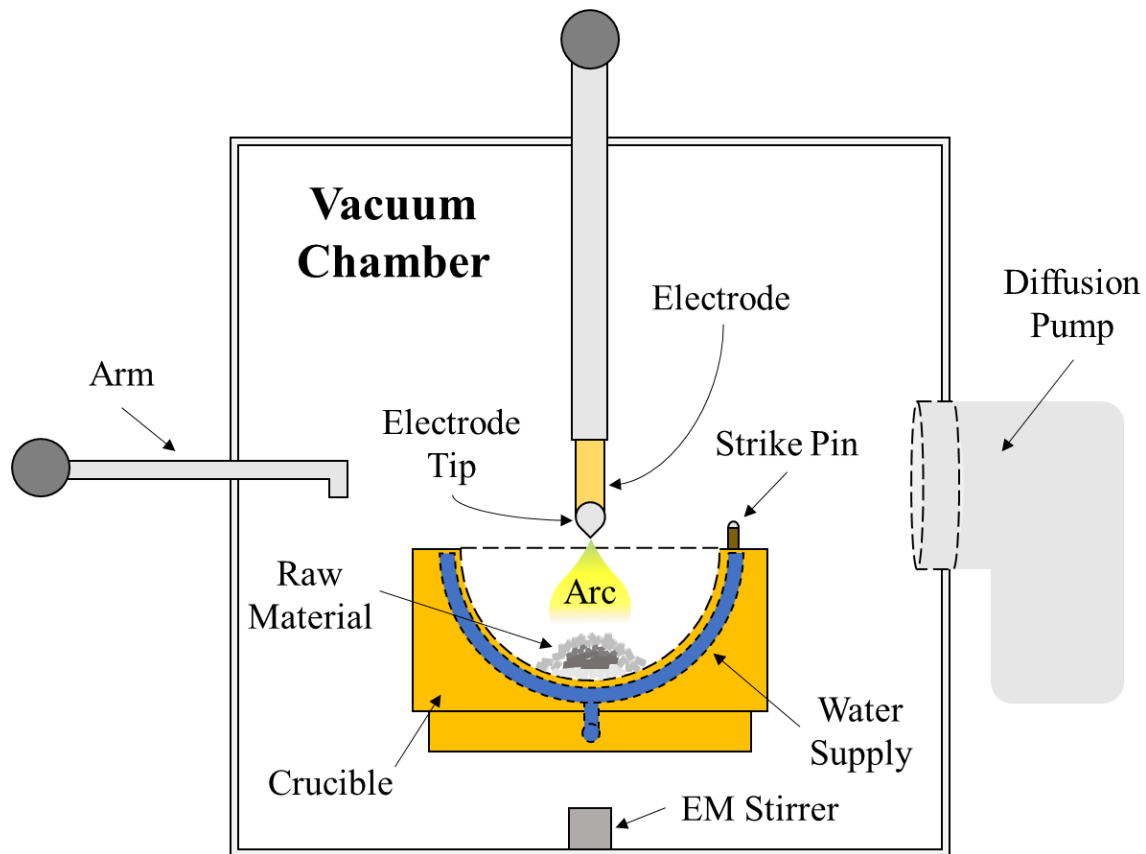


Figure 3.3: Schematic of the interior of the Arcast 200 vacuum chamber.

The Arc 200 contains a water-cooled Cu crucible within a stainless-steel chamber. Above the crucible lies the tungsten (W) electrode which is connected to a direct current power source. The stainless-steel chamber also includes an electromagnetic (EM) stirrer, a manipulation arm to assist with the handling of the alloys during the VAM process and is linked also with a diffusion and a rotary pump. Lastly, a strike pin lies on the top of the Cu crucible to assist with the initiation of the plasma arc. A typical operating procedure of the Arc 200 for this work would be described as follows.

1. The stainless-steel chamber and all its components are thoroughly cleaned with isopropanol and blue roll. This ensures minimal contamination across melts of different alloys and avoids damaging the vacuum pumps due to pre-existing material residue which tends to form during the VAM process.

2. The raw materials are placed within the water-cooled Cu crucible, with the lowest melting point or high vapour pressure elements located near the bottom. This ensures minimal volatile metal evaporation (as happens with e.g., Mn). An alternative setup can be used should no volatile metals be present, where Al is instead layered near the top. By maintaining a lower power current during the melting process, Al is the first element to melt thus creating a molten pool into which, alloying elements with a higher melting point such as V and Cr slowly diffuse within the melt allowing for a significantly more controlled melting process.
3. The chamber is subsequently sealed and is slowly evacuated to a pressure of under 4.0×10^{-2} mbar to remove the atmospheric air. It is then backfilled with a high-purity inert gas (in this case argon) up to 300 mbar. This evacuation-backfilling process is termed “purging” and is repeated at least three times to ensure that the atmospheric impurities within the chamber are minimal.
4. Once the evacuation process of the last purging cycle is complete the rotary pump is disabled, and the diffusion pump takes over. The diffusion pump is operated until a chamber pressure of 5.0×10^{-5} mbar or lower is achieved. The pump is then switched off and the chamber is backfilled to a pressure of 500-700 mbar. The final chamber pressure is determined by the amount and volatility of the raw materials. A sufficiently high chamber pressure to maintain a stable plasma arc during the melting process is required. Furthermore, slightly increasing the chamber pressure may prevent the evaporation of volatile elements such as Mn. At the same time, the chamber pressure can increase significantly when dealing with material quantities close to or over 100 g. Such melts require a higher current thus further expanding the inert gas volume. Additionally, the partial evaporation of volatile elements also contributes to an increase in pressure. This can result in the chamber pressure surpassing 1 bar, compromising the chamber seal. As such, atmospheric oxygen may enter the chamber creating a series of health and machine hazards. Therefore, it is crucial to continuously track the chamber pressure, even during the melting process and make the necessary adjustments.
5. The arc generation process is initiated by touching the strike pin, which is a conductive metal piece attached to the Cu crucible, with the electrode. By supplying the electrode with a sufficiently high current the plasma arc is created. The electrode is then moved away from the strike pin and brought over the raw material. The electric current is controlled manually using a pedal with an availability of up to 500 A. For the purposes

of this work, the maximum current is limited to 380 A which is sufficiently high to comfortably melt all the raw materials.

6. Once the mixture is in the liquid state, electromagnetic (EM) stirring is engaged to ensure a relatively homogeneous distribution of alloying elements within the melt and reduce the number of unmolten particles. After a few seconds, the EM stirring is disengaged, the arc is switched off and the sample is left to cool down to crucible temperature. The sample is then flipped and remelted at least five times to ensure sufficient homogeneity. This methodology has been slightly altered for the purposes of this work as several samples were found to crack extensively during the cooling process and would even explode during reheating. As such the samples were not allowed to cool down completely and were instead flipped and remelted a few seconds after the termination of the arc. This modification managed to effectively address this irregularity. This phenomenon is discussed in more detail in Chapter 5.
7. After the final remelting cycle, the sample is left to cool down to room temperature over several minutes after which the chamber is flushed with Ar to breach the seal and extract the sample. The chamber is then extensively cleaned once again.

3.2.2 Heat Treatments

Heat treatments were carried out to alleviate any inhomogeneities or microsegregation phenomena present in the as cast samples. The alloys were placed in alumina crucibles alongside Ti getters and sprayed with borax powder to ensure minimal oxidation. Trial heat treatments were carried out according to CALPHAD predictions to ensure the selection of a sensible homogenisation treatment temperature and duration. The use of an inert atmosphere was also investigated. As such it was determined that for the purposes of this study, a temperature of 1200°C and a duration of 8h under a flowing Ar atmosphere would be sufficient. It was also discovered that certain samples would be heat treatable under regular atmosphere; however, for the sake of consistency all samples explored within this thesis were heat treated using a flowing Ar atmosphere. The cooling method was varied between water-quenched (WQ), air-cooled (AC) and furnace-cooled (FC) depending on the purposes of each study. Additional details regarding the heat treatments will be provided in Chapters 4-7.

3.2.3 Metallographic Preparation

In cases where the density of the ingots was experimentally determined with the Archimedes principle, a Mettler Toledo NewClassic MF balance was used. These measurements were carried out with three repeats in both water and ethanol to ensure consistency. The samples

would then be transversely sectioned and mounted in conductive bakelite or resin for metallographic preparation. The samples were ground from both sides to expose the metallic surface. This was important for indentation testing as metal-metal contact greatly improves the accuracy of the measurements. The samples were ground down to a thickness of under 6.5 mm using grit papers P120, P240, P600, P1000, P1200 and P4000 with a grinder head rotation of 60 RPM, plate rotation of 251 RPM and a force of 25 N. This was to meet the sample thickness requirements of the X-Ray Diffraction (XRD) equipment. For the polishing steps a 1 μm diamond suspension was applied for 10 mins followed by colloidal silica, namely the Struers OP-U solution, for 20 mins using a head rotation of 60 RPM, plate rotation of 151 RPM and a force of 20 N. These extended polishing durations are necessary to relieve the stress of the sample surfaces and facilitate ideal nanoindentation measurement conditions. As a precaution, a series of samples were etched for 55 – 270 sec using a 0.5 M HF solution to ensure consistent observations would be made between the as-polished and etched state during Optical Microscopy (OM). Therefore, due to the limitations concerning the use of HF as an etching reagent in Sheffield-based laboratories and the rapid compositional modifications made to the alloys, the OM images displayed within this thesis concern samples in the as-polished condition unless stated otherwise.

3.2.4 Stereo Microscopy

Stereo microscopy (SM) is a technique that enables the observation of sample surfaces under a low magnification while providing a three-dimensional perspective. This is achieved by employing two separate optical paths through two objective lenses and eyepieces. As such, this is an efficient method for observing fracture surfaces or complex surface topographies to provide an insight regarding material characteristics before moving to the Scanning Electron Microscope (SEM). In this work, stereo microscopy was used with a Nikon SMZ 1500 to assess the fracture surfaces of selected samples and gain insight regarding their ductility and fracture mechanisms.

3.2.5 Optical Microscopy

Optical microscopy (OM) was used as a precursor to SEM for microstructural characterisation. Given that the polishing step during metallographic preparation revealed topological differences between the grains and microstructural constituents of each alloy, the use of depth-of-field or an angled light source was sufficient to highlight these features and render them observable through OM.

3.2.5.1 Particle Measurements

Particle measurements were conducted on selected samples to evaluate the effect of heat treatments on particle shape and distribution. This was performed using a Nikon Epiphot 300 inverted optical microscope with depth-of-field and the software Image-Pro plus. Over ten images were extracted from central regions of samples of interest at $\times 1000$ magnification. Information regarding the mean diameter and aspect ratio were extracted and analysed with an Analysis of Variance (ANOVA) method using Minitab18 [211] and Matlab 2020a. Tuckey's method is particularly useful for discerning differences between statistical populations and as such is ideal for comparing particles between an as cast and heat treated state to evaluate the effect of heat treatments.

3.2.6 Scanning Electron Microscopy (SE/BSE/EDX)

Scanning Electron Microscopy (SEM) is a high-resolution characterisation technique for imaging the microstructure of materials. Schottky Field Emission Gun (FEG) SEMs (SFEGs) are predominantly used in this work as they possess higher resolution imaging capabilities compared to regular SEMs given that they utilise emitters of W single crystals coated in ZrO_2 instead of a W filament source for the electron beam generation. SFEG-SEMs use an electron gun to generate a 1 – 30 keV electron beam focused into a ~ 1 nm spot by using a series of lenses before reaching and interacting with the material. The beam is directed through scanning coils or deflector plates during its passage through the final lens to raster over a rectangular area of the sample surface. The Philips XL 30/40 SFEGs and Inspect F50 used in thesis are such SEMs. The FEI Scios 2 SEM used in Chapter 7 uses a NICol electron column with a Trinity detector system to further amplify the reception signals and as such produce even higher resolution images by comparison [212].

During the interaction of the electron beam with the surface of the sample, some of the conduction or valence band electrons of the specimen are inelastically scattered. These surface level electrons are termed secondary electrons (SE) and provide information regarding the surface topology of the investigated material. Backscattered electrons (BSE) on the other hand originate from the electron beam itself. They are deflected off the material through elastic scattering interactions with the specimen atoms and as such have a larger interaction volume. Therefore, they contain a higher energy compared to SE and produce a more intense signal but also penetrate deeper into the material. Since heavier elements consist of a bigger nucleus, they can deflect more electrons compared to lighter elements during their interaction with the

electron beam. As such, areas of lighter contrast correspond to atoms with a greater atomic number compared to darker areas [213].

3.2.6.1 Energy Dispersive X-Ray Spectroscopy (EDX)

Energy dispersive X-Ray spectroscopy (EDX) is a semi-qualitative semi-quantitative technique which can provide insight regarding the chemical composition of various areas of a samples' surface during an SEM investigation. The energy transmitted from the electron beam to the sample surface may result in the excitation of inner shell electrons of the sample which in turn discharge X-rays upon returning to their ground state. Given that the magnitude of this discharge is exclusive for each element it is possible to identify compositional differences within a sample. The resolution limitation of this technique ($\sim 1 \mu\text{m}$) is related to the electron beam width itself and by extension the interaction volume of BSE electrons with the sample surface. As the depth resolution for EDX lies at 2-5 μm and the spatial resolution at 2 μm , the results of an EDX analysis are significantly affected by neighbouring and subsurface microstructural features, where these are varying across such scales. Therefore, exclusively relying on SEM-EDX data for deciphering fine features of a microstructure can lead to misinterpretations regarding the compositional characteristics of areas of interest especially when these tend to be similar [214]. Chemical compositions gathered through EDX measurements in this work consist averages of at least three equivalent areas. This does not apply in cases where line scan or quant map data was gathered.

3.2.7 Transmission Electron Microscopy (TEM)

Transmission Electron Microscopy (TEM) is a high-resolution imaging technique used for the characterisation of materials. It also uses an electron beam similar to the SEM; however, the beam itself is powered by a thermionic or field electron emission higher voltage source (100 – 300 kV). In contrast to the SEM, the electron beam is transmitted through the specimen and as such, the samples used for TEM analysis are typically less than $\sim 100 \text{ nm}$ thick. Evolving from the conventional TEM instrument, Scanning Transmission Electron Microscopy (STEM) uses additional scanning coils, detectors and circuits to further focus the beam into a finer spot (0.05 – 0.2 nm) and scan over the sample comparably to the SEM. This deems the STEM suitable for the application of techniques such as annular dark-field imaging and EDX. STEM is capable of three imaging modes bright field (BF), annular dark field (ADF) and high angle annular darkfield (HAADF). The difference between the BF and ADF modes lies in the collection of the signal pertaining to the central beam, which is transmitted through the sample, or signal from a diffracted beam respectively. As such, in BF mode regions with atoms with a greater

atomic number appear darker while in ADF mode these same regions appear brighter. HAADF expands upon the ADF mode by capturing high angle, incoherently scattered electrons [215].

3.2.7.1 Selected Area Diffraction (SAD)

Selected Area Diffraction is a technique used in TEM analysis which allows the measurement of crystal properties. Its function is based on the interaction of the electron beam with the sample where part of the beam can be diffracted or transmitted. A magnetic lens set below the sample deflects the rays of the transmitted beam which intersect at specific locations in the back focal plane forming a diffraction pattern. Analysis of the diffraction pattern can then yield information regarding the crystal structure of the investigated material such as the lattice type, lattice parameters or identify crystal defects [215].

3.2.7.2 Focused Ion Beam (FIB)

Focused Ion Beam (FIB) is an ion milling technique often used for the preparation of thin material sections for TEM analysis. Within the frame of this thesis, FIB sample preparation for TEM analysis was carried out by the University of Warwick. The FIB ion milling process was performed with a ThermoFisher Scientific Scios DualBeam. The selected sections surface areas were $5 \times 5 \mu\text{m}^2$ and were coated by a platinum (Pt) layer to protect the area from stray ion damage during the milling process. The surrounding area was bombarded by a beam of gallium (Ga) ions, milling through the surface. The areas of interest were then attached to W rods using the deposited Pt and were subsequently cut free from the surface. The extracted sections were then attached to carbon coated Cu TEM grids and thinned down using the Ga ion beam.

3.2.8 X-Ray Diffraction (XRD)

X-ray diffraction is a characterisation technique used for the derivation of the crystallographic properties of a material of interest. Through an XRD analysis we can gain information regarding the crystal structure and lattice parameter of an alloy and its constituent phases. It is however incapable of reproducing the exact atomic positions and types as in the case of Atom Probe Tomography (APT). It is also capable of providing insight on lattice strain, crystallinity, and crystal defects although these aspects of the technique were not explored within this thesis. The technique itself makes use of Bragg's law (Equation 3.18) which, when satisfied leads to the development of pronounced peaks in the diffraction pattern [216].

$$2d_{(hkl)}\sin\theta = n\lambda \quad \text{Equation 3.18}$$

where $d_{(hkl)}$ is the grating constant, hkl the miller indices, θ is the glancing angle, n is the diffraction order - a positive integer and λ the wavelength of the incident X-ray. Subsequently,

the lattice parameters are calculated by converting the 2θ peak positions obtained by satisfying Bragg's law into d-spacing and solving for the lattice parameter a according to Equation 3.19. It should be noted that Equation 3.19 is only appropriate in the cases where materials attaining a cubic crystal structure are assessed.

$$a = \sqrt{d^2(h^2 + k^2 + l^2)} \quad \text{Equation 3.19}$$

As previously mentioned, a flat surface and a small sample thickness (under 6.5 mm in our case) is required for an XRD analysis. An incident X-ray beam generated by a cathode ray tube with a Cu target material is directed to the surface of the sample. As the beam interacts with the atoms of the sample surface the beam photons elastically scatter due to the wavelength of the X-rays being similar to the interatomic spacing of solids. As the X-ray source and detector are rotated around the sample the diffraction angle and intensity are recorded and eventually a diffraction diagram is formed. The International Centre for Diffraction Data ICDD Sleve+ was utilised for phase analysis alongside the PDF-4+ database in cases where secondary phases would be present. Due to the novel nature of these alloys, the lattice parameters were derived according to transpositions of Eq. 19 and benchmarked against DFT data while homologous structures were used in appropriate cases.

3.2.9 Vickers Microhardness

The Vickers hardness test is a destructive mechanical testing method used for the determination of the hardness of a material. Microhardness testing refers to the use of smaller loads in comparison to conventional hardness testing, typically up to 10 N. The Vickers method uses a 4-corner pyramidal indenter diamond tip which is inserted within the tested material. Once the indenter is removed the diagonals of the indent are optically measured and the Vickers Hardness (HV) is determined according to Equation 3.20 where F is the applied load in N and d^2 the mean indent diameter in mm^2 .

$$HV = 0.1891 \frac{F}{d^2} [\text{N/mm}^2] \quad \text{Equation 3.20}$$

The HV results presented within this study originated from measurements conducted according to ASTM E384 [217] with an average of over 10 random indents extracted from each sample. The dwell time was set to 20 s while the load was varied between 200 – 1000 g to ensure that the results were independent of size effects.

3.2.10 Nanoindentation Testing

Nanoindentation testing is a destructive mechanical testing technique used for the evaluation of the Young's Modulus (E) of the investigated alloys within the frame of this research.

Similarly to HV testing it employs a much finer 3-corner diamond tip indenter called the Berkovich tip. The technique uses a dynamic loading-unloading cycle where the loading part pertains to the extraction of information regarding plastic deformation and the unloading to elastic deformation. This enables the measurement of the stiffness and subsequently the Young's modulus and hardness of the material by extrapolating from the unloading phase data. This is performed using the Oliver-Pharr polynomial curve-fit method [218] based around the following equations (Equations 3.21 – 3.23):

$$H = \frac{P_{max}}{A} \quad \text{Equation 3.21}$$

$$S = \beta \frac{2}{\sqrt{\pi}} E_r \sqrt{A} \quad \text{Equation 3.22}$$

$$\frac{1}{E_r} = \frac{1 - \nu^2}{E} + \frac{1 - \nu_i^2}{E_i} \quad \text{Equation 3.23}$$

where H is the hardness (Pa), P_{max} the load (N), A the contact area (m^2), S the elastic unloading stiffness (Pa), β the dimensionless parameter, E_r (Pa) the reduced elastic modulus, E (Pa) and E_i (Pa) the Young's modulus of the tested and indenter material respectively, ν and ν_i the Poisson's ratio of the tested and indenter material respectively.

3.2.11 Compression Testing

Compression testing is a destructive mechanical testing technique used to extract information regarding the mechanical properties of a material, in this case the elongation and compressive strength. It is a particularly useful technique for novel alloy development since specimens of smaller dimensions can be used compared to tensile testing. Furthermore, the uncomplicated cylindrical or parallelepipedal geometry requirement for compression specimens is simple to machine compared to the complex geometry requirements for a tensile testing specimen. Subsequently, the method is applicable even in cases where the novel alloys may lack ductility or machinability. The technique can be categorised into static or dynamic depending on the use of lower or higher strain rates during testing. In this case static testing was carried out using an applied strain rate of 0.15 mm min^{-1} ; however, the displacement was tracked through the plate movement without the use of the extensometer. As such, data regarding the elastic properties of the tested alloys could not be extracted. The testing was conducted according to the ASTM E9-09 standard [219], using at least two solid cylindrical specimens with a diameter of 6 mm and a height of 9 mm for each composition to ensure repeatability.

3.2.12 Inert Gas Fusion Analysis (IGFA)

Inert Gas Fusion Analysis (IGFA) is an analytical technique used for the determination of gas content such as hydrogen (H₂), oxygen (O₂) and nitrogen (N₂) in metallic materials. In this case the method was used for determining the O₂ content. The sample is positioned within a high purity graphite crucible and inserted within a furnace. It is then heated up to 3000°C under a high purity (>99.9999 wt. %) helium (He) atmosphere where melting occurs and therefore the gaseous phase is released, fusing with the carbon (C) in the crucible forming CO or CO₂ which is measured through infrared detection. Before the measurement, a standardised steel sample is assessed to calibrate the machine along with three empty graphite crucibles. The machine used for IGFA was the Bruker Galileo G8 [220].

4. Computational Prediction of Elastic Properties in the AlTiVCr-Si system through ICME

This Chapter concerns the development of a computational methodology for predicting the elastic properties of any multiphase Multicomponent Alloy (MCA). This method was applied on the AlTiVCr and AlTiVCr-Si_{7.2} alloys which satisfied certain design criteria. The purpose of the experimental work was to verify the model predictions and establish a better understanding of the AlTiVCr system.

The research encapsulated within this Chapter has been published and is available at:

Journal Paper

1. Stavroulakis, P., Freeman, C. L., Patel, D., Utton, C. and Goodall, R., Successful prediction of the elastic properties of multiphase high entropy alloys in the AlTiVCr-Si system through a novel computational approach. *Materialia*, 2022. 21: p. 101365. [121]

P. S. Contribution: Conceptualisation, methodology, literature review, computational work, experimental work, writing, review, editing.

Conference Papers

2. Daskalopoulos, I., Chaskis, S., Bouzouni, M., Stavroulakis, P., Goodall, R. and Papaefthymiou, S., Microstructural Characterization of AlCrTiV – Si High Entropy Alloy for advanced applications. *MATEC Web of Conferences*, 2021. 349: p. 02003. [221]

P. S. Contribution: Conceptualisation, methodology, review, editing.

3. Chaskis, S., Kiouisis, D., Stavroulakis, P., Goodall, R. and Papaefthymiou, S., Examination of Fracture Mechanisms in two Al – Ti – V – Cr – (Si) High Entropy Alloys. *MATEC Web of Conferences*, 2021. 349: p. 02002. [222]

P. S. Contribution: Conceptualisation, methodology, review, editing.

Diploma Theses

4. Daskalopoulos, I., Study of thermal processes and microstructural characterization of the AlCrTiV-Si high-entropy alloy. 2020. <http://dx.doi.org/10.26240/heal.ntua.19460> [223]

P. S. Contribution: Supervision, conceptualisation, methodology, supervision, computational work, experimental work, review.

5. Kiousis, D., Αξιολόγηση της δυνατότητας παρασκευής κράματος μέσης εντροπίας TiAlCrV με μεθόδους προσθετικής κατασκευής (Additive Manufacturing). 2021. <http://dx.doi.org/10.26240/heal.ntua.21006> [224]

P. S. Contribution: Supervision, conceptualisation, methodology, review.

4.1 Aim

As previously discussed in Chapter 2, the navigation of the compositional space of MCAs can pose a significant challenge. This may be extensively aided through the utilisation of predictive computational tools; however, these methodologies predominantly concern single phase FCC MCAs. Therefore, it was attempted to introduce a simple, yet transferrable and universal methodology capable of predicting the elastic properties of any multiphase MCA. Our general approach combines a variety of different established methods, each of which addresses a part of the problem.

- Thermodynamic Modelling with Thermo-Calc (TC) Software for the prediction of the equilibrium phases present in alloys of interest and their volume fractions.
- Density Functional Theory (DFT) simulations using CASTEP to assess the stability of candidate phases and derive the elastic properties of each phase.
- Finite Element Modelling (FEM) with ABAQUS to homogenise the elastic properties of each phase into a unified material.

The overall accuracy of the approach depends exclusively on the accuracy of each individual computational technique. Therefore, where required, the substitution of each technique with more accurate counterparts would be an option, depending on the availability of computational resources and required databases.

4.2 Computational and Experimental Methods

4.2.1 Computational Methods

4.2.1.1 Thermodynamic Simulations – Thermo-Calc Software

The thermodynamic calculations were carried out using the commercial software Thermo-Calc (TC) 2 version 2020a using SSOL4: SGTE Alloy Solutions Database v.4.9.g [225]. For the alloys studied here, the order to disorder transformation (BCC_B2 to BCC_A2) could not be modelled using this database. This is because the model for the BCC_B2, in this database, does not contain all the elements of interest in the present alloy. Although the formation of the BCC_B2 phase plays a pivotal role in the behaviour of the present system, the focal point of this research was not to strenuously optimise the accuracy of each individual computational technique (potentially developing a redundant level of accuracy if other methods did not reach this level), but rather to demonstrate the effective combination of all the different computational techniques into a streamlined process to successfully predict the elastic properties of novel materials within reasonable error. It must also be noted that our research

group did not have access to a more recent version of the database at that point. The phase volume fraction and matrix composition calculations were performed for 7.2 at. % Si at 800°C. According to the computational results, 800°C would roughly be the temperature where the solubility of Si in the matrix phase nears a minimum and is predicted to have precipitated in the form of Ti_5Si_3 particles at this temperature. Although the material has been heat treated at 1200°C during the experimental assessment, that does not guarantee that no additional formation of the Ti_5Si_3 took place during the air cooling (AC) process as more Si becomes available with a reduction in temperature.

4.2.1.2 Density Functional Theory Calculations – CASTEP

The DFT calculations investigated the matrix phases of the two MCAs and the Ti_5Si_3 intermetallic phase using CASTEP. A $2 \times 2 \times 2$ Body Centred Cubic (BCC) supercell containing a total of 16 atoms was used for the calculations regarding the matrix phase of the AlTiVCr and AlTiVCr-Si_{7.2} alloys. In the first case the supercell contained an equiatomic ratio of alloying elements, while in the latter the tested composition contained 25 at. % Al, 12.5 at.% Ti and 31.25 at.% V and Cr, respectively. This was to reflect the reduction of the Ti content in the matrix phase as a significant amount of Ti is utilised in the formation of the Ti_5Si_3 phase in the AlTiVCr-Si_{7.2} alloy as captured by TC. Ten different AlTiVCr supercells, each with a unique random arrangement of the atoms on the lattice sites were created for each matrix phase and tested in relation to their total energy to ensure that an energetic equivalency is evident between all configurations. From these configurations, three were randomly selected for the subsequent elastic property calculations. To ensure that the structural and elastic property differences between a BCC_A2 and BCC_B2 matrix phase were understood, ten different AlTiVCr BCC_B2 supercells were also tested. The supercells were created according to the atom probe information gathered by Qiu et. al. [97], with an Al atom lying in the centre of the B2 unit cell while the rest of the atoms were randomly distributed in the corners to verify that an energetic equivalency is evident between all configurations. From these configurations, three were also randomly selected for the subsequent elastic property calculations. A $2 \times 2 \times 2$ Hexagonal Close-Packed (HCP) supercell was used for the Ti_5Si_3 calculations, also containing 16 atoms. To achieve good precision in the geometry optimisation routine, a 750 eV and 700 eV cutoff energy was selected for the AlTiVCr-based and Ti_5Si_3 supercells respectively along with 0.014 Monkhorst-Pack [226] grid spacing and a finite basis correction of 5 eV over three steps. Full geometry optimisations were performed where the atoms could relax to their lowest energy state with variation of the lattice parameters and ionic movement while the centre

of mass was constrained. For the AlTiVCr-based supercells, the initial energy, force, stress, and displacement tolerances were specified at 2.5×10^{-5} eV, 4×10^{-2} eV/Å, 4×10^{-2} GPa and 2.5×10^{-3} Å respectively. For the Ti₅Si₃ supercell, the initial energy, force, stress, and displacement tolerances were specified at 5×10^{-5} eV, 10^{-2} eV/ Å, 5×10^{-3} GPa and 5×10^{-3} Å. Once the geometrically optimised structures were generated, we applied a set of deformations as described in Chapter 3.1.2.2.2 and performed a secondary geometry optimisation using the same convergence criteria with a constrained cell size while permitting ionic movement. The elastic constants for each single crystal were extracted through fitting the stress tensor calculated through CASTEP to the strain applied from the deformation patterns. Lastly, the polycrystalline (isotropic) elastic properties of each phase were calculated according to the guidelines provided in section 3.1.2.2.2 using the Voigt-Reuss-Hill (VRH) approximation.

4.2.1.3 Homogenisation Modelling

A homogenisation modelling approach was used to combine the elastic properties of the Ti₅Si₃ intermetallic phase with that of the matrix phase of the AlTiVCr-Si_{7.2} alloy, as calculated through DFT. The employed homogenisation scheme is described in Chapter 3.1.3 while accounting for a Ti₅Si₃ volume fraction of 20% as calculated through TC.

4.2.2 Experimental Methods

4.2.2.1 Materials and Processing

The raw materials used to manufacture the alloy (Al pieces and sheets, Cr pieces, 1 mm Si lumps, Ti wires and rods, V turnings) with purities >99.8% were supplied by NewMet Ltd, Waltham Abbey, UK. Experimental samples in the shape of ellipsoids with a diameter of 25 mm and 10 mm thickness were formed using an Arcast Arc 200 Vacuum Arc Melter (VAM) under a high purity argon (Ar) gas atmosphere and remelted 4–5 times to ensure chemical homogeneity. One AlTiVCr and AlTiVCr-Si_{7.2} sample were sectioned, and one half of each sample was used for metallographic preparation while the other half was heat treated. The heat treatment was carried out according to Chapter 3.2.2 at 1200°C for 8 h followed by air cooling (AC). Density data were extracted using Archimedes' method. The samples were mounted in conductive bakelite and were prepared according to Chapter 3.2.3. The chemical composition of the investigated samples as extracted through EDX is presented in table 4.1 as a reference point since EDX measurements constitute qualitative measurements.

Table 4.1 Chemical composition of the investigated AlTiVCr and AlTiVCr-Si_{7.2} MCAs measured through EDX analysis.

Alloy	Al at. %	Ti at. %	V at. %	Cr at. %	Si at. %
AlTiVCr	25 ± 6	23 ± 2	26 ± 2	25 ± 2	-
AlTiVCr-Si _{7.2}	23 ± 6	23 ± 2	23 ± 1	22 ± 2	8 ± 4

4.2.2.2 Optical (OM), Scanning Electron (SEM) Microscopy & Electron Dispersive X-ray Spectroscopy (EDX)

The microstructures of the samples were investigated using a Nikon Eclipse LV150 and a Nikon Epiphot 300 Optical Microscope (OM) under polarised light, using the analyser and darkfield filters alongside depth-of-field observation. Particle measurements were conducted according to Chapter 3.2.4.2.1. Further microstructural investigation was carried out using the FEI XL30 S and XL40 S Field Emission Gun Scanning Electron Microscope (SEM) with Secondary (SE) and Backscatter Electrons (BSE) under 20 kV accelerated voltage, in conjunction with Energy-Dispersive X-Ray Spectroscopy Analysis (EDS) to evaluate possible segregation phenomena and perform phase analysis and characterisation.

4.2.2.3 X-ray Diffraction Analysis

For the determination of the crystal structure of the bulk alloys, in both the as cast and heat treated conditions, X-ray Diffraction (XRD) was carried out using a Bruker D2 Phaser diffractometer with Ni K-β filtered Cu Kα radiation operating at 30 kV and 10 mA. The upper and lower discriminators were 0.11 and 0.25 V respectively. The scanning angle range was set from 20° to 80° 2θ with a step size of 0.02° and with the sample rotating at 15 rpm. For the as cast AlTiVCr, as cast AlTiVCr-Si_{7.2} and heat treated AlTiVCr-Si_{7.2} a 0.2 mm primary divergence slit was used while for the heat treated AlTiVCr a 1 mm primary divergence slit was used instead. Subsequent phase analysis was undertaken using the International Centre for Diffraction Data's (ICDD) PDF-4+ database (2022 edition) and the associated Sieve+ software.

4.2.2.4 Nanoindentation Testing

For the evaluation of the elastic properties of the tested materials, the nanoindentation testing technique was employed, using a Hysitron Ti Premier and a MicroMaterials Nanotest Vantage nanoindenter. In both cases, standard Berkovich tips were used with a load function consisting of 5 s load, 5 s dwell and 5 s unload times and 30 s load, 60 s dwell and 30 s unload respectively. The tests were load controlled and were limited to a maximum load of 3000 μN

and 300 mN respectively. Also, thermal drift data was collected post indentation with the Nanotest Vantage. The nanoindentation grids used with the Ti Premier were 10×10 with a $10 \mu\text{m}$ spacing for all samples while for the Nanotest Vantage they were a 5×5 grid with $100 \mu\text{m}$ spacing for the as cast AlTiVCr sample, a 10×10 grid with $100 \mu\text{m}$ spacing for the heat treated AlTiVCr sample, a 10×20 grid with $250 \mu\text{m}$ spacing for the as cast AlTiVCr-Si_{7.2} sample and a 10×10 grid with $100 \mu\text{m}$ spacing for the heat treated AlTiVCr-Si_{7.2} sample. An extensive description of the methodology regarding the Young's modulus derivation is presented in Chapter 3.2.6.2.

4.3 Results and Discussion

4.3.1 Modelling Predictions

4.3.1.1 Phase Prediction and Analysis

The first step of the methodology depends on achieving an adequate thermodynamic description of the system of interest. Thus, it is important to evaluate the capability of thermodynamic databases in terms of phase prediction and fraction analysis for the MCA system of interest (noting of course that for other systems an assessment of the databases might yield different results). A similar study, concerning the same alloys, in the AlTiVCr system was carried out by Huang et al. [100], where the TCHEA2: TCS High Entropy Alloys Database was used. Their work showed the formation of a single ordered Body-Centred-Cubic (BCC) B2 phase when assessing the equiatomic AlTiVCr alloy without Si addition, below 700–900°C. They also suggested the initiation of an order-disorder transformation taking place at that temperature. In this work the SSOL4:SGTE Alloy Solutions Database v.4.9.g is instead used. There are limitations to using the SSOL4 database for these systems, since it cannot predict the order to disorder transformation for these alloys. These calculations (Fig. 4.1) indicated that the formation of the ALM_DO19 ($\text{Ti}_{62}\text{Al}_{33}\text{V}_5$) and TiAl phases is instead favoured below the temperature threshold, alongside a disordered BCC phase even in the case of the 0 at. % Si which refers to the equiatomic AlTiVCr alloy. The stability of the B2 phase regarding AlTiVCr at lower temperatures has been previously verified in the work by Qiu et al. [97] both experimentally and computationally, while no evidence was found for the formation of the TiAl and ALM_DO19 phases. While it is highly likely that the CALPHAD databases employed here may be overestimating the number of phases forming at lower temperatures, this could also be a case of the SPPs being characterised by sluggish formation kinetics since CALPHAD calculations refer to equilibrium conditions. This could also explain why SPPs were not identified in the original work given that their experimental investigation only focussed on rapidly cooled as cast samples.

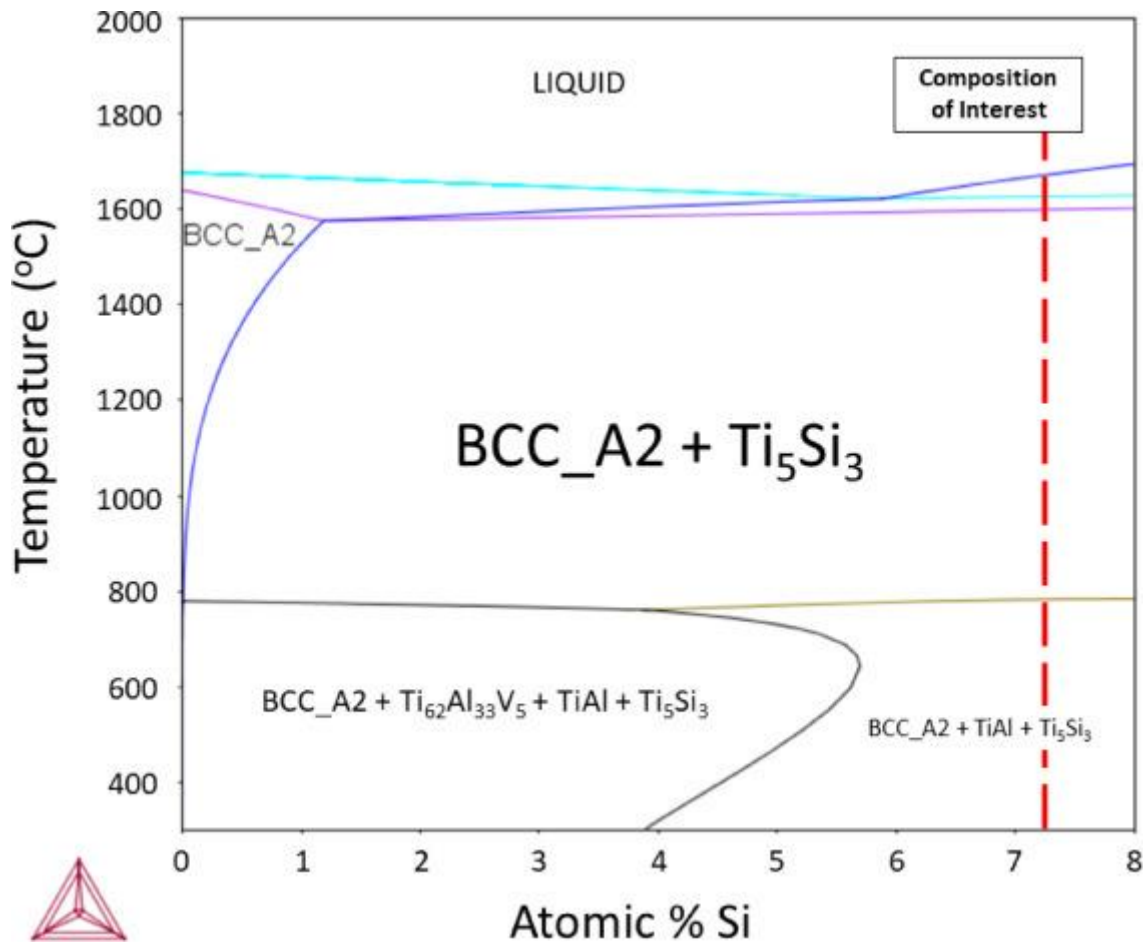


Figure 4.1. Calculated phase diagram of the AlTiVCr-Si_x system using the Thermo-Calc software alongside the SSOL4: SGTE Alloy Solutions database. The region of interest concerning the investigated AlTiVCr-Si_{7.2} alloy is highlighted accordingly.

With the addition of Si, both databases predicted the presence of the Ti₅Si₃ phase for the entire solid-state temperature range. Additionally, this study suggested that for a lower Si content the TiAl and ALM_DO19 SPPs form alongside the Ti₅Si₃ phase, while for a greater Si content the ALM_DO19 phase is no longer evident.

The prediction of these phases at lower temperatures suggests that either the SSOL4 database is not accurate enough in terms of phase prediction in the present MCA system (in contrast to the TCHEA2 database used by Huang et al. [100]) or that the kinetics of formation for the secondary phase particles (SPPs) are relatively sluggish, and thus would require a low-temperature heat treatment of extensive duration for their precipitation to occur. As far as the author is aware, no experimental research has been carried out to date to investigate a lower temperature thermodynamic equilibrium where these transformations are indicated to occur in the present system.

It is once again underlined that the current database is unable to predict this order-disorder transformation and as such the results concerning temperatures under 800°C would be considered questionable. Nevertheless, as the temperature spectrum of interest in this work lies within the dual phase BCC_A2 – Ti₅Si₃ region roughly above 800°C (Fig. 4.1), it was decided that the current thermodynamic predictions using SSOL4 were sufficient for the present study. The expected volume fraction of the Ti₅Si₃ particles in the AlTiVCr-Si_{7.2} alloy was calculated here at approximately 20%. Another phenomenon predicted in the present study is the depletion of the AlTiVCr matrix in both Ti and Si. This occurs as both alloying elements are involved in the formation of the Ti₅Si₃ secondary phase (Table 4.2).

Table 4.2 Predicted chemical composition of the AlTiVCr-Si_{7.2} alloy matrix phase at 800°C compared to the experimentally measured heat treated matrix composition.

Elements	Nom. Composition (at.%)	Exp. Matrix Composition (at.%)	Predicted Matrix Composition (at.%) (using SSOL4)
Al	23.2	27.8	28.70
Ti	23.2	18.8	13.86
V	23.2	25.6	28.70
Cr	23.2	26.9	28.70
Si	7.2	0.99	0.04

4.3.1.2 Computational Elastic Properties

Based on the thermodynamic calculations, it was apparent that the AlTiVCr alloy is composed of a single BCC matrix phase and that the AlTiVCr-Si_{7.2} alloy has a dual phase microstructure containing a BCC matrix phase, which is reduced in Ti content, and the Ti₅Si₃ intermetallic phase. To proceed with the prediction of the alloy properties each phase was assessed individually in terms of their elastic properties, initially through computational means, followed by experimental validation. It should be noted that all DFT calculations were carried out at 0 K. The CASTEP simulations predicted a lattice parameter of 3.053 Å for the AlTiVCr alloy, which compares well to the experimental values of 3.075 Å [97], and 3.008 Å for the matrix phase of the AlTiVCr-Si_{7.2} alloy.

The mean calculated C₁₁, C₁₂ and C₄₄ components of the elastic matrix of the AlTiVCr and the matrix phase of the AlTiVCr-Si_{7.2} alloys are shown in Table 2. The mean bulk modulus (B) of the AlTiVCr A2 alloy was estimated at 147.1 GPa which agrees with the previously computationally reported value of 146.6 GPa for the BCC lattice [97]. Additionally, these estimates for the shear modulus (G) indicated a mean modulus of 65.0 GPa. Lastly, from B and G the Young's modulus (E) and Poisson's ratio (ν) were estimated at 170.1 GPa and 0.307, respectively. These results are almost identical for the AlTiVCr B2 alloy where B was estimated at 150.3 GPa, G at 66.2 GPa, E at 173.3 GPa and ν at 0.308. As for the AlTiVCr-Si_{7.2} matrix, the computational calculations produced a mean B of 166.8 GPa and a G of 73.0 GPa, while E and ν were estimated at 191.2 GPa and 0.31 respectively.

Table 4.3 Mean calculated elastic constants of the AlTiVCr and AlTiVCr-Si_{7.2} alloy matrix phases.

Alloy Matrix Phase	Elastic Constants (GPa)		
	C ₁₁	C ₁₂	C ₄₄
AlTiVCr A2	208.5 ± 18.9	116.4 ± 12.8	82.0 ± 11.0
AlTiVCr B2	212.2 ± 14.5	119.4 ± 9.2	84.1 ± 11.2
AlTiVCr-Si_{7.2}	245.0 ± 1.9	127.7 ± 3.0	84.5 ± 4.9

Regarding the Ti₅Si₃ intermetallic phase, the results of the simulations deviated from the reported elastic constants C₁₁, C₁₂, C₁₃, C₃₃, C₄₄ and C₆₆ found in other computational work [227, 228] by up to 25%. The estimates for the bulk and shear moduli stood at 141.8 GPa and 96.6 GPa respectively while the reported values were 139 GPa and 94 GPa respectively. The Young's modulus and the Poisson's ratio were estimated to be 236.1 GPa and 0.22 in this work while the previously reported computationally-derived values were 231.3 GPa and 0.22,

respectively. However, as the deviation of this work's computational and experimental result for the bulk, shear and Young's moduli is less than 3%, the estimate is deemed satisfactory.

4.3.1.3 Material Homogenisation

All the collected information on the phases present in the AlTiVCr-Si_{7.2} alloy and their elastic properties are used in ABAQUS and homogenised into a unified material. The homogenised computational Young's modulus was estimated at 200.1 GPa with a Poisson's ratio of 0.29.

4.3.2 Experimental Verification and Analysis

4.3.2.1 Microstructure Characterisation

The experimental investigation of the as cast and heat treated conditions of the equiatomic AlTiVCr alloy through OM and SEM also showed no evidence of any secondary phases having formed, as shown in Fig. 4.2. Shrinkage porosity was notable especially in the case of the AlTiVCr sample where cracks were found propagating from one porous region to another. Nevertheless, fine pores were also present in both materials within the interior regions without any indication of cracks. Furthermore, the dendrites evident in both as cast samples were erased during the heat treatment, supporting the assumption that a temperature of 1200 °C is sufficient to enable extensive diffusion to take place in the duration of the heat treatment.

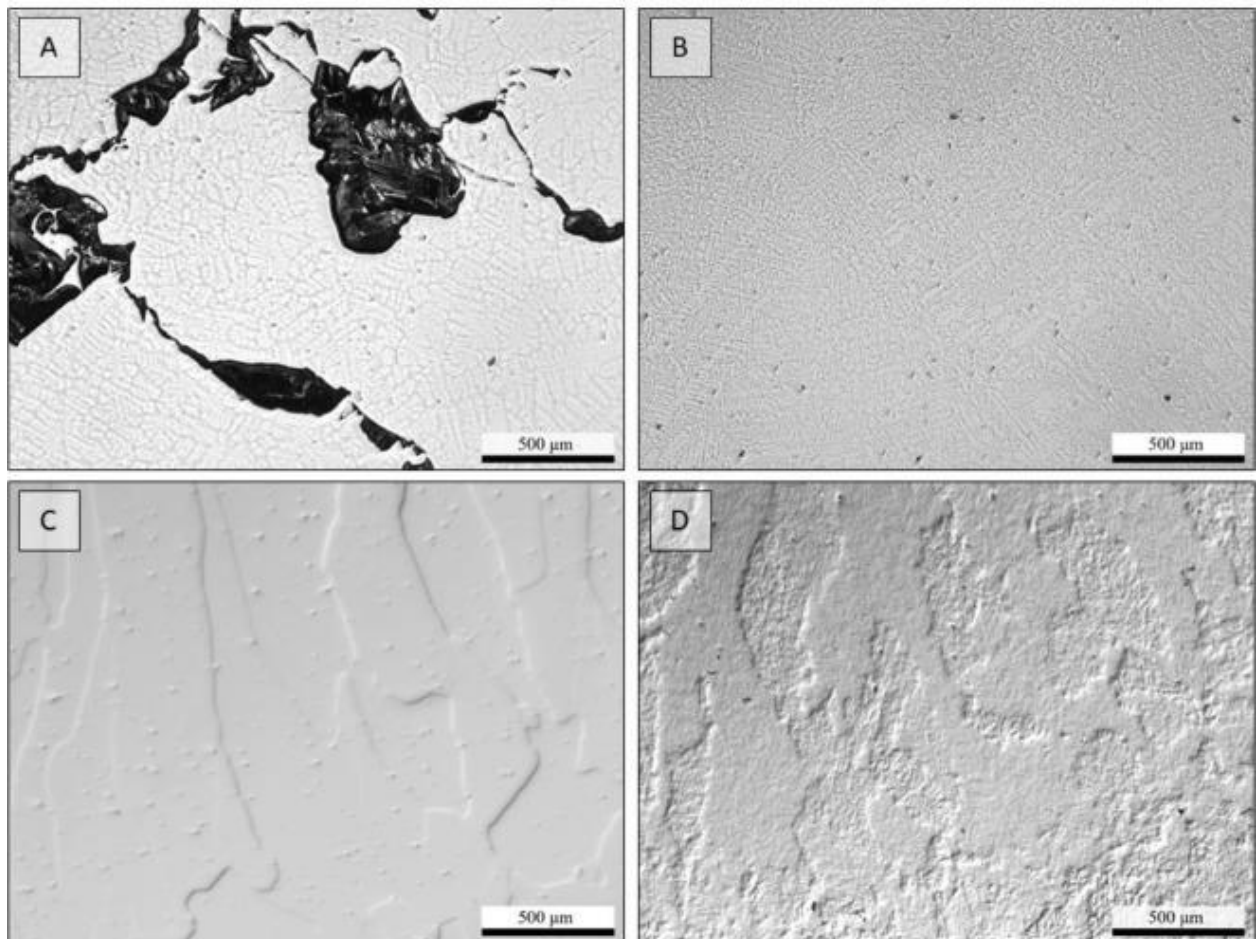


Figure 4.2 Optical micrographs at $\times 50$ magnification of relief polished specimens from the central region of the A) as cast AlTiVCr, B) as cast AlTiVCr-Si_{7.2}, C) heat treated AlTiVCr and D) heat treated AlTiVCr-Si_{7.2} samples.

Experimental validation through OM and SEM showed that the Ti₅Si₃ phase was indeed present in both the as cast and heat treated conditions of the AlTiVCr-Si_{7.2} alloy, with no sign of any other SPPs (Fig. 4.2-4.3). The volume fraction of the Ti₅Si₃ particles was measured as 23% and 24% in the as cast and heat treated condition respectively. The distribution of the

Ti₅Si₃ particles in the AlTiVCr matrix was relatively homogeneous without preferential formation points, while the intermetallics' size and shape varied significantly depending on the local cooling rates, as seen in Fig. 4.3 and 4.4. This resulted in the production of coarse, elongated intermetallics near the centre and very fine spherical particles near the surface of the samples, where the cooling rate was highest. During the heat treatment, the intermetallics in the central region appeared to undergo a fragmentation and partial spheroidisation process. The particles closer to the surface, however, seemed to undergo an agglomeration process, hinting that an Ostwald ripening mechanism may be occurring.

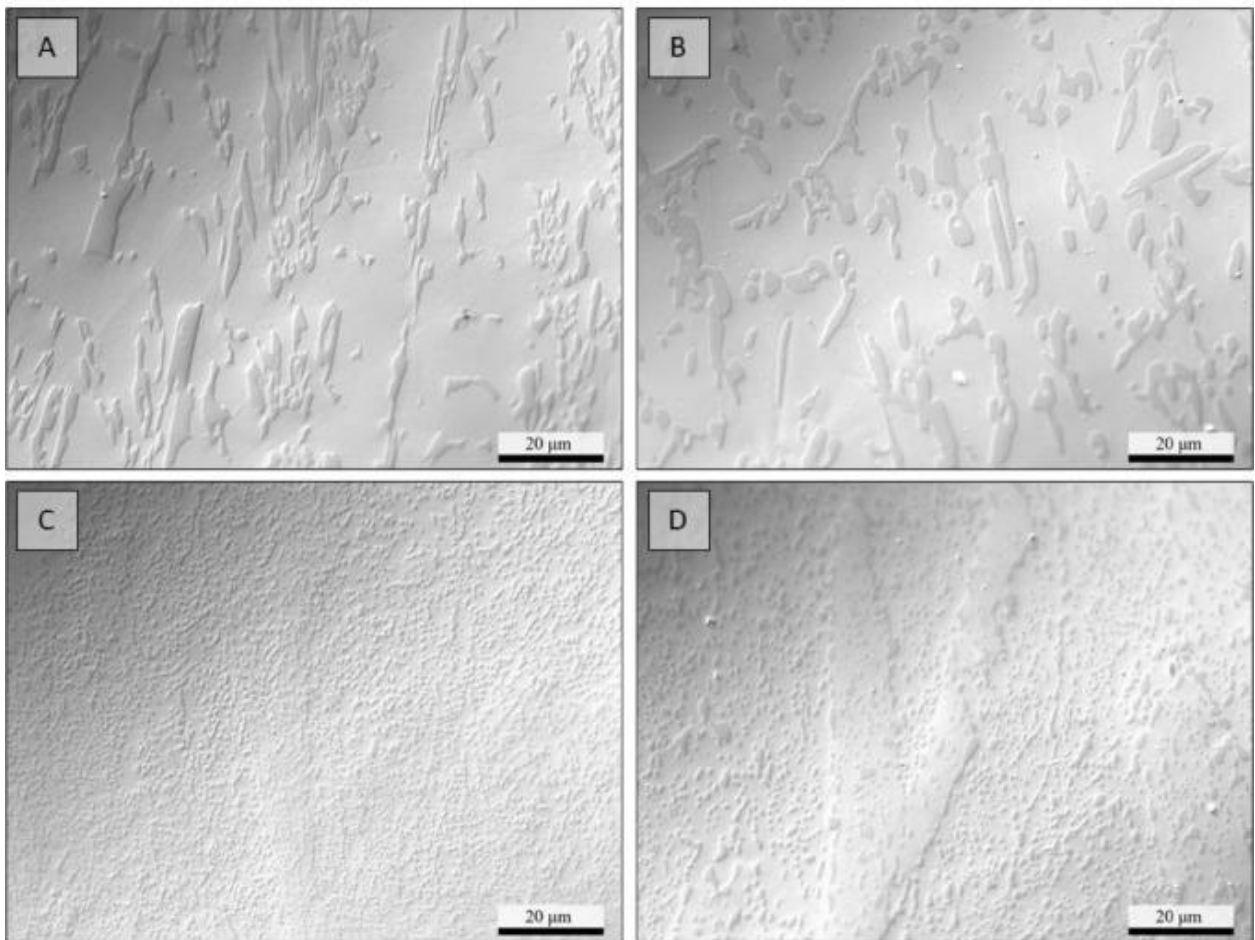


Figure 4.3 Optical micrographs at $\times 1000$ magnification relief polished specimens of the central region of the A) as cast AlTiVCr-Si_{7.2}, B) heat treated AlTiVCr-Si_{7.2} and the surface (high cooling rate) region of the C) as cast AlTiVCr-Si_{7.2}, D) heat treated AlTiVCr-Si_{7.2} samples.

This suggestion is further strengthened by the fact that the apparent number of particles per unit area in the heat treated condition is significantly reduced in comparison to that of the as cast condition. In turn, this observation points to the dissolution of some (likely the smaller) particles and the migration of their constituent alloying elements towards other (likely coarser) particles, resulting in the growth of the latter.

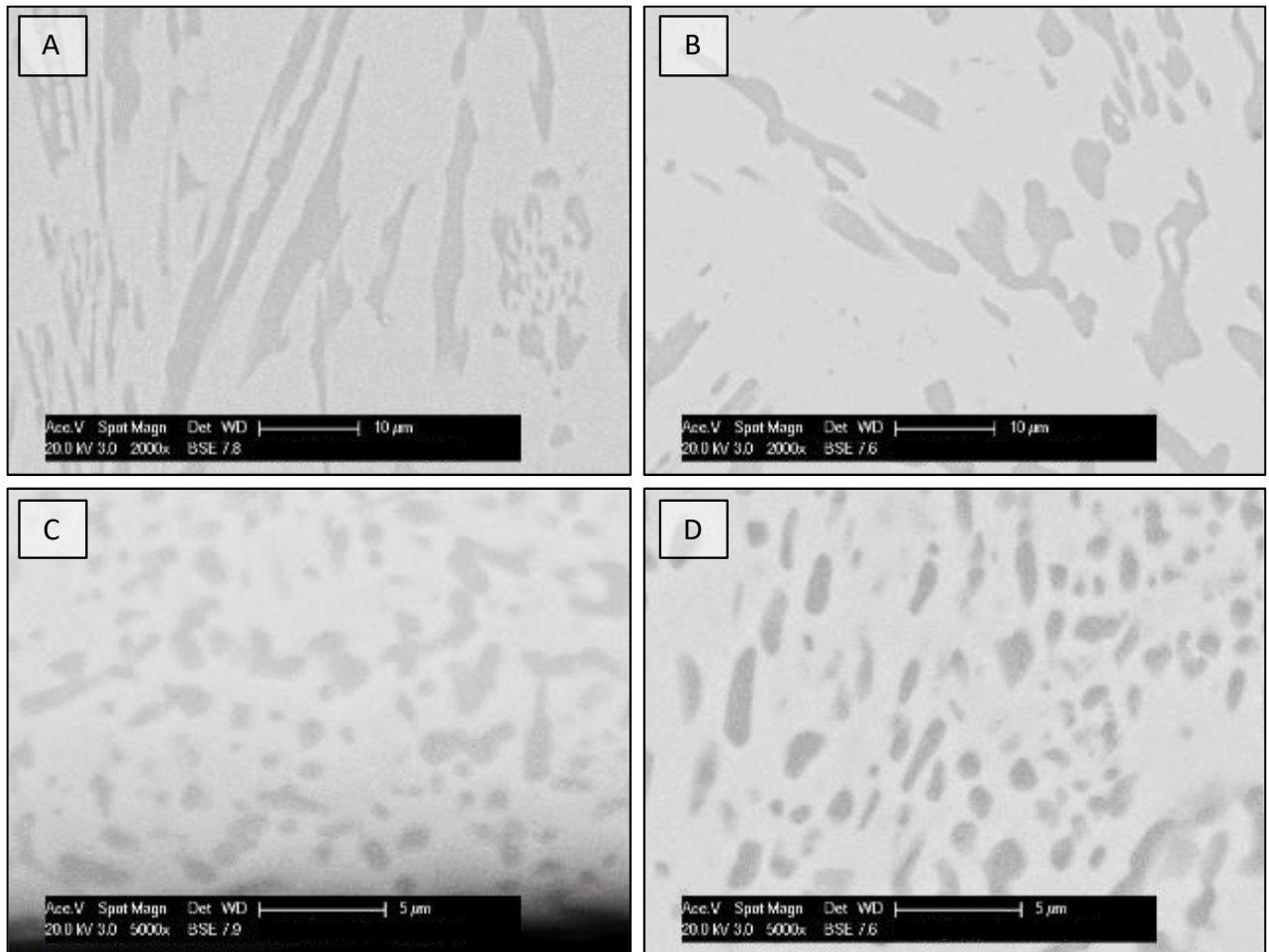


Figure 4.4 SEM BSE images of the A) as cast AlTiVCr-Si_{7.2}, B) heat treated AlTiVCr-Si_{7.2} and the surface (high cooling rate) region of the C) as cast AlTiVCr-Si_{7.2}, D) heat treated AlTiVCr-Si_{7.2} samples.

Upon further evaluation of the microstructural features of the AlTiVCr sample it becomes apparent that any phenomena associated with chemical segregation have been eliminated during the heat treatment. More specifically, the as cast alloy exhibits a complementary segregation of Al-Ti and V-Cr which could be explained by the affinity between Al-Ti and V-Cr as illustrated in Fig. 4.5. This effect is not sufficient nor extensive enough to result in the formation of a separate secondary phase or the manifestation of observable microstructural constituents without the aid of EDX. Nevertheless, this irregularity seems entirely nullified in the heat treated condition where a homogeneous distribution of all alloying elements is instead observed as demonstrated in Fig. 4.6. This complementary segregation phenomenon could not be verified in the AlTiVCr-Si_{7.2} alloy partially due to the significant volume fraction of the Ti₅Si₃ intermetallics (Fig 4.7). Again, this reinforces the concept that indeed the AlTiVCr system seems to be highly responsive to heat treatments in terms of alleviating any segregation phenomena present in the as cast condition.

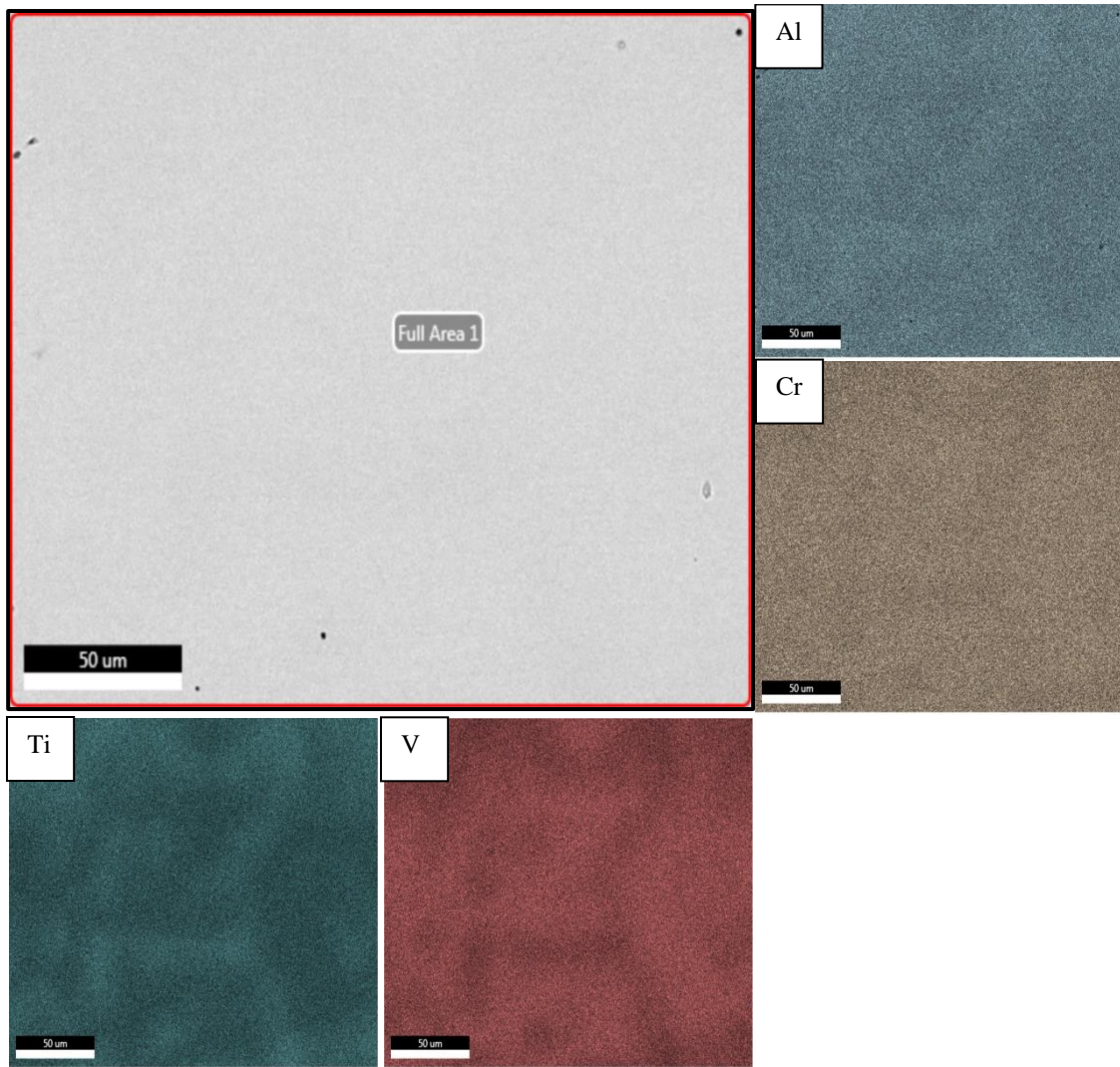


Figure 4.5 EDX quant maps illustrating the distribution of Al, Ti, V and Cr in the investigated material in the as cast condition.

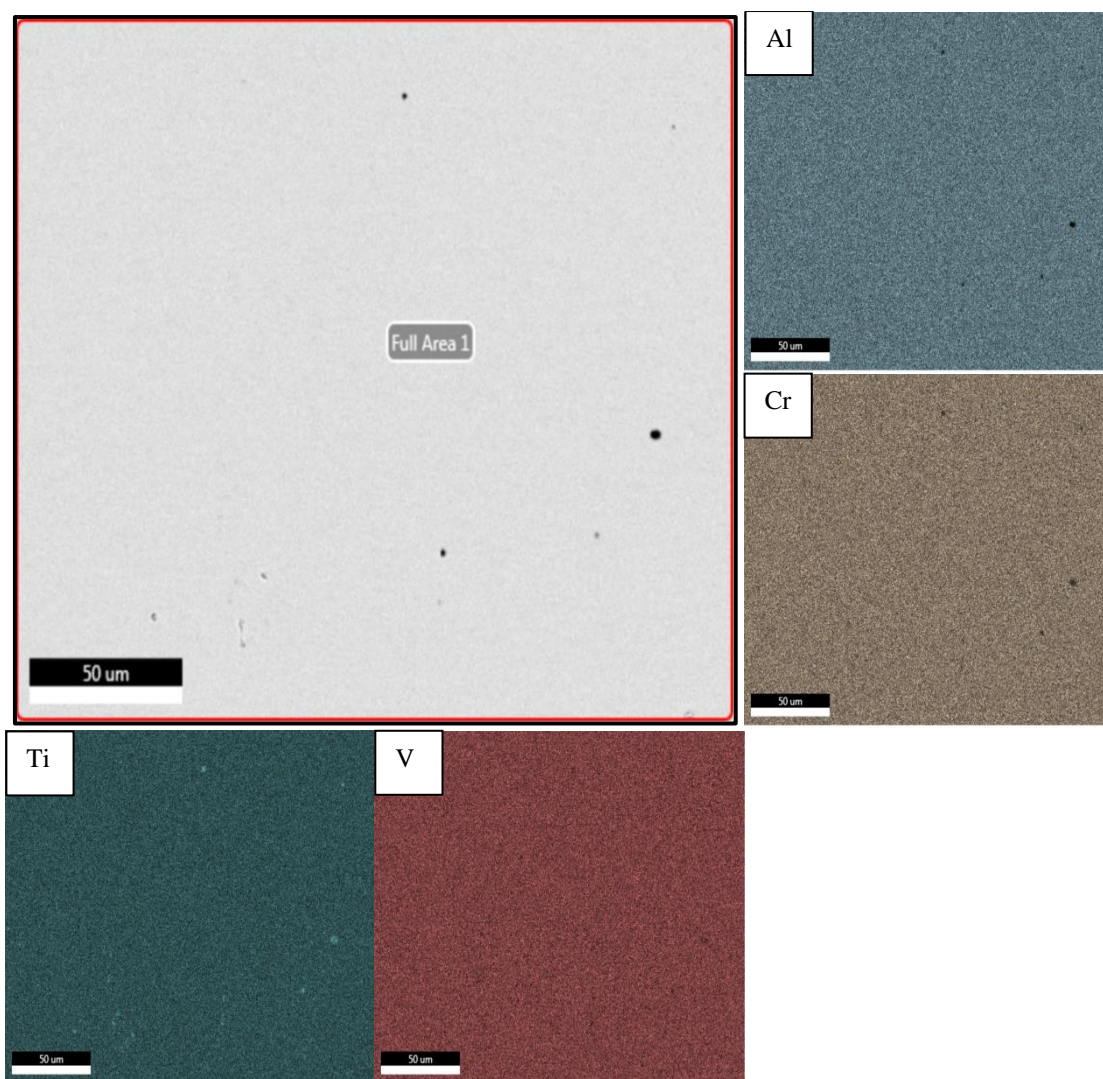


Figure 4.6 EDX quant maps illustrating the distribution of Al, Ti, V and Cr in the investigated material in the heat treated condition.

Both the quantitative analysis of the alloying elements present in the matrix phase of the $\text{AlTiVCr-Si}_{7.2}$ produced using Thermo-Calc software with SSOL4 and the EDX analysis (Fig. 4.7) point to a degree of Ti and Si depletion in the matrix phase. This effect is not, however, as significant as originally predicted using Thermo-Calc software with SSOL4 (Table 4.2) since the thermodynamic calculations refer to an equilibrium state. In turn, this leads to an effective change in the ratio of the alloying elements in the matrix, deviating from an equiatomic composition. This indirect compositional tuning may have altered the elastic properties of the matrix phase. Overall, most of the phenomena that were experimentally verified to occur in the investigated systems were qualitatively captured by thermodynamic modelling with the SSOL4 database; this is an acceptable degree of precision for use as a basis for the subsequent calculations. In conclusion, the thermodynamic simulations showed that the SSOL4 database can provide an adequate description of the behaviour of the AlTiVCr and

AlTiVCr-Si_{7.2} alloys concerning the high-temperature (above 800°C) region. However, there are some points of disagreement with the TCHEA2 database regarding temperatures under 800°C as SSOL4 is unable to predict the order-disorder transformation.

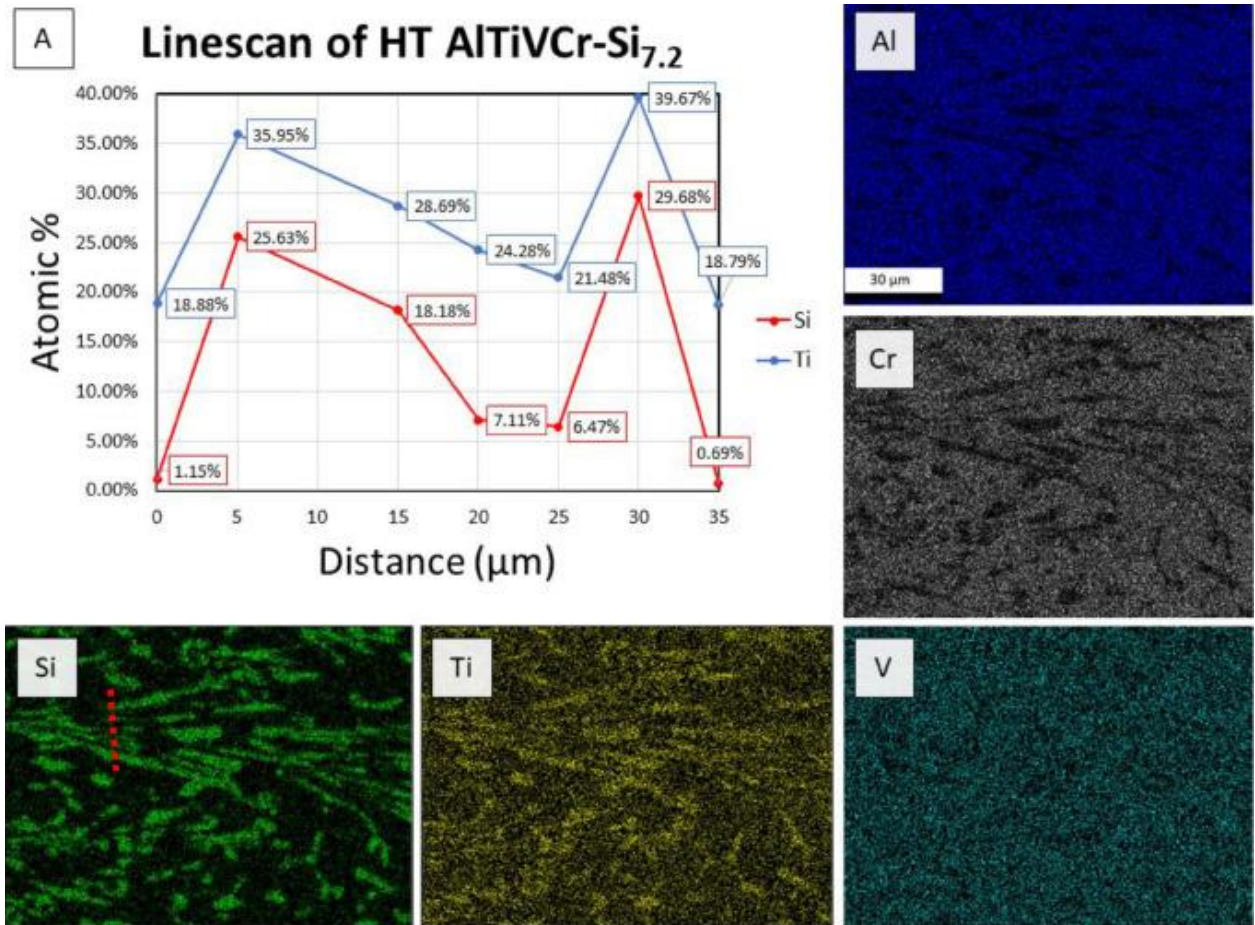


Figure 4.7 Investigation of the heat treated AlTiVCr-Si_{7.2} alloy showing: A) The Si and Ti content along a linescan where increases in both elements suggest the presence of Ti₅Si₃ intermetallics within an AlTiVCr matrix, and the distribution of Al, Ti, V, Cr and Si content in the present sample. Linescan path indicated with a red dotted line on the Si quant map image.

4.3.2.1.1 Statistical Ti₅Si₃ particle analysis

The as cast and heat treated AlTiVCr-Si_{7.2} OM micrographs were scanned to compare the difference in aspect ratio and mean diameter of the intermetallic Ti₅Si₃ phase. First, the data received was statistically analysed through analysis of variance (ANOVA) which revealed notable differences in the particle distributions between the two samples, with a difference of 0.6 μm (Table 4.4, Fig. 4.8) and 1.8 μm (Table 4.5, Fig. 4.9) for the mean aspect ratio and mean diameter respectively between the two samples. The decrease in the average values of the aspect ratio and mean diameter for the heat treated sample can be attributed to the spheroidisation of the intermetallic phases due to the progression of the heat treatment, thus confirming previous OM and SEM findings.

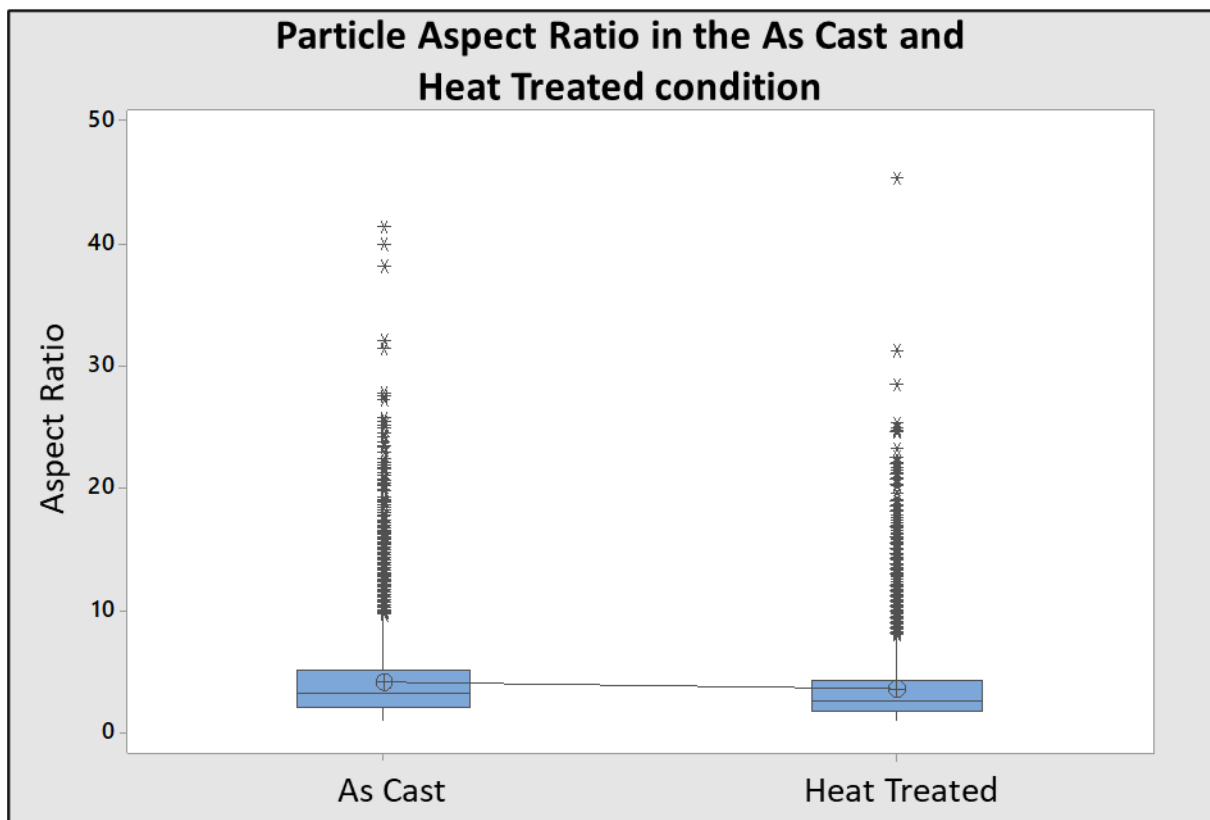


Figure 4.8 Particle aspect ratio in the as cast and heat treated condition of the AlTiVCr-Si_{7.2} alloy as analysed using the ANOVA method.

Table 4.4 Numeric data corresponding to the particle aspect ratio of the AlTiVCr-Si_{7.2} alloy in the as cast (AC) and heat treated (HT) condition.

Aspect ratio	N	Mean	St. Dev
AC	7069	4.1983	3.2429
HT	6013	3.6072	2.8527

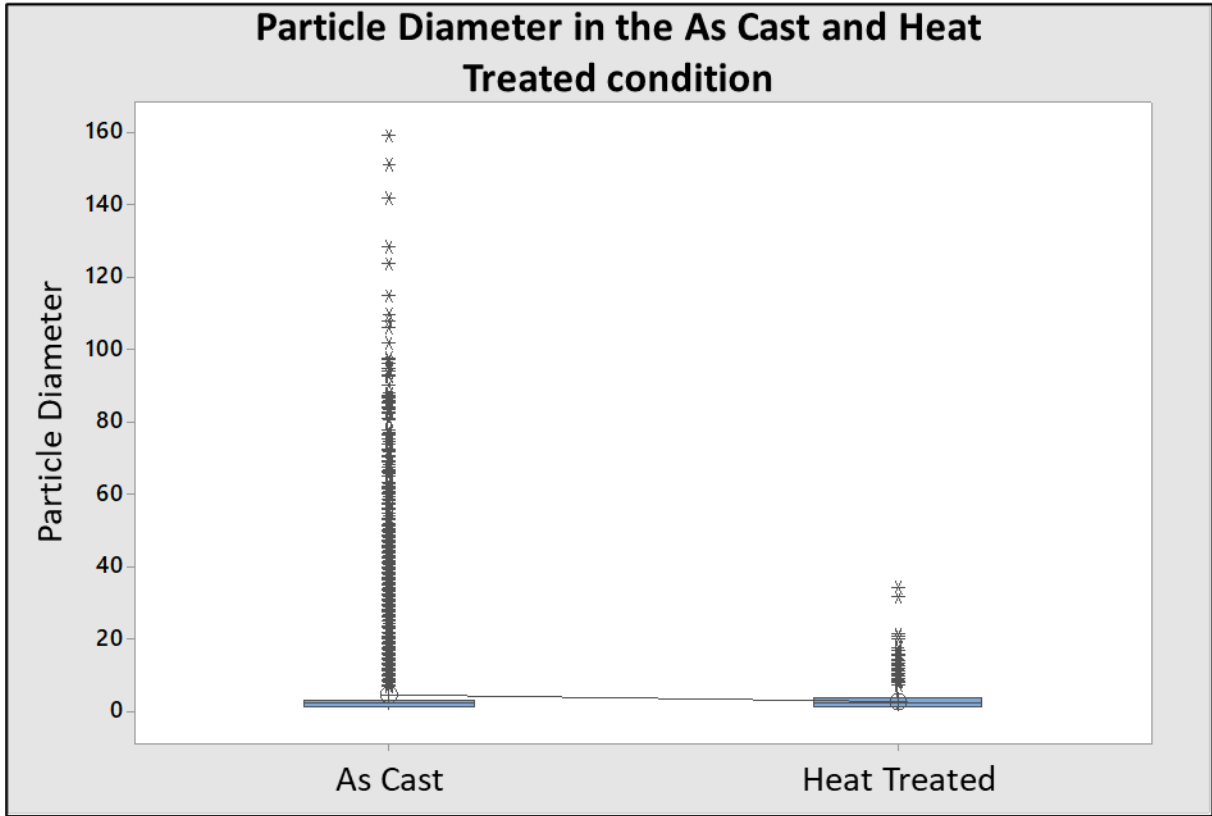


Figure 4.9 Particle diameter distribution in the as cast and heat treated condition of the AlTiVCr-Si_{7.2} alloy as analysed through the ANOVA method.

Table 4.5 Numeric data corresponding to the particle diameter of the AlTiVCr-Si_{7.2} alloy in the as cast (AC) and heat treated (HT) condition.

Diameter	N	Mean	St. Dev
Mean AC	7069	4.683	11.105
Mean HT	6013	2.8225	2.0829

The data was additionally processed with the aim of visualising the particle size distribution. For the heat treated sample the average and median values converged (Figs. 4.10 – 4.11), indicating that during the heat treatment most of the intermetallic phases tend to adopt uniform characteristics, when compared to the as cast sample. Moreover, two different peaks are identified in the distribution of particle diameters corresponding to the mean diameter values for the coarser and finer intermetallic phases (Figs. 4.10 – 4.11). By comparing the two samples it becomes evident that the two peaks tend to separate with the progression of the heat treatment, indicating the growth of the coarser intermetallic phases at the expense of the finer ones. Naturally, this points to an Ostwald ripening [229] effect taking place.

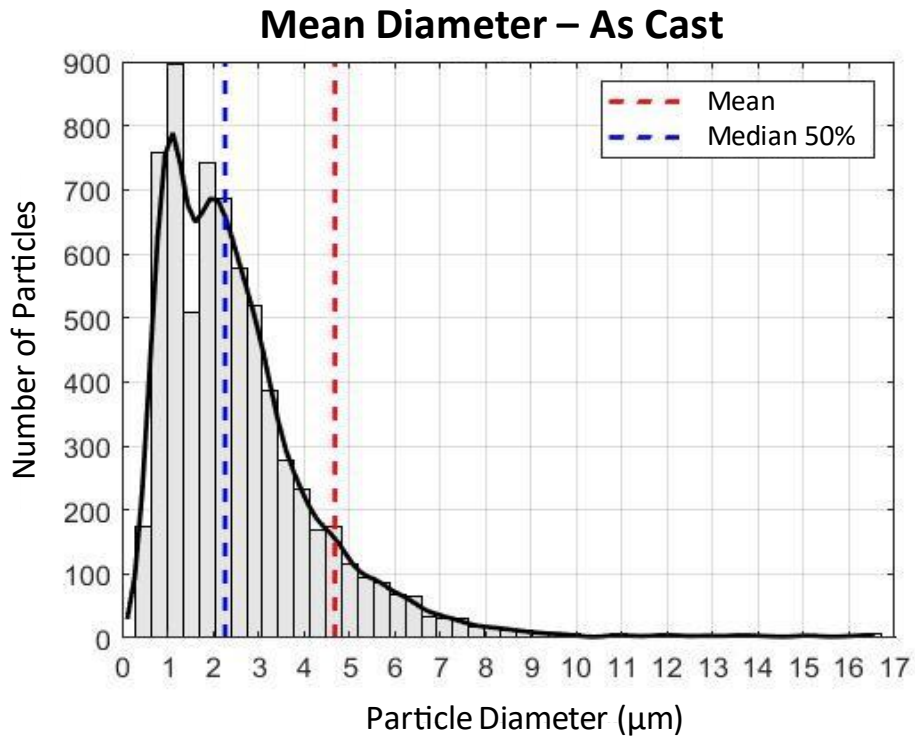


Figure 4.10 Distribution of particle diameters in the as cast condition of the AlTiVCr-Si_{7.2} alloy.

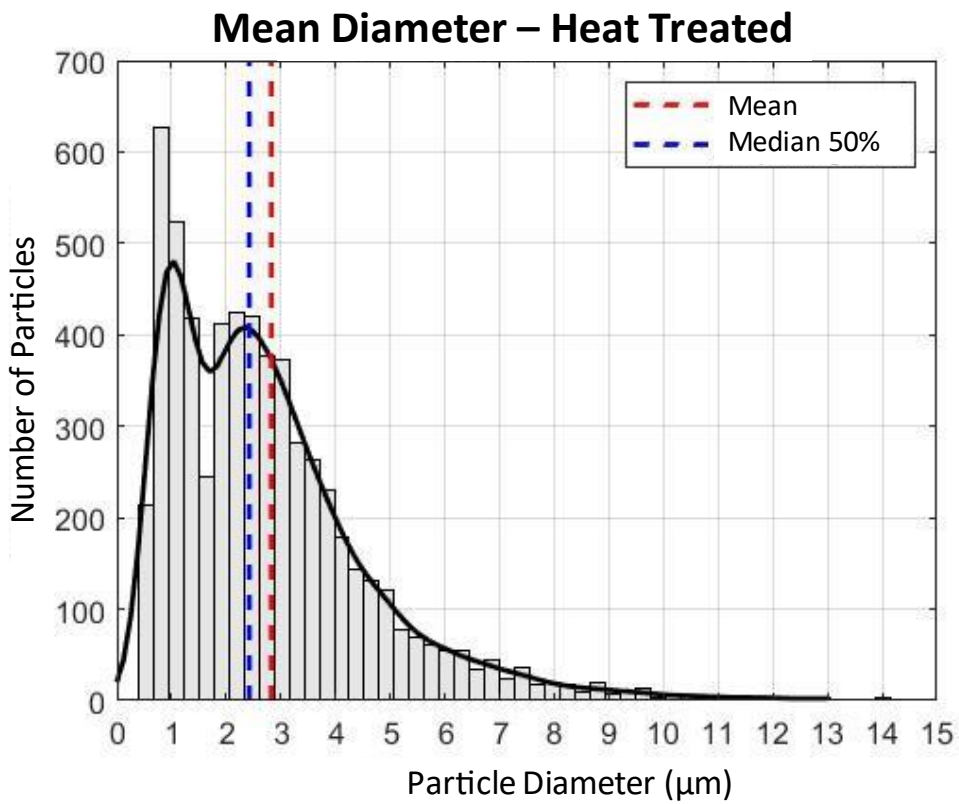


Figure 4.11 Distribution of particle diameters in the heat treated condition of the AlTiVCr-Si_{7.2} alloy.

4.3.2.4 X-ray Diffraction Analysis (XRD)

4.12 shows the normalised experimental XRD patterns for the multicomponent alloys: as cast and heat treated AlTiVCr and as cast and heat treated AlTiVCr-Si_{7.2}. The as cast AlTiVCr pattern was indexed to a single ordered BCC B2 phase analogous to a CuNiTi₂ structure with a space group Pm-3 m (221) and lattice parameter $a \approx 3.05 \text{ \AA}$ [230]. The heat treated AlTiVCr pattern was also indexed to a single B2 phase and is analogous to that identified in the as cast condition. As such, it is likely that AlTiVCr forms a single ordered B2 matrix as the XRD pattern presents an ideal match to that of structures known to be ordered B2. The as cast AlTiVCr-Si_{7.2} pattern was indexed to a BCC phase and an HCP phase. The BCC phase is analogous to a U_{0.65}Pu_{0.13}Mo_{0.22} structure with a space group Im-3 m (229) and a lattice parameter $a \approx 3.05 \text{ \AA}$ [231]. The heat treated AlTiVCr-Si_{7.2} pattern was also similarly indexed to a BCC phase and an HCP phase. The BCC phase is analogous to a Ti_{0.65}Fe_{0.35} structure with a space group Im-3 m (229) and a lattice parameter $a \approx 3.06 \text{ \AA}$ [232]. Nevertheless, it is not possible to clearly discern a BCC from a B2 crystal structure purely from XRD data, especially when the lattice parameters of the two are similar as in the present case [97]. This matter would require additional experimentation which is past the scope of this work. Regardless, no distinct changes in the crystal structure between the as cast and heat treated conditions are evident. The HCP phase is analogous to a Ti₅Si₃ structure with a space group P63/mcm (193) and a lattice parameter $a \approx 7.43 \text{ \AA}$ and $c \approx 5.14 \text{ \AA}$ [233]. The HCP phase in the heat treated sample is analogous to that identified in the as cast condition. Therefore, the Ti-Si intermetallic phase identified during the SEM investigation is indeed the Ti₅Si₃.

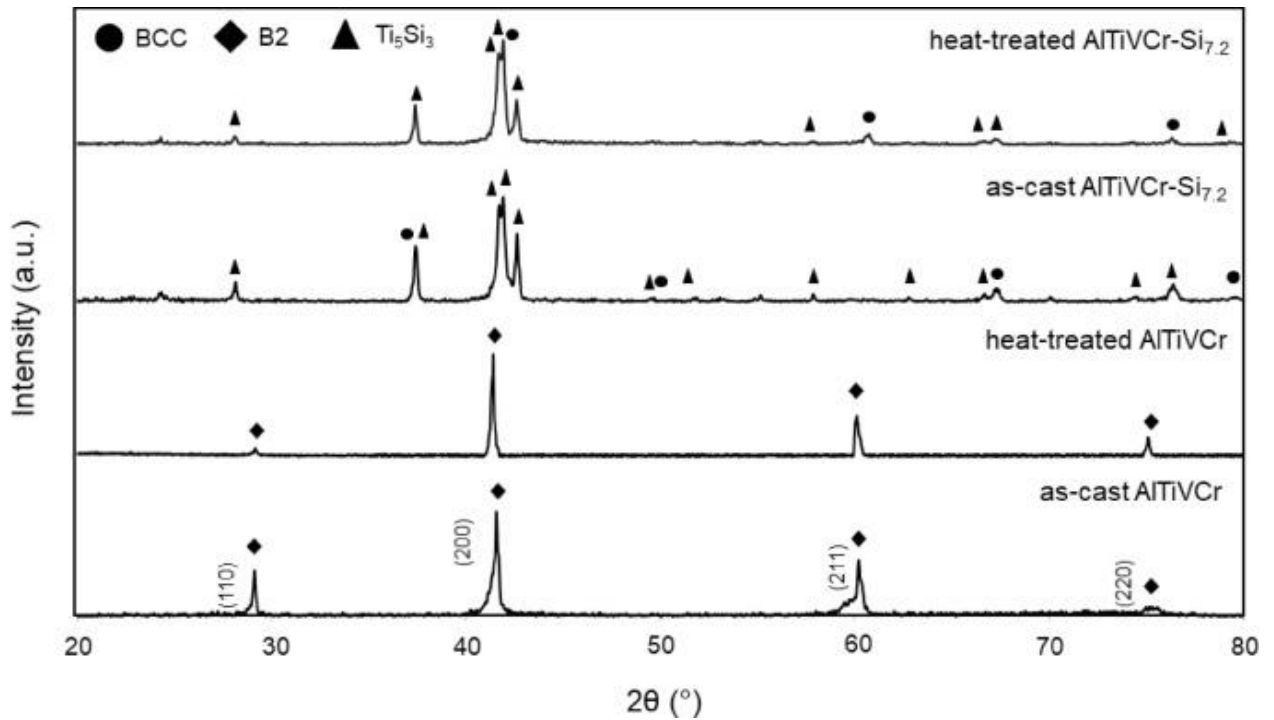


Figure 4.12 Normalised XRD patterns of the as cast and heat treated AlTiVCr and AlTiVCr-Si_{7.2} alloys.

Compared to the work by Qiu et al. [97] the XRD patterns of the AlTiVCr samples presented within this research are shifted by a few degrees. This could be attributed to the different sample preparation routes used in the two studies, as a powdered sample was used in their study. Furthermore, the as cast AlTiVCr and AlTiVCr-Si_{7.2} samples display broader Bragg's peaks compared to their heat treated counterparts, which is attributed to the elimination of pre-existing segregation phenomena through the heat treatment.

4.3.2.3 Experimental Elastic Properties

The as cast condition of the AlTiVCr alloy was measured as having a Young's modulus of 194.8 ± 3.7 GPa and 189.0 ± 3.4 GPa through means of microindentation and nanoindentation, respectively. Measurements on the homogenised alloy with microindentation and nanoindentation also pointed at a Young's modulus of 189.0 ± 3.7 GPa and 185.6 ± 3.7 GPa, showing no significant indentation size effects. The computational estimates of the Young's modulus of the phases individually therefore only deviated by about 10% from the experimentally measured value, with microindentation recording 189.0 GPa in the heat treated condition. The experimental results contrast with those presented in previous computational research by Huang et al. [103], where a significant difference in the Young's modulus between the ordered and disordered BCC phase was found. The main differences between the computational aspects of the two studies were using the disordered BCC phase for the calculations, and the use of a different quantum-mechanical approach in their case with the electron muffin-tin orbital (EMTO) coherent potential approximation (CPA) method. For most alloy development requirements, where modelling would be looked to for an indication of properties, and would be followed up with experimental processing, the level of agreement (up to 10% deviation) observed between the computational and experimental results would be satisfactory (Fig. 4.13).

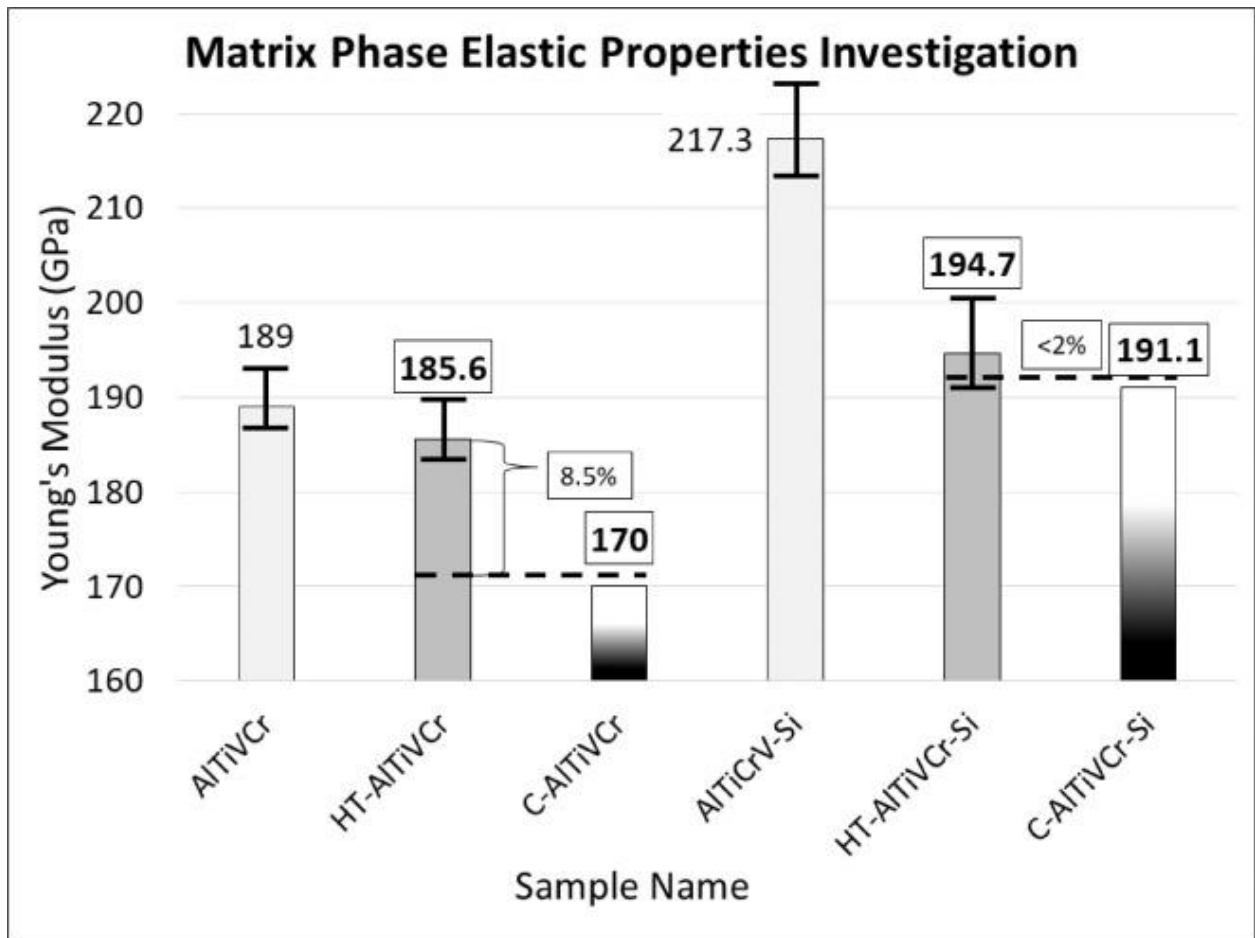


Figure 4.13 Nanoindentation Young's modulus of the matrix phases of the AlTiVCr, heat treated (HT)-AlTiVCr, AlTiVCr-Si_{7.2}, HT-AlTiVCr-Si_{7.2} alloys compared to the ones derived computationally (C) through CASTEP.

When assessing the AlTiVCr-Si_{7.2} alloy experimentally, the nanoindentation measurements showed two groups of results, which are likely to correspond to indents which primarily fall within either the Ti₅Si₃ intermetallic phase or the AlTiVCr matrix (Fig. 4.14). In the case of the as cast sample, these two groups are not as clearly distinguished as in the heat treated condition. Further analysis of the heat treated condition indicated a matrix modulus of 194.7 ± 8.15 GPa and an intermetallic modulus of 241.2 ± 10.92 GPa. A comparison between the heat treated AlTiVCr sample and the matrix of the heat treated AlTiVCr-Si_{7.2} reveals an increase in the Young's modulus of roughly 9 GPa between the two conditions. This effect was also captured by the DFT simulations which estimated the Young's modulus of the matrix phase to be 191.1 GPa (4.13). In turn, the deviation between the computational and experimental results in terms of the Young's modulus of the matrix phase is less than 2%, and thus deemed highly reliable.

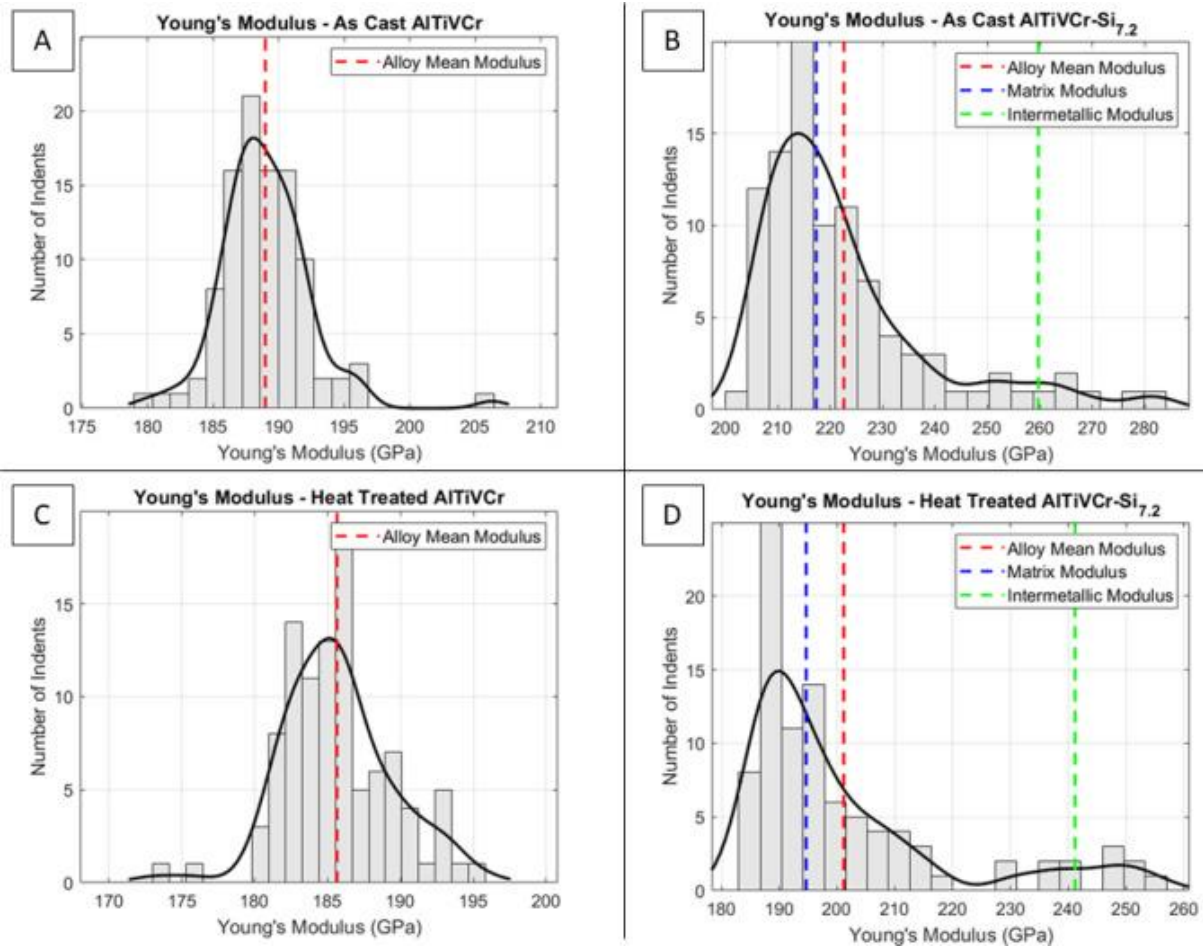


Figure 4.14 Nanoindentation measurements of the matrix phase, intermetallic phase and mean alloy Young's moduli of the A) as cast AlTiVCr, B) as cast AlTiVCr-Si_{7.2}, C) heat treated AlTiVCr and D) heat treated AlTiVCr-Si_{7.2} samples.

An additional important point is the effect the modification of the chemical composition of the matrix phase has on its elastic properties. As previously discussed, this modification occurs due to the formation of the Ti₅Si₃ intermetallic phase, thus depriving the AlTiVCr phase of Ti. There is an indication that this indirect manipulation of the chemical composition of the matrix phase leads to elevated elastic properties. Cr has the highest specific shear and Young's moduli of all the metallic alloying elements, suggesting that the increased Young's modulus of this phase is due to the increased proportion of Cr contained within it.

A more significant difference (just over 10%) was observed in the nanoindentation measurements for Young's modulus between the as cast condition (222.6 ± 35.6 GPa) and the heat treated sample (201.2 ± 35.8 GPa). The microindentation results, however, produced a similar result for both of 205.4 ± 6.2 GPa in the as cast and in the 203.5 ± 10.2 GPa heat treated condition (Fig. 4.15). The measured density of the alloys was $5.07 \text{ g}\cdot\text{cm}^{-3}$ and $4.97 \text{ g}\cdot\text{cm}^{-3}$ for the AlTiVCr and AlTiVCr-Si_{7.2} respectively. The experimental measurements, and particularly those performed on the heat treated sample, were once again in good agreement with the

computational model. In turn, the calculation of the specific Young's modulus of both the AlTiVCr and AlTiVCr-Si_{7.2} alloys, using this study's experimental data for the density and E, produces values of 37.3 GPa.cm³.g⁻¹ and 40.9 GPa.cm³.g⁻¹ respectively, thus outperforming even the more advanced high modulus steels which range from 32 to 33 GPa.cm³.g⁻¹ [96]. This manifestation of an elevated Young's modulus in the case of the AlTiVCr-Si_{7.2} MCA could be due to both the existence of the Ti₅Si₃ intermetallics and possibly the indirect increase of the Cr content of the AlTiVCr matrix. This effect of the indirect modification of the chemical composition of the AlTiVCr matrix in the AlTiVCr-Si_{7.2} alloy through the formation of the Ti₅Si₃ intermetallic phase could provide a novel concept for designing and fine-tuning the composition of high specific modulus MCAs. This practice is well known and documented in the case of Ti alloys for biomedical applications [234] towards the reduction the Young's modulus of the material. A brief survey of the elastic properties of the alloying elements of interest showed that Cr has the highest specific Shear and Young's moduli of all the alloying elements for which such data was available [235]. This phenomenon, if further investigated and verified, could provide a novel pathway for designing high specific modulus MCAs. More specifically, the high compositional freedom related to HEAs could enable the design of alloys tailored to precipitate the alloying elements with lower specific stiffness within intermetallic phases with greater elastic properties than their constituent elements such as TiAl or Ti₅Si₃. At the same time, the alloy matrix could be designed so that it retains the most contributing elements, such as Cr, in solid solution thus increasing its elastic properties. The end-product of such a design process would be an alloy with greater elastic properties compared to those projected through the rule of mixtures.

It is also evident that this computational approach is capable of successfully assessing the elastic properties of the tested alloys with reasonable accuracy. While this does not guarantee that similar success would be met were it applied to other multiphase materials, there is no fundamental barrier provided the required databases were available with appropriate accuracy. The results serve as a demonstration of feasibility and provide a pathway for elastic property prediction in novel multiphase MCA systems in the future.

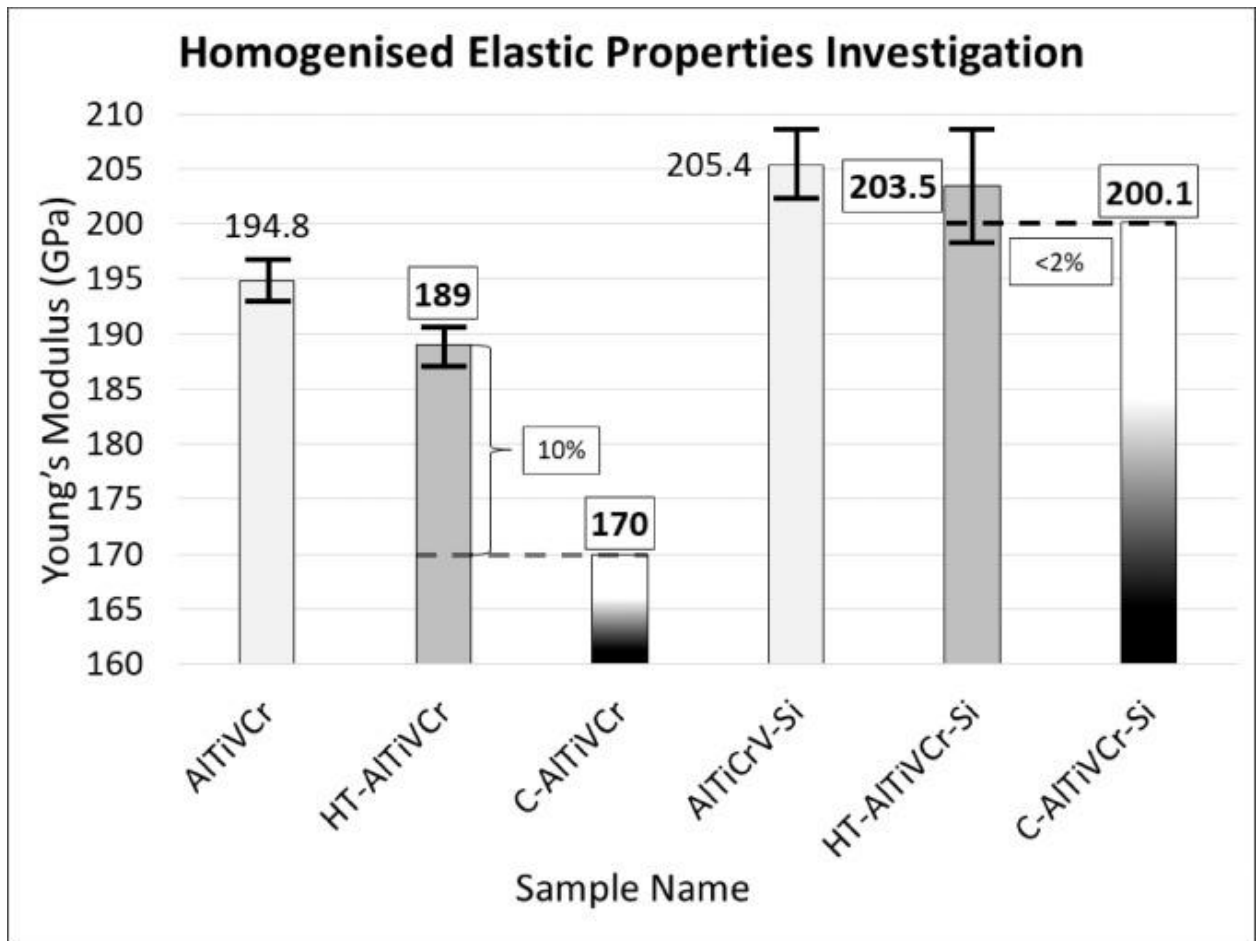


Fig. 8. Microindentation Young's modulus of the AlTiVCr, heat treated (HT)-AlTiVCr, AlTiVCr-Si_{7.2}, HT-AlTiVCr-Si_{7.2} alloys compared to the computationally (C) derived ones through CASTEP and ABAQUS.

4.4 Conclusions

In this chapter a methodology for assessing novel multiphase materials through a multi-principle computational approach was presented. This method consisted of thermodynamic, DFT and homogenisation modelling coupled with experimental validation. It was then applied to the AlTiVCr and AlTiVCr-Si_{7.2} multicomponent alloys and managed to successfully estimate the elastic properties of both materials, yielding a deviation of 10% for the AlTiVCr alloy and only 2% for the AlTiVCr-Si_{7.2} alloy. This is an important outcome, as in principle (given adequate thermodynamic databases and suitable choice of RVE for the relevant case) the applicability of the methodology is alloy-universal and solely depends on the accuracy of each individual modelling technique. Furthermore, this part of the work unveiled the potential of both materials for further development and application within the field of lightweight, high specific modulus structural materials. Therefore, both materials will be assessed in terms of their mechanical behaviour in the following chapters to identify whether they already comply with industrial requirements or if additional optimisation would need to be carried out. The main findings of this chapter are summarised in the following points:

1. Thermocalc is an adequate qualitative tool for assessing the phase formation and their volume fraction in the complex MCA systems explored here.
2. Density Functional Theory (DFT) can calculate the crystallographic characteristics and elastic properties of the single-phase AlTiVCr alloy within <1% and 10% error respectively.
3. When coupled with Homogenisation modelling, DFT can predict the properties of the multiphase AlTiVCr-Si_{7.2} alloy within 2% error.
4. Heat treatment at 1200°C for 8h is sufficient to erase segregation phenomena and enable the spheroidisation of intermetallic phases according to an Ostwald ripening mechanism.
5. The Young's modulus of the AlTiVCr is 194.8 GPa and 189.0 GPa in the as cast and heat treated conditions respectively according to the nanoindentation results.
6. The Young's modulus of the AlTiVCr-Si_{7.2} is 205.4 GPa and 203.5 GPa in the as cast and heat treated conditions respectively according to the nanoindentation results.
7. The Young's modulus of the AlTiVCr matrix in the AlTiVCr-Si_{7.2} alloy is 194.7 GPa in the heat treated condition respectively according to the nanoindentation results while the Young's modulus of the heat treated AlTiVCr alloy is 185.9 GPa.

8. This increase in the Young's modulus of the matrix phase could be attributed to the increased Cr content since Ti is precipitated along with Si in the form of the Ti_5Si_3 intermetallic phase.

5. Assessment of the Fracture Mechanisms in AlTiVCr-based and AlTiVCr-Si_{7.2} alloys

This chapter concerns the evaluation of the AlTiVCr, AlTiVCr-Si_{7.2} and the subsequently developed AlTiVCrMn alloys in terms of their ductility through fractography. It should be underlined that since most aspects of the work presented here were carried out during the peak of the pandemic, this research was faced with significant equipment and software limitations. This was due to significant physical and online access challenges as the regulations for in-house experimental work and remote working regulations were being developed in tandem with this work. This research was partially carried out in collaboration with the National Technical University of Athens (NTUA) within the frame of two Diploma Theses of Mr. Ioannis Daskalopoulos and Mr. Dimitrios Kiouisis co-supervised by PhD candidate Mr. Spyridon Chaskis, Dr. -Ing. Spyros Papaefthymiou and myself. Furthermore, all research concerning the development and assessment of the Mn-containing compositions was carried out during a placement in ELKEME S.A., while the thermal conductivity measurements were performed at the Department of Innovation and Sustainability of Volkswagen Group Research in Wolfsburg, Germany by Dr. Ralf Rablbauer.

Conference Papers

Chaskis, S., Kiouisis, D., Stavroulakis, P., Goodall, R. and Papaefthymiou, S., Examination of Fracture Mechanisms in two Al – Ti – V – Cr – (Si) High Entropy Alloys. MATEC Web of Conferences, 2021. 349: p. 02002. [222]

P. S. Contribution: Conceptualisation, methodology, review, editing.

Diploma Theses

6. Daskalopoulos, I., Study of thermal processes and microstructural characterization of the AlCrTiV-Si high-entropy alloy. 2020. <http://dx.doi.org/10.26240/heal.ntua.19460> [223]

P. S. Contribution: Supervision, conceptualisation, methodology, supervision, computational work, experimental work, review.

7. Kiouisis, D., Αξιολόγηση της δυνατότητας παρασκευής κράματος μέσης εντροπίας TiAlCrV με μεθόδους προσθετικής κατασκευής (Additive Manufacturing). 2021. <http://dx.doi.org/10.26240/heal.ntua.21006> [224]

P. S. Contribution: Supervision, conceptualisation, methodology, review.

5.1 Aim

In the previous Chapter a novel methodology for assessing the elastic properties of multiphase materials was presented. By applying this practice two MCAs with notable elastic properties were identified, namely the equiatomic AlTiVCr and AlTiVCr-Si_{7.2} alloys. Both alloys significantly outperformed advanced high modulus steels by roughly 13% and 24% respectively in terms of the density normalised elastic modulus. An additional critical design property that needs to be considered when designing novel materials is the ductility which has not been assessed for either alloy. Unfortunately, regardless of their notable elastic properties most of the as cast ingots of both alloys would fracture and even explode during the VAM manufacturing process. This had not been previously recorded in the literature regarding this system and contrasted with published claims of “ease of manufacturing” [100]. As such, this chapter aims to understand mechanisms dictating the fracture behaviour of this alloying system. A hypothesis was made that the origins of this phenomenon are in the manufacturing process, the inherent ductility of the phases constituting the alloy itself or even both acting simultaneously.

In terms of the processing, the rapid heating and cooling cycles that the alloys would be subjected to during VAM could be causing inhomogeneous expansion or contraction of the ingots. In turn, this would lead to the development of an internal stress gradient across the volume of the sample. Upon reaching a critical point, this accumulation of internal stresses would cause the ingot to fracture; this effect is called *thermal shock* [236]. Of course, for this effect to manifest in such small samples, the alloy would have to be characterised by both a particularly low thermal conductivity and limited ductility. Had the ductility been more extensive, then the internal stresses may have been accommodated through the plastic deformation of the material. Therefore, this rapid discharge of accumulated energy causing the disintegration or explosion of the ingot may be an indication of limited inherent ductility. An insight regarding the ductility of the alloys, or lack thereof, can be gained by assessing the fracture surfaces of ingots that failed during the manufacturing process.

Limitations regarding the inherent ductility of the alloys could be attributed to two factors. On one hand, the B2 phase constituting their matrix phase is known to severely reduce the room temperature ductility of MCAs due to the directionality of the atomic bonds involved [82-84, 237]. Therefore, perhaps suppressing the order-disorder transformation and retaining a BCC matrix at room temperature would improve the ductility. This could be accomplished in two ways. According to some of the thermodynamic modelling results of the previous Chapter, it

may be possible to revert the order-disorder transformation by inducing the formation of AlTi-based phases. This would be due to the matrix phase becoming depleted of Al, which is known to stabilise the B2 phase compared to the BCC [238, 239]. This could be achieved by subjecting the alloys to low temperature heat treatments aimed at promoting the formation of the aforementioned phases. Another method to retain a BCC matrix phase at room temperature would be the suppression of the order-disorder transformation altogether. This could occur by subjecting the alloy to a high temperature heat treatment followed by rapid cooling. The latter approach will be explored in Chapter 6.

On the other hand, the reduced ductility could also be attributed to the significant amount of Cr present in the alloys investigated in Chapter 4. This is due to the fact that Cr has a very high ductile-brittle transition temperature (DBTT) and thus may reduce room temperature ductility [181]. Nevertheless, it was suggested that Cr may also be the reason behind the increased elastic properties in the present alloying system. Therefore, achieving an increased ductility without reducing the Cr content would be key towards maintaining the competitiveness of this alloying system. As such, the addition of Mn was used which, according to the literature [181], could help maintain a low DBTT and enable room temperature ductility. To offset the increased density caused by the Mn addition, the amount of Al was also increased in one of the Mn-containing compositions.

The aim of this chapter is to evaluate these hypotheses by manufacturing the aforementioned compositions and subjecting them to low temperature heat treatments, while assessing them in terms of their microstructural features and fracture surfaces.

5.2 Computational and Experimental Methods

5.2.1 Computational Methods

5.2.1.1 Thermodynamic Simulations – Thermo-Calc Software

The Thermodynamic calculations were carried out using the commercial software Thermo-Calc (TC) 2 version 2020a using the SSOL4: SGTE Alloy Solutions Database v.4.9.g and the TCHEA4: TCS High Entropy Alloys Database [225]. For the alloys studied here, the order to disorder transformation (BCC_B2 to BCC_A2) could not be modelled using the SSOL4 database. This is because the model for the BCC_B2, in this database, does not contain all the elements of interest in the present alloy. The TCHEA4: TCS High Entropy Alloys database on the other hand, which was accessible during a placement at ELKEME S. A., was capable of making that prediction, with the BCC phase denoted as BCC_B2 and the actual B2 phase as BCC_B2#2 on the phase diagram.

5.2.2 Experimental Methods

5.2.2.1 Materials and Processing

The raw materials used to manufacture the alloy (Al pieces and sheets, Cr pieces, 1 mm Si lumps, Ti wires and rods, V turnings, Mn flakes) with purities >99.8% were supplied by NewMet Ltd, Waltham Abbey, UK. Experimental samples in the shape of ellipsoids with a diameter of 25 mm and 10 mm thickness were formed using an Arcast Arc 200 Vacuum Arc Melter (VAM) under a high purity Ar gas atmosphere and were remelted 4-5 times along with electromagnetic stirring to ensure chemical homogeneity. Most of the as cast ingots would fracture in half upon extended cooling (~10 mins) in the water-cooled copper crucible and shatter upon reheating after the third remelt. To avoid this phenomenon, the samples were allowed to cool down for a brief period (~1 min) and were afterwards toppled and reheated immediately. An AlTiVCr and AlTiVCr-Si_{7.2} ingot that fractured during the manufacturing process was used for the initial fractographic study. The reasoning behind these adaptations to the processing method will be analysed in the results section. The samples were sectioned in half using a Secotom-50 microtome with Al₂O₃ 6" cutting disks. In total, the samples consisted of (2) AlTiVCr, (2) AlTiVCr-Si_{7.2}, (2) AlTiV_{18.75}CrMn_{6.25} and (2) Al₃₅Ti₂₅VCrMn₁₀ ingot halves. One half of each sample was forwarded for metallographic preparation while the other half for a low temperature (LT) heat treatment. The heat treatment was carried out in ELKEME S.A. using a laboratory electric furnace under a regular atmosphere at 700°C for 24h followed by air cooling. An inert atmosphere could not be used at the time. It must be noted that a second batch of samples was subsequently prepared, and heat treated under a flowing Ar atmosphere

at 600°C for 100h followed by air cooling but resulted in the exacerbation of the effects of the heat treatment at 700°C instead, causing the complete disintegration of the samples. Again, this will be further discussed in the results section. The samples were cold mounted in conductive resin and were ground using P220, P600, P1200, and P4000 SiC grinding papers in succession. They were then polished using a 1 µm diamond suspension and Struers OP-U colloidal silica solution for 10 and 20 minutes respectively for relief polishing. Density data were extracted using Archimedes' method. For ductility evaluation the samples were subjected to a basic assessment, with mechanical impact loading using a hammer to determine their deformation tolerance and to fragment the ingots into smaller pieces to subsequently study the fracture surfaces.

5.2.2.2 Optical (OM), Stereo (SM), Scanning Electron (SEM) Microscopy & Electron Dispersive X-ray Spectroscopy (EDX)

The fracture surfaces of the first batch of samples were evaluated using a Nikon SMZ 1500 stereo microscope. The microstructures of the samples were investigated using a Nikon Epiphot 300 inverted Optical Microscope (OM) under polarised light, using the analyser and darkfield filters alongside depth-of-field observation when required. Further microstructural and fracture surface investigation was carried out using a FEI XL30 S and a FEI XL40 S Field Emission Gun Scanning Electron Microscope (SEM) with Secondary (SE) and Backscatter Electrons (BSE) under 20 kV accelerated voltage, in conjunction with Energy-dispersive X-Ray Spectroscopy Analysis (EDX) to evaluate possible segregation phenomena and perform phase analysis and characterisation.

5.2.2.3 Vickers Hardness (HV) Testing

Microhardness testing was conducted using the Vickers hardness testing method on a Duramin-40 M1 hardness tester using a load of 0.5 kg and 10 random measurements for each sample with a dwell time of 20 s. It should be underlined that in this particular case, hardness testing was carried out after grinding with the P220 SiC paper due to equipment availability constraints during the period when this study was conducted. Therefore, the findings concerning the hardness cannot be directly compared to the results of studies presented in the other chapters of this work or values available in the literature. However, comparisons can be made between samples encapsulated within this chapter from a qualitative perspective.

5.2.2.4 Thermal Conductivity Measurements

The thermal conductivity measurements were performed using a Hot Disk TPS 2500S with the 7577 sensor with a radius of 2 mm according to EN ISO 22007-1 and 22007-2 at an ambient temperature of 21°C. The parameters used for the measurements were a power of 50 mW, holding time of 20 s, a resistivity of 1.55 Ohm and a probing depth of 1.8 – 4 mm, resulting in a temperature increase of 3-5°C. The standard analysis method in the single sided modus assuming perfect insulation was used for the evaluation of the thermal conductivities. The associated results are the arithmetic average of the sensor on the top and bottom of the polished sample surfaces. Data sets from point 20 = 1 s to 200 = 20 s were used for evaluation points. It must be underlined that the only sample available for carrying out thermal conductivity measurements on was the equiatomic AlTiVCr at that particular time.

5.3 Results and Discussion

5.3.1.1 Evaluation of the Thermal Conductivity of the AlTiVCr

The mean thermal conductivity of the equiatomic AlTiVCr was measured at $4.77 \pm 0.08 \text{ Wm}^{-1}\text{K}^{-1}$. As a reference point, the thermal conductivity values of other materials are presented in Table 1. It becomes clear that the present alloy is characterised by a particularly low thermal conductivity compared to most pure metals and alloys, and even lies in the same region as some metallic oxides.

Table 5.1 Thermal conductivity and thermal expansion coefficient of typical engineering materials and alloys, common MCAs and the equiatomic AlTiVCr alloy of the present study as measured under ambient conditions.

Material	Thermal Conductivity ($\text{Wm}^{-1}\text{K}^{-1}$)	Thermal Expansion Coefficient (10^{-6}K^{-1})
Copper	398 [120]	16.5 [240]
Aluminium	237 [120]	23.1 [240]
Chromium	94 [240]	4.9 [240]
Low Carbon Steel	52 [120]	11.7 [241]
Al_2O_3	36 [242]	8.4 [243]
Vanadium	30.7 [240]	8.4 [240]
Titanium	22 [120]	8.6 [240]
304 Stainless Steel	15 [120]	17.3 [241]
AlCoCrFeNi MCAs	11-16 [120]	17 [244]
TiAl	11.5 [245]	11 [245]
Inconel 718	11 [120]	12.2 [246]
TiO_2	8.4 [242]	9.0 [247]
Ti-6Al-4V	6 [120]	8.6 [241]
AlTiVCr	4.77	-
SiO_2	1.3 [242]	0.65 [248]

Therefore, it is highly probable that, the low thermal conductivity of the AlTiVCr alloy does not allow for a homogeneous distribution of temperature during the heating and cooling cycles taking place in the VAM process, resulting in the development of cracks according to the process described in Chapter 5.1. Furthermore, based on the rapid thermal cycles associated with the VAM process, it could be assumed that the fracture may occur near the temperature where the order-disorder transformation is occurring. Therefore, it could be suggested that at

that temperature the transformation of the parent BCC phase to B2 phase and vice-versa would be partially complete, leading to fracture, due to the accumulation of additional strains originating from differences in terms of the mechanical properties of the high and low temperature phases. Nevertheless, these assumptions also require a relatively high thermal expansion coefficient, for which there is no available data, and a low inherent material ductility, which will be the next point of focus of this Chapter.

5.3.1.2 Evaluation of the Fracture Surfaces of the AlTiVCr and AlTiVCr-Si_{7.2} alloys

The fracture surfaces of the AlTiVCr and AlTiVCr-Si_{7.2} alloys that failed during the VAM process will be investigated in this section. The highly reflective surface of the AlTiVCr alloy can be seen in Fig. 5.1 pointing at a brittle fracture mechanism and a rather coarse grain size. Sharp, elongated ridges could be seen, with their development indicating an intergranular fracture. In the case of the as cast AlTiVCr-Si_{7.2} alloy, the high reflectance was still present, however less profound compared to the equiatomic alloy. Finer ridges could be observed with the overall characteristics of the fracture surface pointing at a brittle fracture mechanism once again.

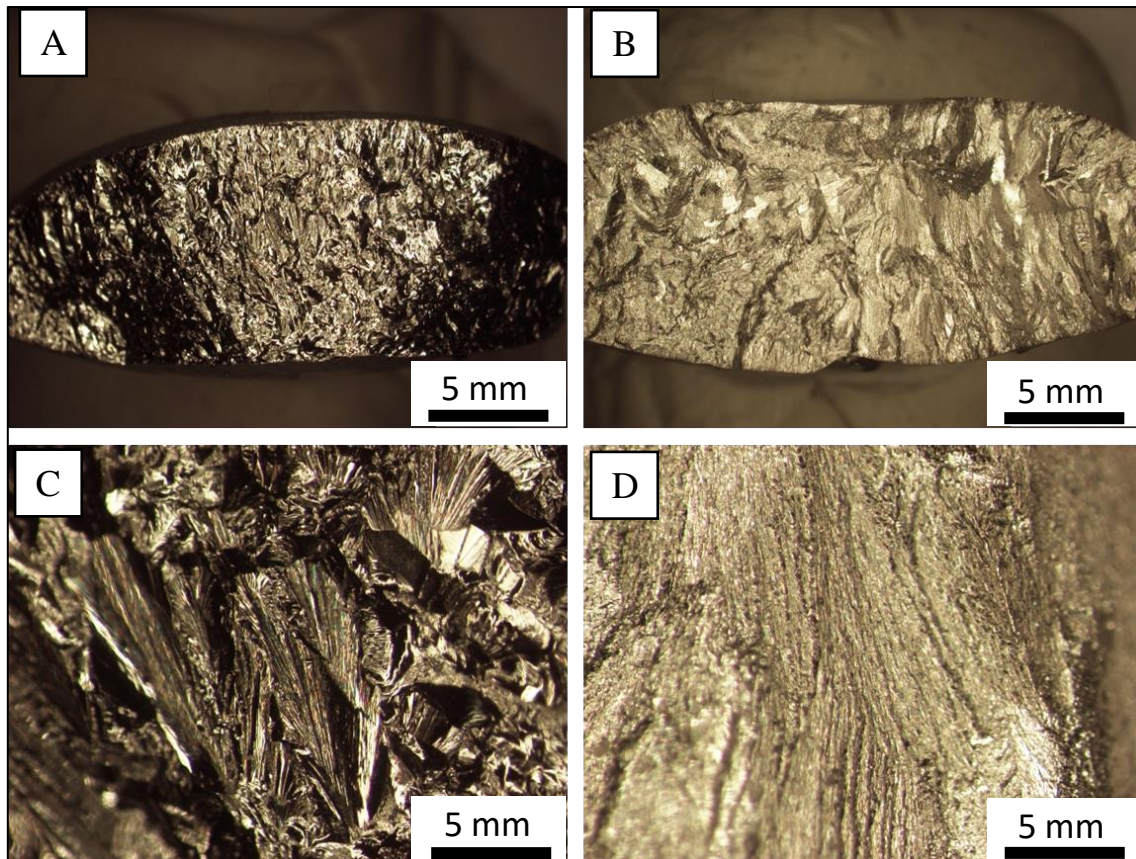


Figure 5.1 Fracture surfaces of the A, C) AlTiVCr and B, D) AlTiVCr-Si_{7.2} alloys.

The SEM images extracted from the fracture surfaces of the AlTiVCr and AlTiVCr-Si_{7.2} specimens also pointed at a brittle fracture mode taking place in both cases, with the latter exhibiting some limited characteristics of ductile behaviour (Fig. 5.2). More specifically, the as cast specimen (Fig. 5.2) was characterised by a fracture surface dominated by shear phenomena with deformation ridges and shear bands covering most of the surface. Elongated and very sharp river features were detected. Judging by the characteristics of the fracture surface it would be considered unclear whether the fracture mechanisms could be explicitly considered intergranular or transgranular.

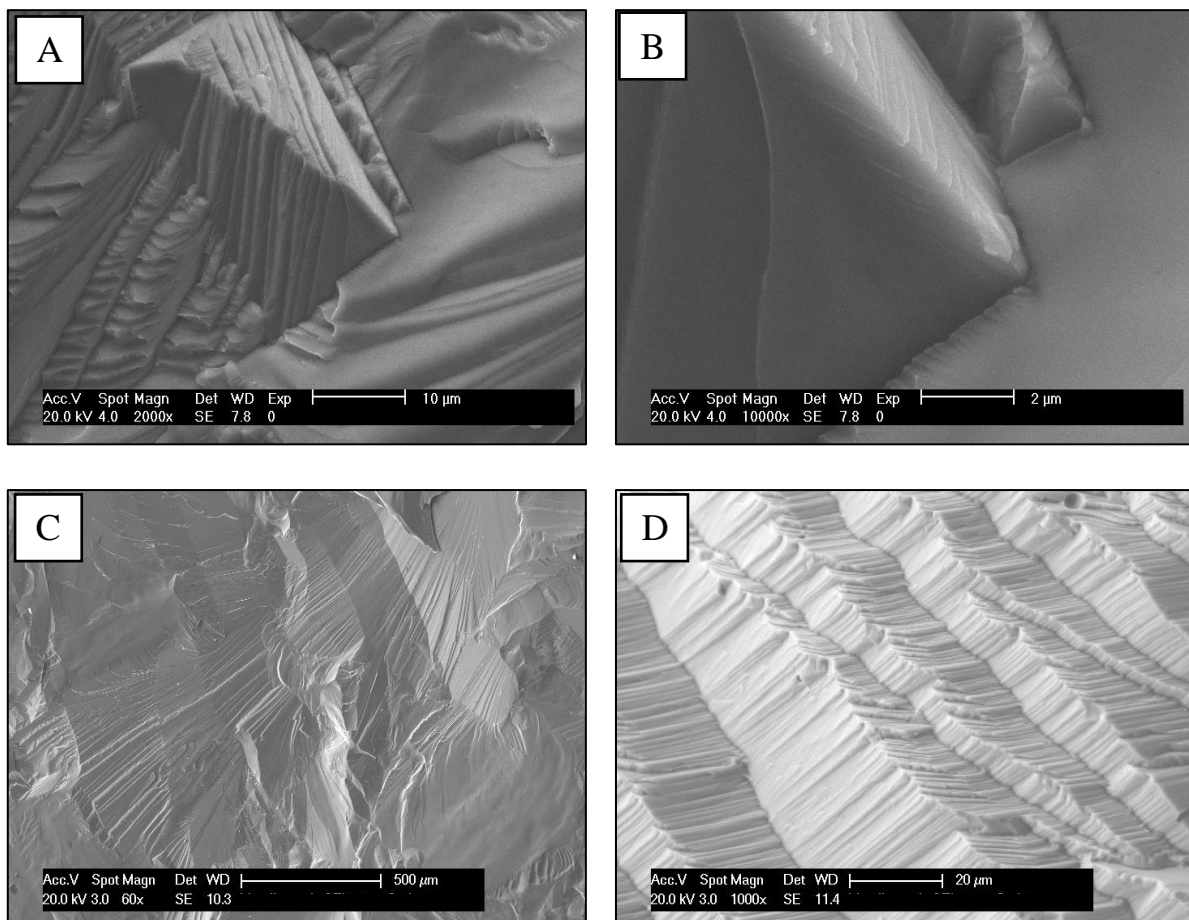


Figure 5.2. Scanning Electron Microscopy (SEM) micrographs illustrating the fracture surface of the as cast AlTiVCr.

In comparison, the AlTiVCr-Si_{7.2} sample (Fig. 5.3) did display some cavities and other minor characteristics hinting at a greater ductility; however, the surface was also predominantly governed by features indicative of a shear fracture process. It is possible that the Ti₅Si₃ intermetallics would be a fracture initiation point in the present alloy. Nevertheless, the relevant fracture surfaces did not present any evidence to support this claim. Furthermore, no unmelted silicon particles or pure metals were found. The formation of elongated ridges was also present

in this case. It was not possible to pinpoint a specific crack initiation point or material flow orientation.

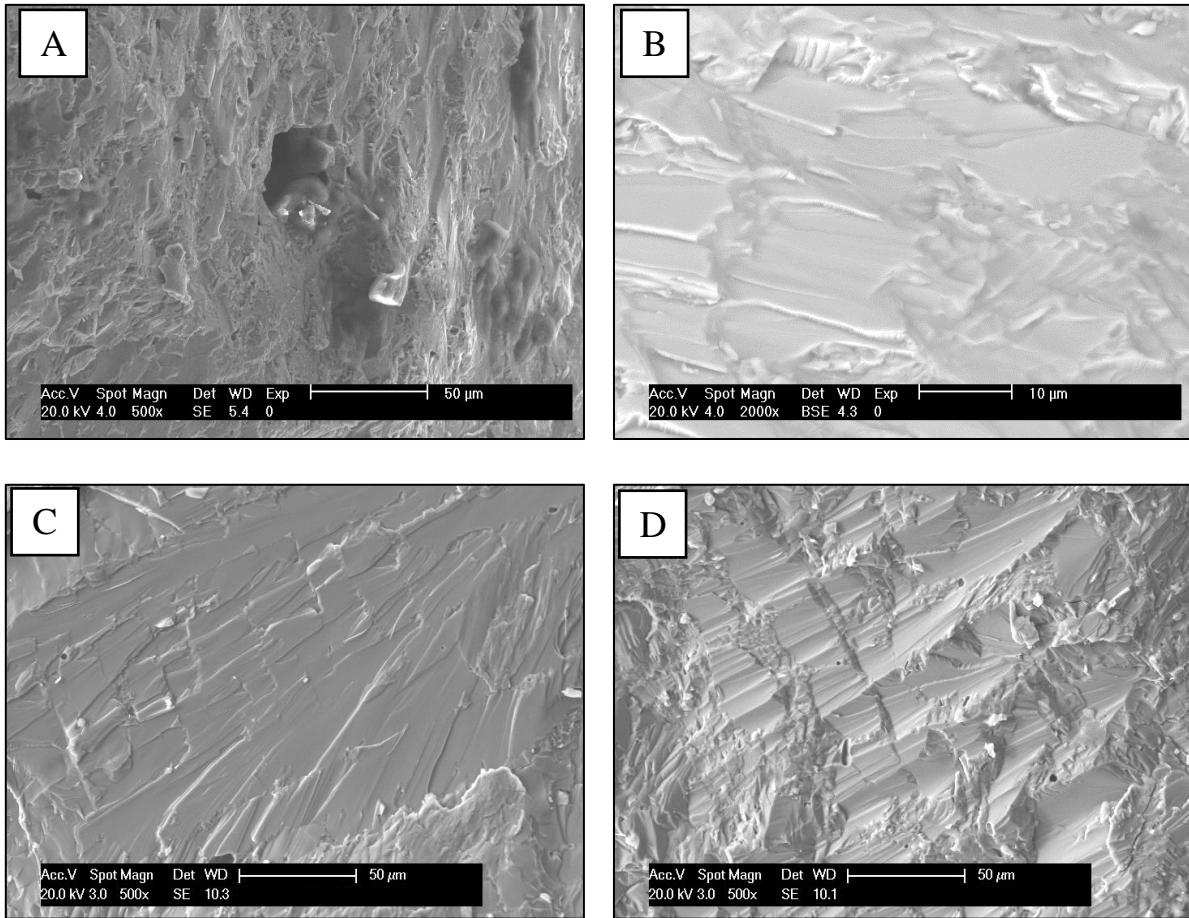


Figure 5.3 Scanning Electron Microscopy (SEM) micrographs illustrating the fracture surface of the as cast AlTiVCr-Si_{7.2}.

These results showed that in the case of the AlTiVCr alloy the fracture mechanism was purely brittle, while in the case of the AlTiVCr-Si_{7.2} alloy the fracture surface exhibited some ductile characteristics but was also predominantly brittle. The type of fracture seems to be a mixed mechanism combining both intergranular and intragranular fracture. It must be underlined no oxides, unmelted material or inclusions were spotted. The pores present in both alloys did not seem to act as crack initiation points. Lastly, the chemical composition as quantified through EDX (Table 5.2) did not deviate from the nominal one to a notable extent.

Table 5.2 Chemical composition of the fracture surfaces of the investigated AlTiVCr and AlTiVCr-Si_{7.2} MCAs measured through EDX analysis.

Alloy	Al at. %	Ti at. %	V at. %	Cr at. %	Si at. %
AlTiVCr	26.2 ± 3.9	24.7 ± 1.2	24.08 ± 1.0	24.8 ± 1.3	-
AlTiVCr-Si _{7.2}	21.8 ± 6.00	23.4 ± 1.7	23.05 ± 1.5	22.3 ± 2.0	9.5 ± 5.6

Therefore, it has now been established that while the failure of the samples could be traced back to the manufacturing process, both alloys exhibited fracture surfaces with limited to no ductile features. As such, apart from a low thermal conductivity, both alloys were also characterised by limited inherent ductility. As mentioned in Chapter 5.1, according to the relevant literature two reasonable explanations could be found related to the increased Cr and Al content, respectively. A high ductile to brittle transition temperature or the existence of the ordered B2 matrix.

5.3.2 The addition of Mn towards the improvement of the Fracture Behaviour

Given that the inception of the concept of the incorporation of Mn into the AlTiVCr system happened during the peak of the pandemic, one of the primary limitations encountered here was the transfer of the licensing scheme of ThermoCalc from a local to a remote license. As such, the investigation using the SSOL4 database was forcefully concluded prematurely. Later, an opportunity to indirectly access the TCHEA4 database through a collaboration presented itself. This incentivised the CALPHAD investigation to shift from SSOL4 to TCHEA4 entirely. At the same time, most of the experimental work could not be carried out in Sheffield for several months due to restrictions associated with the pandemic. As such, the heat treatments and characterisation were carried out during a short-term placement at ELKEME. Coordinating the alloy manufacturing in Sheffield, shipping the samples internationally and conducting the rest of the experimental work during such a short timeframe did not allow for a sufficient enough window to conclude the computational alloy screening. As such, only two compositions were selected, the $\text{Al}_{35}\text{Ti}_{25}\text{VCrMn}_{10}$ and the $\text{AlTiV}_{18.25}\text{CrMn}_{6.25}$, a decision which was based on empirical knowledge and preliminary CALPHAD results.

According to the previous SSOL4 CALPHAD results concerning the AlTiVCr equiatomic system it could be argued that during a low-temperature heat treatment both Al and Ti were expected to precipitate off of the matrix phase and form Al_xTi_y compounds. In turn, this would produce a matrix phase consisting exclusively of Cr and V in a 1:1 ratio. In the case of the $\text{AlTiV}_{18.25}\text{CrMn}_{6.25}$ alloy the matrix phase could consist of 50 at. % Cr, 37 at. % V and 13 at. % Mn under the same assumption. This would suffice to evaluate the magnitude of the effect of the Mn addition on the ductility of the manufactured alloys in both the as cast and heat treated condition. The intention was to also manufacture and evaluate the $\text{AlTiV}_{15}\text{CrMn}_{10}$ alloy with an expected retainment of up to 20 at. % Mn in the matrix phase. It was however expected that this addition of Mn may have had detrimental effects on the alloy density and significantly increase the likelihood of Laves phase formation during prolonged high temperature heat treatments. As such, the decision was made to also increase the amount of Al from 25 to 35 at. % which may have been able to alleviate both effects.

5.3.2.1 Thermodynamic Simulations (Thermocalc)

The initial thermodynamic simulations concerned the addition of 10 at. % Mn in an Al-enriched AlTiVCrMn system ($\text{Al}_{35}\text{Ti}_{25}\text{VCrMn}_{10}$) using the SSOL4 database (Fig. 5.4). The rationale regarding the elevated Al addition would be to offset the potential density increase associated with the incorporation of Mn. At 25 at. % Ti content the alloy crystallises in the disordered BCC structure at high temperature, while at lower temperatures AlTi compounds would also be formed. At about 100°C under equilibrium conditions the Cr_3Mn_5 phase is predicted to precipitate; however, due to the low phase transformation temperature its formation is rather unlikely under the current manufacturing and processing conditions. It must be noted though, that the SSOL4 database is unable to predict the formation of the B2 phase. As such, the quality of the calculation in terms of the matrix phase is questionable.

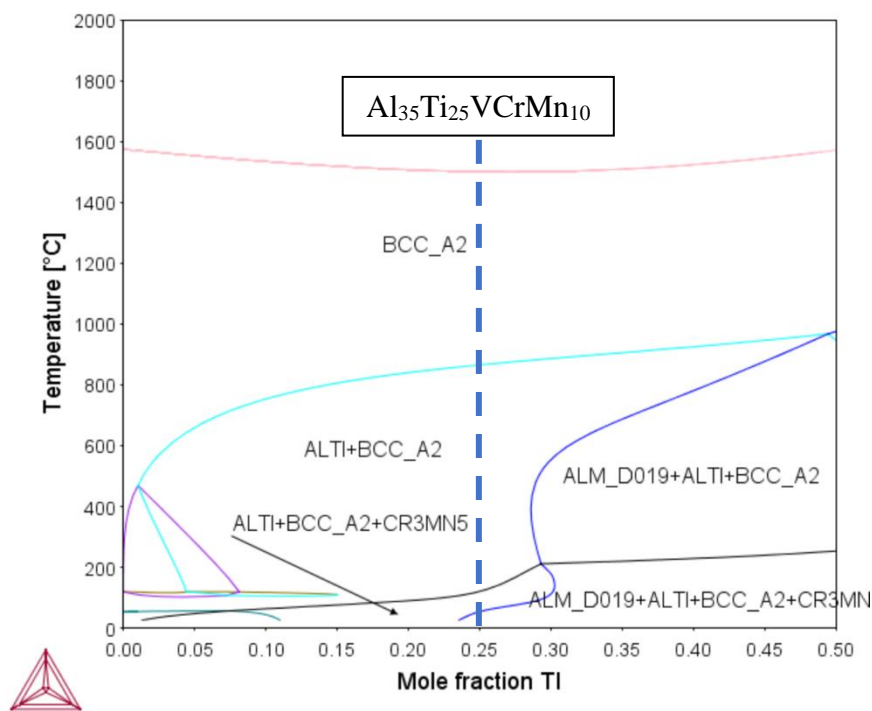


Figure 5.4. Calculated phase diagram of the AlTiVCrMn system with Thermo-Calc Software using the SSOL4: SGTE Alloy Solutions database where Al=35%, V=Cr, Mn=10% and Ti=balance.

Therefore, the same calculation was performed using the TCHEA4 database, which was the most advanced database available for HEAs at the time of this study (Fig. 5.5A).

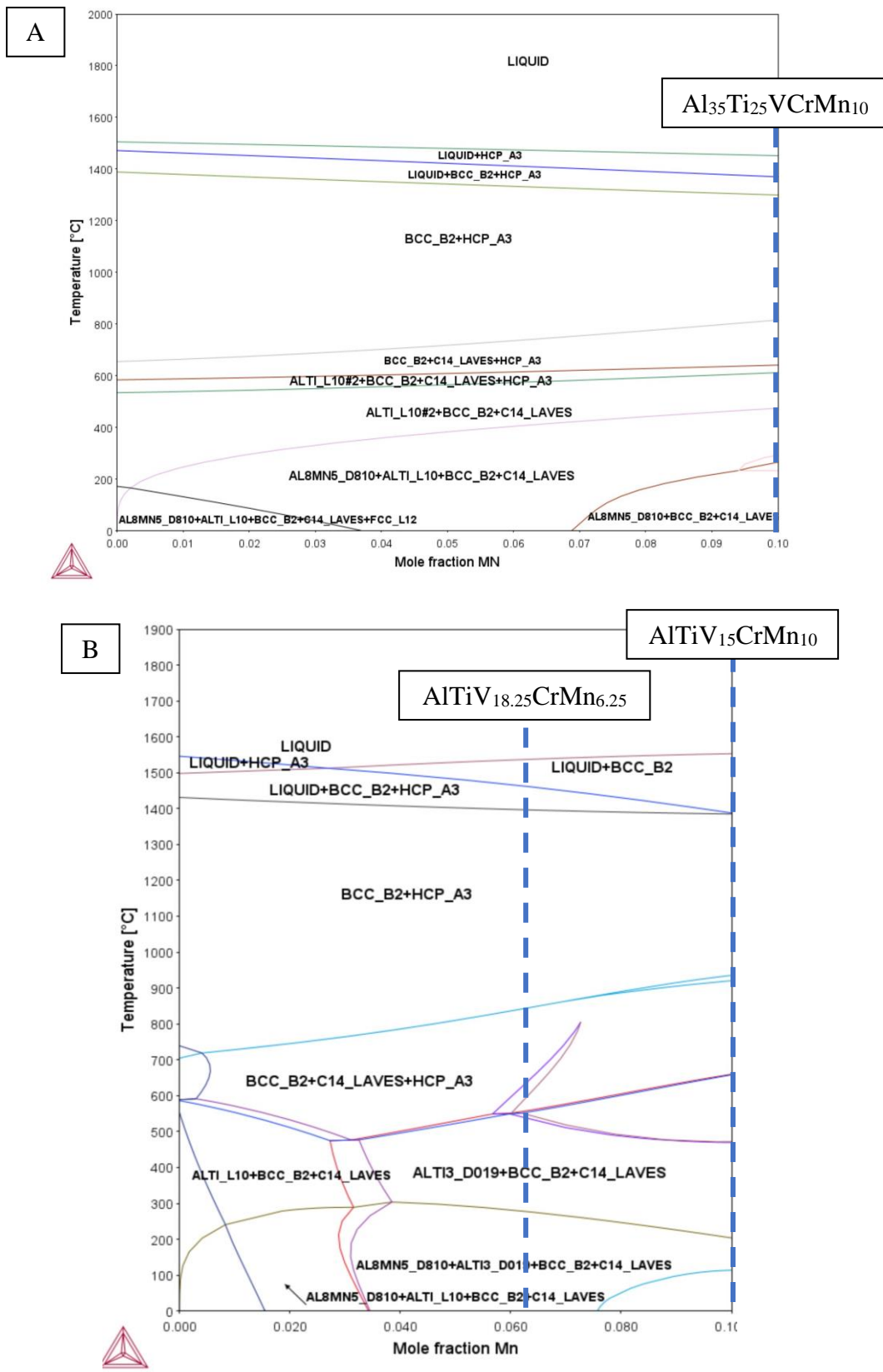


Figure 5.5. Calculated phase diagram of the AlTiVCrMn system using the Thermo-Calc software alongside the TCHEA4: TCS High Entropy Alloys where A) Al=35%, V=Cr, Ti=25% and Mn=balance, B) Al=Ti=Cr, V=(25-Mn)%.

Compared to the SSOL4 database, TCHEA4 (Fig. 5.5A) yielded significantly different results for the $Al_{35}Ti_{25}V_{10}Cr_{10}Mn_{10}$ case. In this case, the alloy is predicted to be multiphase at higher

temperatures, consisting of the ordered B2 and an HCP phase. As the temperature drops below 700°C, the formation of a Laves phase is also observed, followed by AlTi and lastly the Al₃Mn₅ phase resulting in the complete decomposition of the HCP phase below roughly 550°C. The AlTiV_{18.25}CrMn_{6.25} alloy (Fig. 5.5B) is also predicted to consist of similar phases to the Al₃₅Ti₂₅VCrMn₁₀ one. Again, the presence of the HCP and Laves phase is noted while the formation of AlTi₃ instead of AlTi particles is expected. It is also observed that should the Mn content had been raised to 10 at. % without the simultaneous increase of Al as originally designed, the formation of the Laves phase could be expected to take place at temperatures above 900°C. Based on these results the original AlTiVCr-Si_x phase diagram was calculated using the TCHEA4 database to benchmark to the previous work and what has been reported in the literature (Fig.5.6).

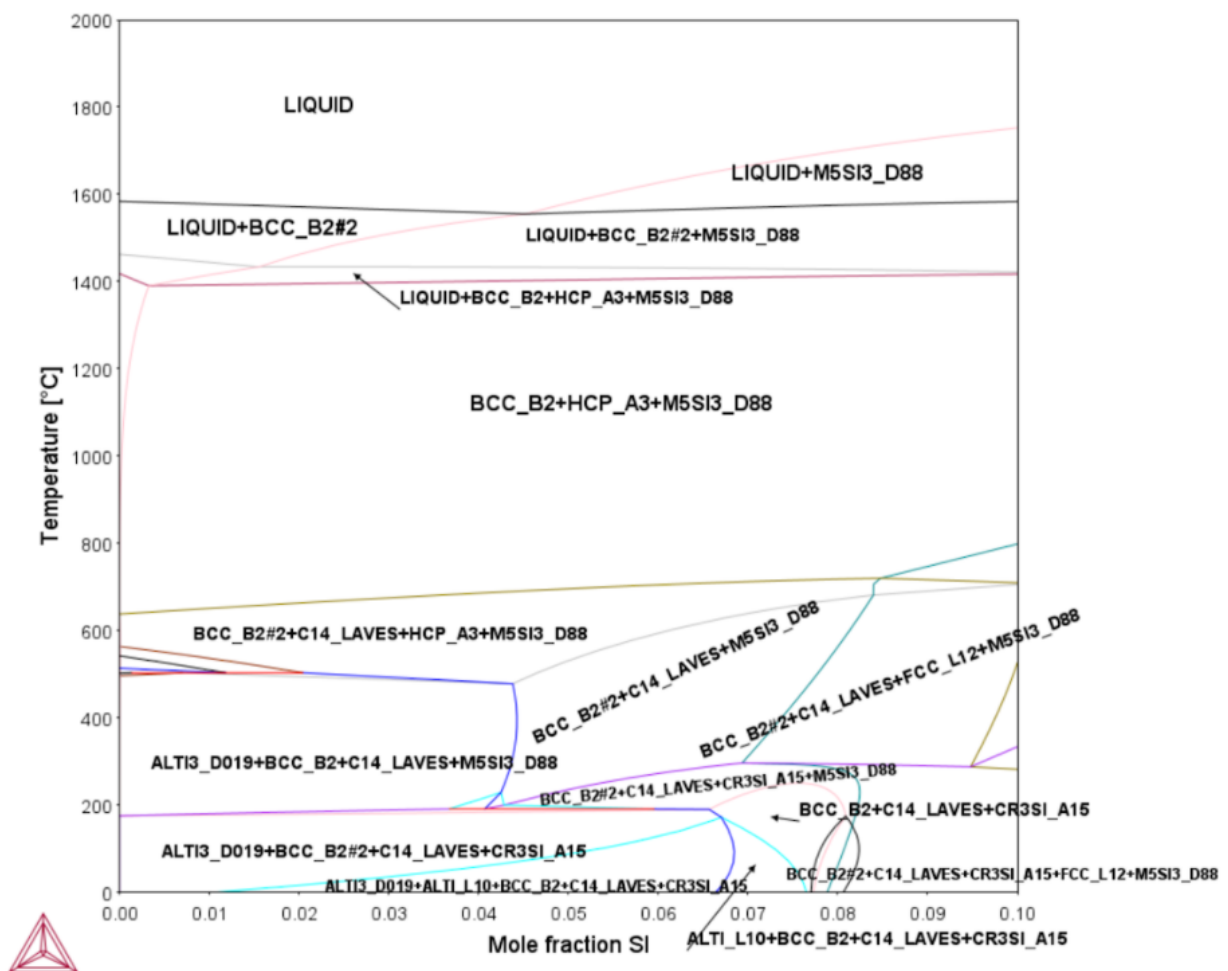


Figure 5.6. Calculated phase diagram of the AlTiVCrSi system with Thermo-Calc Software using the TCHEA4: TCS High Entropy Alloys where Al=Ti=V=Cr and Si=balance.

In this case it should be once again underlined that the BCC_B2 phase on Fig. 5.6 refers to a BCC solid solution while the BCC_B2#2 corresponds to the B2 phase. As such, it could be

seen that TCHEA4 predicts an order-disorder transformation taking place with the alloy attaining a BCC structure at higher temperatures and B2 at lower ones. Furthermore, a high temperature HCP phase was also observed alongside the M_5Si_3 phase which corresponds to the Ti_5Si_3 intermetallics. With a further reduction in temperature multiple phases begin to form, while the HCP phase decomposes. It is interesting to highlight that the model predicts the formation of a BCC matrix phase at lower temperatures as a higher volume fraction of SPPs is formed. These results directly contradict those published in the literature using the TCHEA2 database, which suggest the formation of a BCC or B2 solid solution alongside the Ti_5Si_3 particles [100]. Furthermore, the experimental work of Chapter 4 with X-ray diffraction analysis (XRD) demonstrated that the alloy only contained Ti_5Si_3 intermetallics alongside a BCC or B2 matrix phase even after a prolonged homogenisation heat treatment followed by air cooling. Therefore, TCHEA4 does not seem to be a reliable database for predicting the thermodynamic properties of the present system as it gravely overestimated the number of SPPs forming at lower temperatures. This could be attributed to the fact that all of the conducted relevant research looked at paraequilibrium conditions with the samples being in either the as cast condition or a heat treated condition that was however followed by air cooling. Therefore, perhaps the kinetics of the SPPs formation are relatively sluggish and thus require an extensive low-temperature heat-treatment for their precipitation to occur. Another possibility would be the usage of a revised Al-Ti phase diagram in TCHEA4 compared to previous TCHEA database versions which could have altered the relevant thermodynamic equilibria in certain regions of the phase diagram.

5.3.2.2 Optical Microscopy (OM), Scanning Electron Microscopy (SEM/EDX)

Regarding the results of the optical microscopy investigation on the alloys of interest AlTiVCr, AlTiVCr-Si_{7.2}, AlTiV_{18.75}CrMn_{6.25} and Al₃₅Ti₂₅VCrMn₁₀, in the first two cases no significant changes were observed in the microstructure compared to the previously conducted work. The novel alloy composition containing 6.25 at. % Mn showed similar features to the equiatomic AlTiVCr (Fig. 5.7). Specifically, in the as cast condition the microstructure consisted mainly of dendrites and pores. However, after the LT heat treatment the alloy started exhibiting different microstructural features, perhaps indicating a rougher surface. Unfortunately, these features could not be distinguished any further due to the resolution limitations associated with both OM and SEM.

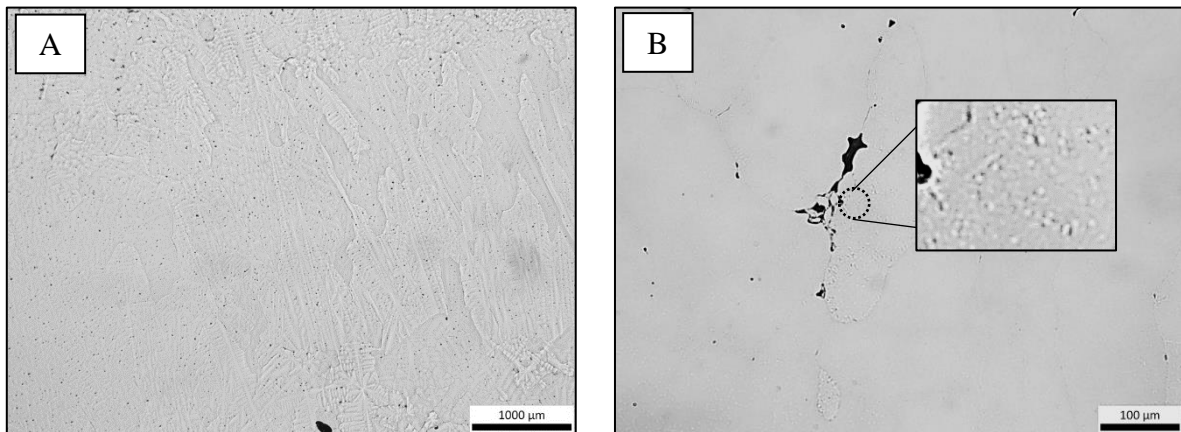


Figure 5.7. Optical micrographs of relief polished specimens from the central region of the A) as cast AlTiV_{18.75}CrMn_{6.25} and B) LT heat treated AlTiV_{18.75}CrMn_{6.25} alloy.

The microstructure of the Al₃₅Ti₂₅VCrMn₁₀ in the as cast state consisted primarily of elongated dendrites along the heat transfer direction and pores. In the LT heat treated condition the central region of the alloy seemed to have entirely disintegrated into a network of voids. Massive cracks also seem to have formed and seem to propagate from the centre of the sample towards the outer surface (Fig. 5.8). Upon investigating the area closer to the exterior surface of the sample the porous network encountered in the central region of the sample seems to have subsided. Instead, the microstructure now appeared to consist of a range of elongated particles. The darker ones could correspond to oxides while the ones with the lighter colour were barely distinguishable from the matrix phase and, as in the case of the 6.25 at. % alloy, seemed to form a rough texture on the observable surface. In both cases, this could indicate that the phase transformation leading to their formation could have shear characteristics (Fig. 5.9).

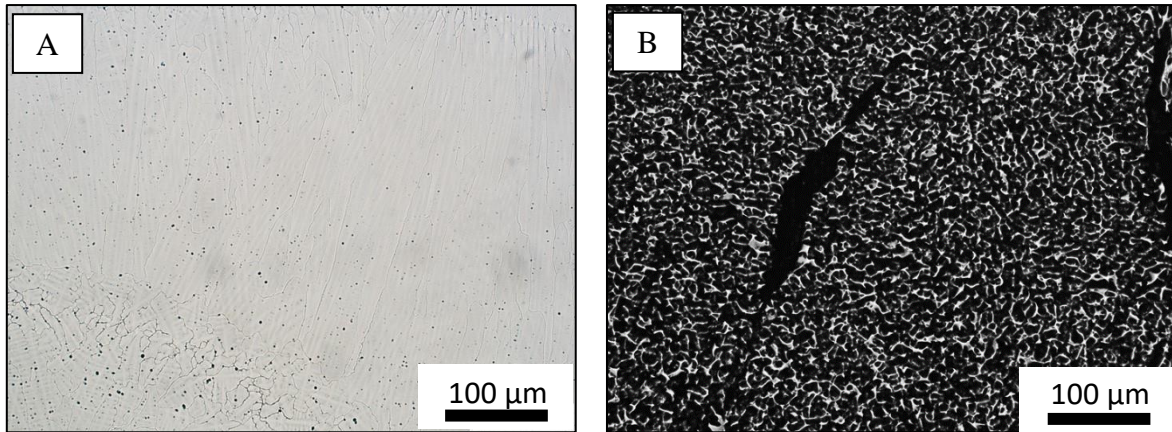


Figure 5.8. Optical micrographs of relief polished specimens from the central region of the A) as cast $Al_{35}Ti_{25}VCrMn_{10}$ and B) LT heat treated $Al_{35}Ti_{25}VCrMn_{10}$ alloy.

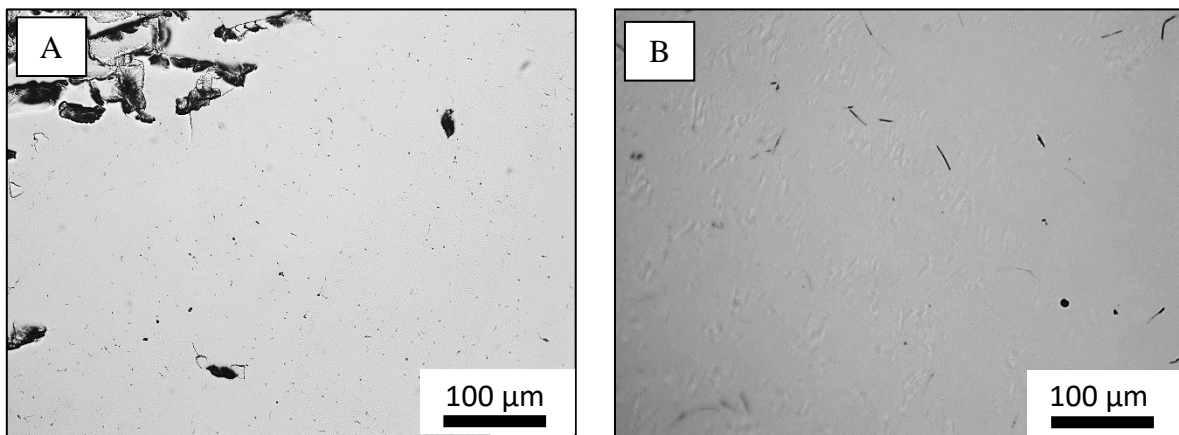


Figure 5.9. Optical micrographs of relief polished specimens from the external region of the LT heat treated $Al_{35}Ti_{25}VCrMn_{10}$ alloy.

Focussing on the identity of the darker particles the microstructural analysis with SEM verified that they were indeed Al-based oxides according to the EDX analysis. It was also revealed that the oxides were in fact present in the as cast condition as well (Fig. 5.10-5.11). The same rough texture encountered during the OM investigation was also prevalent in the LT heat treated condition during the SEM investigation using the BSE detector. Using a greater magnification this texture seemed to correspond to two types of needle-like phases forming a network with mild contrast differences between one another (Fig. 5.12). EDX analysis was not able to clearly demonstrate compositional differences between the two phases as the needle size approaches the resolution limit of the SEM detector. It should be noted that due laboratory access restrictions XRD could not be used at the time to determine the type of phases present in any of the investigated alloys.

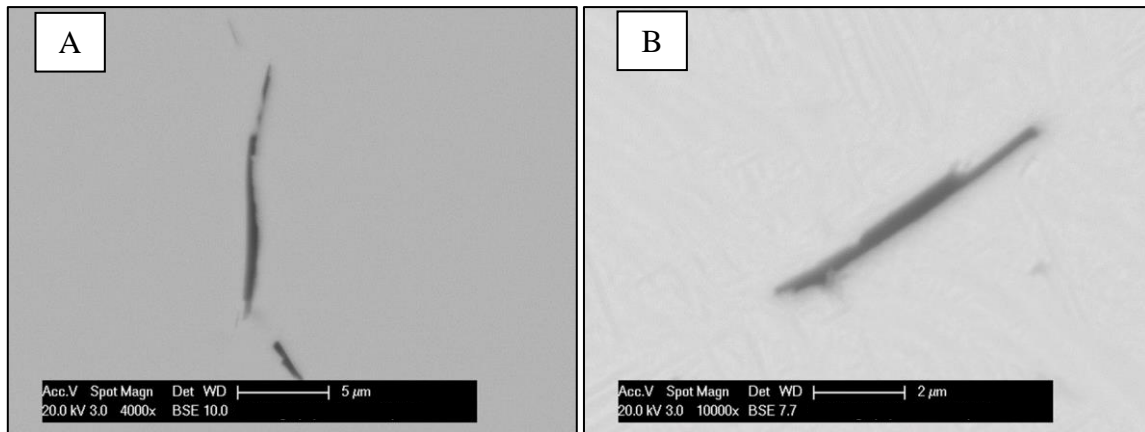


Figure 5.10. SEM micrographs of the A) as cast and B) LT heat treated $Al_{35}Ti_{25}VCrMn_{10}$ alloy using the BSE detector showing the Al-based oxides and, in the LT heat treated condition, the rough texture of the sample.

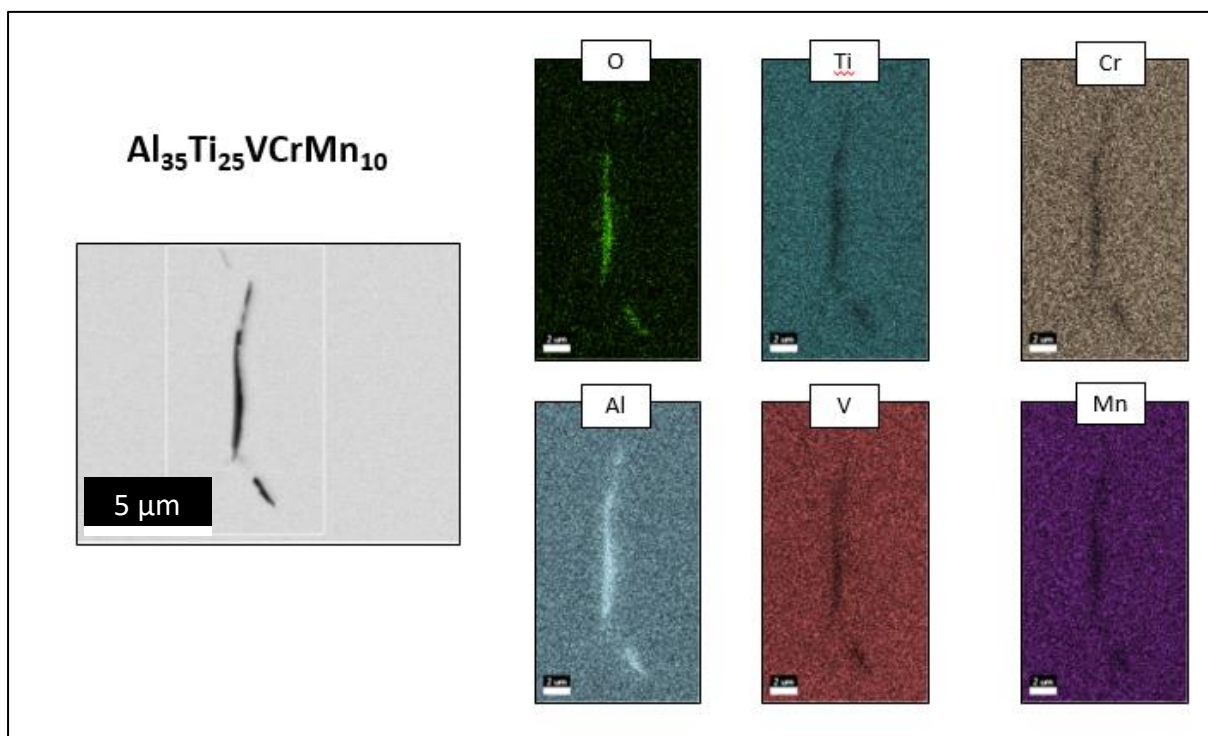


Figure 5.11. EDX quant map of the LT heat treated $Al_{35}Ti_{25}VCrMn_{10}$ alloy focussing on the region surrounding an elongated Al-based oxide.

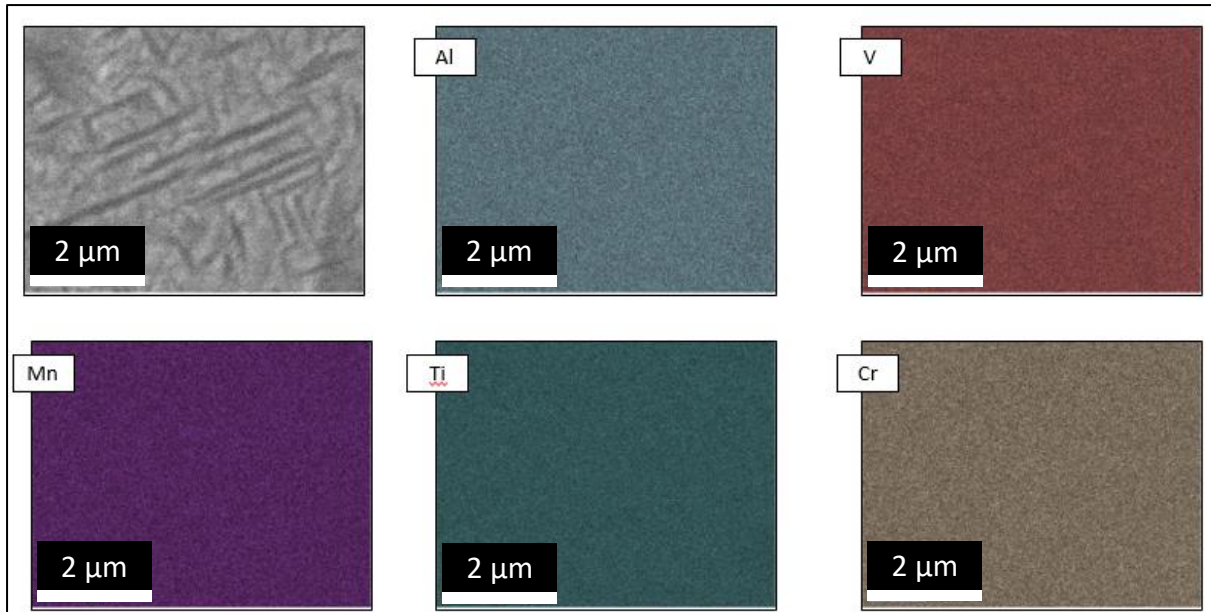


Figure 5.12. EDX quant map of the LT heat treated $Al_{35}Ti_{25}VCrMn_{10}$ alloy focussing on the rough surface region demonstrating a needle-like two-phase structure with mild compositional differences between one another.

The central region of the sample, originally thought to contain an interconnected network of voids, reveals a fully cracked surface instead (Fig. 5.13). Between the cracks lay unaffected rectangular regions. Using greater magnification, small particles were revealed to cover the surface of the sample, possibly originating from colloidal silica remnants, while mild compositional differences were highlighted using BSE (Fig. 5.14). An EDX scan along a crack revealed a distinct lack of Al along the crack path which could be attributed to topographic effects but otherwise very mild compositional differences (Fig. 5.15). Again, this could be attributed to the features of interest being finer than the resolution of the equipment.

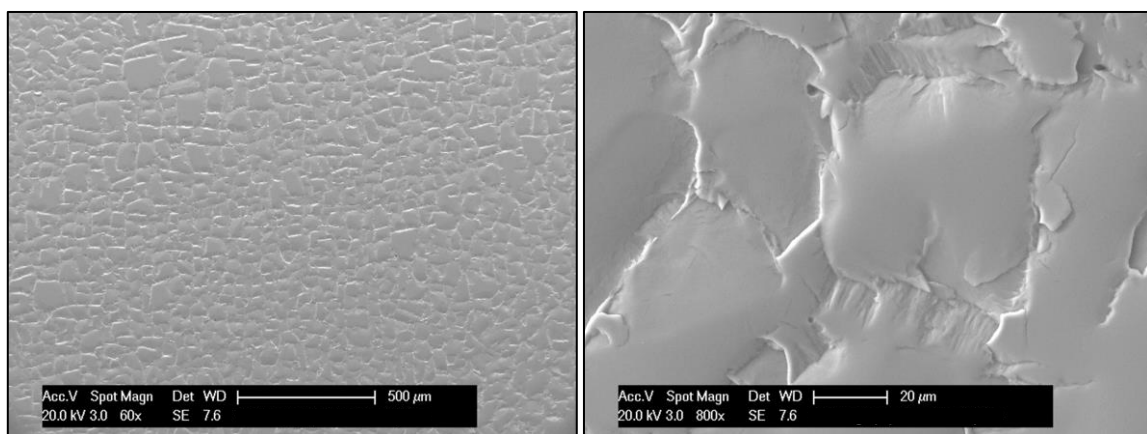


Figure 5.13. SEM micrographs of the LT heat treated $Al_{35}Ti_{25}VCrMn_{10}$ alloy using the SE and BSE detectors showing the crack network.

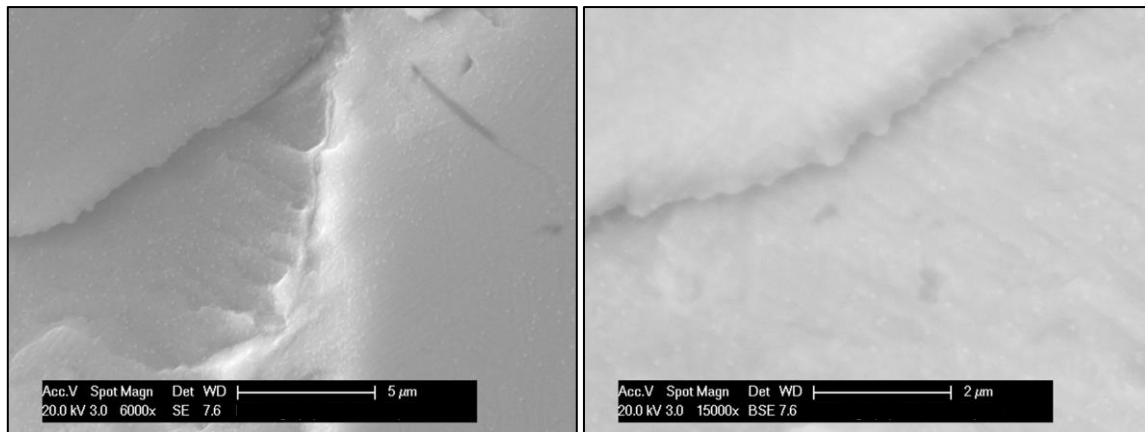


Figure 5.14. SEM micrographs of the LT heat treated $Al_{35}Ti_{25}VCrMn_{10}$ alloy using the SE and BSE detectors focussing on a cracked region.

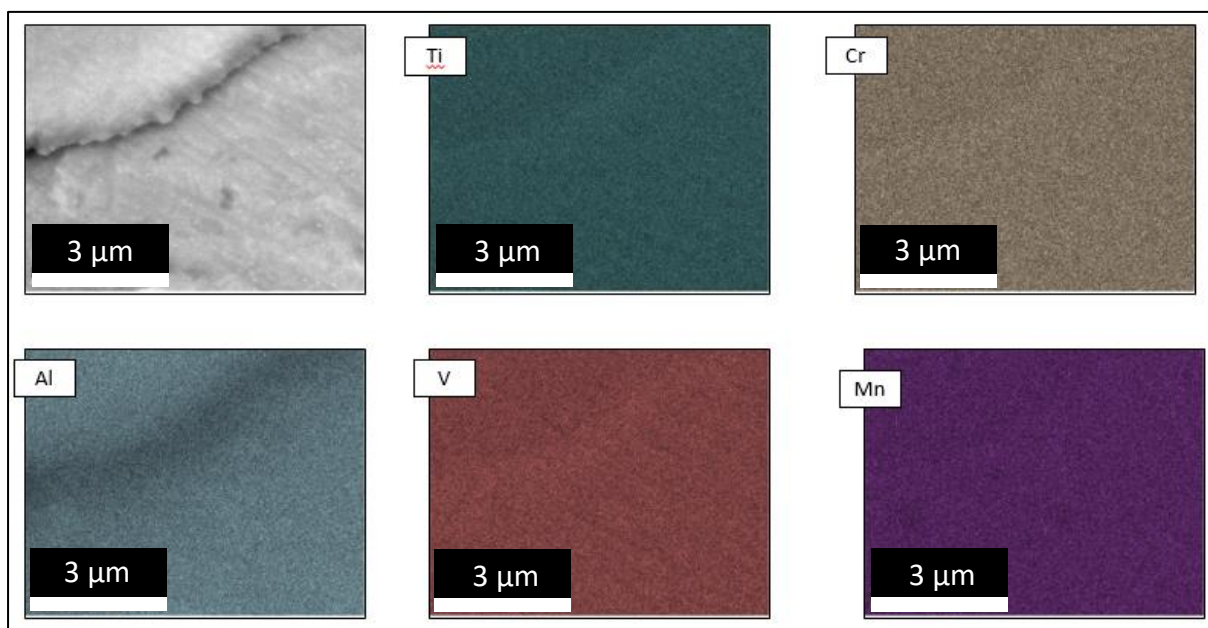


Figure 5.15. EDX quant map of the LT heat treated $Al_{35}Ti_{25}VCrMn_{10}$ alloy focussing on a cracked region demonstrating a slight elemental segregation.

In summary, in terms of the microstructural features, the LT heat treatment did not seem to have a profound effect on most of the tested samples, at least when surveyed with SEM resolution. That is, however, not the case for the $Al_{35}Ti_{25}VCrMn_{10}$ sample where the LT heat treatment seems to have completely fractured the sample surface in the central region. Furthermore, when observed at higher magnifications the present sample seemed to exhibit a microstructure similar to that encountered in the WQ $AlTiVCr$ sample and the $Al_{0.5}NbTa_{0.8}Ti_{1.5}V_{0.2}Zr$ alloy in the work of Soni et al. in the LT heat treated condition [82]. In the latter case the phase transformation was fully suppressed through water quenching, but the chemical composition of their alloy was significantly different to the ones presented in this work to draw conclusions, perhaps apart from the Al content playing a role in the stabilisation

of the B2 phase. Another interesting point about the $\text{Al}_{35}\text{Ti}_{25}\text{VCrMn}_{10}$ alloy was the existence of the Al-base oxides. Since the alloy was manufactured under vacuum the only way for the oxides to have formed would be from oxygen already contained within the alloying elements. This would also require the alloy to have a strong affinity for oxygen and perhaps the raw materials having a high oxygen content to begin with.

5.3.2.3 Mechanical Properties, Density Measurements and Fractography

The density of the alloys is presented in Table 5.3. Overall, the lightest alloy is the $\text{Al}_{35}\text{Ti}_{25}\text{VCrMn}_{10}$ with a density of 4.84 g/cm^3 in the as cast state, followed by the AlTiVCr at 5.07 g/cm^3 , $\text{AlTiVCr-Si}_{7.2}$ at 5.11 g/cm^3 and $\text{AlTiV}_{18.75}\text{CrMn}_{6.25}$ at 5.18 g/cm^3 . The alloys' density remained relatively unchanged throughout the heat treatment process (Table 5.3).

Table 5.3 Density data for the tested compositions measured using ethanol with the Archimedes' method.

Density (Ethanol)		
Alloy	As Cast (g/cm^3)	LT heat treated (g/cm^3)
AlTiVCr	5.07	5.1
$\text{AlTiVCr-Si}_{7.2}$	5.11	4.99
$\text{AlTiV}_{18.75}\text{CrMn}_{6.25}$	5.18	5.15
$\text{Al}_{35}\text{Ti}_{25}\text{VCrMn}_{10}$	4.84	4.74

The microhardness tests showed a significant increase in hardness between the as cast and LT heat treated state in all tested compositions, thus highlighting the potential for age hardening in the present alloying system. More specifically, the equiatomic AlTiVCr alloy showed an increase in hardness from 594 HV to 672 HV (13% increase), the $\text{AlTiVCr-Si}_{7.2}$ an increase from 709 HV to 807 HV (14% increase), the $\text{AlTiV}_{18.75}\text{CrMn}_{6.25}$ a slight increase from 646 HV to 695 HV (8% increase) and the $\text{Al}_{35}\text{Ti}_{25}\text{VCrMn}_{10}$ a significant increase from 663 HV to 883 HV (33% increase) in the as cast and LT heat treated condition respectively (Table 5.4). These findings imply that a phase transformation should be taking place upon heat treating at lower temperatures resulting in these strengthening effects. A plausible mechanism would be through the precipitation of SPPs which, however, was not resolved under the SEM since no significant changes were observed in the microstructural features of the AlTiVCr , $\text{AlTiVCr-Si}_{7.2}$ and $\text{AlTiV}_{18.75}\text{VCrMn}_{6.25}$. Specifically in the case of the $\text{Al}_{35}\text{Ti}_{25}\text{VCrMn}_{10}$, which exhibited the greatest increase in hardness, some particles were evident but nearly indistinguishable from the matrix phase under high magnification.

Table 5.4. Vickers microhardness data for the tested compositions using a load of 0.5 kg.

Microhardness 0.5 kg				
Alloy	As Cast (HV _{0.5})	LTHT (HV _{0.5})	StD – AC (HV _{0.5})	StD – LTHT (HV _{0.5})
AlTiVCr	594	672	36.33	19.93
AlTiVCr-Si _{7.2}	709	807	33.41	43.7
AlTiV _{18.75} CrMn _{6.25}	646	695	12.55	17.62
Al ₃₅ Ti ₂₅ VCrMn ₁₀	663	883	16.62	25.53

There is also the matter of the severe cracking phenomenon taking place which completely undermined any potential for application in the present alloy. A possible scenario explaining the cracking incident could be the extended precipitation of SPPs with a significant lattice density difference to the matrix phase. Although the total density of the alloy would remain relatively constant, significant compressive or tensile stresses could develop within the material leading to a progressive crack formation process taking place, the magnitude of which would be directly related to the total precipitation volume. Again, XRD was not available during this part of the investigation. During the ductility testing minor differences were observed between the as cast and LT heat treated condition of the samples while all of the tested alloys once again displayed a limited degree of ductility. To further investigate the effect of the LT heat treatment and the capabilities of the novel compositions in terms of ductile fracture, the fracture surfaces formed during the ductility testing in the SEM were evaluated. Overall, all of the alloys were characterised by a predominantly brittle fracture surface both in the as cast and in the LT heat treated state; however, characteristics pertaining to ductile fracture were evident in certain cases. A distinct fine dimple-like structure was observed in the LT heat treated condition of the AlTiVCr sample. Similar features were also observed in the as cast and LT heat treated condition of the Al₃₅Ti₂₅VCrMn₁₀ samples. Ductile features were also evident in the AlTiV_{18.75}CrMn_{6.25} samples in both the as cast and LT heat treated conditions but to a lesser degree (Fig. 5.16). Therefore, the addition of Mn alone was not enough to enable ductile behaviour in the present system.

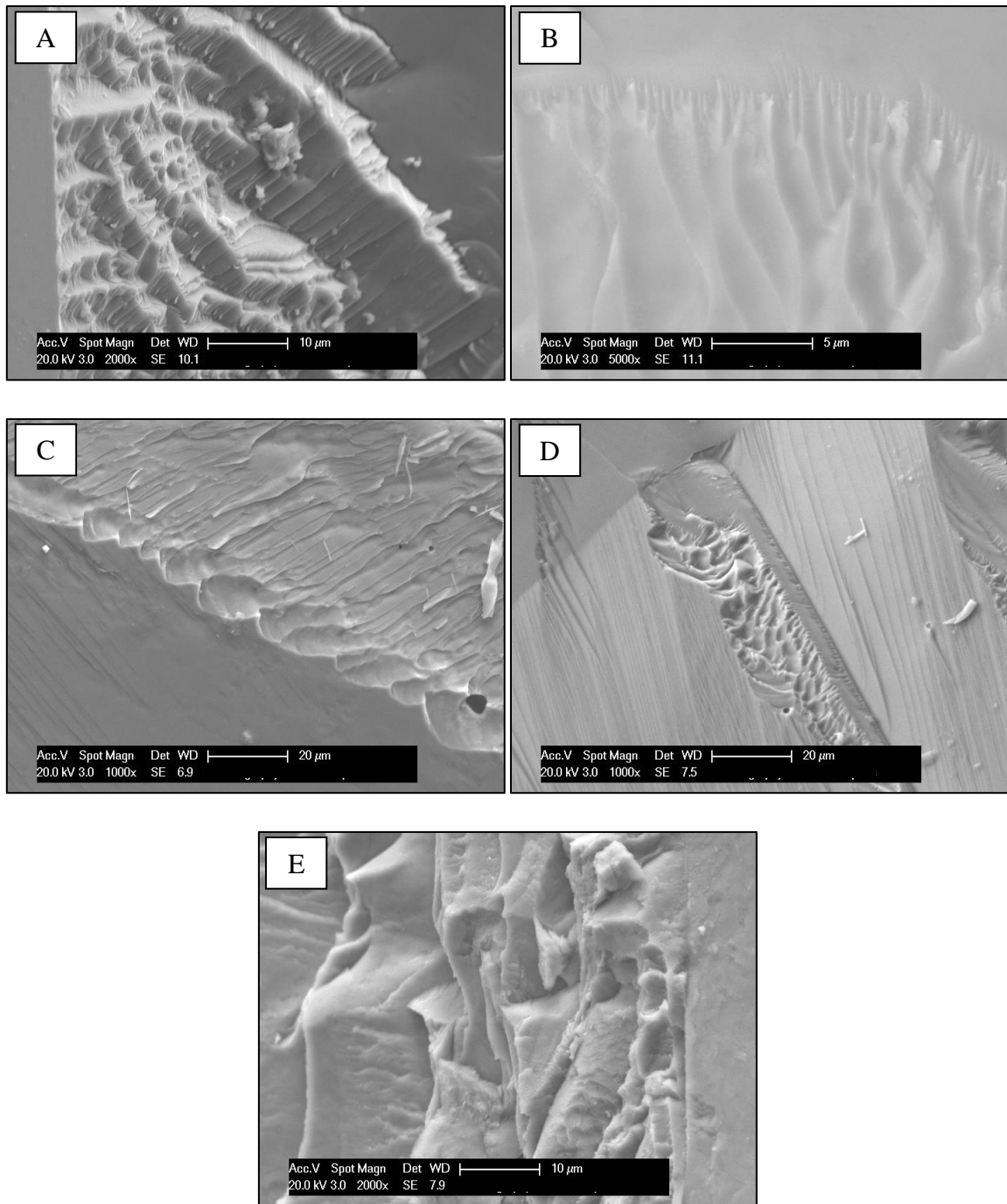


Figure 5.16. SEM images showing the fracture surface of the A) LT heat treated AlTiVCr, B) as cast AlTiV_{18.65}CrMn_{6.25}, C) LT heat treated AlTiV_{18.65}CrMn_{6.25}, D) as cast Al₃₅Ti₂₅VCrMn₁₀ and E) LT heat treated Al₃₅Ti₂₅VCrMn₁₀ samples.

5.4 Conclusions

The results of this research showed that both the AlTiVCr and AlTiVCr-Si_{7.2} alloys exhibited a brittle fracture mechanism. While the reason behind the failure of the ingots during the VAM process predominantly lay in the low thermal conductivity of the associated alloys, the lack of inherent ductility enabled the manifestation of the phenomenon. Attempts were made to increase the ductility by alloying with Mn and subjecting the original and new series of alloys to a LT heat treatment. It was believed that should the alloys be characterised by a high DBTT due to the increased Cr content, the introduction of Mn would be able to partially alleviate that phenomenon based on the respective DBTT of the elemental materials. The intent behind the LT heat treatment was to enable the formation of AlTi-based phases and other Al-based SPPs in order to reduce the amount of Al of the matrix phase. Subsequently, this could cause a reverse order-disorder transformation resulting in a BCC matrix phase at room temperature. However, neither of these modifications had a notable effect on the ductility of the tested materials as determined by assessing their fracture surfaces as formed through mechanical impact loading. Therefore, the next sensible step forward was to attempt to suppress the order-disorder transformation by subjecting the equiatomic AlTiVCr alloy to a high temperature heat treatment followed by water quenching. This was investigated in chapter 6. The key findings of this part of the work are summarised in the following points:

1. The thermal conductivity of the equiatomic AlTiVCr alloy was measured at $4.77 \text{ Wm}^{-1}\text{K}^{-1}$, which is significantly lower than most pure metals and alloys.
2. During the rapid thermal cycles associated with the VAM process the accumulated heat in the ingot would not be distributed homogeneously due to the low thermal conductivity. In turn this would lead to the inhomogeneous expansion/contraction of the ingot, resulting in the accumulation of internal stresses and eventually failure.
3. The fracture surfaces of failed ingots of the AlTiVCr and AlTiVCr-Si_{7.2} exhibited brittle characteristics with the latter indicating hints of ductile behaviour.
4. The Mn addition did not have a notable effect on the microstructure or the fracture behaviour of the samples in the as cast condition.
5. Upon being subjected to a LT heat treatment at 700°C for 24h, all samples showed an increase in hardness by 8-33%.
6. The LT heat treatment did not affect the microstructure of the AlTiVCr, AlTiVCr-Si_{7.2} and the AlTiV_{18.75}CrMn_{6.25} while it resulted in the deterioration of the Al₃₅Ti₂₅VCrMn₁₀

alloy. Nevertheless, the lack of discernible features could be associated with the resolution limitation of the available equipment.

7. Although microstructural differences could be observed between the as cast and LT heat treated condition of the $\text{Al}_{35}\text{Ti}_{25}\text{VCrMn}_{10}$ alloy these could not be associated with any specific phenomenon.
8. The LT heat treatment did not improve the ductility of any composition to a notable extent.
9. The LT heat treatment at 600°C resulted in the disintegration of all samples.

6. Compositionally Invariant Phase Transformation Control in the AlTiVCr alloy

This Chapter concerns the application of a heat treatment cycle aimed at suppressing the order-disorder (BCC-B2) phase transformation taking place in the AlTiVCr alloy with a view towards generating ductility improvements as a result. Aspects of this work were carried out by the author in the Department of Innovation and Sustainability of Volkswagen Group Research in Wolfsburg, Germany within the frame of a research placement. The preparation of samples by FIB was carried out at the University of Warwick, by staff with expertise in the process, while the TEM analysis was performed by Dr. Alexander Carruthers at the University of Manchester.

6.1 Aim

As demonstrated in Chapter 5, both the equiatomic AlTiVCr and the AlTiVCr-Si_{7.2} alloys exhibited significant limitations in terms of ductility. To tackle this challenge certain hypotheses were formed for possible origins of this lack of ductility. The possible presence of a B2 matrix at room temperature due to an order-disorder transformation taking place, or the potential for low ductile-brittle transition temperature originating from the elevated amounts of Cr in the alloys of interest were both investigated. An attempt to tackle the issue should the latter assumptions be the case, was made through the incorporation of Mn, and for the former, low temperature heat treatments aiming at the formation of a Cr-V-rich BCC matrix phase and the precipitation of Al_xTi_y-based phases were performed according to the available thermodynamic data. However, both pathways failed to address the ductility issues, with both the introduction of Mn and the low temperature heat treatments in fact causing a notable deterioration of the microstructural and mechanical properties of the investigated alloys. This also further highlighted the limitations originating from the use of an older thermodynamic database when performing thermodynamic simulations on MCAs.

After assessing the findings of this part of the investigation, it was decided that an alternative route would need to be employed based on the available thermodynamic properties derived from the work of Qiu et al. [97] and Huang et al. [100]. As previously discussed in Chapter 2, the work of V. Soni [82] et al. demonstrated that performing a high temperature heat treatment, followed by a rapid quenching process could inhibit the order-disorder transformation in a different MCA system. As such, the aim of this part of the work was to test the feasibility of the application of a heat treatment cycle of this type to inhibit the order-disorder transformation in the equiatomic AlTiVCr alloy, and to assess its effect on the ductility.

6.2 Experimental Methods

The raw materials Al, Cr, Ti, V, used to manufacture the alloy, were sourced in wire, sheet, and bulk form with purities >99.8%. Experimental samples were formed using an Arcast Arc 200 Vacuum Arc Melter (VAM) under a high purity Ar gas atmosphere and were remelted 4-5 times using electromagnetic stirring to ensure chemical homogeneity. The samples were allowed to cool down for a brief period (~1 min) between remelts and were afterwards flipped over and remelted immediately. The samples were sectioned in half using a Secotom-50 microtome with Al₂O₃ 6" cutting disks.

This batch of samples consisted of two AlTiVCr ingot halves. Both sample halves were subjected to a heat treatment, carried out in a laboratory electric resistance heated tube furnace under a flowing Ar atmosphere along with two Ti pieces to ensure minimal oxidation at 1200°C for 8h. One sample was then furnace cooled (FC) down to room temperature over a 4h period, while the other was water quenched (WQ) down to room temperature directly from 1200°C. The samples were mounted in conductive bakelite and were ground using P120, P280, P600, P1000, P1200, P2500 and P4000 SiC grinding papers in succession. They were then polished using a 1 µm diamond suspension and Struers OP-U colloidal silica solution for 10 and 20 minutes respectively for relief polishing.

6.2.1 X-ray Diffraction Analysis

The diffraction patterns of the as WQ and FC AlTiVCr samples were extracted under ambient conditions using an X'Pert³ Powder diffractometer. The samples subjected to testing under non-ambient conditions were also tested using the same settings. The diffractometer utilised N K-β filtered Cu Kα radiation operating at 45 kV and 40 mA. The Programmable Divergence Slit (PDS) was set to 0.25° while the Anti-Scatter slit at 0.5°. The scanning angle range was set from 20° to 120° 2θ with a step size of 0.02°. All powder samples originated from the same bulk AlTiVCr sample and consisted of a <1 mm particle size.

6.2.1.1 X-ray Diffraction Analysis under non-ambient conditions

To gain information regarding the evolution of the crystal structure of the AlTiVCr alloy as a function of temperature, X-ray Diffraction (XRD) under non-ambient temperature conditions was carried out using an X'Pert³ Powder diffractometer with the Anton Paar HTK12N furnace attachment under a 5×10^{-5} mbar atmosphere. It must be noted that no inert atmosphere could be used with the available instruments, while the vacuum levels were found to continuously drop during the experiment to the order of 10^{-3} mbar. An automatic stage mover was used to

automatically adjust the height of the specimen during the experiment to account for the thermal expansion of the furnace components. The scan setting used in these series of experiments are the same as those used during testing under ambient conditions as presented above. Two powder samples with a particle size of <1 mm were used which originated from the same bulk sample to which different heating profiles were applied (Fig. 6.1-2).

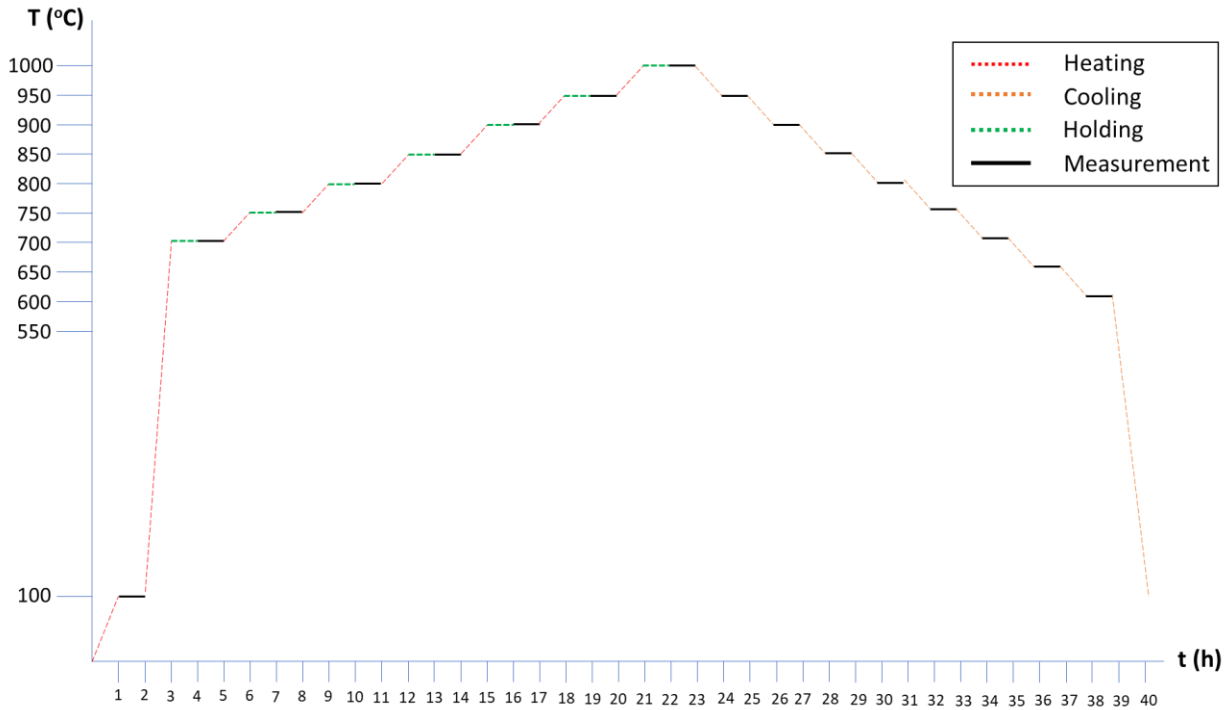


Figure 6.1 Heating profile corresponding to sample 1.

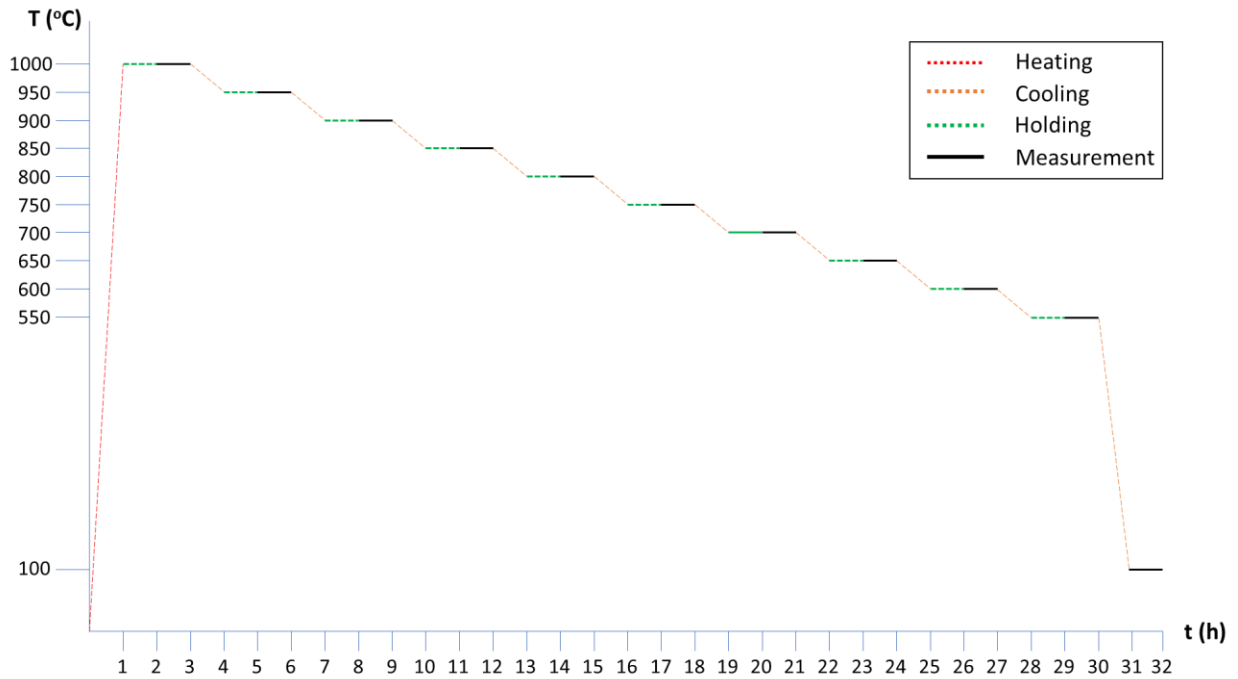


Figure 6.2 Heating profile corresponding to sample 2.

6.2.2 Focused Ion Beam (FIB) SEM and Transmission Electron Microscopy (TEM)

The second batch of samples was forwarded to the University of Warwick to be prepared for TEM analysis using Focused Ion Beam (FIB) milling with a ThermoFisher Scientific Scios DualBeam. The selected section surface area was $5 \times 5 \mu\text{m}^2$ and consisted of a grain boundary between two primary matrix phase grains. In both cases particles were evident along the grain boundaries. The selected area was coated by a Pt layer to protect the area from damage. The surrounding area was bombarded by a beam of Ga ions, milling through the surface. The area of interest was then attached to a tungsten rod using the deposited Pt and was subsequently cut free from the surface. The extracted section was then attached to a carbon coated copper TEM grid and thinned down using the Ga ion beam. STEM was subsequently carried out in the University of Manchester with a ThermoFisher Talos F200 X-FEG S/TEM, operating at 200 kV. The chemical composition of the alloy and the phases evident in the microstructure were determined using energy dispersive spectroscopy (EDX) with Super X EDX alongside 4 Silicon Drift Detectors (SDDs) and by extracting the diffraction patterns in each case.

6.2.2 Mechanical Testing

6.2.2.1 Vickers Hardness (HV) Testing

Hardness testing was carried out using the Vickers method as described in Chapter 3.2.6.1 on a WQ and FC AlTiVCr sample. The indentation grid was a 4×3 grid with a 2000 μm spacing for both samples using a load of 0.5 kg with a dwell time of 20 s on a Leco AMH 43.

6.2.2.2 Nanoindentation Testing

For the evaluation of the effect of the cooling rate on the elastic properties of the alloy, the nanoindentation testing technique was employed using a MicroMaterials Nanotest Vantage nanoindenter. Standard Berkovich tips were used with a load function consisting of 30 s load, 60 s dwell and 30 s unload respectively. The tests were load controlled and were limited to a maximum load of 300 mN. Thermal drift data was also collected post indentation. The indentation grid was a 5×5 grid with a 100 μm spacing for both samples. An extensive description of the methodology regarding the Young's modulus derivation is presented in Chapter 3.2.6.2.

6.2.2.3 Compression Testing

Compression testing was performed using an Instron 68FM-100 under ambient condition with a strain rate of 0.15 mm/min using 2 cylindrical samples for the WQ and FC condition with a diameter of 6 mm and a height of 9 mm according to the ASTM E9-09 standard. It should be noted that an extensometer was not used during the experiment.

6.2.4 Inert Gas Fusion Analysis (IGFA)

Three AlTiVCr samples from the heat treated condition (6 in total) were tested using IGFA to determine the O_2 content present within the material on a supplementary basis. The methodology used to carry out these measurements is extensively described in chapter 3.2.8.

6.3 Results and Discussion

6.3.1 Microstructural Characterisation

6.3.1.1 X-ray Diffraction Analysis (XRD)

As previously discussed in Chapter 4, the AlTiVCr alloy is characterised by a B2 crystal structure at room temperature while it transforms into a BCC structure instead upon reheating to higher temperatures. According to the available literature the temperature where this order-disorder transformation is taking place could lie between 600-1000°C [97, 100, 105]. Given the wide temperature spectrum, a series of high temperature XRD experiments were carried out in an attempt to pinpoint the exact transformation temperature. Before that, a comparison between a WQ and an FC AlTiVCr sample was made through XRD under ambient conditions (Fig. 6.3). The differences between the two patterns were, however, slight. Contrasting the XRD patterns corresponding to the as cast and heat treated conditions presented in Chapter 4.3.2.4, both the WQ and FC samples lack the distinct B2 peak at roughly 30° [101]. Nevertheless, it must be noted that the XRD diagrams corresponding to the AlTiVCr-Si_{7.2} samples were also lacking that specific peak. Again, this could point to the fact that the matrix phase of the AlTiVCr-Si_{7.2} alloy crystallises in the BCC structure, although this is highly unlikely as the AlTiVCr-Si₅ alloy studied by Huang et al. [100] exhibited a B2 matrix. Apart from that, both the WQ and FC samples exhibited peak splitting in all observable peaks. This could indicate the coexistence of two BCC/B2 phases with similar lattice parameters; however, this should not be the case in the FC condition given that the literature suggests that only B2 would be present at room temperature [97]. Therefore, it could be argued that exclusively relying on XRD to differentiate between the BCC and B2 structure in this system may yield unreliable results. Nonetheless, any notable differences between the B2 and the BCC structure may be unveiled through high temperature XRD experiments.

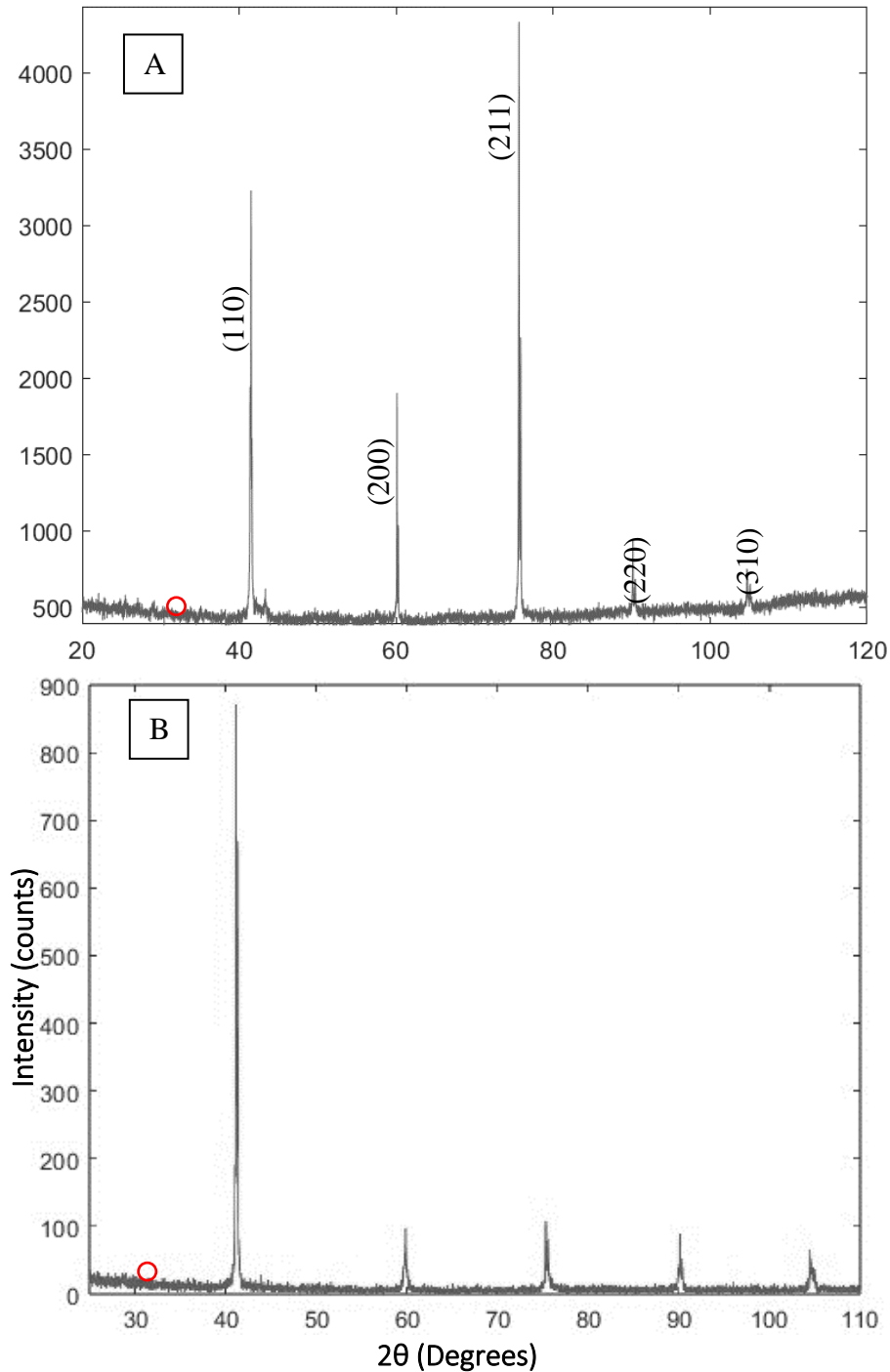
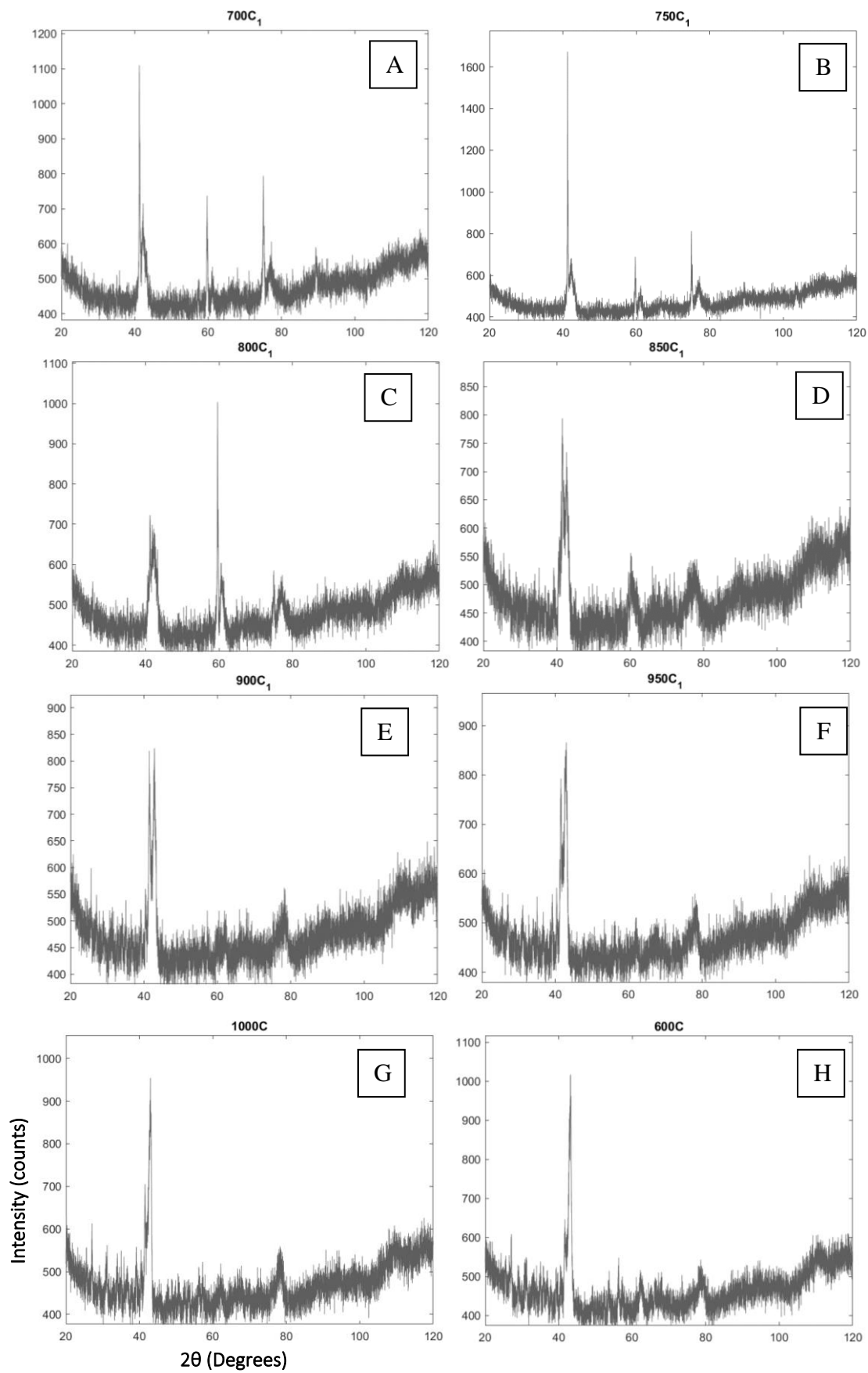


Figure 6.3 X-ray diffraction patterns of the equiatomic AlTiVCr alloy in the A) water quenched (WQ) and B) furnace cooled (FC) condition. The red circle is used to highlight the region where a B2 peak would be expected.

The XRD pattern corresponding to the reference powder sample (an equiatomic AlTiVCr alloy in powder form) used is shown in Fig. 6.4I. In terms of features, the relevant diagram looks identical to that of the WQ sample with a distinct lack of the B2 peak once again (Fig. 6.3A). When assessing the results corresponding to sample 1 (Fig. 6.1) it becomes apparent that an increase in temperature would result in a progressively deteriorating measurement quality. More specifically, the associated peak size would reduce to levels similar to that of the noise

profile while the peaks themselves were significantly broader in comparison to the reference powder sample. The only discernible feature evolution is the growth of secondary peaks (Fig. 6.4.A) next to the original ones shown in Fig. 6.4I. The size of the secondary peaks increased progressively, eventually overtaking the original ones at a temperature beyond 900°C. Apart from the growth of secondary peaks it is difficult to notice the development of other features between 700-1000°C due to the combined effect of small peak size and elevated noise levels. One could argue that there could be evidence of the development of the B2 peak between 900-1000°C. Naturally, that contradicts what is known in the literature where it has been established that the high temperature phase corresponds to BCC instead of B2 and is much more likely for the relevant peaks to be associated with noise. Nevertheless, the fact that the XRD pattern extracted at 600°C during the cooling process looks nearly identical to the one at 1000°C suggests that perhaps any additional peaks could be attributed to stable phases that may have formed with the progressive increase in temperature.

Indeed, given the fact that the measurements were carried out under a high vacuum instead of an inert atmosphere seemed to have contributed to the deterioration of the sample, most probably due to the system exhibiting leakages. Upon removing the sample, it became clear that the powder particles had consolidated during the heating cycle due to sintering process taking place. The surface layer of the powder had also gained a black tint indicating significant reaction had taken place with the atmosphere. Even more pronounced results were obtained using sample 2 (Fig. 6.2) because of the elongated exposure to a higher temperature environment from the initial steps of the process. To ensure that these results were consistent and were not attributed to any equipment malfunctions, sample 1 and 2 were once again analysed post-process under ambient conditions (Fig. 6.4 J, K). Although the peaks were more distinct compared to the high temperature measurements, the overall XRD profile quality was not sufficient to allow for further analysis or characterisation. Nevertheless, all patterns in Fig. 6.4(G, H, J, K) bore significant resemblance to each other, meaning that whichever phase formed under non-ambient conditions was also stable throughout the entire temperature spectrum during the cooling process.



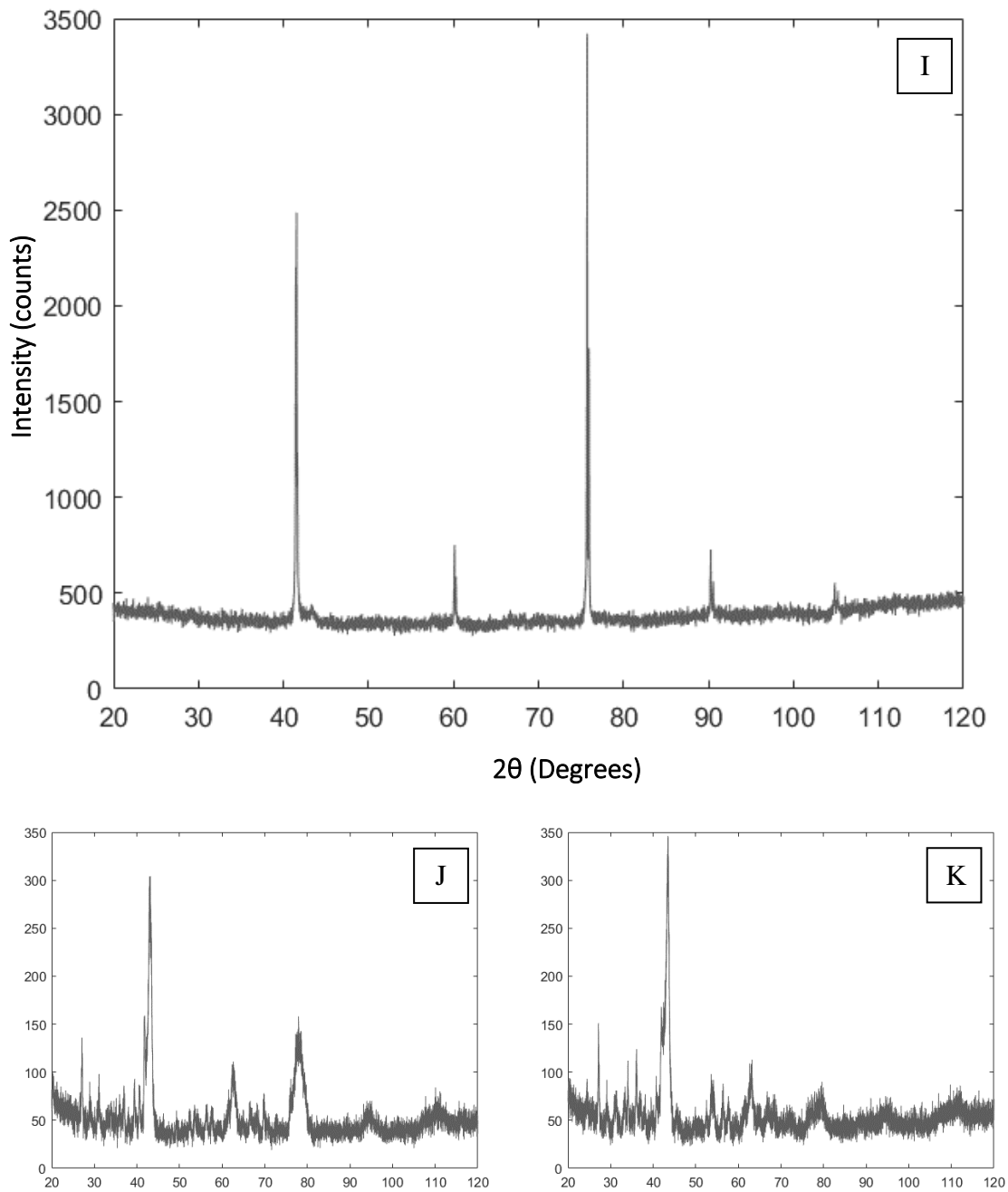


Figure 6.4 X-ray diffraction patterns illustrating the dependence of the crystal structure of the equiatomic AlTiVCr alloy regarding the testing temperature with diagrams A-H corresponding to sample 1. Patterns A-G show the evolution of the crystal structure with an increase in temperature ranging between 700-1000°C. Pattern H shows the diffraction pattern of the alloy as measured at 600°C during the cooling step. Pattern I refer to the diffraction pattern of the powder sample before its subjection to the heating-cooling cycle. Patterns J and K correspond to samples 1 and 2 respectively as measured under ambient conditions after the completion of the relevant heating-cooling cycle in each case.

In conclusion, high temperature XRD was unsuccessful in capturing the process of the order-disorder phase transformation or any features that would differentiate between the B2 and the BCC crystal structures. This could be attributed to the lack of an inert atmosphere being used during the experiment which may have allowed for atmospheric air to leak into the heating chamber and react with the sample (the increasing pressure recorded during the run indicates

that the vacuum is not perfect in the chamber). Regardless, it is also unlikely that any differences would have been observed between the B2 and the BCC during the high temperature process given that the XRD diagrams of the WQ and FC samples did not exhibit significant differences. That could of course suggest that either both samples consisted of the same microstructural components or that the order-disorder transformation was only partially inhibited. As such, higher resolution characterisation techniques were required.

6.3.1.2 Transmission Electron Microscopy (TEM)

Two AlTiVCr samples were considered for the TEM analysis. As previously mentioned, both were heat treated at 1200°C for 8h but underwent different cooling processes, namely water quenching and furnace cooling respectively. Starting with the FC sample the investigated area contained two grains and a titanium nitride (TiN) particle along the grain boundary (Fig. 6.5 and 6.6). The presence of nitrogen (N) in the alloy was not unexpected given that it could have been absorbed into the material during the VAM process despite the use of a high purity inert atmosphere. Since the distribution of N was limited to the TiN particle its effect on the rest of the microstructural features can be assumed insignificant. The intergranular area was completely lacking any features indicating evidence of secondary phase particles (SPPs). This was further explored and facilitated through the EDX scans pointing at a homogeneous distribution of the alloying elements within the grains while a slight segregation was observed along the grain boundary (Fig. 6.7 and 6.8) where increased Ti content was detected. It is important to underline that the lack of any notable segregation phenomena at such a fine scale reinforce the positive response of the alloy to heat treatments.

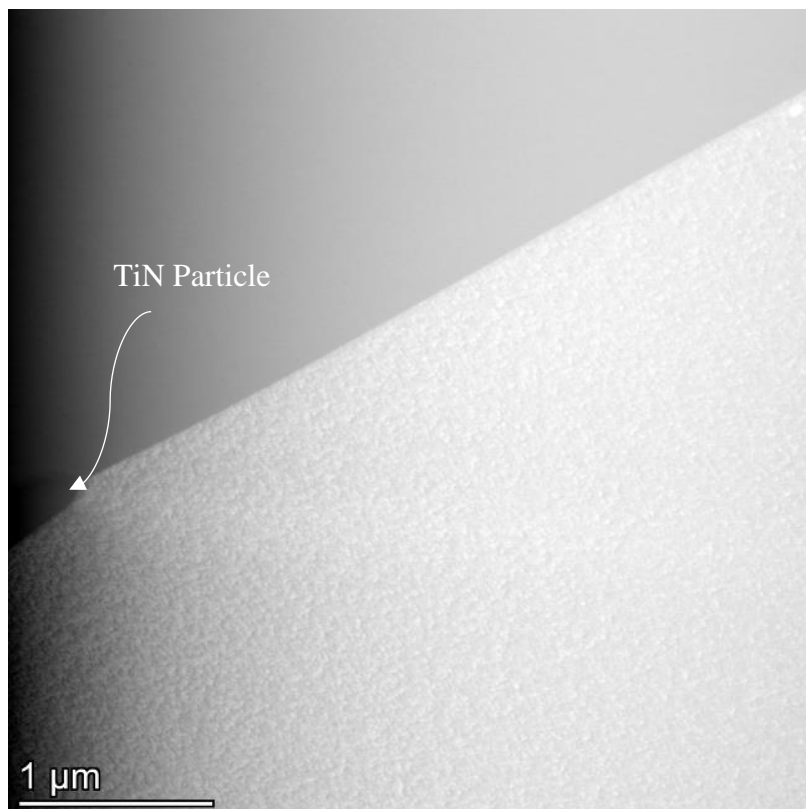


Figure 6.5 Bright field (BF) image showing the investigated region of the furnace cooled sample containing a grain boundary and a TiN particle.

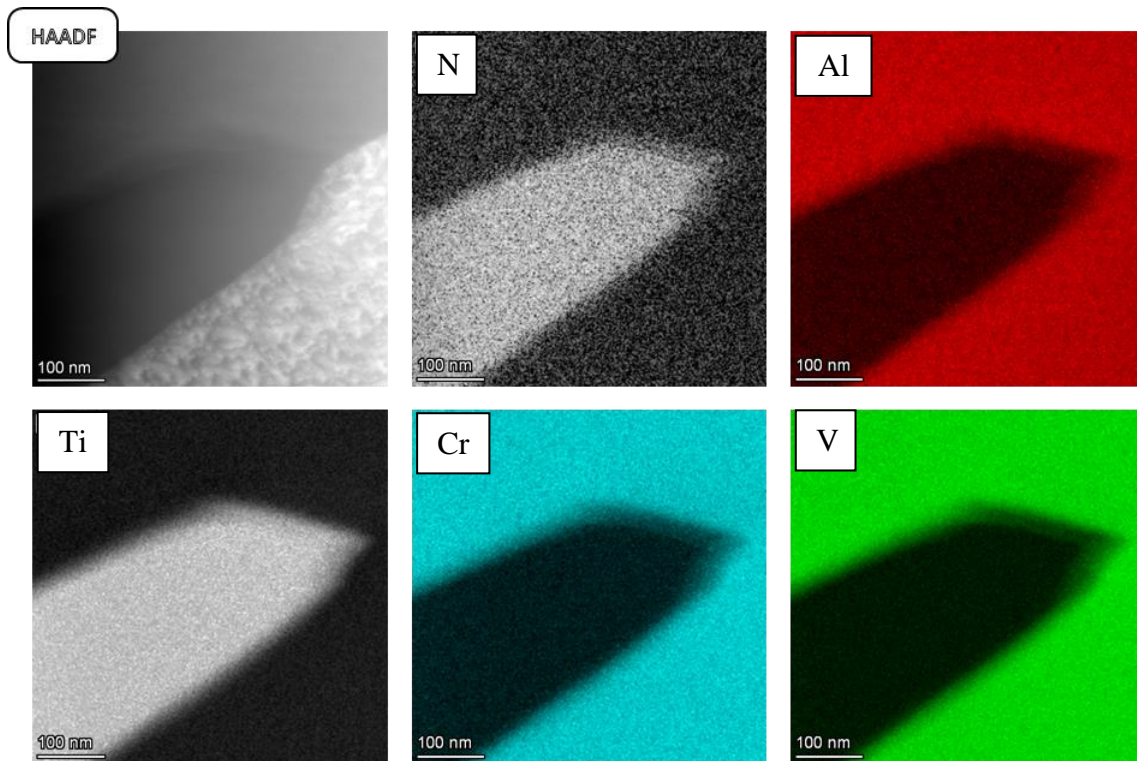


Figure 6.6 EDX quant map scans illustrating the distribution of the alloying elements and impurities around a TiN particle.

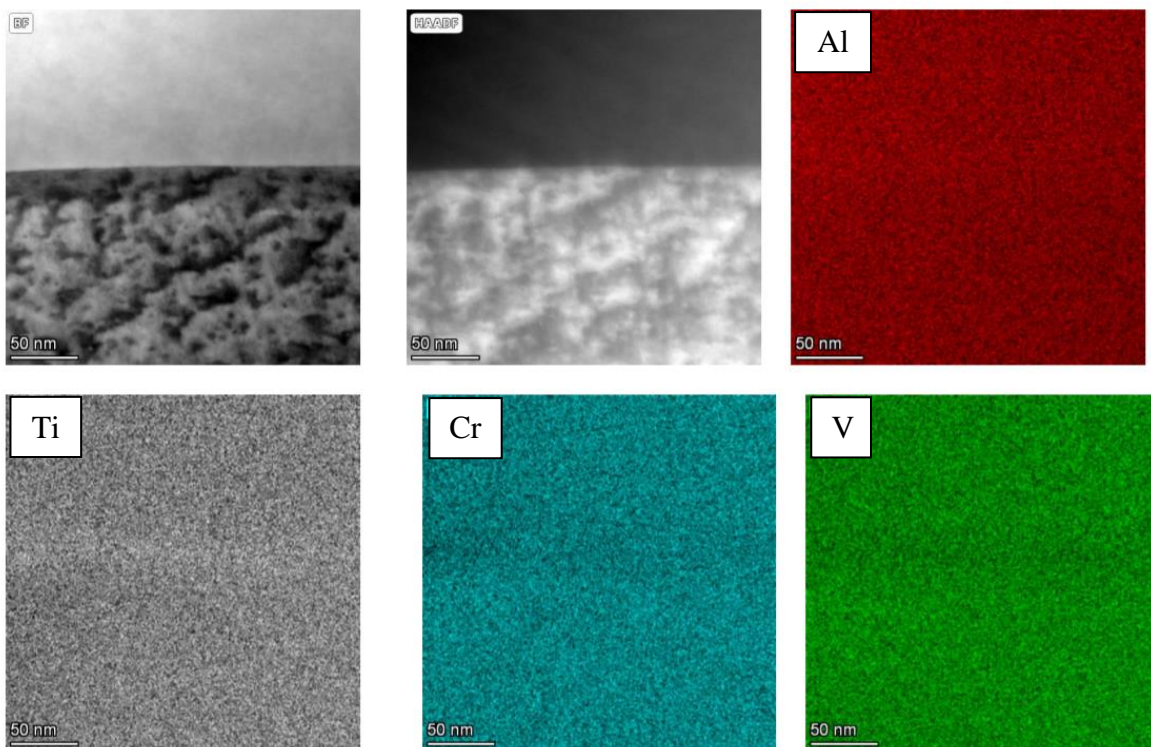


Figure 6.7. EDX quant map scans showing the distribution of Al, Ti, V and Cr around a grain boundary and within the B2 matrix grains.

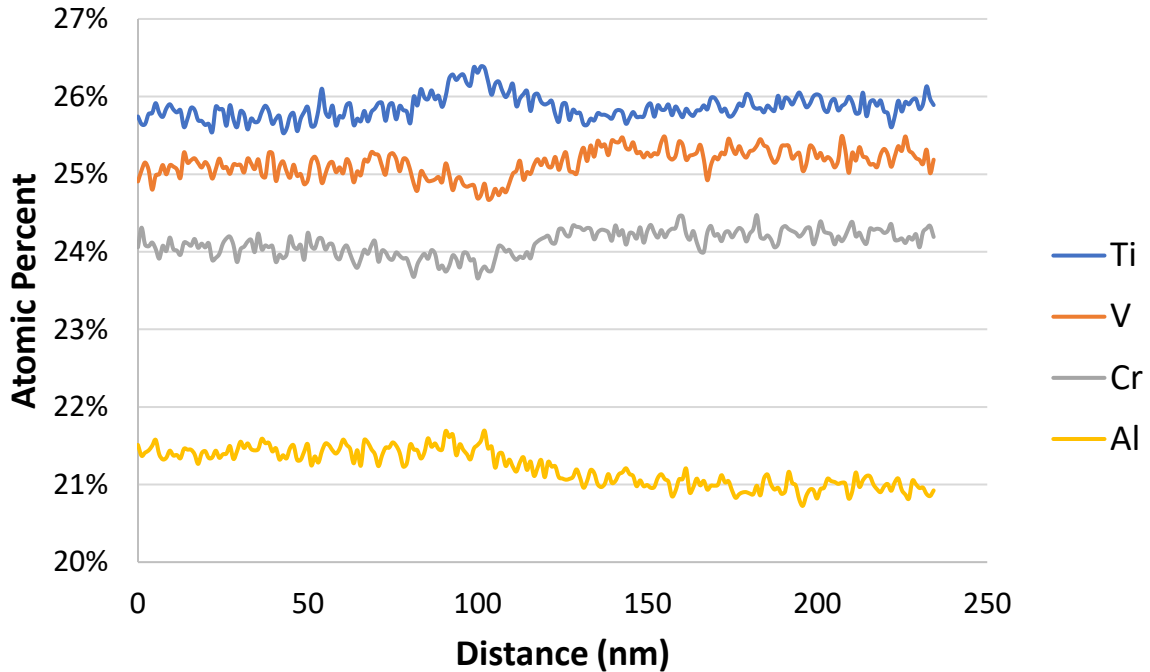


Figure 6.8 Linescan across a grain boundary of the FC sample illustrating the distribution of Al, Ti, V and Cr.

Nevertheless, it must be noted that the amount of Al measured in the region of the sample examined has deviated from the nominal value of 25 at. % down to roughly 21-22 at. %, while Ti, V and Cr lie at 25 ± 1 at. %. Given that the material under survey using the TEM consists of a <100 nm thin film the interaction volume would naturally be significantly smaller compared to a bulk SEM sample. Furthermore, the take-off angle is much harder to properly setup compared to the SEM and as such the quantification of lighter elements is inaccurate [249]. Therefore, these slight deviations in the Al content from the nominal values can be attributed to the measurement technique itself rather than inconsistencies in the alloy manufacturing process. As such, the relevant observations in terms of the distribution of the alloying elements do hold true; however, from a qualitative standpoint.

In terms of the crystallographic properties of the AlTiVCr alloy it comprised exclusively of a single B2 phase, as evident from the relevant diffraction pattern shown in Fig. 6.9. This is in line with the previously published literature [97, 100] and contradicts the results of the thermodynamic simulations shown in Chapter 4; this was expected given the limitations concerning the relevant thermodynamic database. The fact that the material comprised a B2 phase in the FC condition also creates additional questions regarding the XRD results shown previously. Namely the lack of the distinct B2 peak at roughly 30° . It could be argued that perhaps the reason behind the peak appearing clearly in the samples investigated in Chapter 4

compared to the results shown in Fig. 6.3B would be the lower levels of noise in the former case. Indeed, there are indications of a peak having formed in the region of 30° in Fig. 6.3B the intensity of which however is similar to the noise levels. Judging from this information it would be probable that the WQ sample would also be characterised by a similar microstructure due to the significant similarity between the diffraction patterns of the WQ and FC sample (Fig. 6.3A and 6.3B respectively). This assumption also seems reasonable given the rapid nature of order-disorder transformations where the ordering process may even complete during rapid cooling [105, 250]. Nevertheless, variations in the intensity of the B2 peak could also be attributed to varying degrees of ordering being present in the material depending on the processing route or the inherent crystallographic properties of the material. Of course, gaining the relevant information would require higher resolution characterisation techniques such as Atom Probe Tomography (APT), which is beyond the scope of this research.

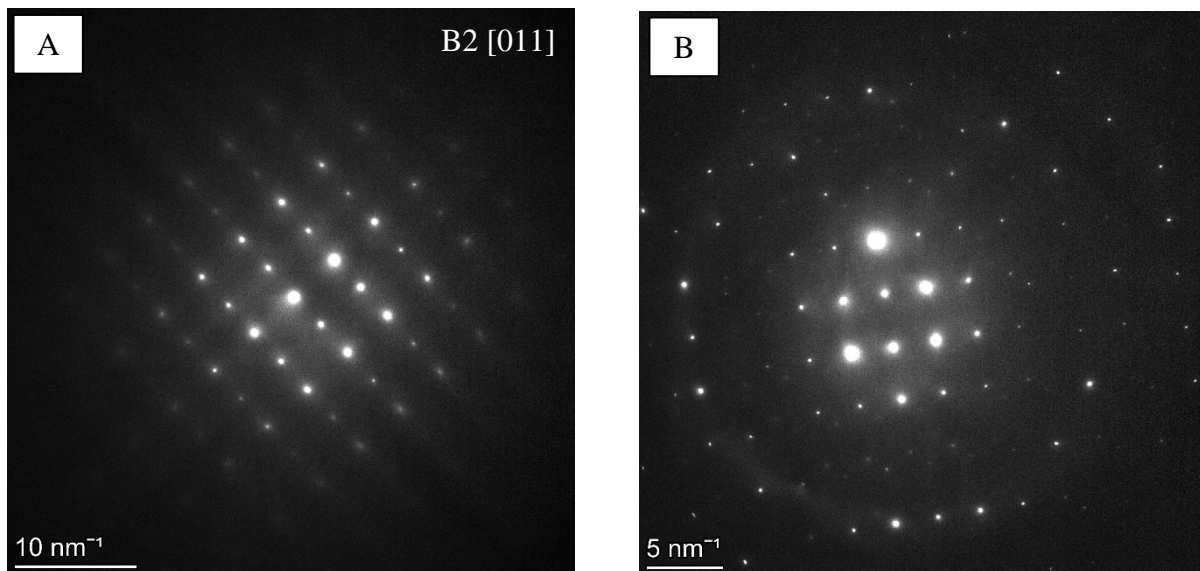


Figure 6.9. A) The diffraction pattern corresponding to a B2 matrix as observed from the [011] zone axis, B) the diffraction pattern corresponding to the TiN particle.

The microstructure of the WQ sample was more complicated by comparison as shown in Fig. 6.10A. TiN were observed along the grain boundaries but this time a sulphide (TiS) was present as well (Fig. 6.11). In both conditions, the formation of these particles was attributed to the existence of impurities and as such should not be considered as inherent microstructural features of the investigated alloying system. In this particular case, the sulfur (S) probably originated from the raw materials, specifically Cr or V given their lower purity compared to Al and Ti. Again, as both N and S were constrained to the areas where the corresponding TiN and TiS lie, the chemical composition of the intragranular regions was unaffected. The intragranular regions consist of a dual phase microstructure containing a matrix and a plate-like phase. It is expected that the matrix phase corresponds to the BCC phase while the plates to the B2, due to the nature of the order-disorder transformation. This is further supported by the diffraction patterns extracted from the area (Fig. 6.10D-E). Upon closer inspection the B2 phase seems to arrange itself in both a plate and a needle form. This could be attributed to a fine plate thickness, meaning that a side-on view would make it seem like a needle instead of a plate. The extraction of a pure BCC diffraction pattern was relatively challenging due to interference from the B2 phase and was only possible near the edge of the foil. The exact positions of extraction are unfortunately unavailable since this work was carried out externally. This further supports the previous discussion concerning the lack of a distinct B2 peak in the XRD patterns of both the WQ and FC sample. Analysis through EDX quant maps (Fig. 6.12-6.13) revealed that Cr and V preferentially migrate towards the B2 plates while Ti is instead predominantly found within the BCC phase. Al seems indifferent in terms of its affiliation to either one of the primary phases. Lastly, the volume fraction of the plate-like phase assumed to belong to the B2 phase as derived from 5 images was averaged out at 25.3 %. Due to the low number of available images this should be used as a rough guide in terms of the microstructural constitution of the sample rather than as a definitive value.

These results are consistent with the findings of V. Soni et al. [82] concerning an RHEA of the AlNbTaTiVZn system with the microstructures of both studies bearing striking similarity. Such microstructures are frequently encountered in the case of Ni-base superalloys in the form of γ' (typically Ni₃Al) precipitation within a γ (FCC) matrix [251]. This is typically achieved through a controlled heat treatment process incorporating rapid cooling steps alongside aging treatments. The same principles can be applied in MCAs to allow for a good combination between strength and ductility [82, 237, 252]. More information regarding these principles has been laid out in Chapter 2. The key difference between the work of Soni [82] and that reported

here is that in the former case the order-disorder transformation was completely suppressed through the quenching process while in this case it was only partially inhibited. Therefore, due to the limitations with employing an even higher cooling rate (e.g., cryogenics) to completely suppress the transformation in the equiatomic AlTiVCr alloy, compositional modifications must be made.

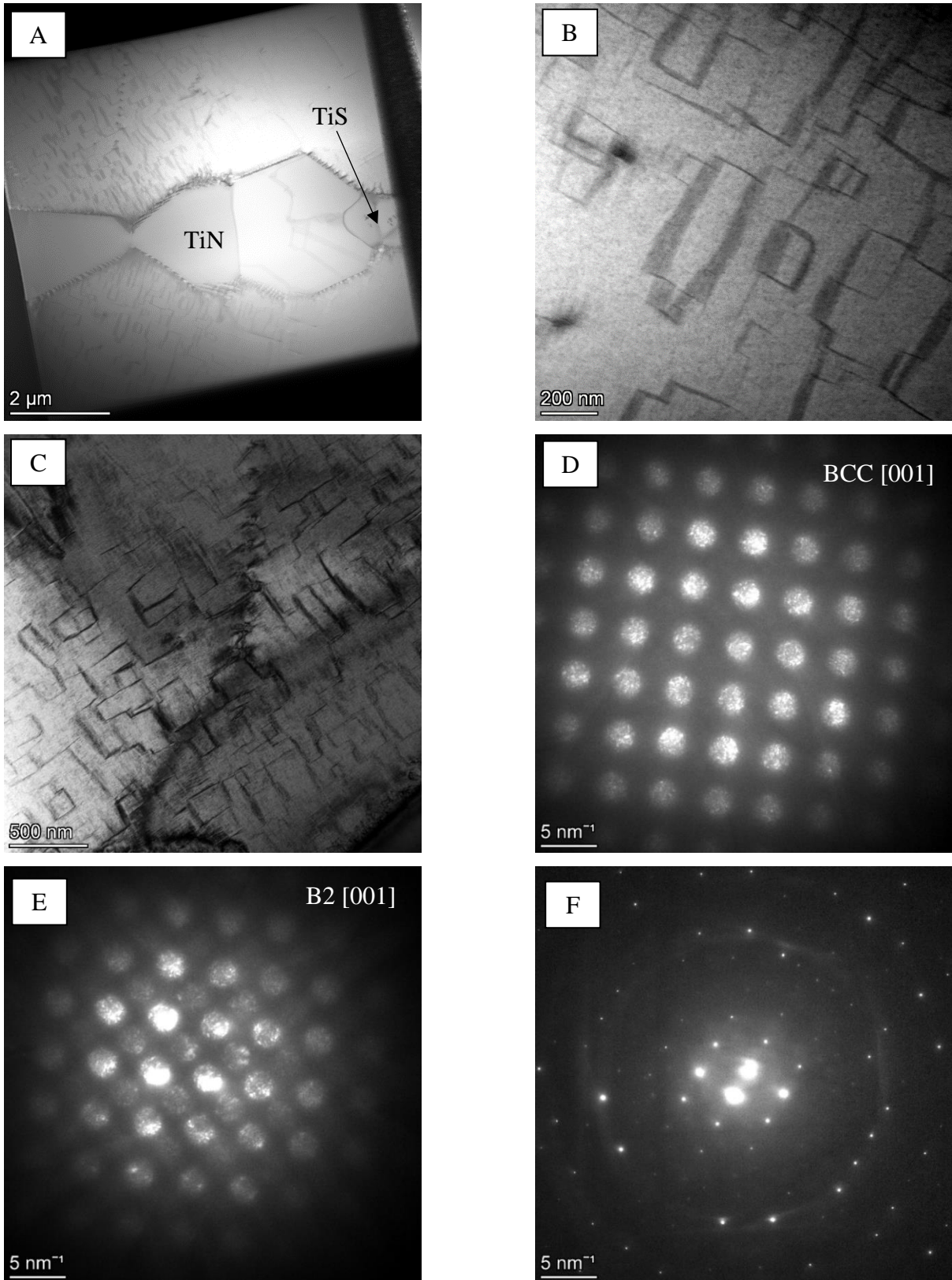


Figure 6.10. A) Bright field (BF) image showing the investigated region of the water quenched sample containing a grain boundary, TiN particles and a sulfide, B, C) the intergranular region containing a BCC matrix alongside B2 plates, D) the diffraction pattern corresponding to the BCC phase, E) the diffraction pattern corresponding to the B2 phase, F) the diffraction pattern corresponding to the sulphide.

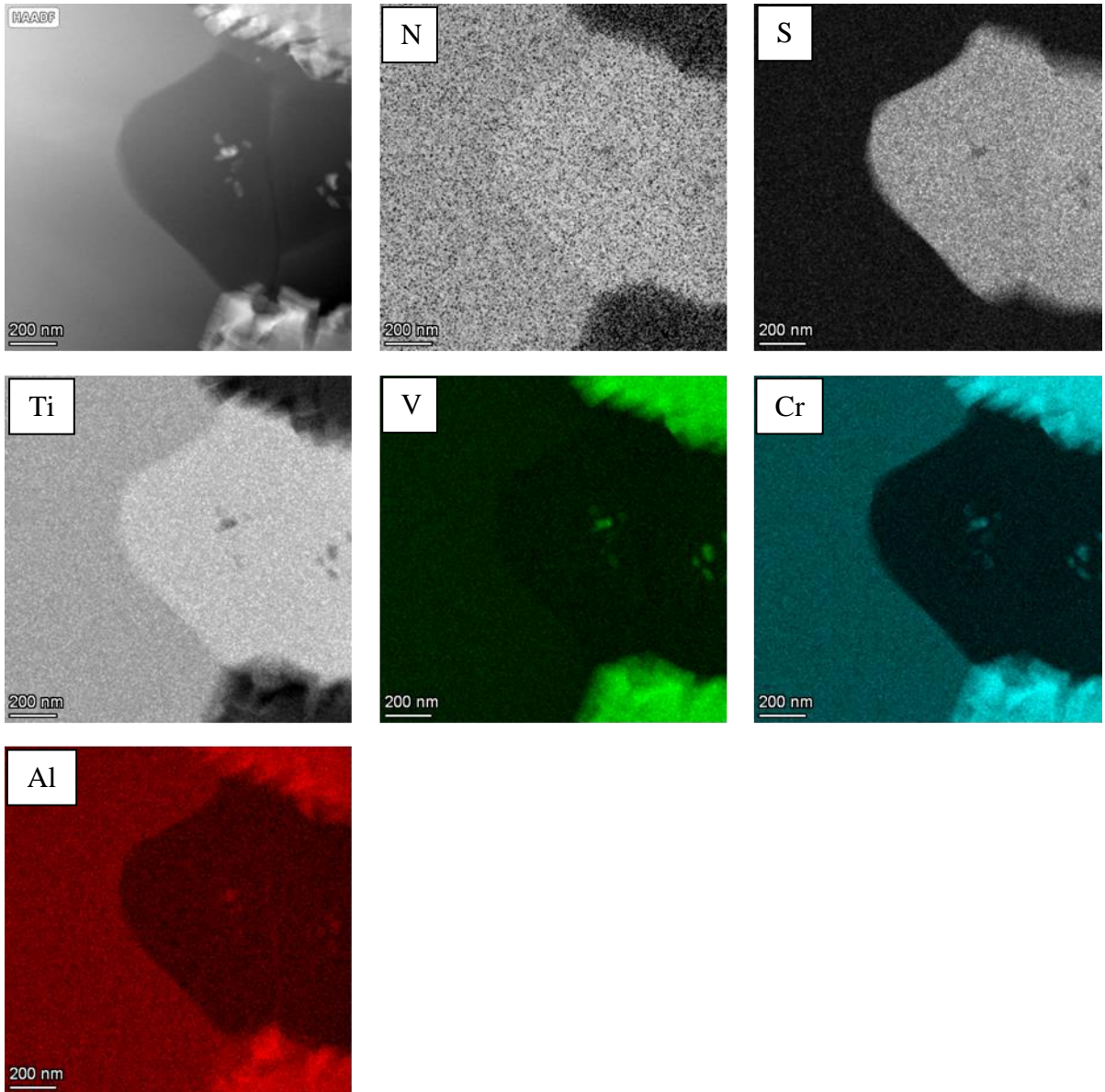


Figure 6.11 EDX quant map scans showing the distribution of Al, Ti, V and Cr within the region of interest. Cr and V are preferentially distributed within the B2 plates while Ti is encountered mostly within the BCC matrix (image has been enhanced to highlight the differences between the areas of distribution of V-Cr and Al-Ti).

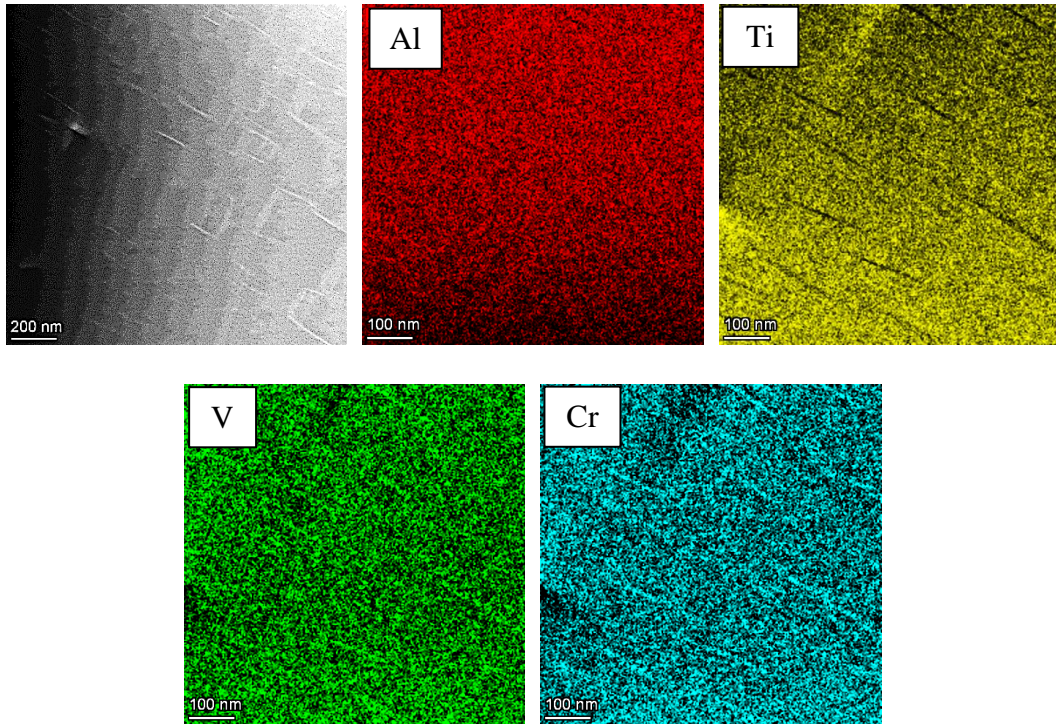


Figure 6.12. EDX quant map scans showing the distribution of Al, Ti, V and Cr within the intragranular region. Cr and V are preferentially distributed within the B2 plates while Ti is encountered mostly within the BCC matrix (image has been enhanced to highlight the differences between the areas of distribution of V-Cr and Al-Ti).

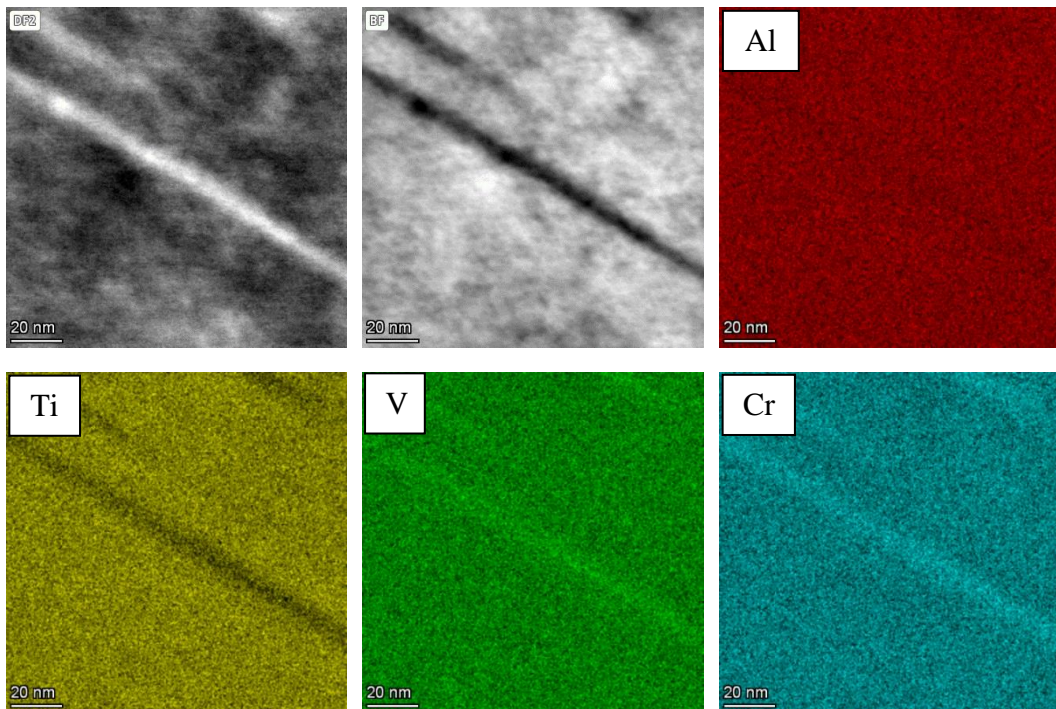


Figure 6.13. EDXS quant map scans showing the distribution of Al, Ti, V and Cr within the intragranular region. Cr and V are preferentially distributed within the B2 plates while Ti is encountered mostly within the BCC matrix (image has been enhanced to highlight the differences between the areas of distribution of V-Cr and Al-Ti).

6.3.2 Mechanical Properties

6.3.2.1 Vickers Hardness (HV) Testing

The hardness of the FC sample was measured at $590 \pm 12 \text{ HV}_{0.5}$ while the WQ sample at $529 \pm 19 \text{ HV}_{0.5}$ gives a difference of $61 \text{ HV}_{0.5}$ (~10%) between the two samples. While the hardness corresponding to the WQ condition agrees with the values found in the published literature concerning the equiatomic AlTiVCr alloy [97, 100, 105] the hardness of the FC sample deviates significantly. This is attributed to the fact that in the published literature the alloy was always investigated in the as cast condition which reflects a paraequilibrium state. Since the microstructure of the FC sample consists exclusively of a B2 phase while WQ contains both BCC and B2 there seems to be a correlation between the hardness of the alloy and its crystal structure. This can be further demonstrated by considering the volume fraction of the B2 phase in the WQ condition (Fig. 6.10C). It must be underlined that this is an assumption since it is still uncertain whether the plates correspond to the B2 or the BCC phase and the number of images used to extract the volume fraction is relatively low.

6.3.2.2 Elastic Properties

This phenomenon is not observed when assessing the elastic properties. More specifically, the Young's Modulus (E) of the FC condition was $204.6 \pm 3.3 \text{ GPa}$ and the WQ condition $196.7 \pm 4.0 \text{ GPa}$. In a similar manner to the previous section, the E of the BCC phase is estimated at 194.0 GPa . This shows that compared to the hardness, the difference in E between the BCC and B2 crystal structure of the present system is minimal, at only 10.6 GPa . These values slightly deviate from the ones that were experimentally measured in Chapter 4; however, these referred to a different set of samples investigated in the as cast and a heat treated condition followed by air cooling. Therefore, they should not be directly compared. This similarity between the BCC and B2 phase in terms of their elastic properties was predicted through DFT in Chapter 4.3.1.3 and is now confirmed. Nevertheless, the values predicted through CASTEP were in the region of 170 GPa which deviates from the experimental values by roughly 13% and 15% for the BCC and B2 phase respectively. On the contrary, in the work by Huang et al. [103] the EMTO-CPA DFT approach was used compared to conventional DFT to predict the elastic properties of various RHEAs and MCAs, among which was the equiatomic AlTiVCr alloy. In the part of their study concerning the AlTiVCr alloy, the B2 phase was predicted to have a modulus of roughly 225 GPa while the BCC phase at 185 GPa deviating by 10% and 5% respectively compared to the experimental values. This shows that although the EMTO-CPA method seems to be more accurate compared to conventional DFT in this particular case,

it also significantly overestimates the differences between the elastic properties of the two structures. Subsequently, it appears as if the two methods complement each other in terms of accuracy.

6.3.2.3 Compression Testing

The results of the compression testing are shown in Fig. 6.14. and Table 6.1. All tested samples lack any notable ductility regardless of the cooling method used in each case. Furthermore, there is significant deviation between the properties of the FC1 and FC2 samples. Therefore, the samples could have failed prematurely. This could be possible when considering the results presented in Chapter 5 concerning the evidence of low thermal conductivity in the AlTiVCr alloy. Cracks may have developed during the manufacturing or heat treatment process due to the temperature differentials forming along the sample. That is especially important in the case of water quenching where the surface of the sample is rapidly cooled with the internal regions still retaining an elevated temperature due to the low thermal conductivity of the material. In turn, as the cooler areas contract, significant strains develop between the internal and external regions of the sample which, upon exceeding a critical point, lead to the manifestation of cracks. In terms of the shape of the compression stress-strain curves it can be observed that in the case of the FC samples the uniform plastic deformation A_g coincides with the total elongation at fracture A_{50} . Contrasting that, the WQ samples display a difference between A_g and A_{50} hinting at a comparatively more ductile failure mechanism. It is thus possible that the inherent ductility of the material may have improved in the WQ condition due to the partial inhibition of the order-disorder transformation. However, due to the rapid cooling step associated with both the VAM and WQ process, cracks may have formed in the samples pre-testing, resulting in the compromise of the structural integrity of the material. Naturally, this would translate into severely reduced ductility upon testing.

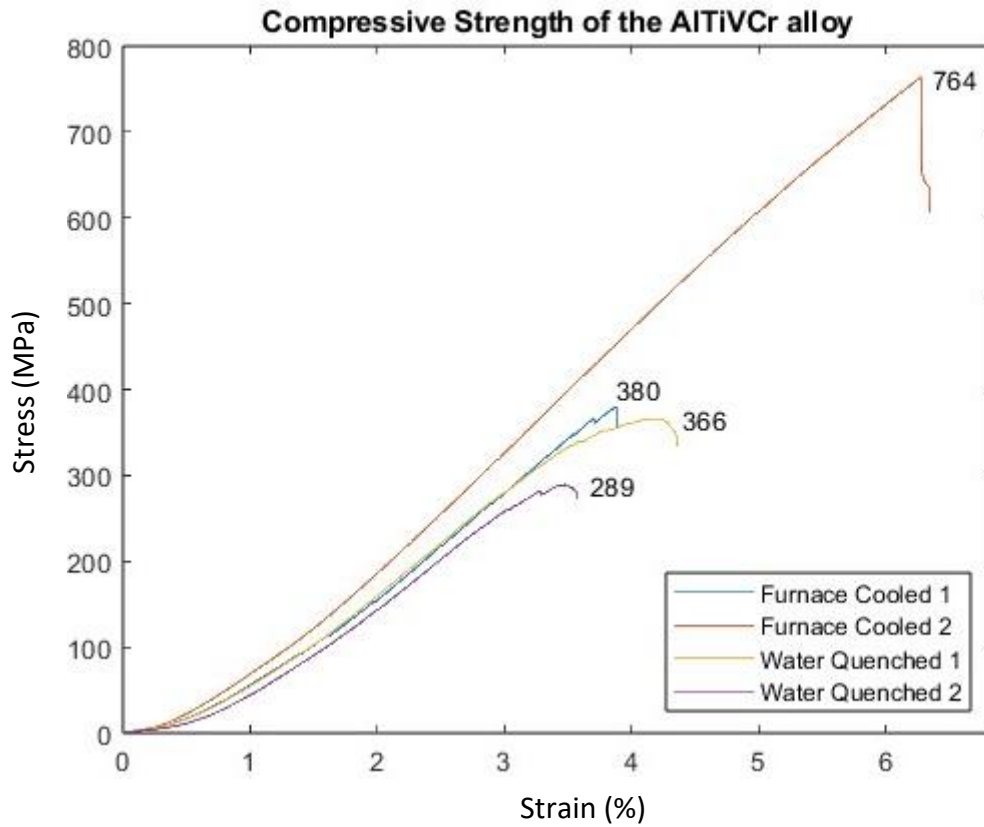


Figure 6.14 Compressive strength (MPa) to elongation (%) diagram of the AlTiVCr alloy in the furnace cooled (FC) (2 samples) and water quenched (WQ) (2 samples) condition during testing under ambient conditions.

Table 6.1 Mechanical properties of the AlTiVCr alloy as extracted through compression testing where σ_m corresponds to the maximum compressive strength, σ_f to the compressive strength at failure, A_g the uniform plastic deformation and A_{50} the total elongation at fracture.

Sample Name	σ_m (MPa)	A_g (%)	σ_f (MPa)	A_{50} (%)
Furnace Cooled 1	380	3.9	353	3.9
Furnace Cooled 2	764	6.3	713	6.3
Water Quenched 1	366	4.1	332	4.4
Water Quenched 2	289	3.5	271	3.6

6.3.3 Oxygen Content Measurements (IGFA)

In terms of the oxygen content, while the surface of the heat treated samples were enriched in O_2 , the interior remained largely unaffected. High levels of oxygen may have a negative impact on the ductility of the alloy, and as such had to be ruled out. Values between 105-125 ppm would be considered acceptable given that in other MCA systems that were manufactured through VAM the oxygen levels typically lie between 100 – 1,000 ppm while even reaching values above 10,000 ppm in certain cases [167, 253-258]. Even when assessing the surface layer of the AlTiVCr sample, which undergoes significant oxidation during the heat treatment process, the oxygen content did not exceed 600 ppm. Therefore, this level of oxygen accumulation should not affect the ductility of the alloy, while also having minimal impact on phase stability.

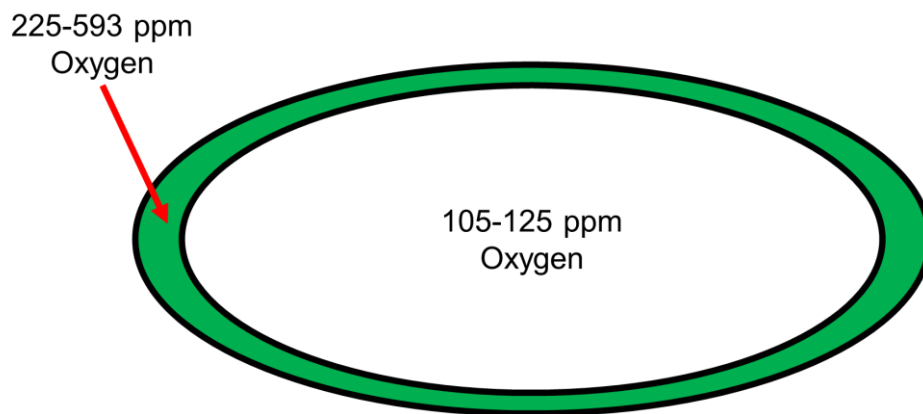


Figure 6.15 Diagram illustrating the mean distribution of Oxygen in the AlTiVCr alloy in the as cast and heat treated condition.

6.4 Conclusions

This research enabled the identification of a pathway towards the successful suppression of the BCC-B2 transformation in AlTiVCr-based MCAs. This is an important step towards achieving ductile behaviour in the present system. It has been established that the manufacturing route may be the culprit behind the reduced ductility. However, redesigning the manufacturing process using milder techniques in terms of heating and cooling cycles was not feasible at the time. Consequently, it was decided to proceed by optimising the microstructure instead of the manufacturing process. This would require to further stabilise the BCC in favour of the B2 by manipulating the ratios of the alloying elements. It was demonstrated that Cr-V preferably migrate into a different phase than Ti or Al. Furthermore, the literature supports the concept that reducing the amount of Al may be key into destabilising the B2 phase. However, this must be done with great care as Cr could be a paramount alloying element for achieving an elevated Young's modulus in this alloying system as established in Chapter 4. The main findings of this Chapter are summarised in the following points:

1. The XRD techniques used are insufficient for differentiating between the BCC and B2 phase in the AlTiVCr system.
2. High temperature XRD requires the use of an inert atmosphere when working with the present alloying system to prevent oxidation.
3. The FC equiatomic AlTiVCr alloy contained a single B2 phase, alongside some impurities even after furnace cooling for several hours from 1200°C down to room temperature.
4. Heat treatment at 1200°C for 8h is sufficient to fully erase segregation phenomena down to TEM resolution in the equiatomic AlTiVCr system.
5. Water quenching from 1200°C down to room temperature is sufficient to partially inhibit the order-disorder transformation and retain the metastable BCC high temperature phase at room temperature.
6. In the case of the WQ sample the preferential migration of Cr-V and Ti in different phases is observed, while Al does not exhibit such tendencies.
7. While the hardness of the AlTiVCr alloy was dependent on the cooling rate, the Young's modulus remained largely unaffected. Therefore, the hardness of the B2 phase is notably higher than that of the BCC phase while the Young's modulus is similar between the phases with that of B2 being slightly higher.

- 8.** Although our DFT method shown in Chapter 4 was able to capture the similarity between the Young's modulus of the BCC and B2 phase it underestimated the relevant values by 13% and 15% respectively. Comparatively, the EMTO-CPA method used in the literature predicted the Young's modulus of both phases with greater accuracy but completely overestimated the difference in modulus between the BCC and B2 phase. Therefore, it would seem that both methods are complementary.
- 9.** The ductility of the AlTiVCr alloy was unaffected by the partial stabilisation of the BCC phase through WQ. Nevertheless, it is possible that the reason behind the limited ductility of the alloy lies in the processing route and not in its microstructural constituents due to its low thermal conductivity.
- 10.** The amount of solute oxygen in the AlTiVCr alloy is insufficient to affect the ductility to a notable extent.

7. Design of Novel Single phase BCC AlTiVCr-based alloys through ICME

This Chapter concerns the design of a novel series of AlTiVCr-based alloys aimed at suppressing the order-disorder (BCC-B2) phase transformation. Aspects of this work were carried out in the Department of Innovation and Sustainability of Volkswagen Group Research in Wolfsburg, Germany within the frame of a placement by the author. FIB sample preparation was carried out at the University of Warwick while the TEM investigation was performed by Dr. John Nutter of the University of Sheffield.

7.1 Aim

As shown in chapter 6 it is possible to partially suppress the order-disorder transformation in the equiatomic AlTiVCr alloy by heat treating at 1200°C for 8h followed by water quenching. Nevertheless, no measurable ductility improvements were evident between the water quenched (WQ) and furnace cooled (FC) condition of the AlTiVCr alloy, consisting of a dualphase BCC-B2 and single phase B2 microstructure respectively. This was partially attributed to the processing route utilised for the manufacture and heat treatment of the samples combined with their low thermal conductivity as reported in chapter 5. As seen in the work of Soni et al. [82] Hot Isostatic Pressing (HIP) was carried out between the VAM and heat treating process to consolidate their alloy. Then, they assessed the ductility of the alloy heat treated at 1400°C for 24h followed by WQ compared to its FC counterpart and identified a single phase BCC and a dualphase BCC-B2 microstructure in the two samples respectively. It was found that the single phase BCC alloy was characterised by extensive ductility compared to the dualphase BCC-B2. Therefore, it is highly probable that achieving a single phase BCC microstructure in the AlTiVCr system should yield considerable increases in ductility. As such, this Chapter combines all the findings and techniques encountered in Chapters 4-6 to design a novel single phase BCC AlTiVCr-based alloy. To do this, thermodynamic simulations with ThermoCalc were carried out alongside DFT calculations to survey the compositional boundaries where the alloy would be single phase and most likely to retain the high temperature BCC phase after WQ. This search was supplemented through the use of pyMPEA to assess the candidate alloys in terms of the empirical properties dictating solid solution formation, according to section 3.1.4. The findings of the computational work aided the design of a novel AlTiVCr-based alloy where the order-disorder transformation was fully suppressed after the WQ process.

7.2 Computational and Experimental Methods

Before proceeding with the computational and experimental methodologies concerning this chapter it is important to establish how the investigated compositions were arrived at. While this work was tailored to design a composition where the order-disorder transformation could be fully suppressed, an overall assessment of the thermodynamic properties of AlTiVCr-based alloys would provide additional insight. As such, three distinct alloy design methodologies were established based on the findings of preliminary work through pyMPEALab, CALPHAD and DFT. The first design pathway was aimed at assessing the effect that Al exclusively would have on the stability of the B2 and consisted of alloys where the Al content was reduced to levels where according to CALPHAD a partial or complete suppression of the order-disorder transformation could be achieved. The second case concerned the simultaneous increase or reduction in both Al and Ti to evaluate whether intermetallic phases would manifest for higher Al and Ti contents and whether the simultaneous reduction of the two would have the same effect as solely reducing Al. The final case focused on the exclusive increase of the Ti content in accordance with the work of Huang et al. {Huang, 2022 #2} to also evaluate the phase stability of these systems and identify the compositional boundaries where the transition from a single phase to a multi-phase material would be observed. Therefore, the following alloy series were created, $\text{Al}_x(\text{TiVCr})_{100-x}$, $(\text{AlTi})_x(\text{VCr})_{100-x}$, $\text{Al}_{26}\text{Ti}_x(\text{VCr})_{74-x}$. The exact chemical composition of the alloys that would end up being manufactured would be arrived at in accordance with the computational predictions, the available literature and the empirical knowledge gained during the work shown in the previous chapters.

7.2.1 Computational Methods

7.2.1.1 pyMPEALab Toolkit

All of the candidate compositions were assessed in terms of their Atomic Size Difference (δ), Enthalpy of Mixing (ΔH_{mix}), Entropy of Mixing (ΔS_{mix}), Omega parameter (Ω), Electronegativity difference ($\Delta\chi$) and Valence Electron Concentration (VEC) using the pyMPEALab Toolkit. The findings were correlated with the Thermodynamic and DFT calculations but should be considered supplementary.

7.2.1.2 Thermodynamic Simulations – Thermo-Calc Software

The Thermodynamic calculations were carried out using the commercial software Thermo-Calc (TC) 2 version 2022a using the TCHEA2 and TCHEA5: TCS High Entropy Alloys databases [225]. For simplicity, each alloy is denoted according to Table 7.1 on the phase diagrams.

Table 7.1 Code name of the investigated alloys as displayed on the relevant phase diagrams.

Code Name	Alloy Name
C1	Al ₁₄ Ti ₂₀ VCr
C2	Al ₁₄ Ti ₂₆ VCr
C3	Al ₇ Ti ₇ VCr
C4	Al ₁₀ Ti ₁₀ VCr
C5	Al ₁₇ Ti ₁₇ VCr
C6	Al ₂₀ Ti ₂₀ VCr
C7	Al ₆ TiVCr
C8	Al ₉ TiVCr

7.2.1.3 Density Functional Theory Calculations – CASTEP

For the DFT study it was assumed that all of the tested compositions would constitute single phase BCC or B2 alloys. This was done to assess these solid solutions in terms of their stability from both an energetic and mechanical standpoint. The DFT calculations with CASTEP used $3 \times 3 \times 3$ Body Centred Cubic (BCC) supercell containing a total of 54 atoms for the calculations regarding all of the investigated compositions and a repeat of the original equiatomic AlTiVCr alloy. Due to the constraints of the 54 atom supercell, the AlTiVCr supercell contained 14 Al, 14 Ti, 13 Cr and 13 V atoms. The naming convention of the investigated alloys is directly related to the quantity of each atom type in each supercell. For

example, the Al_6TiVCr alloy contained 6 Al, 14 Ti, 14 V and 14 Cr atoms while the $\text{Al}_{14}\text{Ti}_{26}\text{VCr}$ contained 14 Al, 26 Ti, 7 V and 7 Cr atoms. Ten different AlTiVCr supercells, each with a unique random arrangement of the atoms on the lattice sites were created for each composition and tested in relation to their total energy to ensure that an energetic equivalency is evident between all configurations. At this point the energetic stability of each alloy was assessed using the methodology described in section 3.1.2.4. From these configurations, three were randomly selected for the subsequent elastic property calculations. To achieve good precision in the geometry optimisation routine, a 650 eV cutoff energy was selected for the AlTiVCr-based supercells along with a k-point Monkhorst-Pack grid spacing of 0.02 [8]. This is equivalent to a k-point grid of $6 \times 6 \times 6$. A finite basis correction of 5 eV over three steps was also applied during the initial geometry optimisation step. Full geometry optimisations were performed where the atoms could relax to their lowest energy state with variation of the lattice parameters and ionic movement while the centre of mass was constrained. The initial energy, force, stress, and displacement tolerances were specified at 5×10^{-5} eV, 2×10^{-1} eV/Å, 3.5×10^{-1} GPa and 5×10^{-3} Å respectively. Once the geometrically optimised structures were generated, a set of deformations was applied as described in section 3.1.2.3 and performed a secondary geometry optimisation using the same convergence criteria with a constrained cell size while permitting ionic movement. The elastic constants for each single crystal were extracted through fitting the stress tensor calculated through CASTEP to the strain applied from the deformation patterns. Lastly, the polycrystalline (isotropic) elastic properties of each phase were calculated according to the guidelines provided in section 3.1.3 using the Voigt-Reuss-Hill (VRH) approximation.

7.2.2 Experimental Methods

7.2.2.1 Materials and Processing

The raw materials Al, Cr, Ti, V, used to manufacture the alloy, were sourced in wire, sheet, and bulk form with purities >99.8%. Experimental samples were formed using an Arcast Arc 200 Vacuum Arc Melter (VAM) under a high purity Ar gas atmosphere and were remelted 4-5 times along with electromagnetic stirring to ensure chemical homogeneity. The samples were allowed to cool down for a brief period (~1 min) between remelts and were afterwards flipped and reheated immediately. The samples were sectioned in half using a Secotom-50 microtome with Al₂O₃ 6” cutting disks. The nominal compositions of the tested alloys can be seen in Table 7.2.

Table 7.2 Nominal compositions of the novel AlTiVCr-based alloy series.

Alloy Name	Al at. %	Ti at. %	V at. %	Cr at. %
Al ₆ TiVCr	11.1	29.6	29.6	29.6
Al ₉ TiVCr	16.7	27.8	27.8	27.8
Al ₇ Ti ₇ VCr	13	13	37	37
Al ₁₀ Ti ₁₀ VCr	18.5	18.5	31.5	31.5
Al ₁₇ Ti ₁₇ VCr	31.5	31.5	18.5	18.5
Al ₂₀ Ti ₂₀ VCr	37	37	13	13
Al ₁₄ Ti ₂₀ VCr	26	37	13	13
Al ₁₄ Ti ₂₆ VCr	26	48	13	13

This batch of samples consisted of (2) ingot halves from each composition. They were subjected to a heat treatment, carried out in a laboratory electric furnace under a flowing Ar atmosphere along with Ti pieces to ensure minimal oxidation at 1200°C for 8h. One sample per composition was then furnace cooled (FC) down to room temperature over 4h while the other was water quenched (WQ) down to room temperature. The samples were mounted in conductive bakelite and were ground using P120, P280, P600, P1000, P1200, P2500 and P4000 SiC grinding papers in succession. They were then polished using a 1 μm diamond suspension and Struers OP-U colloidal silica solution for 10 and 20 minutes respectively for relief polishing.

7.2.2.2 Optical (OM), Scanning Electron (SEM) Microscopy & Electron Dispersive X-ray Spectroscopy (EDX)

The microstructures of the samples were investigated using a Nikon Eclipse LV150 and an Optical Microscope (OM) under polarised light, using the analyser and darkfield filters alongside depth-of-field observation. Further microstructural investigation was carried out using an Inspect F50 high-resolution Field Emission Scanning Electron Microscope (SEM) and a ThermoFisher Scientific Scios 2 ultra-high-resolution analytical DualBeam SEM with Secondary (SE) and Backscatter Electrons (BSE) under 20 kV accelerated voltage, in conjunction with Energy-Dispersive X-Ray Spectroscopy Analysis (EDS) to evaluate possible segregation phenomena and perform phase analysis and characterisation.

7.2.2.3 Focused Ion Beam (FIB) SEM and Transmission Electron Microscopy (TEM)

The four Al₆TiVCr (WQ, FC) and Al₉TiVCr (WQ, FC) samples were sent to the University of Warwick to be prepared for TEM analysis using Focused Ion Beam (FIB) milling with a ThermoFisher Scientific Scios DualBeam. The selected section surface area was $5 \times 5 \mu\text{m}^2$ and consisted of a grain boundary between two grains. In certain cases, particles were visible along the grain boundaries. The selected area was coated by a Pt layer to protect the area from damage. The surrounding area was bombarded by a beam of Ga ions, milling through the surface. The area of interest was then attached to a tungsten rod using the deposited Pt and was subsequently cut free from the surface. The extracted section was then attached to a carbon coated copper TEM grid and thinned down using the Ga ion beam. STEM was subsequently carried out in the University of Manchester with a JEOL JEM-F200 X-FEG S/TEM, operating at 200 kV. The chemical composition of the alloy and the phases evident in the microstructure were determined using energy dispersive spectroscopy (EDX) and by extracting the diffraction patterns in each case.

7.2.2.3 X-ray Diffraction Analysis

The diffraction patterns of the tested bulk samples were extracted under ambient conditions using an X'Pert³ Powder diffractometer. The samples subjected to testing under non-ambient conditions were also tested using the same settings. The diffractometer utilised N K- β filtered Cu K α radiation operating at 45 kV and 40 mA. The Programmable Divergence Slit (PDS) was set to 0.25° while the Anti-Scatter slit at 0.5° . The scanning angle range was set from 20° to $100^\circ 2\theta$ with a step size of 0.02° .

7.2.2.4 Vickers Hardness (HV) Testing

Hardness testing was carried out using the Vickers method as described in chapter 3.2.9 on all samples. The indentation grid was a 4×3 grid with a $2000 \mu\text{m}$ spacing for both samples using a load of 0.5 kg with a dwell time of 20 s on a Leco AMH 43.

7.2.2.5 Nanoindentation Testing

For the evaluation of the effect of the cooling rate on the elastic properties of the alloy, the nanoindentation testing technique was employed using a MicroMaterials Nanotest Vantage nanoindenter. Standard Berkovich tips were used with a load function consisting of 30 s load, 60 s dwell and 30 s unload respectively. The tests were load controlled and were limited to a maximum load of 300 mN. Thermal drift data was also collected post indentation. The indentation grid was a 5×5 grid with a $100 \mu\text{m}$ spacing for both samples. An extensive description of the methodology regarding the Young's modulus derivation is presented in Chapter 3.2.10.

7.2.2.6 Compression Testing

Compression testing was performed using an Instron 68FM-100 under ambient condition with a strain rate of 0.15 mm/min using 2 cylindrical samples for each sample with a diameter of 6 mm and a height of 9 mm according to the ASTM E9-09 standard. It should be noted that an extensometer was not used during the experiments. Also, some additional clarifications concerning the compression testing must be provided. According to the TEM findings of Chapter 6 it was seen that Cr and V would migrate towards the plate-like phase assumed to be the B2. It was thus considered that by reducing the amount of both alloying additions it would perhaps be possible to suppress the formation of the B2 phase. This is counterintuitive compared to the findings of the literature where the amount of Al had been found to be responsible for the stabilisation of the B2 phase [82, 83, 101, 105]. Nevertheless, reducing the amount of Al was expected to have a detrimental effect to the density and subsequently specific mechanical properties of the alloys. As such, it was determined that the high Al-Ti-containing spectrum of compositions would be manufactured and assessed before the low Al-Ti-containing ones. Therefore, the alloys used for the initial compression testing were the $\text{Al}_{17}\text{Ti}_{17}\text{VCr}$, $\text{Al}_{20}\text{Ti}_{20}\text{VCr}$ and $\text{Al}_{14}\text{Ti}_{20}$, which were also confirmed to consist of a single phase microstructure in at least the WQ condition. On a side note, compression testing of the rest of the low Al-Ti compositions has been planned but due to time constraints, the experiments will not be encapsulated within the frame of this work.

7.2.2.7 Thermal Conductivity Measurements

The thermal conductivity measurements were performed using a Hot Disk TPS 2500S with the 7577 sensor with a radius of 2 mm according to EN ISO 22007-1 and 22007-2 at an ambient temperature of 21°C. The parameters used for the measurements were a power of 50 mW, holding time of 20 s, a resistivity of 1.55 Ohm and a probing depth of 1.8 – 4 mm, resulting in a temperature increase of 3-5°C. The standard analysis method in the single sided modus assuming perfect insulation was used for the evaluation of the thermal conductivities. The associated results are the arithmetic average of the sensor on the top and bottom of the polished sample surfaces. Data sets from point 20 = 1 s to 200 = 20 s were used for evaluation points.

7.3 Results and Discussion

7.3.1 Computational Predictions

7.3.1.1 pyMPEALab Toolkit

As seen in Table 7.3 all of the alloys were characterised by a similar degree of atomic size difference (δ) and nearly identical electronegativities ($\Delta\chi$) with both values satisfying the criteria for solid solution formation in MCAs [259]. The same also applies to the entropy of mixing (ΔS_{mix}) at room temperature, which is expected given that all alloys were comprised of four primary alloying elements. Nevertheless, the enthalpy of mixing differs (ΔH_{mix}) significantly between the compositions; but remain negative in all cases. The two most crucial parameters for solid solution (SS) formation would be the omega (Ω) parameter and the valence electron concentration (VEC), dictating the likelihood of SS formation and the respective crystallographic properties. A VEC < 6.8 shows that all alloys would be comprised by a BCC (or B2) matrix phase while an $\Omega < 1$ indicates that a single phase SS formation is unlikely and that the alloy will probably be comprised of multiple phases. Therefore, it was expected that the $\text{Al}_{17}\text{Ti}_{17}\text{VCr}$, $\text{Al}_{20}\text{Ti}_{20}\text{VCr}$ and $\text{Al}_{14}\text{Ti}_{26}\text{VCr}$ alloys would be multiphase while the $\text{Al}_{14}\text{Ti}_{20}\text{VCr}$ would possibly form a SS, although rather unlikely.

Table 7.3 Assessment of the empirical parameters pertaining to each novel AlTiVCr-based composition through pyMPEALab, namely the atomic size difference (δ), enthalpy of mixing (ΔH_{mix}), entropy of mixing (ΔS_{mix}) at room temperature, omega (Ω) parameter, electronegativity ($\Delta\chi$) and valence electron concentration (VEC).

Alloy Name	δ (%)	ΔH_{mix} (kJ/mol)	ΔS_{mix} (kJ/mol)	Ω	$\Delta\chi$	VEC
Al_6TiVCr	6.52	-11.32	11.02	1.9	0.05	4.78
Al_9TiVCr	6.45	-13.86	11.36	1.55	0.05	4.67
$\text{Al}_7\text{Ti}_7\text{VCr}$	5.88	-9.89	10.53	2.09	0.04	4.98
$\text{Al}_{10}\text{Ti}_{10}\text{VCr}$	6.26	-13.12	11.24	1.62	0.04	4.76
AlTiVCr	6.3	-16.82	11.53	1.23	0.04	4.5
$\text{Al}_{17}\text{Ti}_{17}\text{VCr}$	5.96	-20.41	11.24	0.94	0.04	4.24
$\text{Al}_{20}\text{Ti}_{20}\text{VCr}$	5.35	-23.36	10.53	0.73	0.04	4.02
$\text{Al}_{14}\text{Ti}_{20}\text{VCr}$	6.04	-19.37	11.16	1.01	0.05	4.3
$\text{Al}_{14}\text{Ti}_{26}\text{VCr}$	5.46	-20.96	10.25	0.85	0.05	4.13

7.3.1.2 Thermodynamic Modelling

The thermodynamic modelling results with ThermoCalc (Fig. 7.1-7.6) showed that IM formation was expected in all of the tested compositions with the potential exception of C3 assuming that the alloy would reach equilibrium by the end of the FC process. Nevertheless, significant differences were observed between the predictions of TCHEA2 and TCHEA5. Before any direct comparisons are drawn it would be advisable to refer to the previous findings of this work and the available literature regarding the microstructural characteristics of the equiatomic AlTiVCr alloy and novel AlTiVCr-based systems. In Chapter 6 it was established that the equiatomic AlTiVCr alloy would consist of a single phase B2 structure even after FC over several hours from the heat treatment temperature. Therefore, unless the kinetics of SPPs are so slow that the alloy is not approaching equilibrium even after this slow cool, TC predictions suggesting that the AlTiVCr alloy would decompose into multiple AlTi-based or Laves phases at lower temperatures are unlikely to be true. Furthermore, experimental Differential Scanning Calorimetry (DSC) measurements have shown that the order-disorder transformation is unlikely to be taking place at temperatures below 900°C [105]. Computational calculations have indicated that perhaps the order-disorder transformation could occur at lower temperatures between 600-700°C [97]. However, this has not been proved experimentally.

Regarding the alloys C1 ($\text{Al}_{14}\text{Ti}_{20}\text{VCr}$) and C2 ($\text{Al}_{14}\text{Ti}_{26}\text{VCr}$), both the TCHEA2 (Fig. 7.1) and the TCHEA5 (Fig. 7.2) predicted multiphase microstructures, which was in line with the findings of the pyMPEALab toolkit. The presence of AlTi-based particles was expected, with the TCHEA5 also showing the formation of a Laves phase at equilibrium. It is interesting to note that the TCHEA5 also predicted the formation of a hexagonal close packed (HCP) phase between ~600-840°C for C2. Furthermore, there is a significant discrepancy on the order-disorder transformation temperature between the two databases with both predictions deviating from experimentally confirmed values, with TCHEA2 underestimating and TCHEA5 overestimating. Since this trend was prominent across this Chapter, it should be established that the TCHEA2 prediction on the order-disorder transformations aligned with the findings of previous computational work [97] and was thus deemed more reliable.

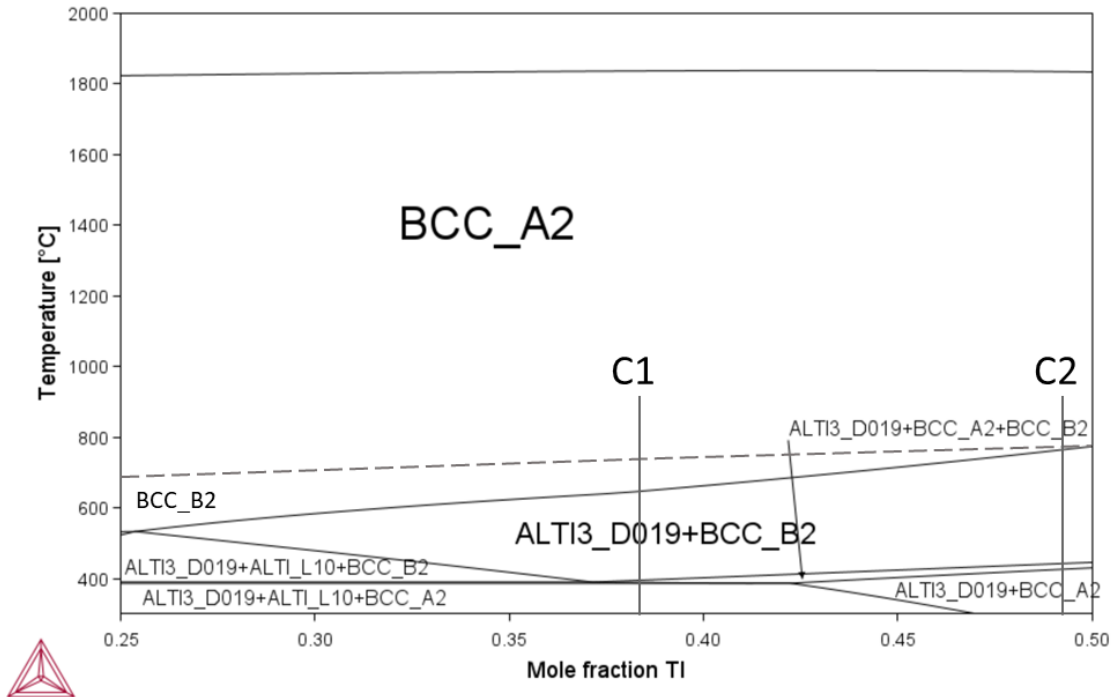


Figure 7.1 Calculated phase diagram of the AlTiVCr system using the Thermo-Calc software alongside the TCHEA2: TCS High Entropy Alloys where Al=26 at. %, V=Cr and Ti=balance. Compositions of interest are denoted accordingly.

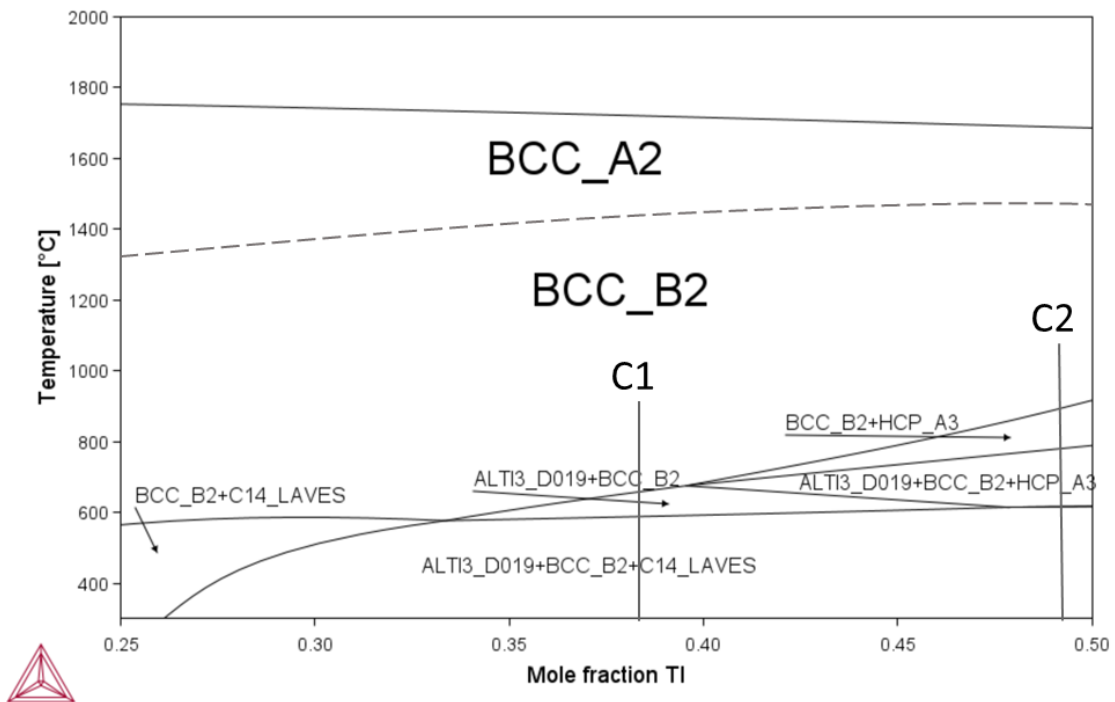


Figure 7.2 Calculated phase diagram of the AlTiVCr system using the Thermo-Calc software alongside the TCHEA5: TCS High Entropy Alloys where Al=26 at. %, V=Cr and Ti=balance. Compositions of interest are denoted accordingly.

In the case of the C3 (Al₇Ti₇VCr), C4 (Al₁₀Ti₁₀VCr), C5 (Al₁₇Ti₁₇VCr) and C6 (Al₂₀Ti₂₀VCr) alloys the presence of AlTi-based and other SPPs was expected once again; however, contradicting the findings of section 7.3.1.1 regarding alloys C3 and C4. Again, there is a

disagreement between TCHEA2 and TCHEA5 regarding the type of SPPs present, with TCHEA2 exclusively predicting AlTi-based SPPs while TCHEA5 predicts the formation of a Laves phase at equilibrium. TCHEA5 predicted the formation of an HCP phase at the higher end of the Al and Ti content spectrum. In the case of C6 specifically, the HCP phase is evident at the temperature range where the heat treatment would take place. Therefore, the HCP phase may be present in the WQ condition of C6. Naturally, this would require the formation of the HCP phase to ensue within the duration of the heat treatment. Nevertheless, both the TCHEA2 (Fig. 7.3) and TCHEA5 (Fig. 7.3) show a BCC + B2 region manifesting at the lower end of Al and Ti content. This is not an unexpected finding given that it has been suggested in the literature [239] that a higher Al content is generally the driving force behind B2 stabilisation. Notably, according to TCHEA2, the formation of SPPs may even be promoting the formation of a single BCC phase at equilibrium, according to the principles described in Chapter 5. Namely, AlTi-based SPPs withdraw Al from the originally B2 matrix phase resulting in its stabilisation and eventual transformation into BCC. Although this seems like an optimistic evaluation, certain conclusions can be drawn by correlating the findings of both databases. C3 and C4 may be expected to contain both BCC and B2, with the volume fraction of the B2 phase decreasing proportionally to the Al content. Furthermore, it could even be possible that C3 would be comprised by a single BCC phase at equilibrium.

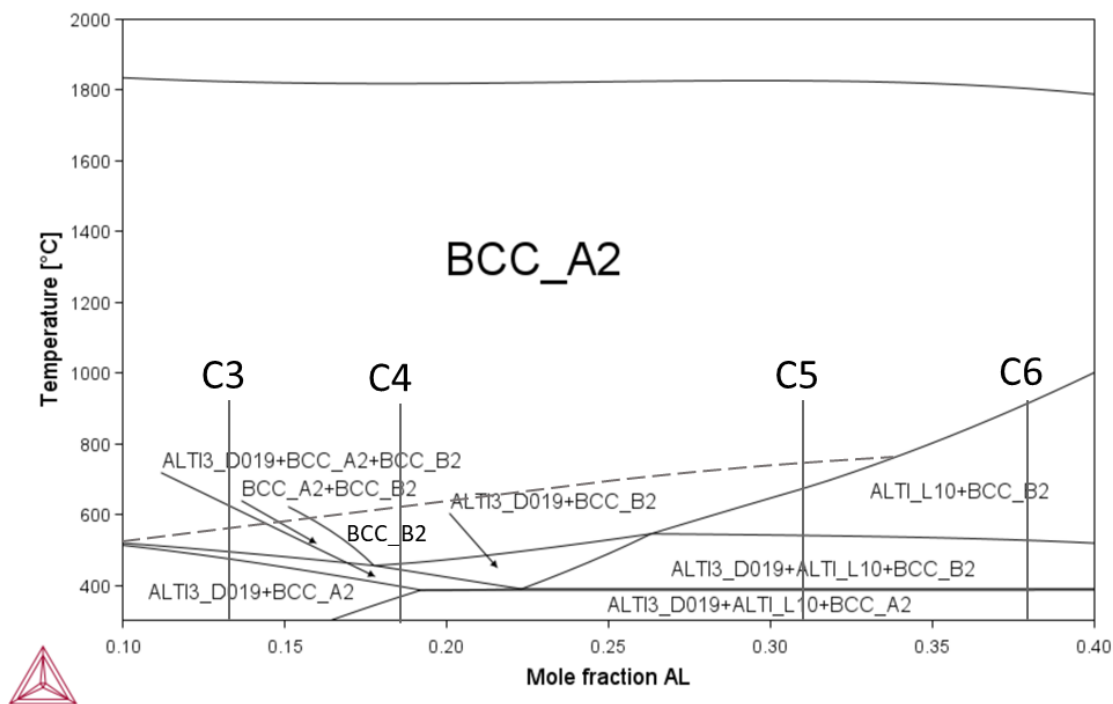


Figure 7.3 Calculated phase diagram of the AlTiVCr system using the Thermo-Calc software alongside the TCHEA2: TCS High Entropy Alloys where Al=Ti and V=Cr. Compositions of interest are denoted accordingly.

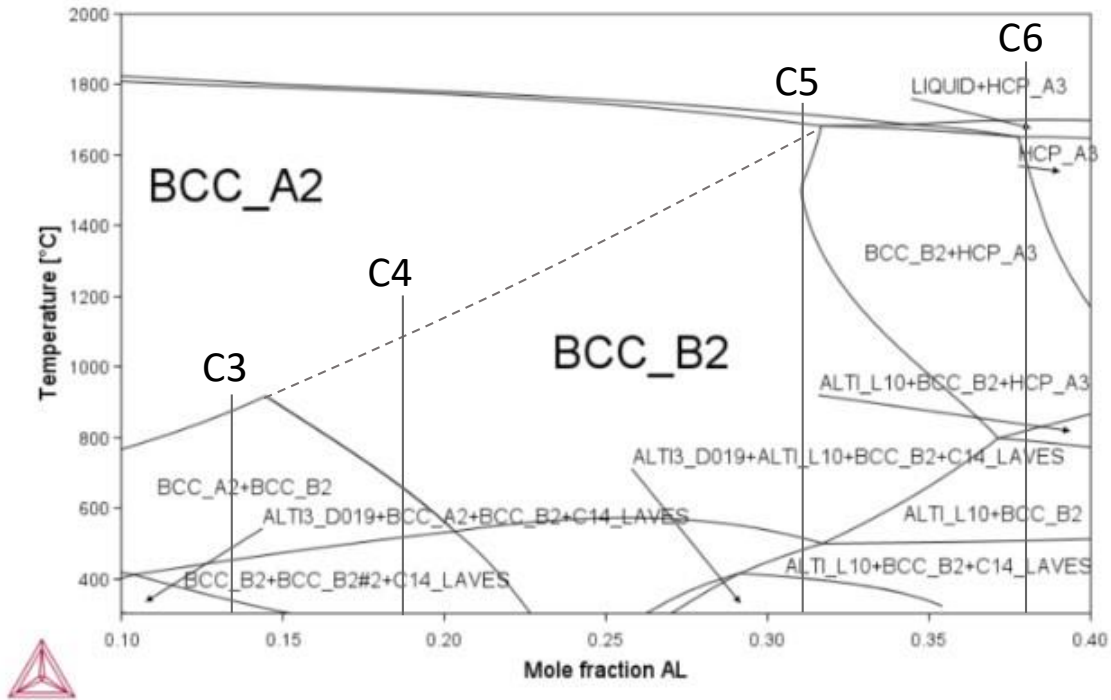


Figure 7.4 Calculated phase diagram of the AlTiVCr system using the Thermo-Calc software alongside the TCHEA5: TCS High Entropy Alloys where Al=Ti and V=Cr. Compositions of interest are denoted accordingly.

Lastly, in the case of the C7 (Al_6TiVCr) and C8 (Al_9TiVCr) alloys, the presence of a BCC + B2 region was also observed although notably more extensive than previously. It could thus be argued that controlling the Al instead of the Ti content would be more impactful towards the stabilisation of the BCC phase. Again, both TCHEA2 (Fig. 7.5) and TCHEA5 (Fig. 7.6) predicted the formation of AlTi-based SPPs while TCHEA5 also showed the formation of Laves phases, however at a relatively higher Al content than TCHEA2. An extensive BCC region was present in the case of TCHEA2. This was also predicted by TCHEA5 but for a comparatively lower Al content. Nevertheless, the composition of C7 coincides with the stable BCC equilibrium regions of both TCHEA2 and TCHEA5. As such, it was highly probable that C7 would be characterised by a BCC phase at equilibrium, or that at least it would be possible to fully retain the BCC by WQ after the heat treatment process given the favourable thermodynamics.

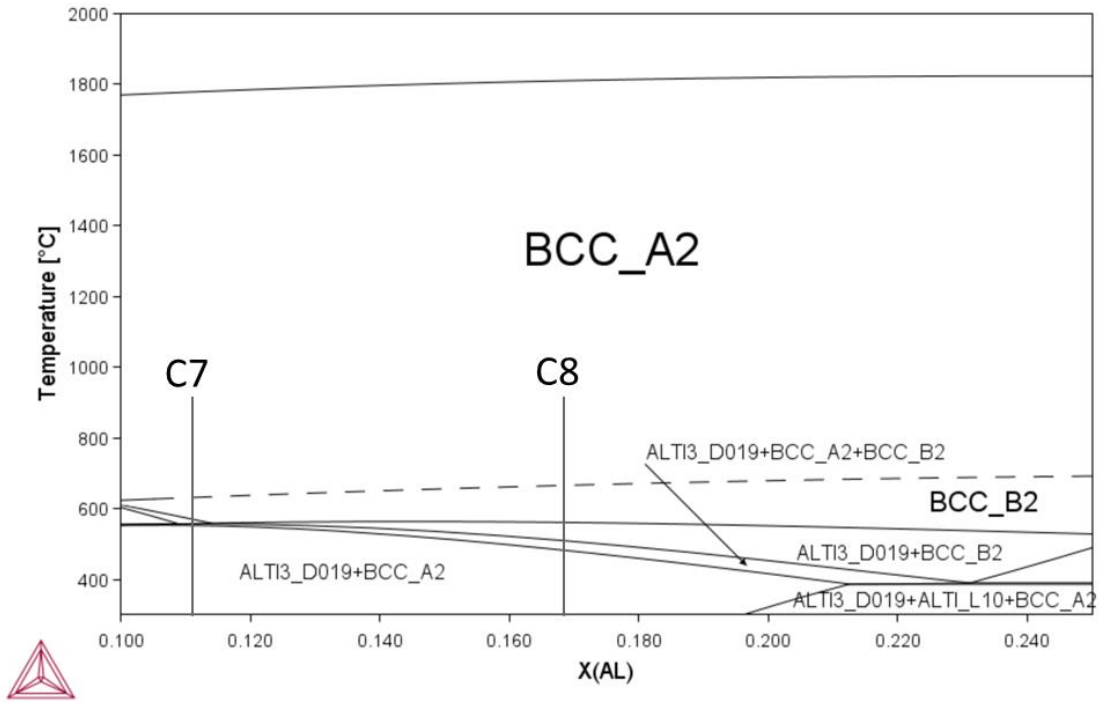


Figure 7.5 Calculated phase diagram of the AlTiVCr system using the Thermo-Calc software alongside the TCHEA2: TCS High Entropy Alloys where Ti=V=Cr and Al=balance. Compositions of interest are denoted accordingly.

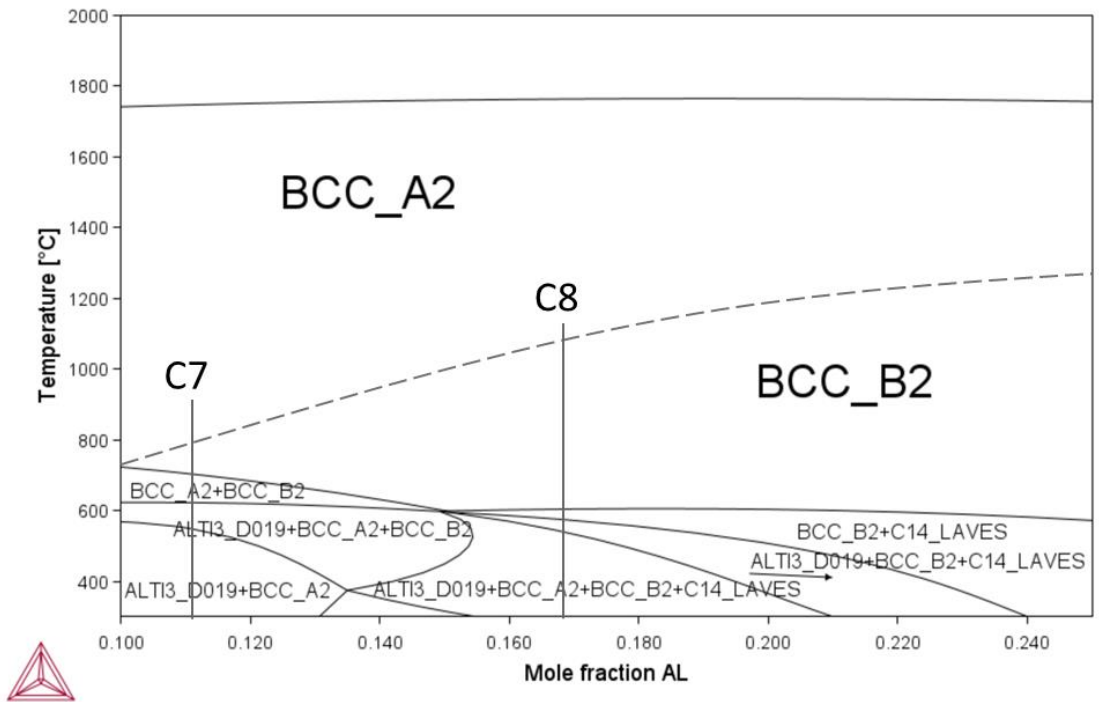


Figure 7.6 Calculated phase diagram of the AlTiVCr system using the Thermo-Calc software alongside the TCHEA5: TCS High Entropy Alloys where Ti=V=Cr and Al=balance. Compositions of interest are denoted accordingly.

7.3.1.3 Density Functional Theory Calculations – CASTEP

The DFT calculations with CASTEP showed similar trends to those explored in sections 7.3.1.1 and 7.3.1.2 (Fig. 7.7, Table 7.4). Single phase microstructures would not be favourable to form in the cases of the $\text{Al}_{16}\text{Ti}_{26}\text{VCr}$ and $\text{Al}_{20}\text{Ti}_{20}\text{VCr}$ alloys, while the $\text{Al}_{17}\text{Ti}_{17}\text{VCr}$, although predicted to be single phase, would be highly unstable. The same could also be applied to $\text{Al}_{16}\text{Ti}_{20}\text{VCr}$, although with a lesser degree of confidence. These findings are extremely well aligned with the predictions of the pyMPEALab toolkit, especially when correlating both predictive tools. It would therefore be possible to not only make predictions in terms of which alloys would be unstable but also to what degree they would be considered unstable by combining the two methods. Overall, the $\text{Al}_{10}\text{Ti}_{10}\text{VCr}$, $\text{Al}_7\text{Ti}_7\text{VCr}$, $\text{Al}_9\text{Ti}_9\text{VCr}$ and $\text{Al}_6\text{Ti}_6\text{VCr}$ alloys were considered extremely stable and would be expected to form single phase or perhaps BCC + B2 microstructures without the presence of SPPs.

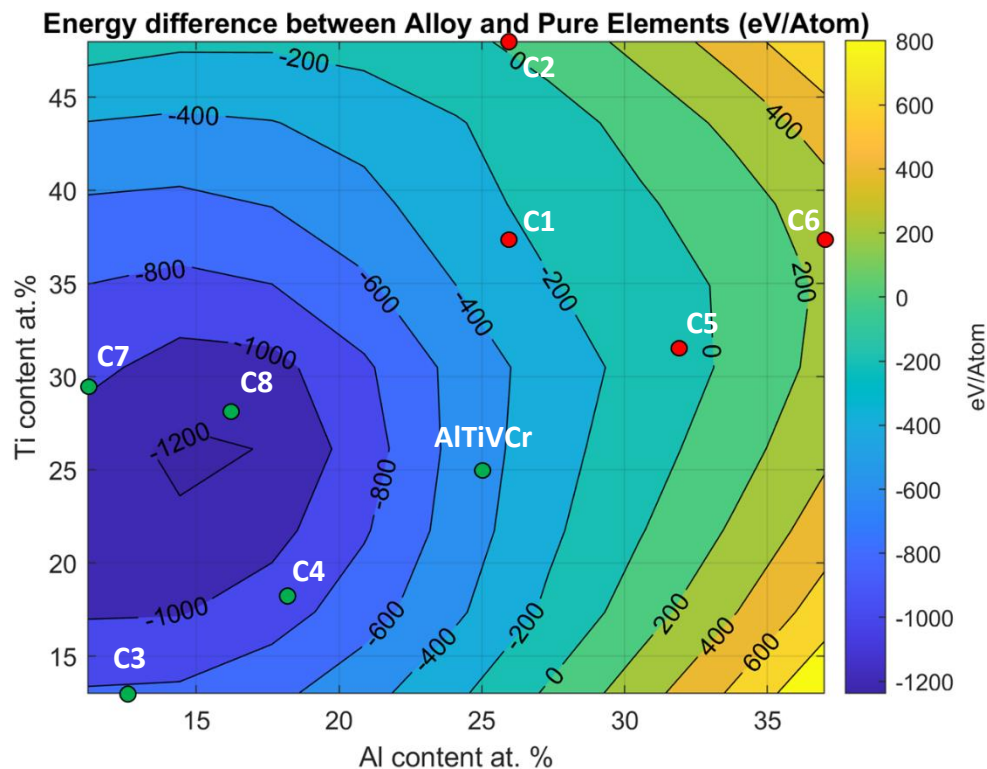


Figure 7.7 Contour plot illustrating the energy difference between the final energy of the alloys per atom against the sum of the energies of their constituting alloying elements depending in their Al (at. %) and Ti (at. %) content.

In terms of the lattice parameters of the novel compositions, DFT predicted a trend proportional to the Al and Ti content, where reduced amounts of both alloying additions would lead to a progressively lower lattice parameter. This has an adverse effect on density, which is not only affected by the atomic weight of each alloying element but also the overall unit cell volume. Therefore, compositions rich in Cr and V have a significantly higher density by comparison. Nevertheless, the predicted densities of the Al/Ti-rich compositions were made under the

assumption that these alloys would be single phase which, given the available information, was unlikely.

Table 7.4 Computationally derived lattice parameter, density, and difference between the final energy of the investigated alloys per atom against the sum of the energies of their constituting alloying elements.

Alloy Name	Lattice Parameter (Å)	Density (g/cm³)	Diff. (eV/atom)
Al₆TiVCr	3.038	5.65	-976.5
Al₉TiVCr	3.044	5.46	-783.9
Al₇Ti₇VCr	2.992	5.91	-1240.2
Al₁₀Ti₁₀VCr	3.017	5.59	-896.2
AlTiVCr	3.061	5.07	-437.5
Al₁₇Ti₁₇VCr	3.098	4.76	-93.5
Al₂₀Ti₂₀VCr	3.132	4.45	250.5
Al₁₄Ti₂₀VCr	3.106	4.87	-210.5
Al₁₄Ti₂₆VCr	3.147	4.62	16.4

A DFT study was also carried out regarding the elastic properties of the investigated compositions (Fig. 7.8). It would seem that lower Al and Ti content, and therefore higher Cr and V content, would lead to the manifestation of an elevated Young's modulus (E). This effect would be most prominent in cases where the Al and Ti content would be equally as low, even if the cumulative amount of Cr and V would be roughly the same. Such an example would be the comparison between the Al₁₀Ti₁₀VCr and the Al₉TiVCr alloy. Therefore, a high amount of Ti would be more detrimental than Al; although both additions should be restricted to lower contents to achieve an elevated E. This effect was maximised in the case of the Al₁₀Ti₁₀VCr alloy, while a progressive decrease was observed with a linear increase in both the Al and Ti content. Nevertheless, the Al₇Ti₇VCr alloy showed a dip in E compared to the Al₁₀Ti₁₀VCr. Therefore, it would seem that reducing both alloying additions below 18.5 at. % would be detrimental to the elastic properties. Lastly, a mild increase in E was observed in the case of the Al₁₄Ti₂₆VCr alloy. The specific E was also found to follow a similar trend, although slightly diminished due to the significantly higher densities of the Cr-V-rich compositions. In terms of the Bulk (B) and Shear (G) modulus as seen in Table 7.5, it could be seen that a higher G would dictate a higher E regardless of B. This notable influence of G on E was pointed earlier in Chapter 4. The elastic constants C₁₁, C₁₂ and C₄₄ can be seen in Table 7.6 as they were

calculated in each of the three iterations of each composition. Interestingly, it could be seen that Al and Ti rich supercells would exhibit a notable variance between the elastic constants of different iterations, particularly the C_{11} . An exception to this would be the Al_6TiVCr alloy which, although stable, exhibited some variance and the $Al_{14}Ti_{20}VCr$ alloy which instead displayed limited variation. Naturally, these implications regarding the elastic constants were also transferred to B, G and subsequently E. Therefore, it could be argued that as the instability of the supercell would increase, the reliability of the calculations would decrease. Nevertheless, experimental verification of these findings is required before these trends and assumptions are confirmed.

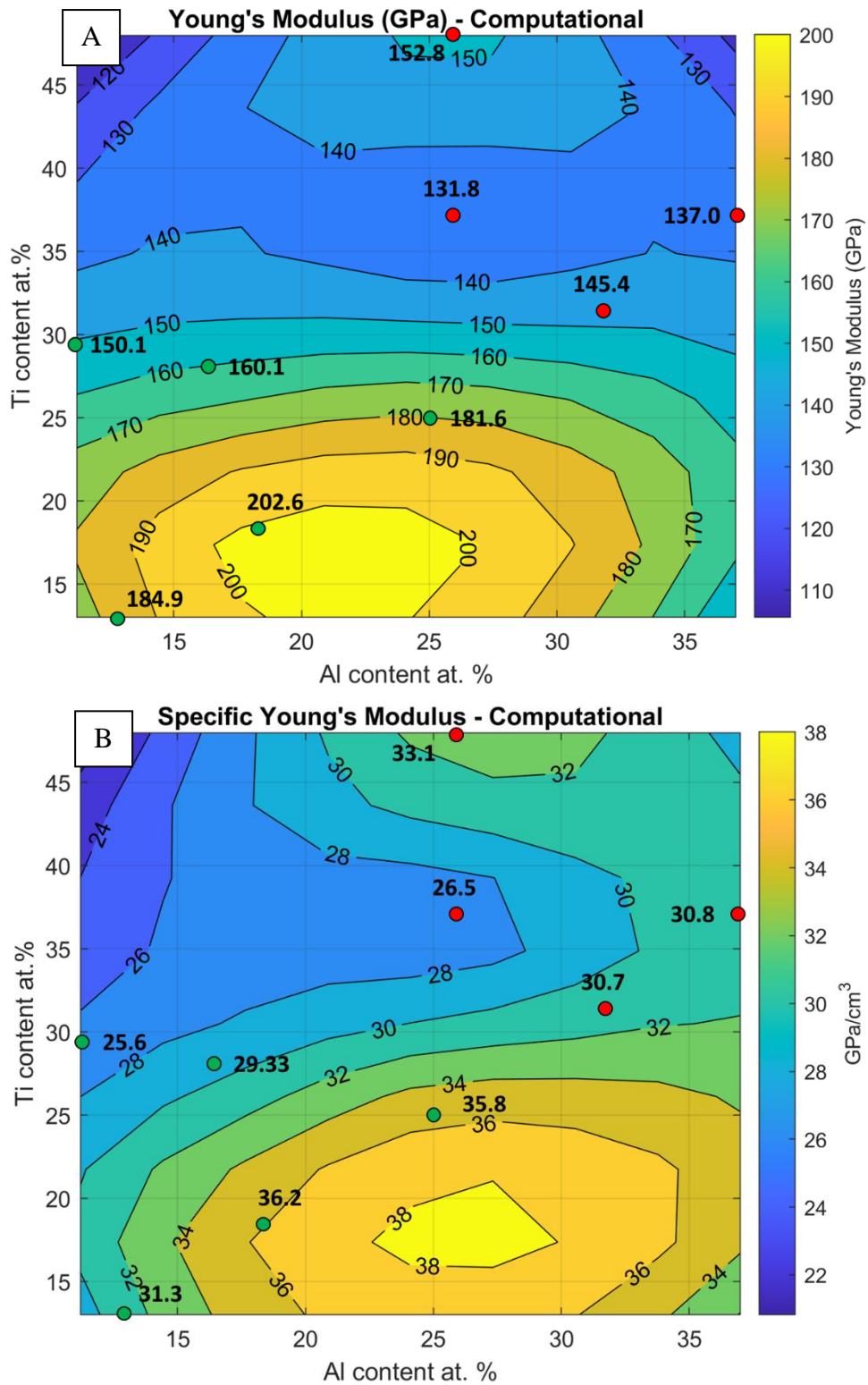


Figure 7.8 Contour plots showing the dependence of the computationally derived A) Young's modulus and B) specific Young's modulus on the Al (at. %) and Ti (at. %) content of AlTiVCr-based alloys.

Table 7.5 Summary of the computationally derived density, mean elastic and energetic properties of the investigated compositions.

Alloy Name	B (GPa)	G (GPa)	E (GPa)	ν	Final Energy (eV/atom)
Al₆TiVCr	159.3	55.9	150.1	0.34	-1829.66
Al₉TiVCr	164.9	59.8	160.1	0.34	-1722.27
Al₇Ti₇VCr	193.8	68.9	184.9	0.34	-1902.37
Al₁₀Ti₁₀VCr	183.1	77.0	202.6	0.32	-1744.9
AlTiVCr	154.7	69.7	181.6	0.30	-1534.91
Al₁₇Ti₁₇VCr	132.2	55.6	145.4	0.32	-1377.44
Al₂₀Ti₂₀VCr	121.8	52.2	137.0	0.31	-1219.98
Al₁₄Ti₂₀VCr	127.6	49.6	131.8	0.33	-1384.74
Al₁₄Ti₂₆VCr	128.6	58.7	152.8	0.30	-1459.83

Table 7.6 Computationally calculated elastic constant and the derived elastic properties of all investigated compositions.

Alloy Name	C₁₁	C₁₂	C₄₄	B	G	E	ν
Al₆TiVCr	233.15	119.95	54.29	157.7	55.2	148.3	0.34
	211.22	122.06	56.79	151.8	51.5	138.9	0.35
	267.18	118.89	53.47	168.3	61.0	163.2	0.34
Al₇Ti₇VCr	346.82	124.09	48.8	198.3	68.4	184.0	0.35
	308.22	129.27	57.53	188.9	68.7	183.8	0.34
	339.42	121.55	51.26	194.2	69.7	186.7	0.34
Al₉TiVCr	248.67	116.65	59	160.7	61.7	164.1	0.33
	252.8	117.49	55.83	162.6	60.3	161.0	0.33
	261.86	126.02	51.46	171.3	57.5	155.2	0.35
Al₁₀Ti₁₀VCr	339.14	118.04	66.035	191.7	81.3	213.6	0.31
	320.58	111.35	60.01	181.1	75.1	197.9	0.32
	310.8	109.5	61	176.6	74.6	196.3	0.31
AlTiVCr	256.2	109.57	78.29	158.4	76.3	197.2	0.29
	249.89	118.83	72.98	162.5	69.9	183.4	0.31
	206.5	111.39	75.63	143.1	62.8	164.3	0.31
Al₁₇Ti₁₇VCr	125.81	105.71	68.57	112.4	32.9	89.9	0.37
	171.08	112.06	80.37	131.7	53.8	142.1	0.32
	245.42	105.79	87.74	152.3	80.1	204.4	0.28
Al₂₀Ti₂₀VCr	149.5	101.56	83.69	117.5	50.9	133.3	0.31
	143.37	104.88	80.23	117.7	45.6	121.2	0.33
	181.49	104.37	81.11	130.1	60.2	156.4	0.30
Al₁₄Ti₂₀VCr	170.71	109.7	75.7	130.0	52.6	139.0	0.32
	165.38	105.73	69.53	125.6	49.5	131.3	0.33
	163.54	108.8	67.04	127.0	46.8	125.1	0.34
Al₁₄Ti₂₆VCr	175.63	97.8	71.05	123.7	55.8	145.5	0.30
	206.79	104.18	79.95	138.4	66.9	172.9	0.29
	166.04	102.34	75.5	123.6	53.4	140.0	0.31

7.3.2 Experimental Assessment of Novel Compositions

7.3.2.1 Thermal Conductivity Measurements

The thermal conductivity values of all novel compositions were similar to that of the original equiatomic AlTiVCr alloy. Furthermore, no trend could be established between the different compositions in terms of their alloying elements. Overall, the WQ values of the thermal conductivity were lower than those corresponding to the FC condition; however, this was expected as the WQ samples exhibited additional cracks compared to the FC ones. Again, this general lack of thermal conductivity in all alloys may have compromised their structural integrity upon their subjection to rapid heating and cooling cycles. This phenomenon was extensively explained in Chapter 5.

Table 7.7 Thermal conductivity of the AlTiVCr-based alloys of the present study as measured under ambient conditions.

Alloy Name	Furnace Cooled Thermal Conductivity ($\text{Wm}^{-1}\text{K}^{-1}$)	Water Quenched Thermal Conductivity ($\text{Wm}^{-1}\text{K}^{-1}$)
Al₆TiVCr	4.60	4.65
Al₉TiVCr	3.65	3.34
Al₇Ti₇VCr	5.52	4.37
Al₁₀Ti₁₀VCr	4.68	4.49
AlTiVCr	-	4.77
Al₁₇Ti₁₇VCr	5.00	3.51
Al₂₀Ti₂₀VCr	4.57	3.81
Al₁₄Ti₂₀VCr	-	4.68
Al₁₄Ti₂₆VCr	4.78	3.80

7.3.2.2 Microstructure Characterisation

In terms of their microstructural features, it was confirmed that the $\text{Al}_{14}\text{Ti}_{26}\text{VCr}$ (WQ, FC), $\text{Al}_{14}\text{Ti}_{26}\text{VCr}$ (WQ, FC) and $\text{Al}_{20}\text{Ti}_{20}\text{VCr}$ (FC) exhibited a multiphase microstructure. All other samples were characterised by a single phase microstructure with the inclusion of impurity-based SPPs forming at grain boundaries.

The $\text{Al}_{14}\text{Ti}_{26}\text{VCr}$ alloy (Fig. 7.9 A, B) exhibited “C”-shaped particles in both the WQ and FC condition with a homogeneous intergranular and a combined intergranular-intragranular distribution respectively. Another type of angular, plate-like particles was additionally identified to form intergranularly in the FC condition. The $\text{Al}_{14}\text{Ti}_{20}\text{VCr}$ alloy (Fig. 7.9 C, D), seemed to consist of a single phase at OM resolution in the WQ state. Nevertheless, the formation of needle-like particles was clearly visible in the FC condition.

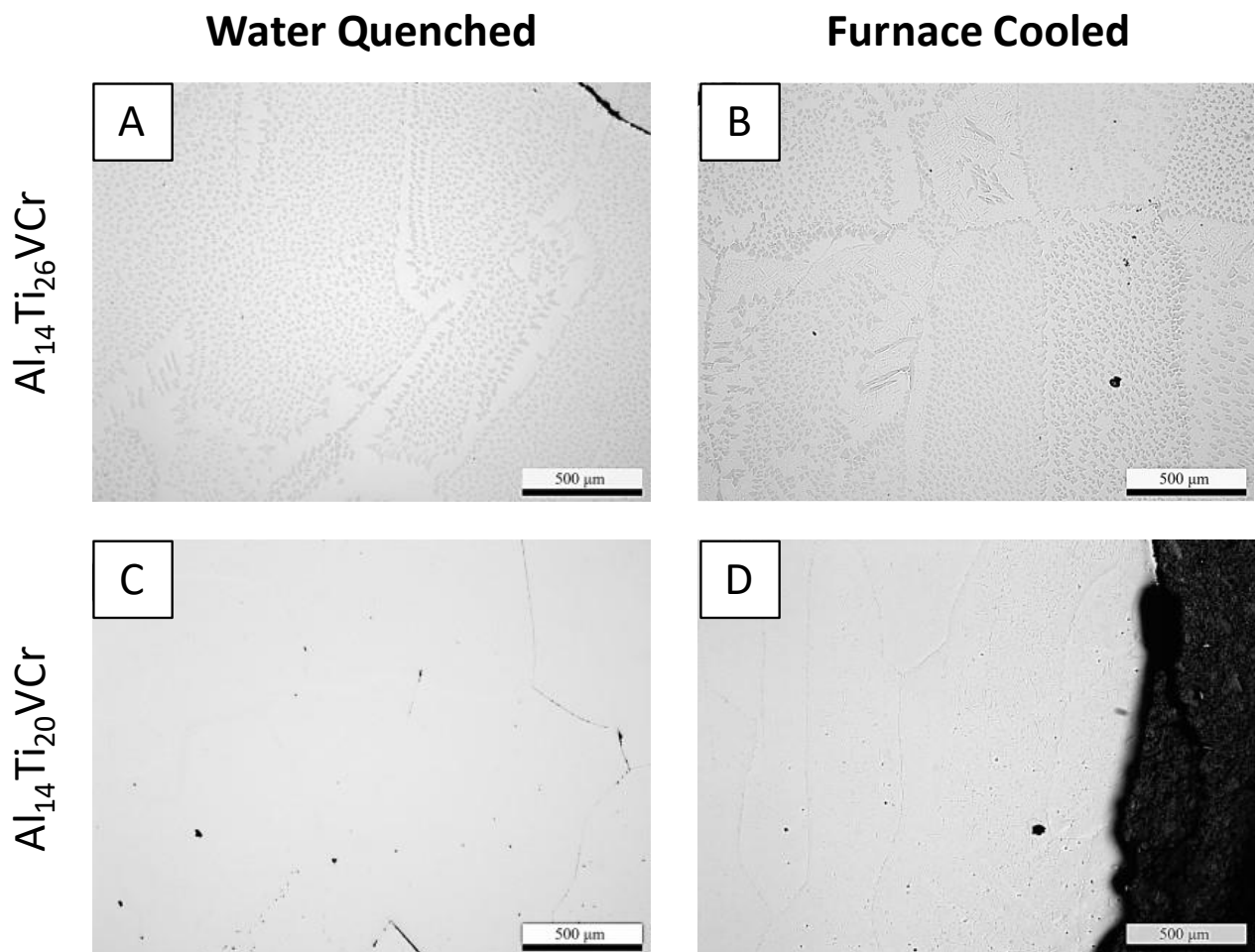


Figure 7.9 Optical micrographs of the water quenched (WQ) and furnace cooled (FC) $\text{Al}_{14}\text{Ti}_{26}\text{VCr}$ (A, B), $\text{Al}_{14}\text{Ti}_{20}\text{VCr}$ (C, D) alloys.

The SEM results showed that the WQ $\text{Al}_{14}\text{Ti}_{26}\text{VCr}$ sample (Fig. 7.10 A) consisted of AlTi particles with a composition nearing that of AlTi_3 . The particles of the same composition were

identified in the WQ $Al_{14}Ti_{26}VCr$ (Fig. 7.10 C) alloy but at a much lower volume fraction. In the FC condition, the $Al_{14}Ti_{26}VCr$ (Fig. 7.10 B) consisted of two types of particles with distinctly different morphologies. EDX analysis showed that both types of particles had a similar composition, again corresponding to $AlTi_3$. The particles seen in the FC $Al_{14}Ti_{20}VCr$ (Fig. 7.10 D) alloy were nearing the composition of $AlTi_3$. These findings verify the predictions made by ThermoCalc in Fig. 7.1-7.2 by both TCHEA2 and TCHEA5 in terms of the SPPs present in the microstructure, however with the lack of a Laves phase which was predicted with TCHEA5.

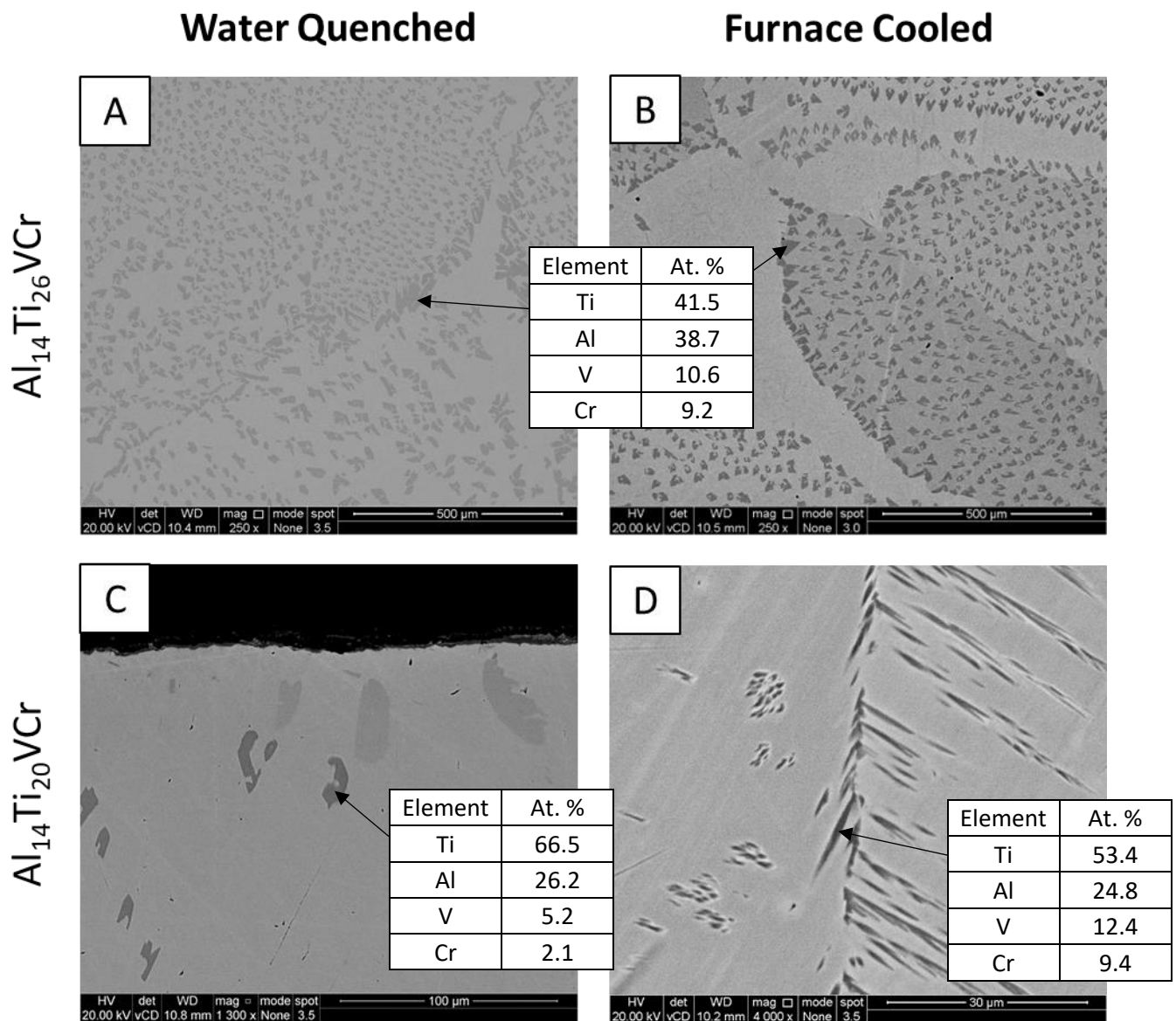


Figure 7.10 SEM micrographs of the water quenched (WQ) and furnace cooled (FC) $Al_{14}Ti_{26}VCr$ (A, B), $Al_{14}Ti_{20}VCr$ (C, D) alloys.

The $\text{Al}_{20}\text{Ti}_{20}\text{VCr}$ alloy (Fig. 7.11 A, B), while single phase in the WQ condition, exhibited a high volume fraction of needle-like particles in the FC condition, potentially forming intergranularly. On the other hand, the $\text{Al}_{17}\text{Ti}_{17}\text{VCr}$ alloy (Fig. 7.11 C, D) was single phase in both conditions.

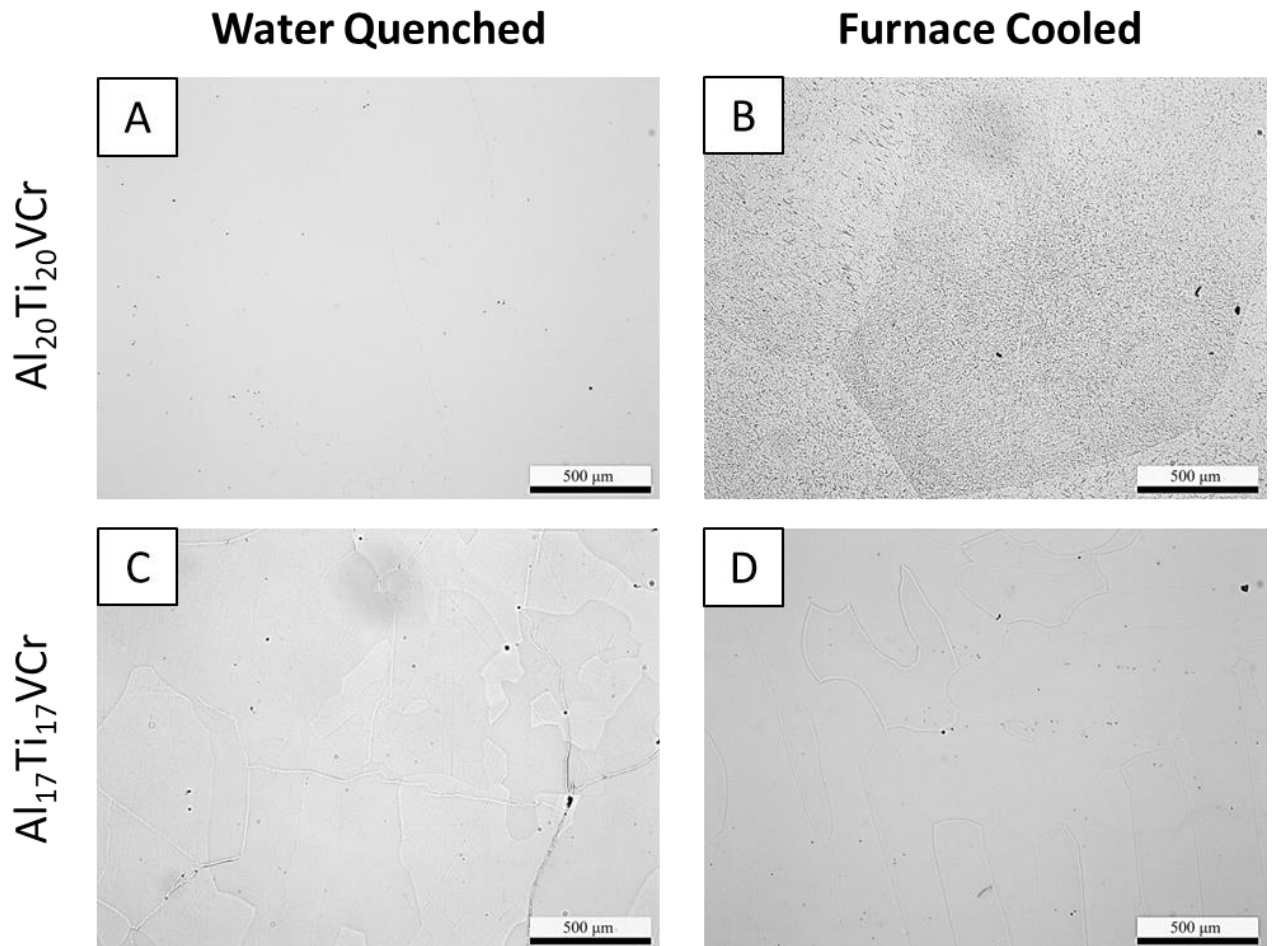


Figure 7.11 Optical micrographs of the water quenched (WQ) and furnace cooled (FC) $\text{Al}_{20}\text{Ti}_{20}\text{VCr}$ (A, B), $\text{Al}_{17}\text{Ti}_{17}\text{VCr}$ (C, D) alloys.

As seen in Fig. 7.12 indeed the $\text{Al}_{17}\text{Ti}_{17}\text{VCr}$ (WQ, FC) and $\text{Al}_{20}\text{Ti}_{20}\text{VCr}$ (WQ) alloys were single phase with cracks being clearly visible in the WQ state. The FC $\text{Al}_{20}\text{Ti}_{20}\text{VCr}$ (Fig. 7.12 B) alloy however, was comprised of a matrix phase and the highly angular, needle-like particles. They seemed to be uniformly distributed predominantly in the grain interior. EDX showed that these particles seemed to have a 1:1 ratio of Al:Ti. Due to the fact that the $\text{Al}_{20}\text{Ti}_{20}\text{VCr}$ (FC) alloy exhibited some interesting properties, some additional characterisation work was carried out to better understand its properties, which is discussed later in this thesis.

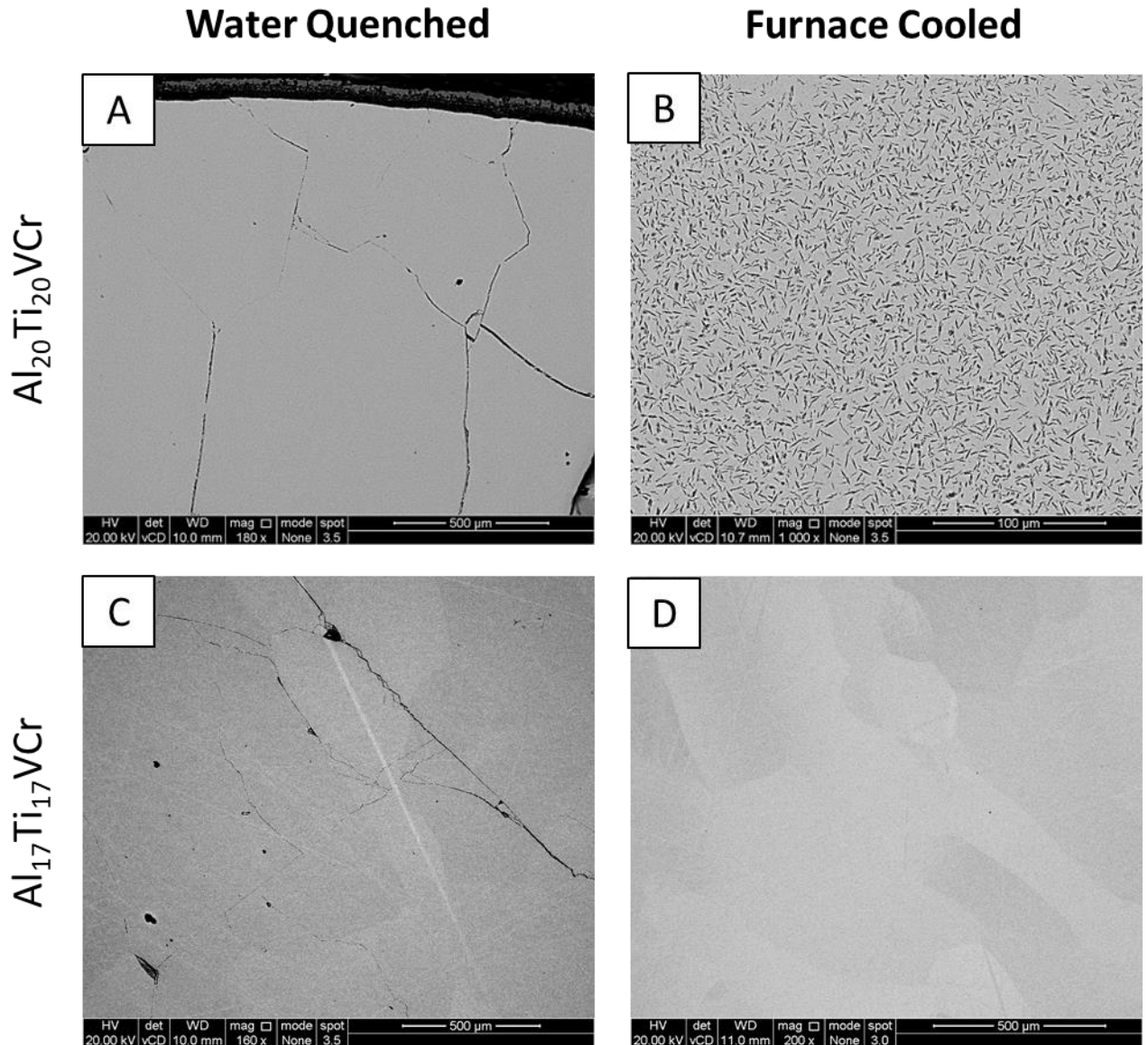


Figure 7.12 SEM micrographs of the water quenched (WQ) and furnace cooled (FC) $Al_{20}Ti_{20}VCr$ (A, B), $Al_{17}Ti_{17}VCr$ (C, D) alloys.

As evident in Fig. 7.13, the coarser particles seemed to contain a high amount of cracks while the finer ones did not exhibit the same behaviour. Furthermore, they did not seem to attain a specific orientation and were rather randomly but homogeneously distributed with smaller particles often intersecting one another. XRD (Fig. 7.14) revealed that indeed the particles were AlTi. AlTi are evident in Fig. 7.3-7.4 alongside $AlTi_3$ in the case of TCHEA2 while TCHEA5 predicted the formation of the Laves phase with the AlTi particles. Nevertheless, both TCHEA2 and TCHEA5 contained distinct low temperature regions of B2 + AlTi exclusively. However, in TCHEA2 this region spread towards lower Al-Ti contents. This once again shows that ThermoCalc was relatively accurate in predicting the phase constitution of the novel compositions thus far. Particular attention should be given to the matrix region in-between the

particles which seems to exhibit certain linear features which may be pointing to additional phase transformations taking place. Nevertheless, XRD did not unveil any other phases being present, meaning that should this indeed be evidence of a phase transformation, the products of the transformation may exhibit similar crystallographic characteristics as in the case of order-disorder transformations. However, the multi-phase nature of this alloy meant that it would not be investigated any further for the purposes of this work.

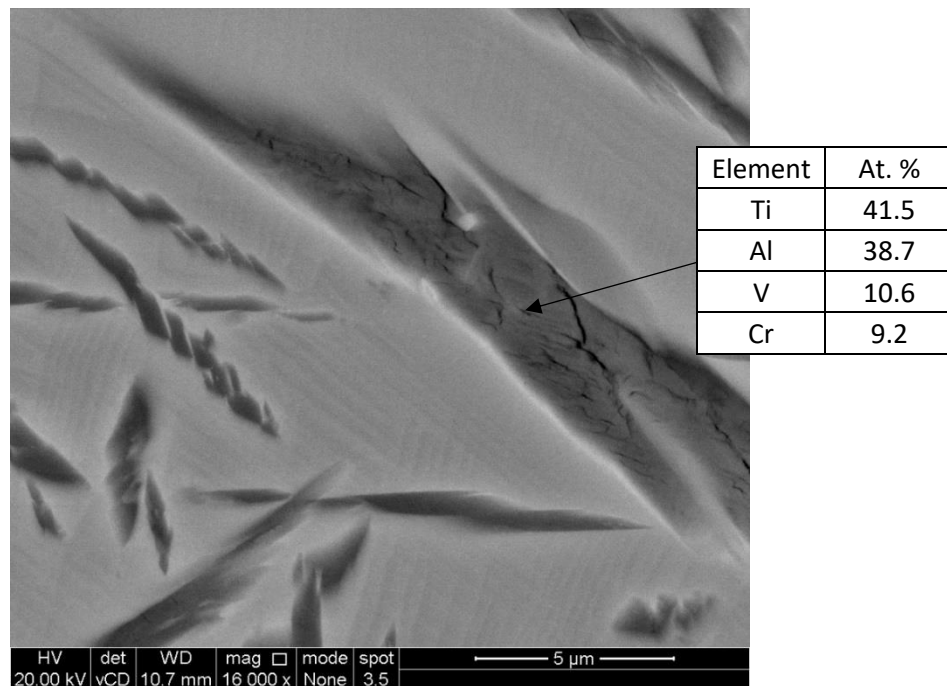


Figure 7.13 SEM micrograph of the furnace cooled (FC) $Al_{20}Ti_{20}V_{10}Cr_{10}$ alloy illustrating cracked AlTi plate-like particles and a matrix phase exhibiting linear features.

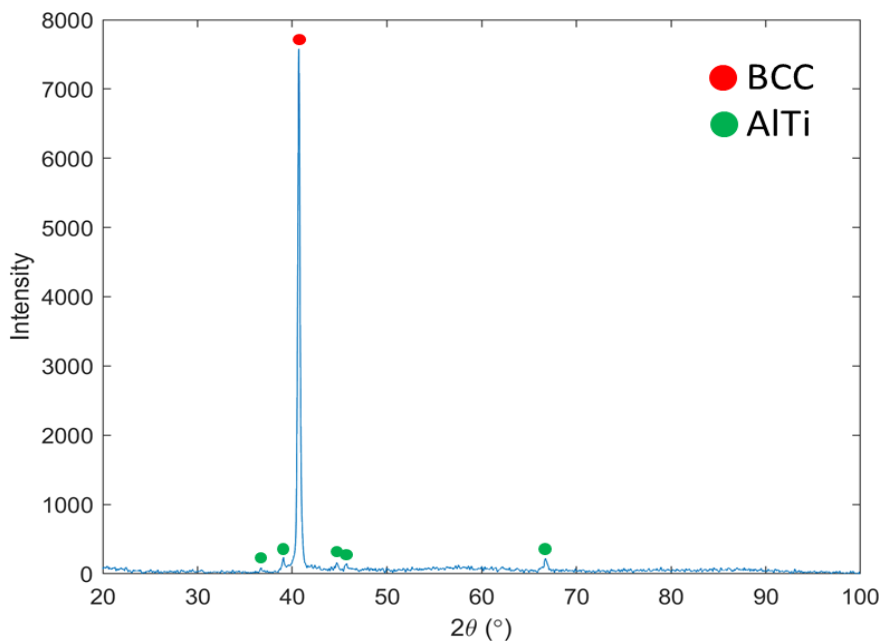


Figure 7.14 XRD pattern of the furnace cooled (FC) $Al_{20}Ti_{20}V_{10}Cr_{10}$ alloy demonstrating the presence of AlTi alongside a BCC/B2 matrix phase.

Both the $\text{Al}_{10}\text{Ti}_{10}\text{VCr}$ (Fig. 7.15 A, B) and Al_9TiVCr (Fig. 7.15 C, D) alloys exhibited single phase microstructures. However, the WQ condition of the $\text{Al}_{10}\text{Ti}_{10}\text{VCr}$ alloy showed severe transgranular cracks which were entirely absent in the FC condition. On the contrary, the Al_9TiVCr alloy was not characterised by extensive cracking in either case.

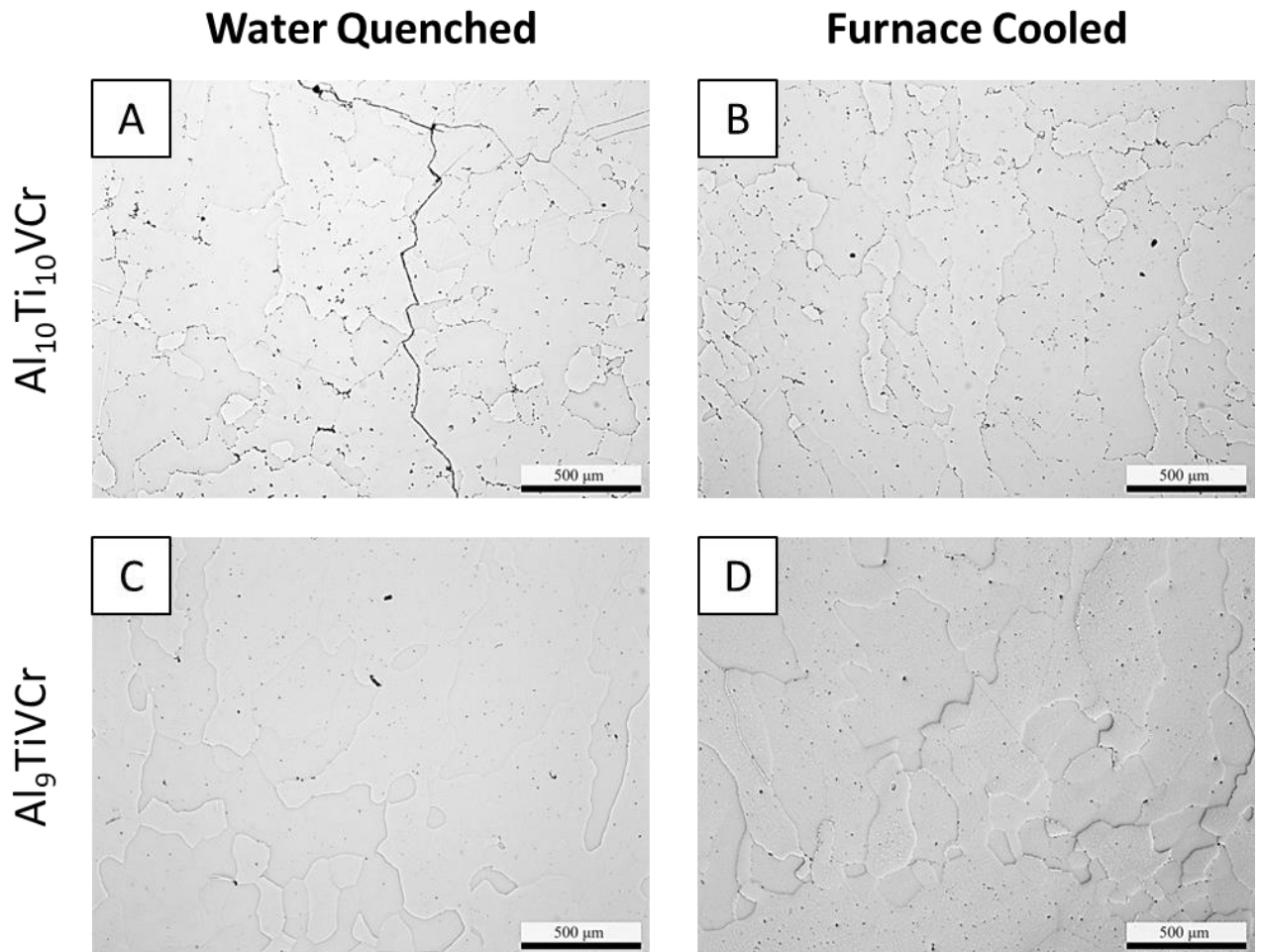


Figure 7.15 Optical micrographs of the water quenched (WQ) and furnace cooled (FC) $\text{Al}_{10}\text{Ti}_{10}\text{VCr}$ (A, B), Al_9TiVCr (C, D) alloys.

The SEM images show the formation of TiN particles in the case of the WQ $\text{Al}_{10}\text{Ti}_{10}\text{VCr}$ (Fig 7.16 A) and FC Al_9TiVCr (Fig. 7.16 D) alloys. Furthermore, Al oxide formation was observed in the FC $\text{Al}_{10}\text{Ti}_{10}\text{VCr}$ (Fig. 7.16 B) alloy with TiN particles forming in the oxide-matrix interphase regions and grain boundaries. These impurity-based SPPs are expected given that the heat treatment was carried out in a flowing Ar furnace where atmospheric air may leak into the system. The WQ Al_9TiVCr (Fig. 7.16) alloy did not exhibit any notable TiN formation along gran boundaries. Lastly, in the case of the FC Al_9TiVCr (Fig. 7.16 D) another phase was observed to form adjacent to TiN and Al-oxide particles. This was especially prominent around

TiN particles formed along grain boundaries. Therefore, it would seem that ThermoCalc overestimated the number of phases forming in this composition.

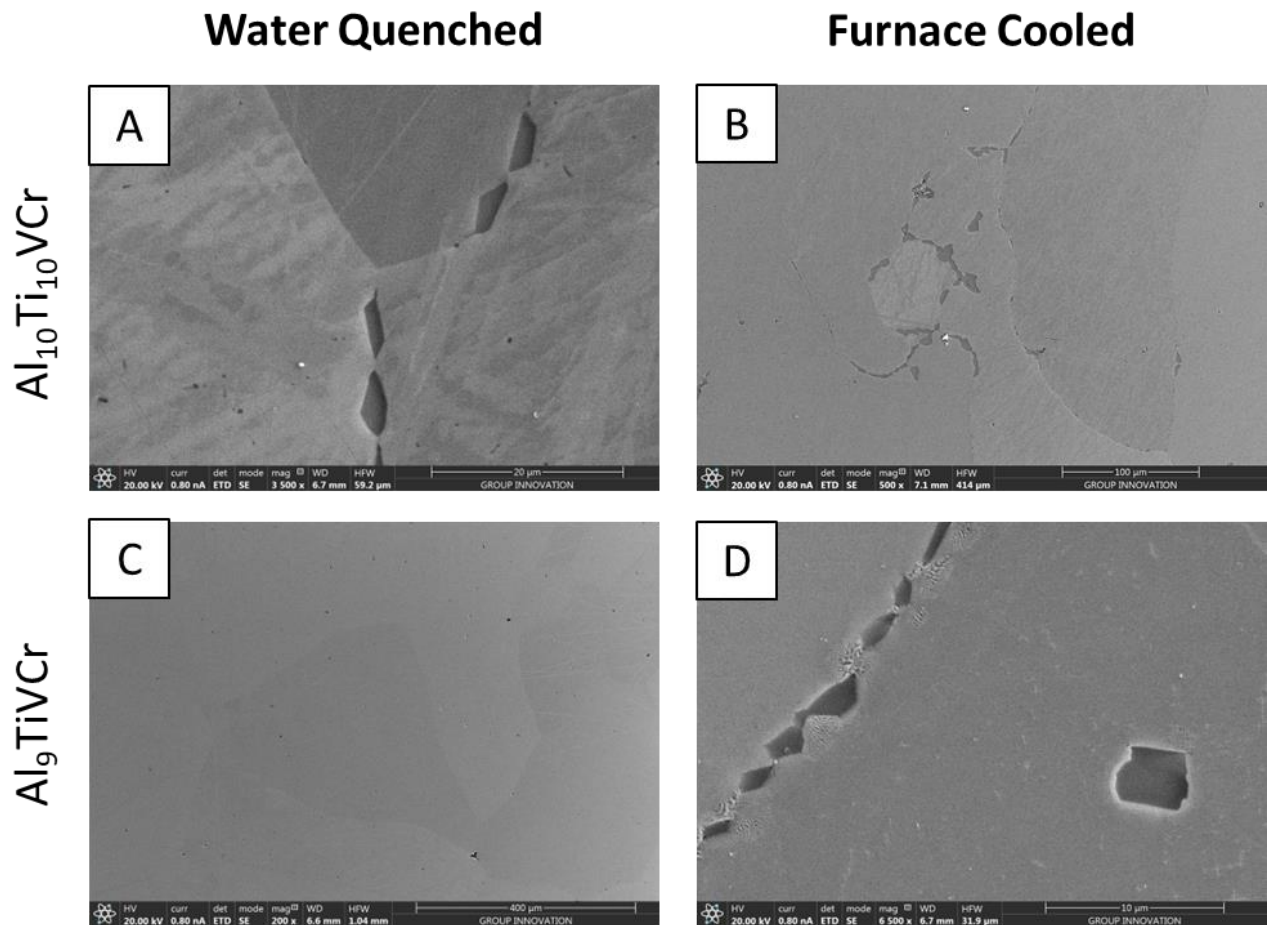


Figure 7.16 SEM micrographs of the water quenched (WQ) and furnace cooled (FC) $Al_{10}Ti_{10}VCr$ (A, B), Al_9TiVCr (C, D) alloys.

Upon closer investigation of the FC Al_9TiVCr alloy (Fig. 7.17) more microstructural features could be revealed. Specifically, a structure consisting of alternating plates could be seen forming near the Al-oxides and at the grain interior (Fig. 7.17 A, B). Furthermore, a similar structure could be identified originating from the TiN particles at the grain boundaries. This microstructural constituent seemed to spread from the grain boundaries toward the interior of the grains. It was comprised of alternating plates of two different phases which would become progressively refined towards the interior of the grains. Nevertheless, it should be noted that this structure was limited to the grain boundaries and did not penetrate too deeply into the grain. EDX quant maps (Fig. 7.18) hinted that the alternating plates consisted of a phase rich in Cr and V, and another phase rich in Al and Ti. These findings are similar to those of chapter 6 and perhaps indicate that this would be a BCC + B2 structure.

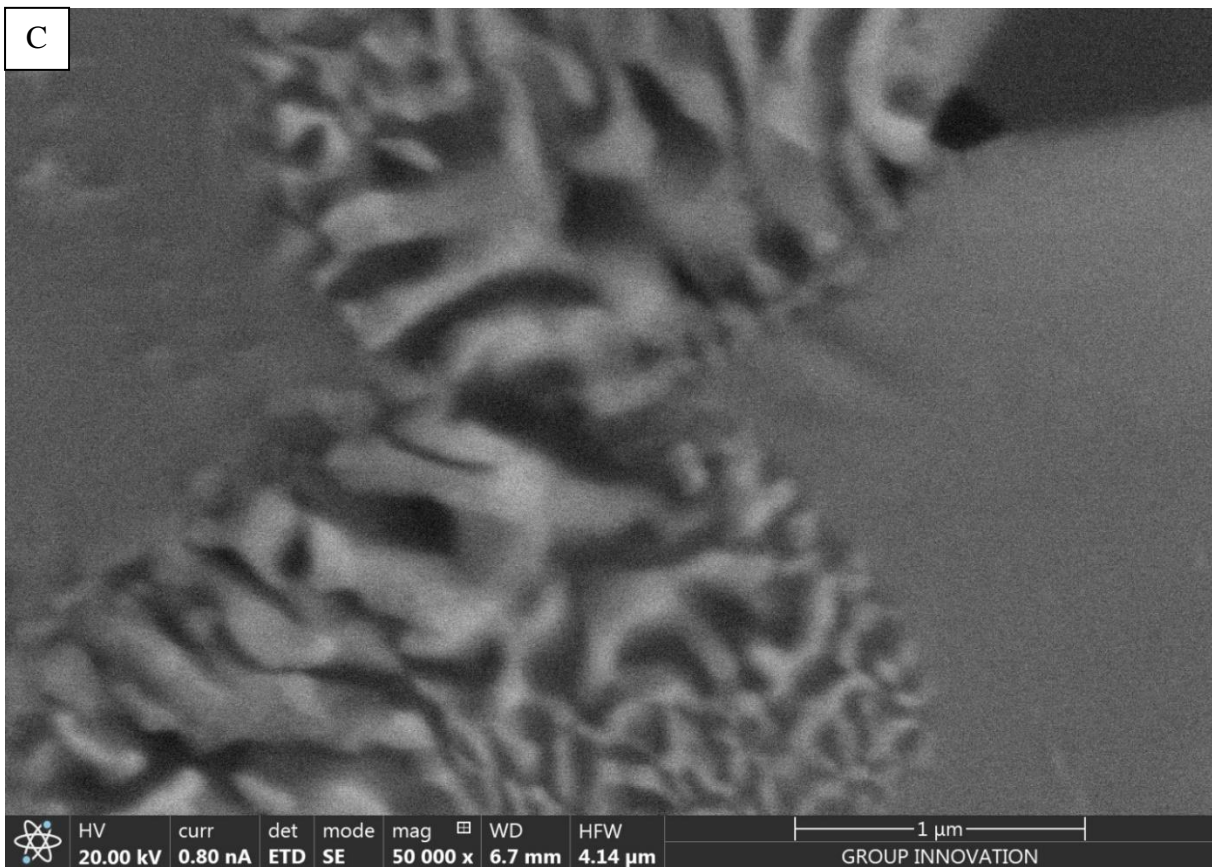
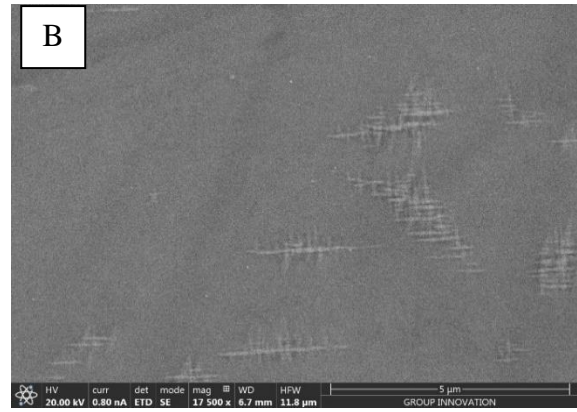
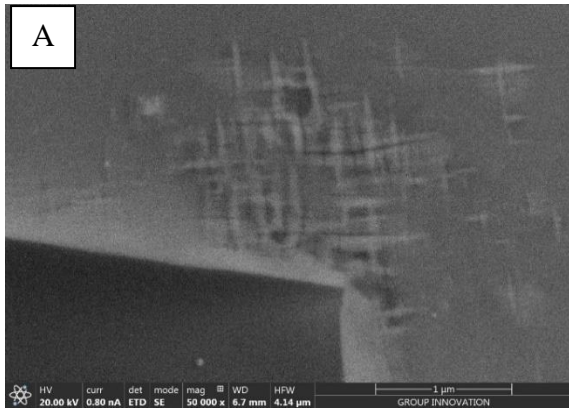


Figure 7.17 SEM micrographs of the furnace cooled (FC) Al₉TiVCr alloy showing the A) nucleation point of the microstructural constituent, B) nucleation of the phase in the grain interior and C) the alternating plate structure.

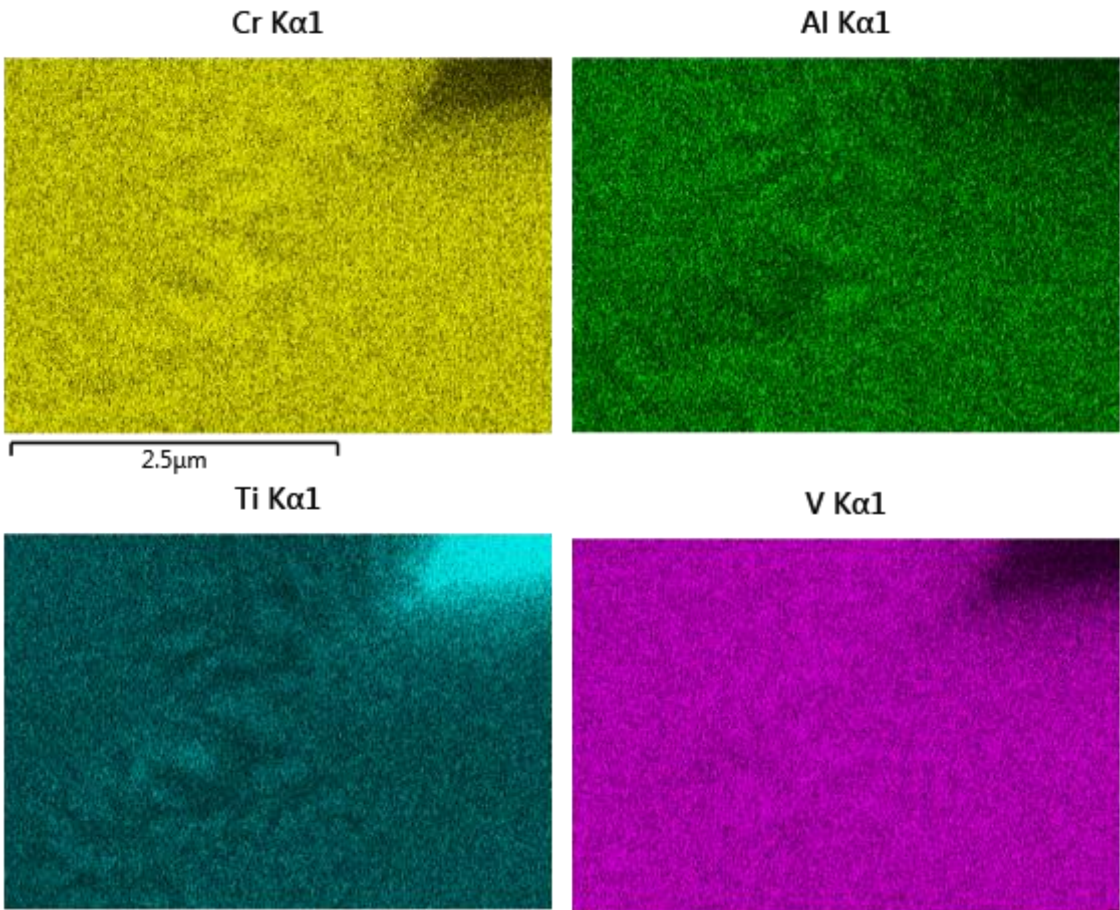


Figure 7.18 EDX quant maps illustrating the distribution of the alloying elements along the alternating plates of image 7.17C.

Similarly to Fig. 7.15, the $\text{Al}_7\text{Ti}_7\text{VCr}$ (Fig. 7.19 A, B) alloy showed significant cracking in the WQ condition, while the Al_6TiVCr (Fig. 7.19 C, D) was comparatively more structurally integral. Nevertheless, both compositions were characterised by single phase microstructures.

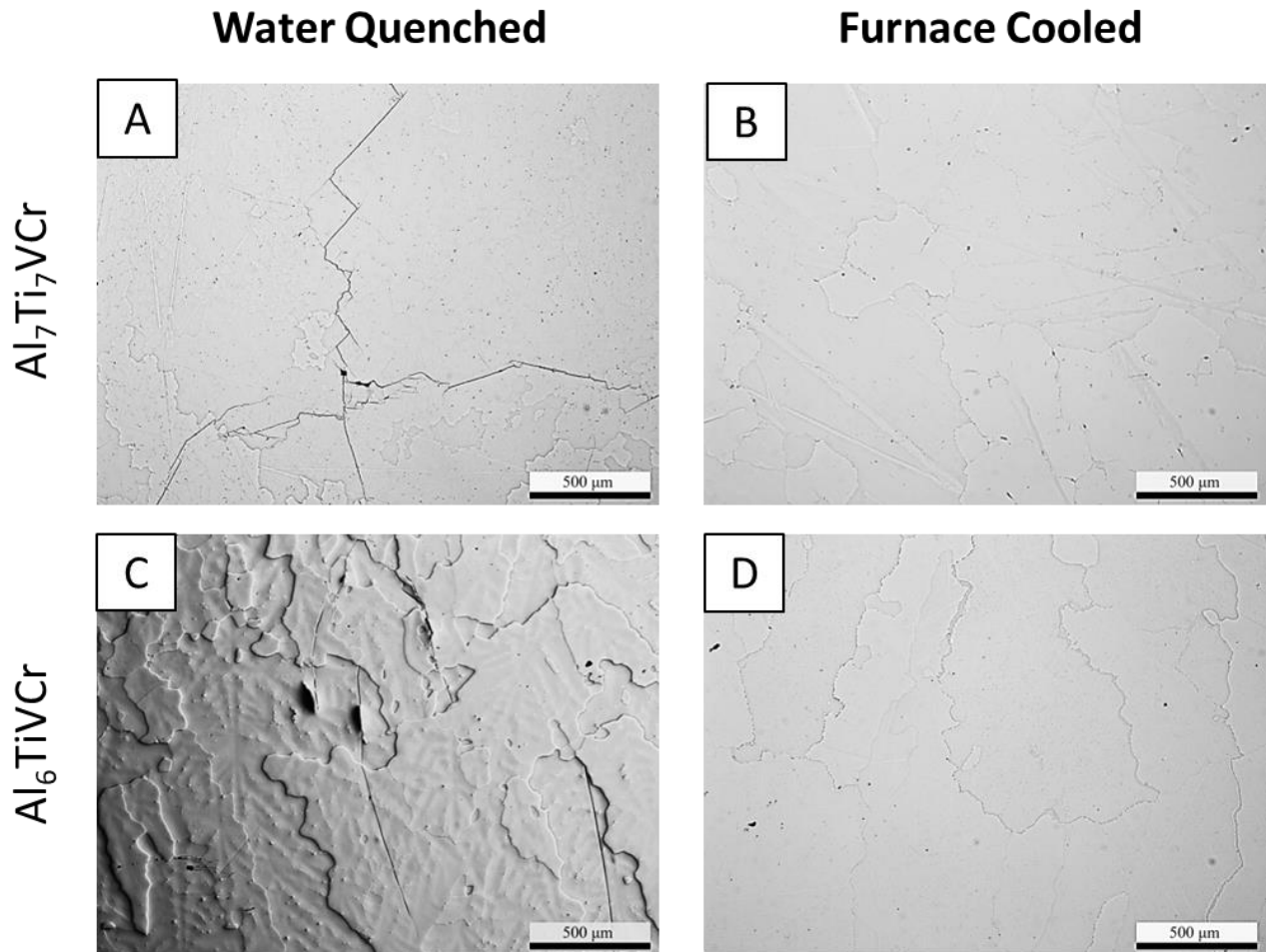


Figure 7.19 Optical micrographs of the water quenched (WQ) and furnace cooled (FC) $\text{Al}_7\text{Ti}_7\text{VCr}$ (A, B), Al_6TiVCr (C, D) alloys.

Again, the formation of TiN particles in the case of the $\text{Al}_7\text{Ti}_7\text{VCr}$ (Fig 7.20 A, B) and FC Al_6TiVCr (Fig. 7.20 D) alloys was observed. The WQ Al_6TiVCr (Fig. 7.20 C) alloy did not exhibit any notable TiN formation, instead, severe surface cracks had developed. In the case of the FC Al_6TiVCr (Fig. 7.20 D), similarly to Al_9TiVCr , another phase was observed to form adjacent to TiN particles. This was also most prominent around TiN particles at the grain boundaries. Nevertheless, it was found that this phase would also form at TiN-free grain boundary regions. Overall, ThermoCalc once again overestimated the number of phases.

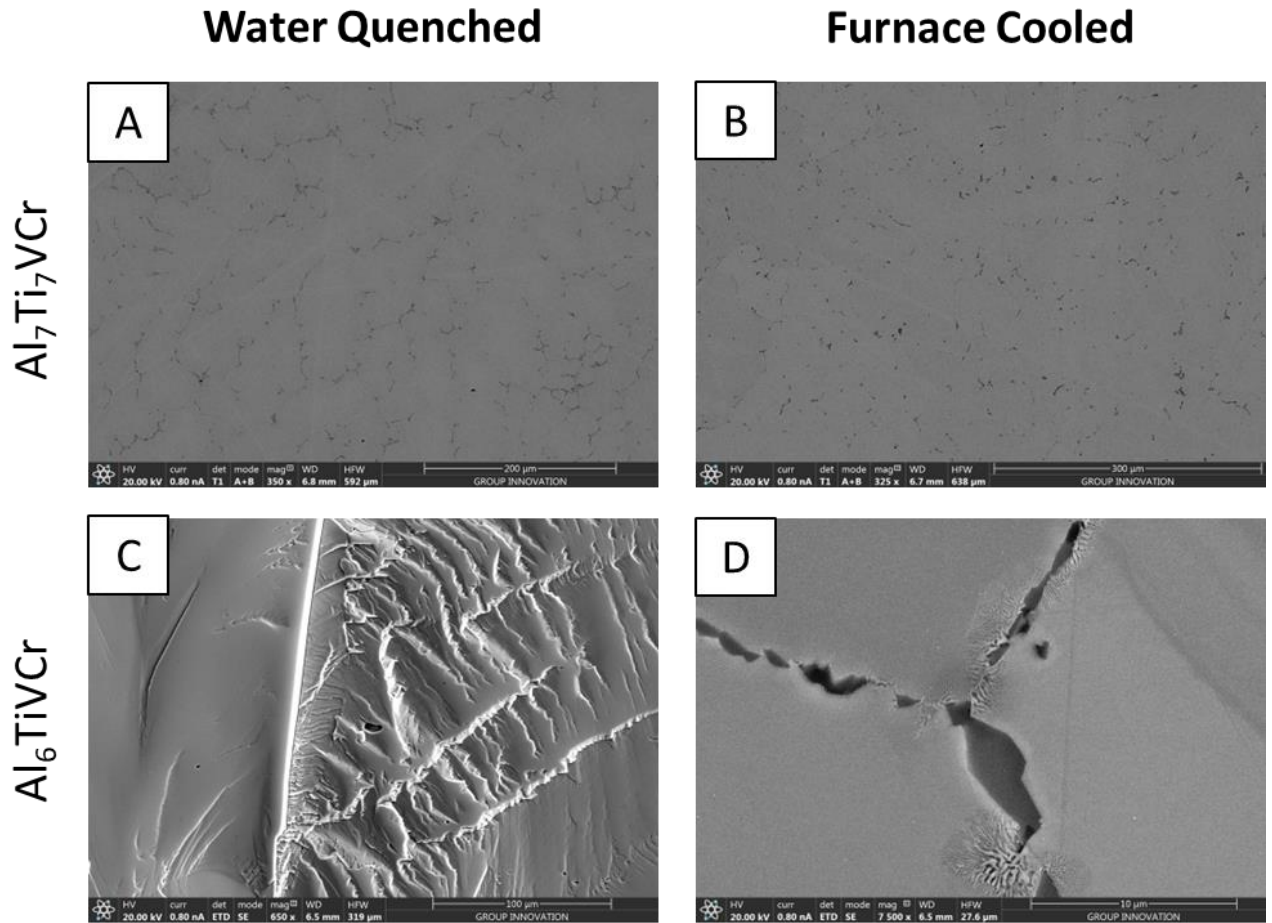


Figure 7.20 SEM micrographs of the water quenched (WQ) and furnace cooled (FC) Al_7Ti_7VCr (A, B), Al_6TiVCr (C, D) alloys.

An SEM investigation at a higher resolution showed that the FC Al_6TiVCr (7.21) also contained a similar structure to that encountered in FC Al_9TiVCr . Comparatively, this structure was well defined in the current case and penetrated more deeply into the grains. It should also be noted that it was also found to nucleate from TiN-free regions of the grain boundaries showing that there is a higher driving force for its formation in the present alloy. This time, EDX quant maps (Fig. 7.22) were able to capture this selective distribution of the alloying elements with much greater accuracy, mirroring the results seen in Chapter 6. Therefore, it is most probable that both the Al_9TiVCr and Al_6TiVCr alloys contain a BCC + B2 structure at the FC condition, meaning that a metastable BCC is expected in the WQ condition of both alloys. It should be underlined that ThermoCalc did predict BCC + B2 regions for both the Al_9TiVCr and Al_6TiVCr alloys; with, however, the addition of SPPs. Nevertheless, a minor elevated temperature region in of the phase diagram calculated with TCHEA5 did comprise exclusively of BCC + B2.

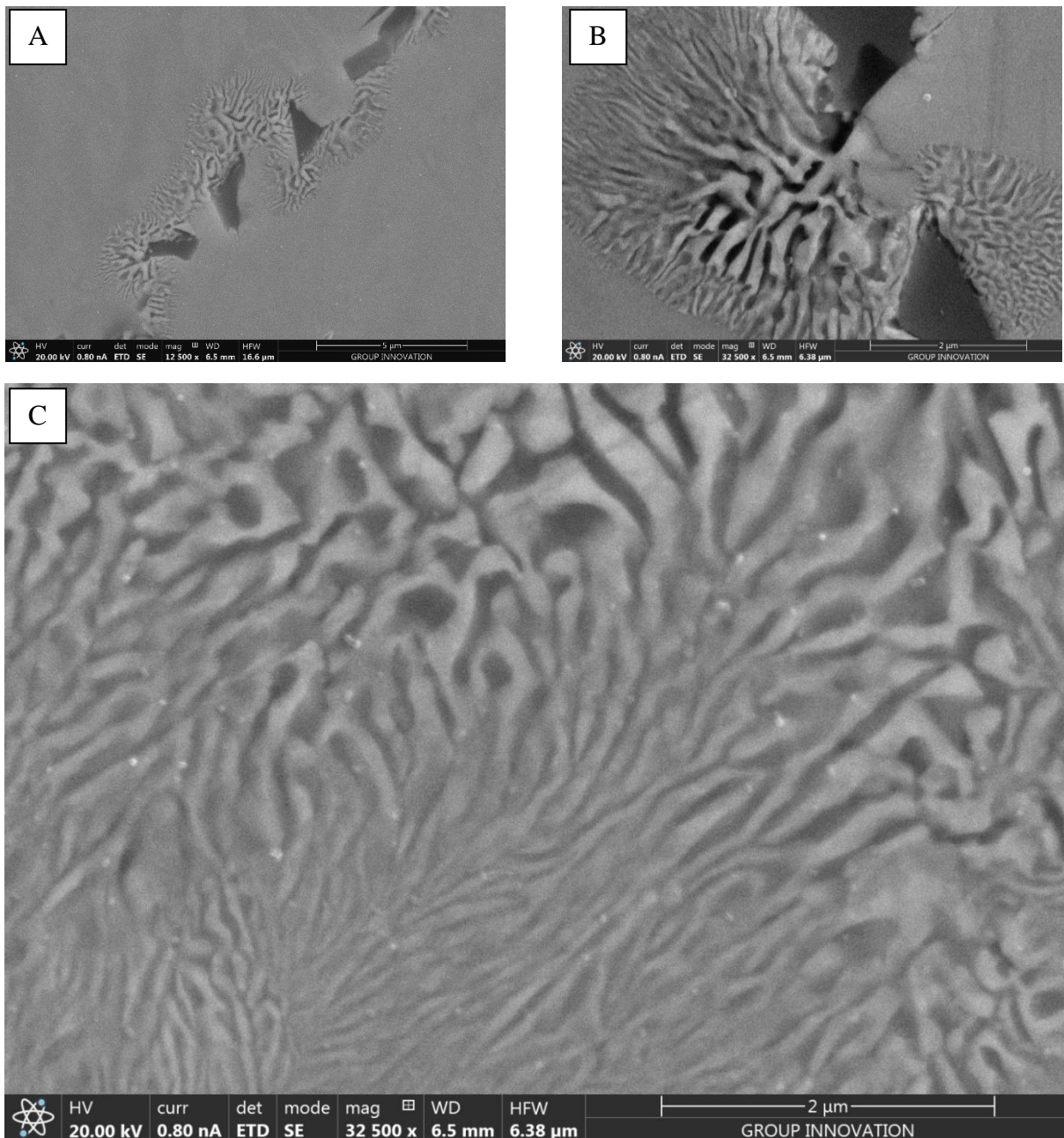


Figure 7.21 SEM micrographs of the furnace cooled (FC) Al₆TiVCr alloy showing the A, B) nucleation points of the microstructural constituent and C) the alternating plates.

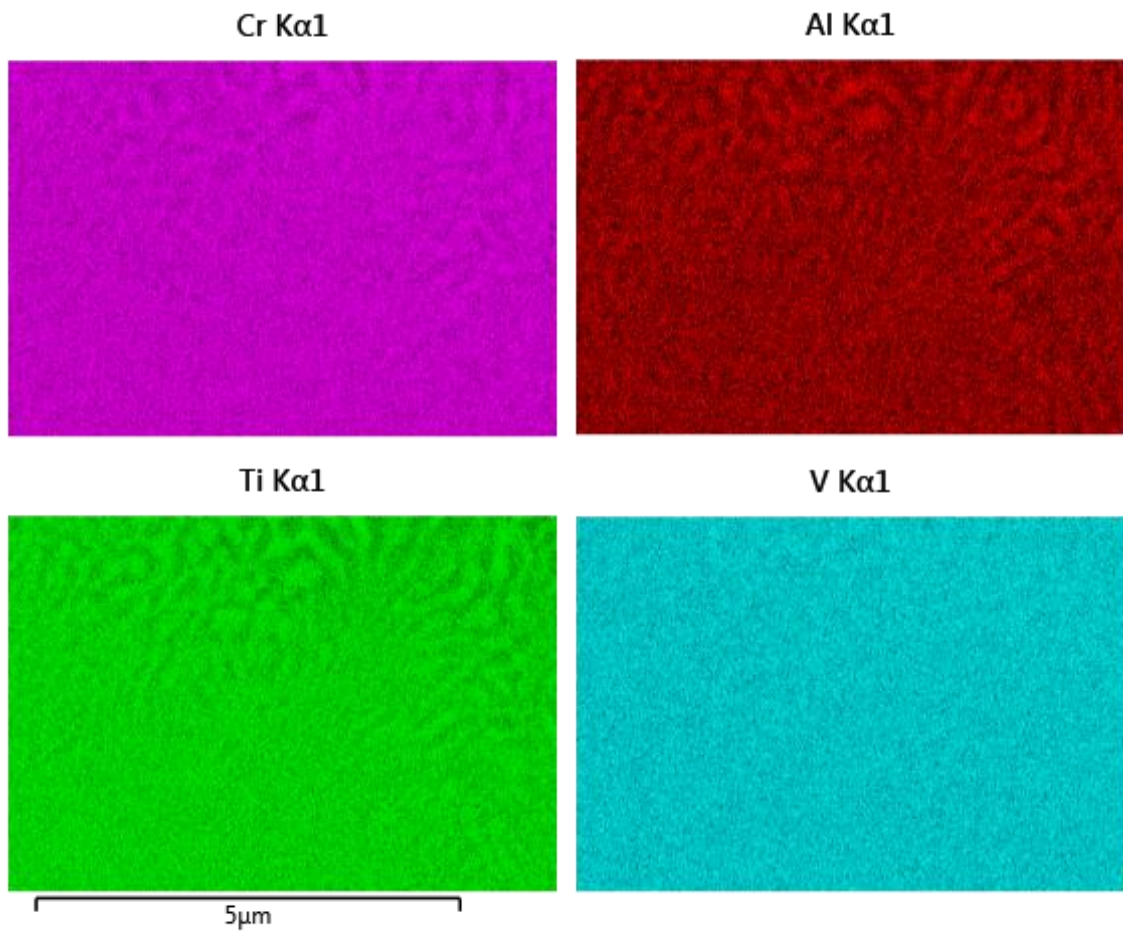


Figure 7.22 EDX quant maps illustrating the distribution of the alloying elements along the alternating plates of image 7.21C.

The lattice parameters of the matrix BCC/B2 phases of all alloys were extracted through XRD (Table 7.8, Appendix Fig. 10.1-10.8). These are in extremely good agreement with the computationally predicted ones and follow the same trends discussed in Chapter 7.3.1.3. It should therefore be established that DFT with CASTEP is a reliable tool for the prediction of lattice parameters even in cases where the evaluated compositions may consist of multiple phases.

Table 7.8 Experimentally measured lattice parameters of the water quenched (WQ) and furnace cooled (FC) AlTiVCr-based alloys through XRD alongside the computationally derived lattice parameters.

Alloy Name	Exp. Lat. Par. WQ (Å)	Exp. Lat. Par. FC (Å)	Comp. Lat. Par. (Å)
Al₆TiVCr	3.073	3.077	3.038
Al₉TiVCr	3.077	3.068	3.044
Al₇Ti₇VCr	3.02	3.015	2.992
Al₁₀Ti₁₀VCr	3.042	3.043	3.017
AlTiVCr	3.071	3.085	3.061
Al₁₇Ti₁₇VCr	3.105	3.122	3.098
Al₂₀Ti₂₀VCr	3.125	3.132	3.132
Al₁₄Ti₂₀VCr	3.122	3.121	3.106
Al₁₄Ti₂₆VCr	3.147	3.141	3.147

Before moving on to the next section of this Chapter the key findings of this section should be highlighted. Most alloys high in Al-Ti were found to be multiphase in either the WQ or FC condition (Table 7.9). Of the single phase alloys, the Al₉TiVCr and Al₆TiVCr were found to contain a structure comprised of alternating Cr-V-rich and Al-Ti-rich plates. These findings make it highly probable that both alloys contain a BCC + B2 microstructure in the FC condition and subsequently possibly a fully retained metastable BCC in the WQ condition. As such, two candidate compositions were identified and are further investigated using higher resolution techniques in section 7.3.2.3.

Table 7.9 Summary of microstructural and phase constitution of the investigated alloys. All alloys contained impurity-based SPPs.

Alloy Name	Water Quenched	Furnace Cooled
Al₆TiVCr	Single phase	BCC+B2
Al₉TiVCr	Single phase	BCC+B2
Al₇Ti₇VCr	Single phase	Single phase
Al₁₀Ti₁₀VCr	Single phase	Single phase
Al₁₇Ti₁₇VCr	Single phase	Single phase
Al₂₀Ti₂₀VCr	Single phase	Multiphase (Al-Ti SPPs)
Al₁₄Ti₂₀VCr	Multiphase (Al-Ti SPPs)	Multiphase (Al-Ti SPPs)
Al₁₄Ti₂₆VCr	Multiphase (Al-Ti SPPs)	Multiphase (Al-Ti SPPs)

7.3.2.3 Evaluation of Mechanical Properties

The HV_{0.5} values of the novel compositions are shown in Table 7.10. Most of the alloys predominantly lied in the region of 500-600 HV_{0.5} with the exception of Al₆TiVCr. There was also a notable difference in hardness between the FC and WQ condition among all samples. A trend was established showing a direct relationship between the amount of Al and hardness change between the two conditions (Fig. 7.23).

Table 7.10 Vicker's Hardness of the novel AlTiVCr-based compositions in the water quenched (WQ) and furnace cooled (FC) condition using a load of 0.5 kg.

Alloy Name	Hardness (HV _{0.5}) -WQ	Hardness (HV _{0.5}) -FC
Al ₆ TiVCr	465 ± 20	663 ± 16
Al ₉ TiVCr	520 ± 14	587 ± 8
Al ₇ Ti ₇ VCr	468 ± 7	540 ± 7
Al ₁₀ Ti ₁₀ VCr	479 ± 13	580 ± 16
Al ₁₇ Ti ₁₇ VCr	575 ± 13	602 ± 12
Al ₂₀ Ti ₂₀ VCr	588 ± 8	571 ± 15
Al ₁₄ Ti ₂₀ VCr	537 ± 7	574 ± 11
Al ₁₄ Ti ₂₆ VCr	596 ± 11	546 ± 29

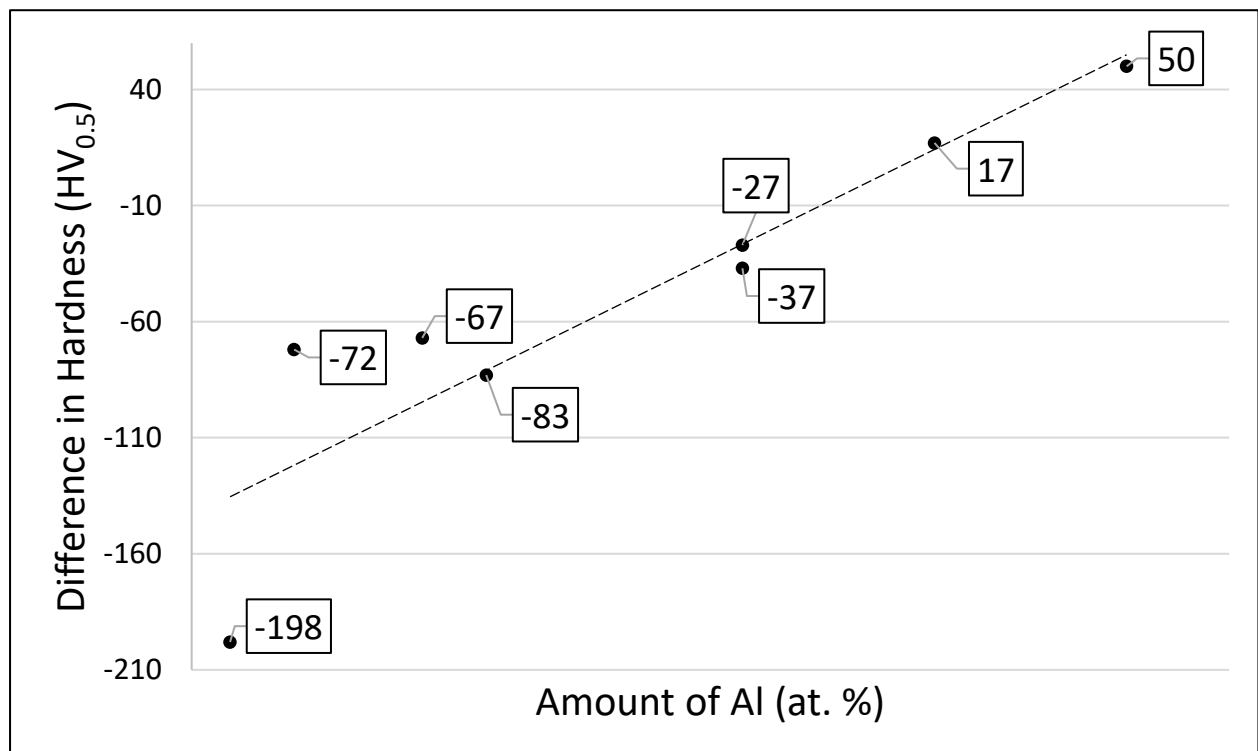


Figure 7.23 Hardness difference between the WQ and FC condition of the novel AlTiVCr-based compositions.

This difference in hardness between the two conditions is most prevalent in the case of the Al_6TiVCr alloy. Given the similarity of the microstructures between the FC and WQ condition of the Al_6TiVCr at the grain interior, it may be probable that the crystal structure of the grain interior is radically different. According to relevant studies, the B2 phase is characterised by a significantly higher yield strength (and subsequently higher hardness) in other BCC MCAs [82, 84, 237]. Naturally, the crystal structure here needs to be verified, but this is strong evidence in favour of the WQ Al_6TiVCr crystallising in the BCC structure and its FC counterpart in the B2 structure in the intergranular regions.

In terms of the experimentally measured elastic properties there was no notable difference between the WQ and FC conditions of the alloys (Fig. 7.24). Overall, it could be seen that the highest E was achieved in the equiatomic AlTiVCr alloy in both the WQ and FC condition. Nevertheless, multiple alloys displayed an $E > 180$ GPa demonstrating that significant compositional modifications would be needed produce the alloys that deviate from relatively high E values. As such, there did not seem to be a strong correlation between the amount of Al or Ti and E . Nonetheless, E did drop off for excessively high amounts of Al and Ti. Subsequently, it would also seem that higher amount of the Cr addition did not have an effect on E . Therefore, the hypothesis made in chapter 4 that a higher Cr would result in an elevated E has been disproved. Taking the *specific* E into consideration did however significantly alter the interpretation of these results. As seen in Fig. 7.25, the specific E of Al-Ti rich compositions is comparatively much higher than that of the Cr-V rich ones. More specifically, in both the WQ and FC condition the best performing composition would be the $\text{Al}_{14}\text{Ti}_{20}\text{VCr}$. This shows that achieving a lower density should be a critical design factor to consider when designing AlTiVCr -based alloys, given that otherwise E did not exhibit significant variation between the different compositions. Furthermore, the compositional freedom when designing with specific E in mind compared to simply E is more limited. Excessive or insufficient addition of either alloying element would seemingly lead to the manifestation of a lower specific E . As such, to achieve a sufficiently high specific E , a relative balance between the Al and Ti condition must be ensured. In contrast to the hardness, the lack of notable differences between the E of the Al_6TiVCr alloy in the WQ and FC condition indicates that the BCC and B2 phase would not differ significantly in terms of their elastic properties. Again, this is in line with the findings presented in Chapter 4.

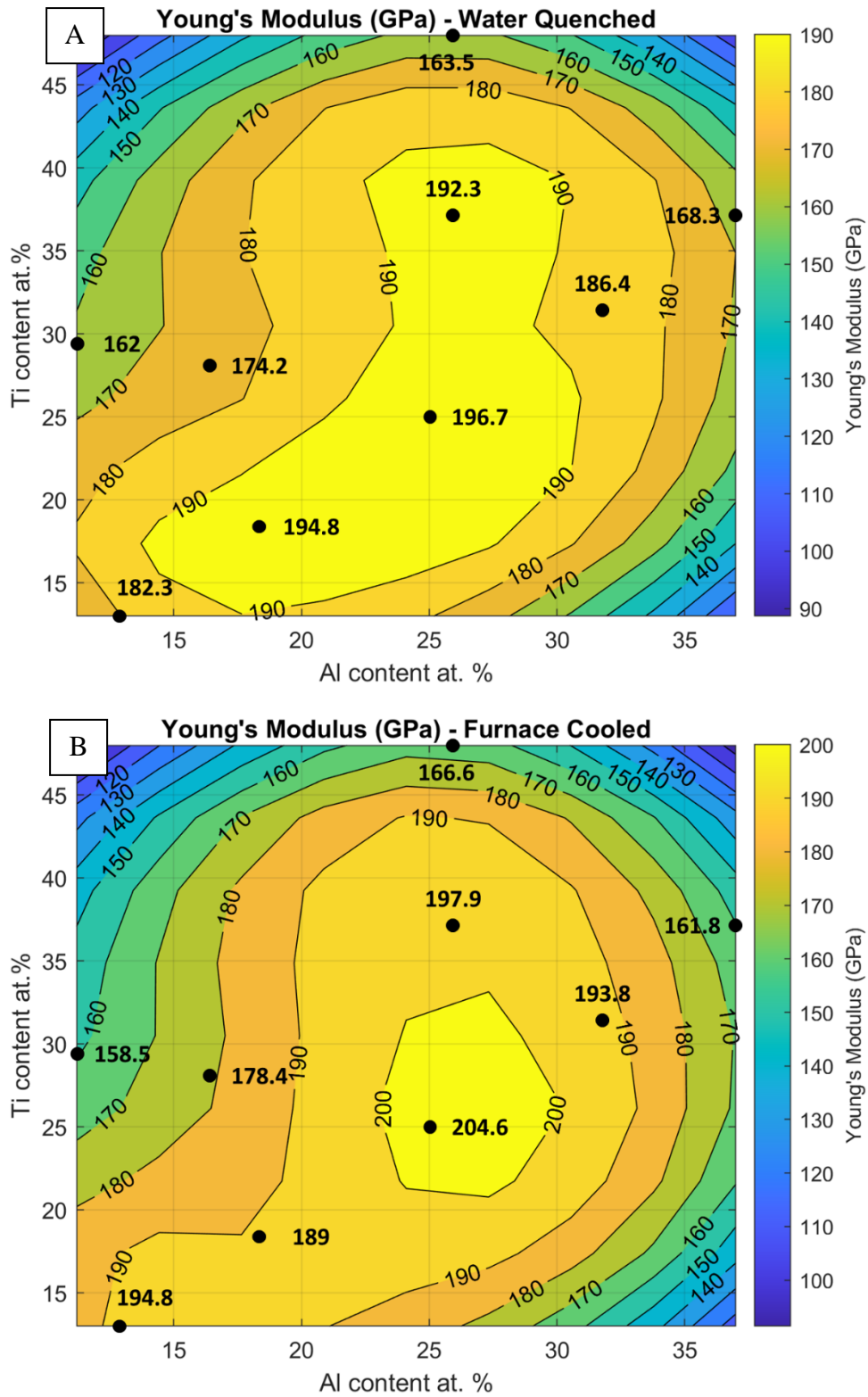


Figure 7.24 Experimentally measured Young's modulus of the novel AlTiVCr-based alloys in the A) water quenched (WQ) and B) furnace cooled (FC) conditions plotted in relation to the Al (at. %) and Ti (at. %) content.

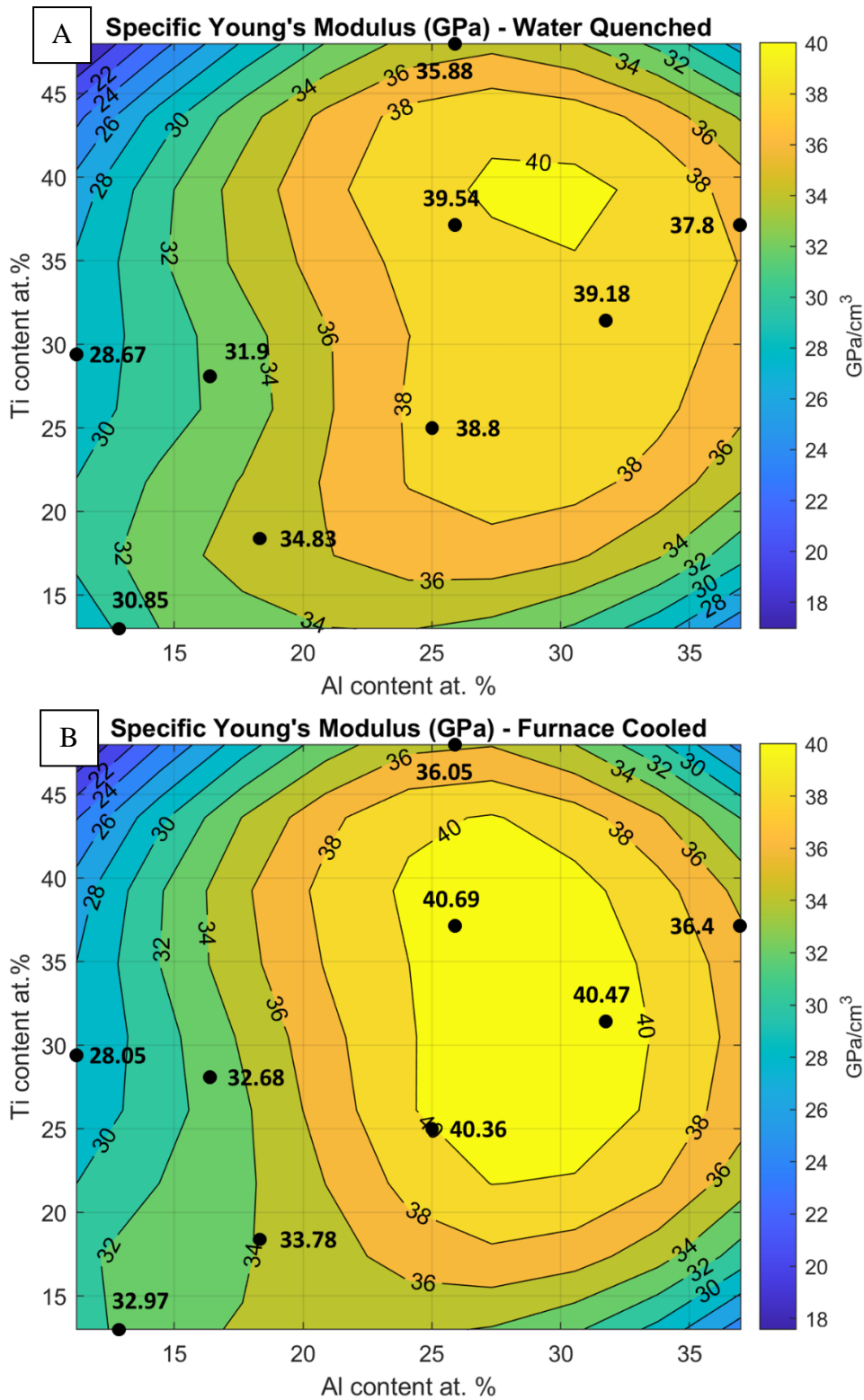


Figure 7.25 Specific Young's modulus of the novel AlTiVCr-based alloys in the A) water quenched (WQ) and B) furnace cooled (FC) conditions plotted in relation to the Al (at. %) and Ti (at. %) content. Density data was extracted using DFT calculations.

The stress-strain curves of the compression testing of the best performing novel AlTiVCr-based alloys are presented in Fig. 7.26. Unfortunately, all of the presented alloys achieved their maximum ductility in the FC condition, and this was still relatively limited. It is believed that

the reason behind the limited ductility of these alloys originated from the rapid cooling and heating cycles they were subjected to, causing them to develop extensive cracks. The relevant mechanism for this has been explained in chapter 5. The only exception to this would be the $\text{Al}_{20}\text{Ti}_{20}\text{VCr}$ alloy which showed a total elongation of over 12% with a notable compressive strength of 1320 MPa. The investigation of the origins of said ductility in this alloy is however outside the scope of this work as this alloy has been ruled out of the investigation due to its multiphase nature. The summary of the mechanical properties of all tested samples is provided in Table 7.11.

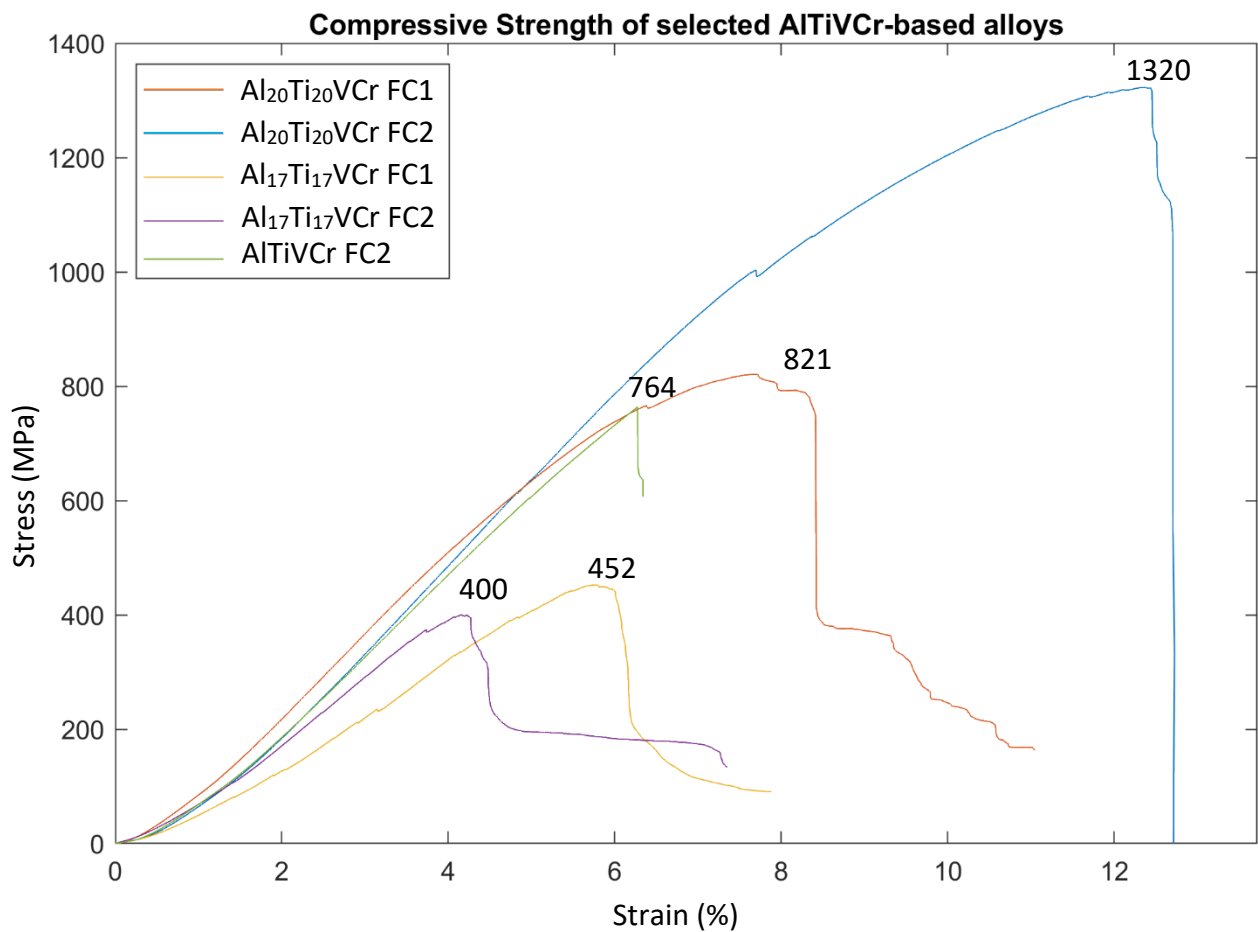


Figure 7.26 Compression testing curves of the $\text{Al}_{37}\text{Ti}_{37}\text{VCr}$ (FC), $\text{Al}_{31.5}\text{Ti}_{31.5}\text{VCr}$ (FC) and AlTiVCr (FC) alloys.

Table 7.11 Mechanical properties of the AlTiVCr-based alloys as extracted through compression testing where σ_m corresponds to the maximum compressive strength, σ_f to the compressive strength at failure, A_g the uniform plastic deformation and A_{50} the total elongation at fracture.

Alloy Name	σ_m (MPa)	A_g (%)	σ_f (MPa)	A_{50} (%)
Al ₂₀ Ti ₂₀ VCr FC2	1320	12.4	1320	12.4
Al ₂₀ Ti ₂₀ VCr FC1	821	7.7	164	11.1
Al ₁₇ Ti ₁₇ VCr FC1	452	5.8	90.4	7.9
Al ₁₇ Ti ₁₇ VCr FC2	400	4.2	133	7.4
AlTiVCr FC2	764	6.3	606	6.3
AlTiVCr WQ1	366	4.1	332	4.4
Al ₁₄ Ti ₂₀ VCr FC2	409	4.2	382	4.4
Al ₁₇ Ti ₁₇ VCr WQ2	387	3.8	373	3.9
AlTiVCr FC1	380	3.9	353	3.9
AlTiVCr WQ2	289	3.5	271	3.6
Al ₁₄ Ti ₂₀ VCr WQ1	373	3.3	370	3.3
Al ₂₀ Ti ₂₀ VCr WQ1	273	3.2	246	3.3
Al ₁₇ Ti ₁₇ VCr WQ3	76.8	2.8	33.2	3.2
Al ₁₇ Ti ₁₇ VCr WQ1	191	2.6	164	2.9
Al ₂₀ Ti ₂₀ VCr WQ3	149	2.8	144	2.9
Al ₁₄ Ti ₂₀ VCr WQ2	216	2.6	171	2.7
Al ₁₄ Ti ₂₀ VCr FC1	61.4	2.1	37.6	2.5
Al ₂₀ Ti ₂₀ VCr WQ2	178	2.2	173	2.3

7.3.2.4 Transmission Electron Microscopy

7.3.2.4.1 Al₉TiVCr – Water Quenched (WQ)

The microstructure of the investigated section of the WQ Al₉TiVCr (Fig. 7.27) alloy consisted of a grain boundary and two grains. Interestingly, the diffraction pattern of both grains corresponded to a B2 crystal structure.

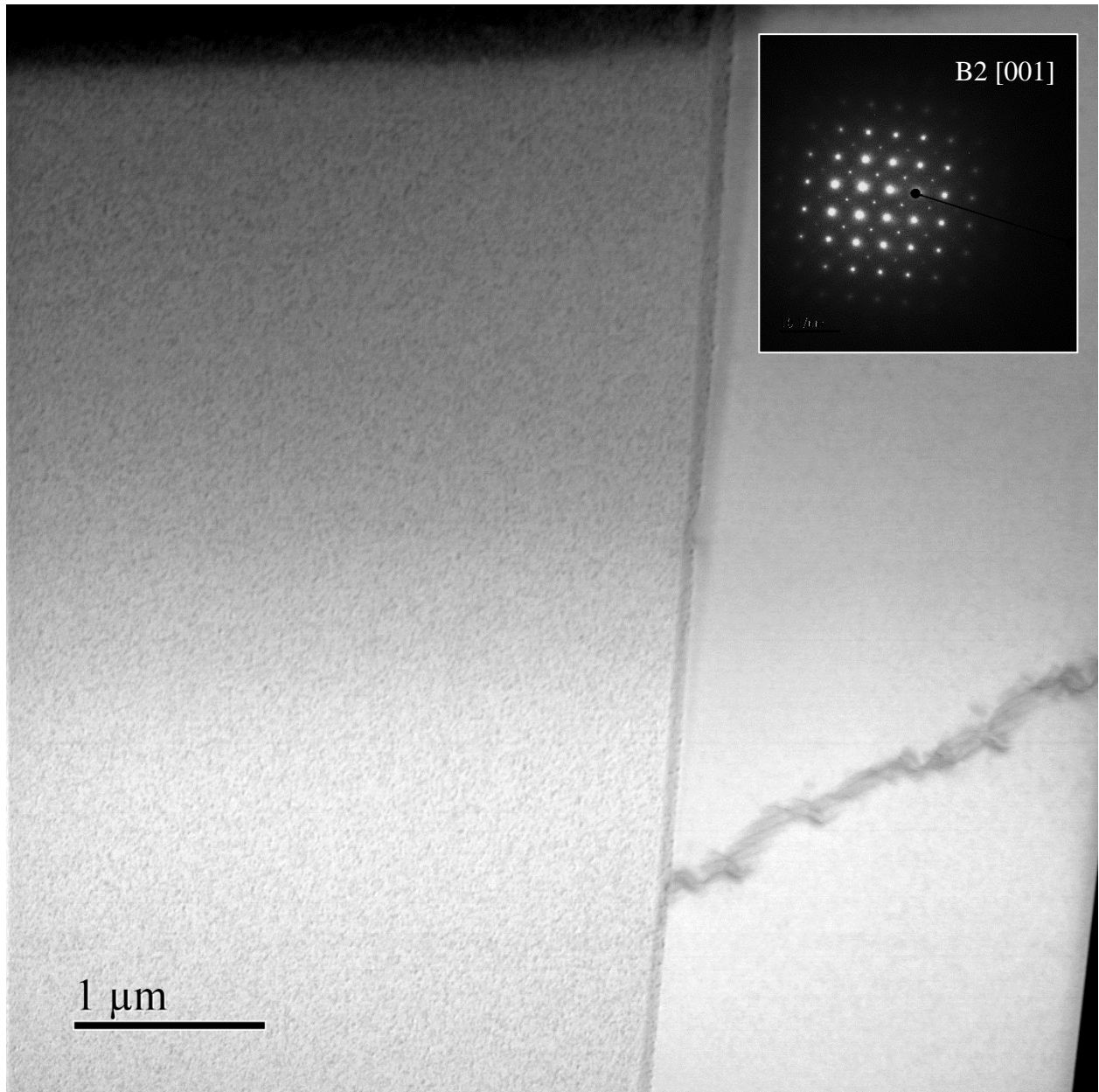


Figure 7.27 Bright field (BF) STEM image showing a section of the microstructure of the water quenched (WQ) Al₉TiVCr sample consisting of two grains and a grain boundary, and the relevant diffraction pattern. Both grains were characterised by a B2 crystal structure.

This finding was rather unexpected given the observations made in sector 7.3.2.2. This could indicate that the heat treatment temperature was improperly set or that the temperature where the order-disorder transformation would occur in this alloy would be higher than the heat

treatment temperature. Nevertheless, this finding is rather questionable and not truly in line with the subsequent findings of the investigation since it would indicate that either the heat treatment was not carried out properly or that the order-disorder transformation temperature may lie above 1200°C. However, a repeat experiment could not be performed within the available time.

7.3.2.4.2 Al₉TiVCr – Furnace Cooled (FC)

In the FC condition, the Al₉TiVCr alloy was characterised by a dualphase microstructure consisting of alternating BCC and B2 plates (Fig. 7.28). As previously mentioned, the nucleation of this microstructural constituent originated from TiN particles formed along the grain boundaries. Although a finer structure is visible inside the grains, reliable diffraction patterns could not be extracted. Instead, the grains were found to crystallise in the B2 crystal structure. Judging from the darkfield (DF) image, the alternating phases are each comprised by lighter and heavier elements respectively. This is reinforced by the EDX results (Fig. 7.29) illustrating the Cr and V predominantly occupying one phase and Al, Ti the other. However, it was not possible to correlate a distinct BCC or B2 pattern to specific phases due to the B2 superlattice reflections distorting the clarity of diffraction patterns corresponding to a BCC crystal structure. This could also indicate that the BCC phase is instead characterised by a minor degree of ordering. This was originally proposed in chapter 6 and was also mentioned in the literature [82].

Fig. 7.30 shows an EDX quant map of the intergranular region containing the alternating plate-like structure or particles. These were enriched in Cr and V while their neighbouring region was enriched in Al and Ti instead. It could be that the Cr-V-rich phase started forming within an original B2 grain and either constitutes a BCC particle or a Cr-V-based Laves phase. The latter case should not be possible given the extensive solubility of the Cr-V binary and the distinct lack of Al and Ti detected in the region of interest, given that Ti especially would be necessary for the formation of the Laves phase [260]. As a reference point, the Laves phase suggested to be present in this alloying system by ThermoCalc would be a C14 (Al,Ti)_xCr_y, resulting in additional HCP superlattice reflections. Therefore, the remaining option would be for the particle to correspond to the BCC phase which has significant implications regarding the phase formation mechanisms encountered in this system.

More specifically, the relevant literature [84, 261-264] regarding BCC-B2 transformation suggests that it occurs through a spinodal decomposition mechanism [165] which has also been

described in chapter 2. However, for the BCC phase to be forming intergranularly would imply that the matrix phase would be the B2 as the decomposition occurs. This would then mean that the B2 phase would be stable up to the heat treatment temperature, that being 1200°C or perhaps even higher. Therefore the transformation sequence would occur as follows. Assuming that a high temperature BCC does exist, the alloy must have undergone a BCC to B2 phase transformation, only to start spinodally decomposing at even lower temperatures back into B2 + BCC or even completely into BCC eventually. These transitions are in fact predicted by thermodynamic calculations using TCHEA2 (Fig. 7.5) showing the Al₉TiVCr alloy displays a high temperature BCC region (above ~670°C), a lower temperature B2 region (~500-550°C), a low temperature BCC + B2 region (480-500°C) before eventually reaching the single phase BCC region. The same effect can be identified using the TCHEA5 database (Fig. 7.6) but for an Al content below 15 at. %. Alternatively, a different phenomenon manifests at the grain boundaries where the nucleation of the BCC/B2 microstructural constituent possibly takes place at the TiN interphase boundaries as evident through the SEM/TEM. There this dualphase structure spreads towards the interior of the grain and appeared to have a point of origin meaning that it is unlikely to be the product of a spinodal decomposition process. This hypotheses mechanism would require significant research efforts to prove through a series of low temperature heat treatments.

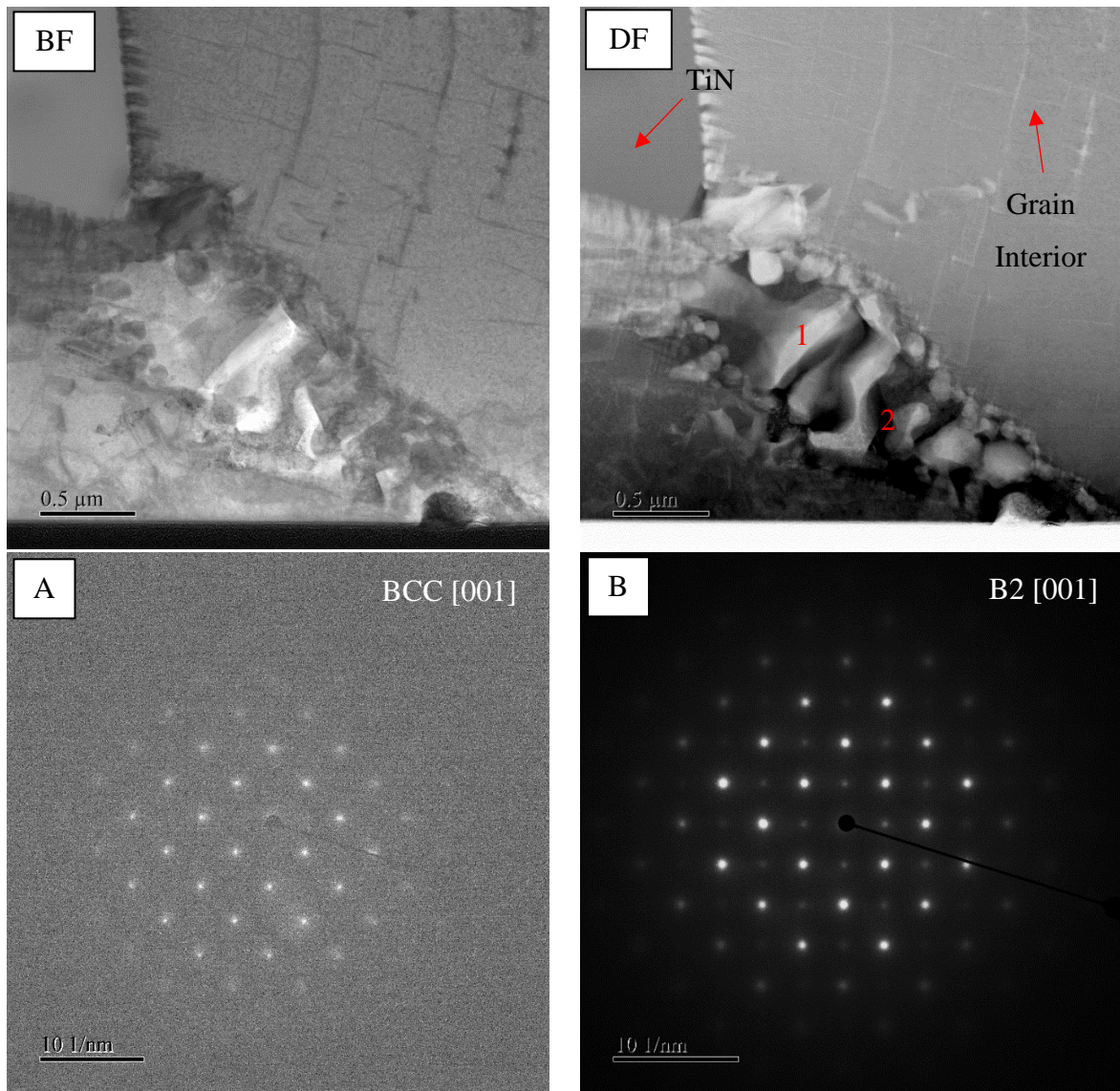


Figure 7.28 STEM bright field (BF) and dark field (DF) images showing the edge of a TiN particle and the surrounding dualphase BCC/B2 microstructure as evident in the A, B) diffraction patterns at positions 1 and 2 respectively as denoted on the DF image.

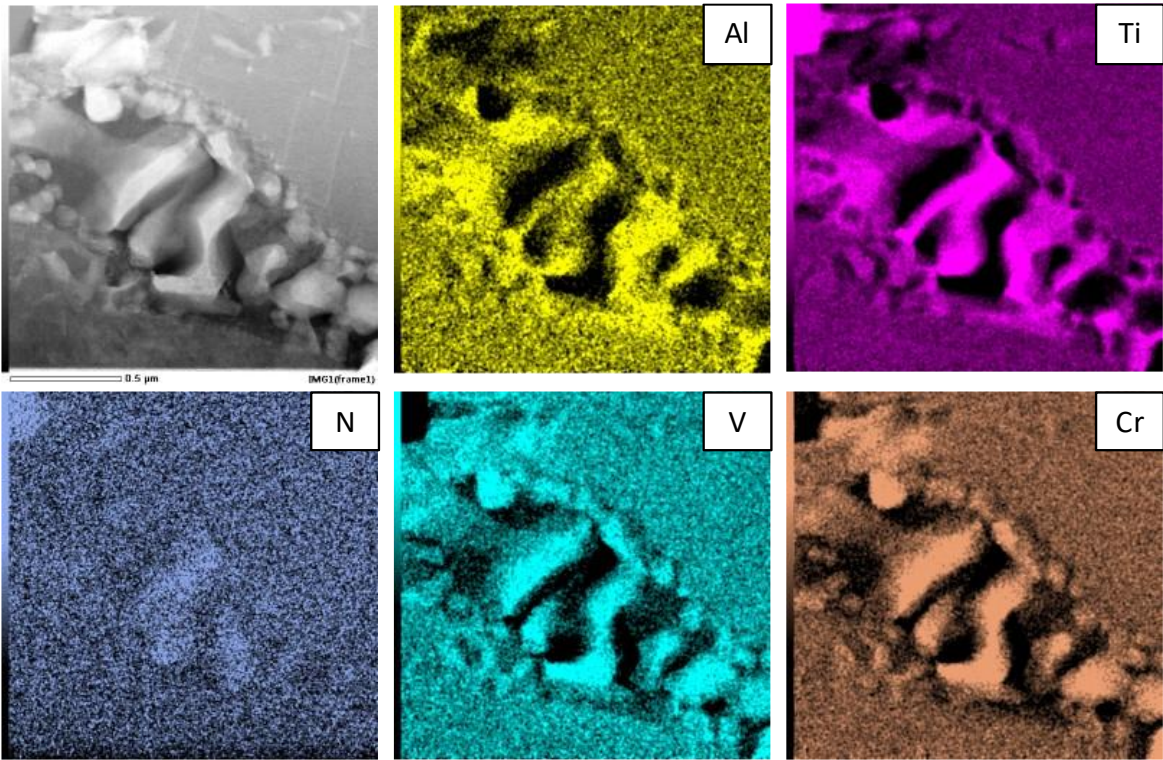


Figure 7.29 EDX quant maps illustrating the distribution of the alloying elements.

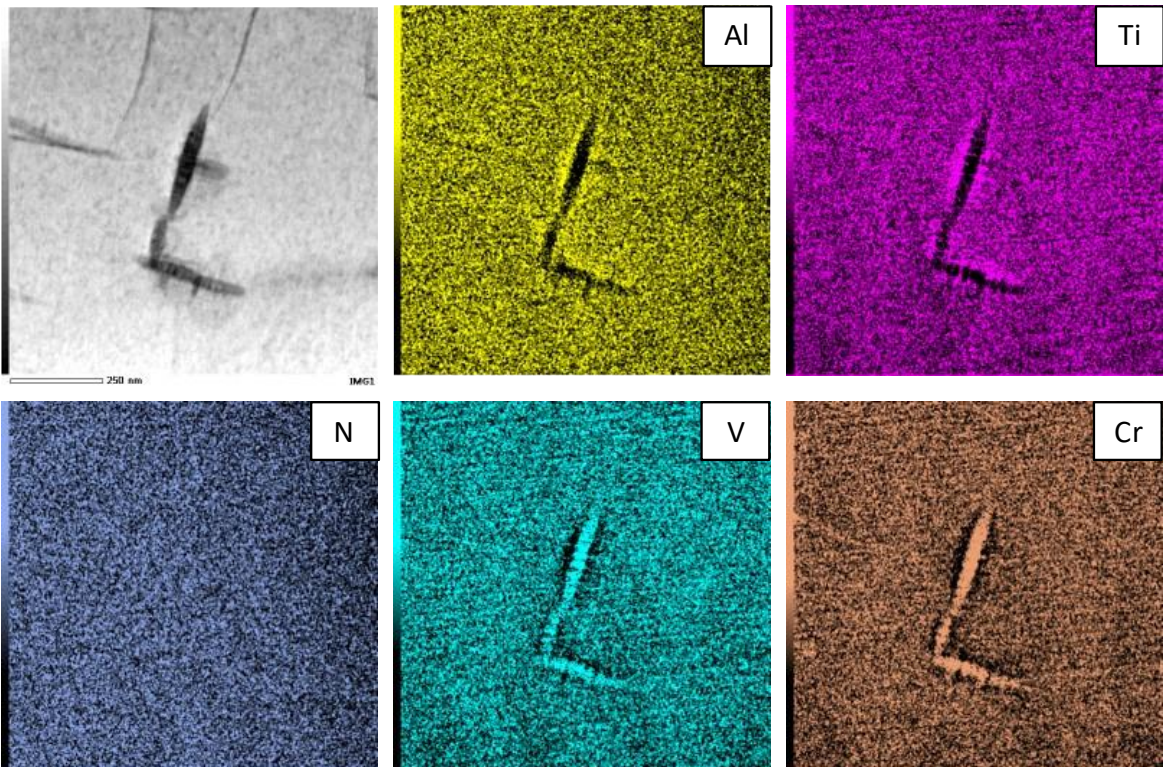


Figure 7.30 EDX quant maps illustrating the distribution of the alloying elements around a particle.

7.3.2.4.3 Al₆TiVCr – Water Quenched (WQ)

The microstructure of the investigated section of the WQ Al₆TiVCr (Fig. 7.31) alloy consisted of a grain boundary and two grains. The diffraction pattern of both grains corresponded to a BCC crystal structure which was expected according to all the aforementioned results. Therefore, the retention of a single phase metastable BCC phase to room temperature was achieved.

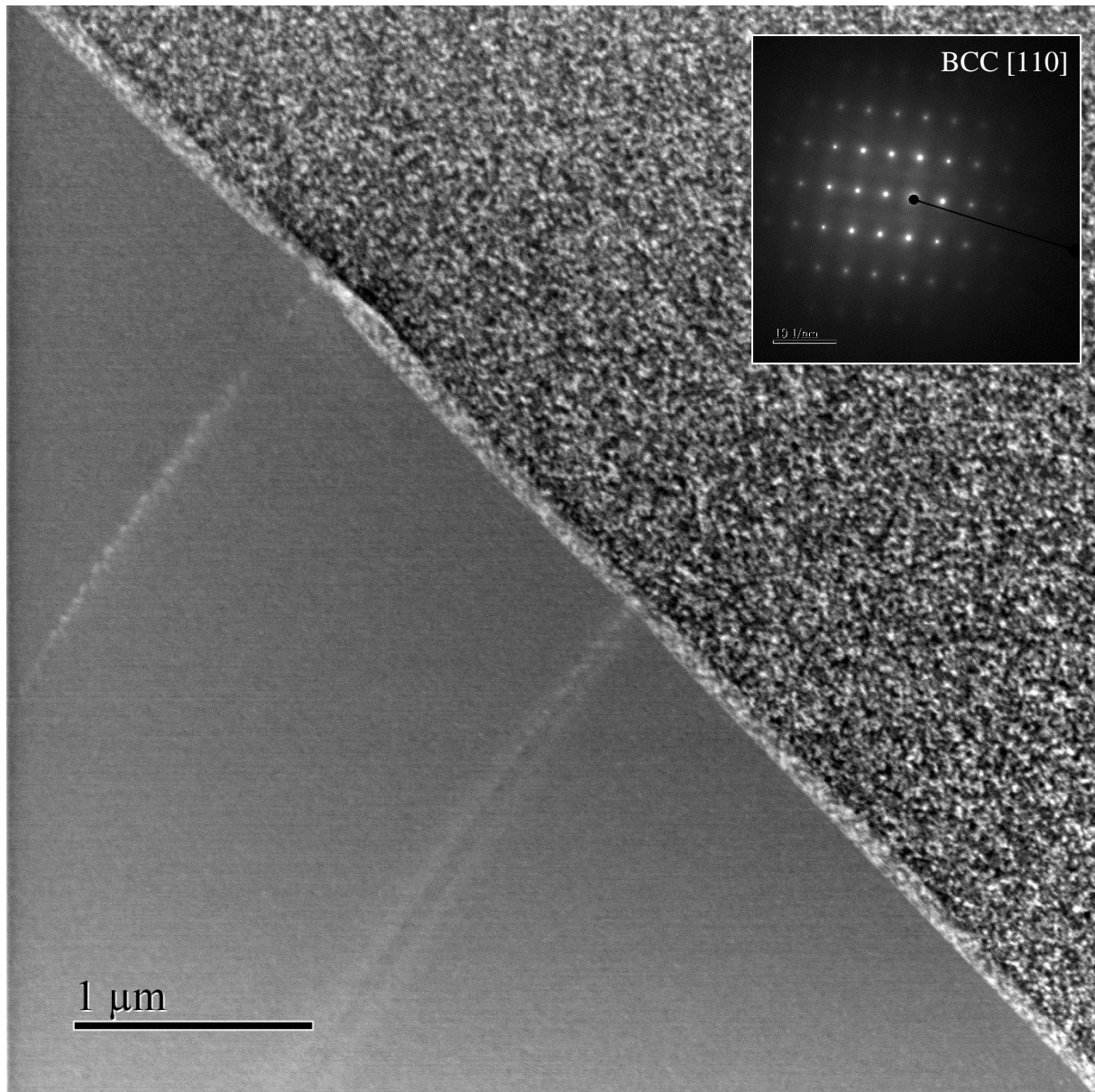


Figure 7.31 High angle annular dark field (HAADF) image showing a section of the microstructure of the water quenched (WQ) Al₆TiVCr sample consisting of two grains and a grain boundary, and the relevant diffraction pattern. Both grains were characterised by a BCC crystal structure.

7.3.2.4.4 Al₆TiVCr – Furnace Cooled (FC)

In the FC condition, the Al₉TiVCr alloy was characterised by a dualphase microstructure consisting of alternating BCC and B2 plates (Fig. 7.32-7.33). Again, the intergranular region was found to crystallise in the B2 crystal structure. TiN particles are evident alongside the BCC-B2 structure.

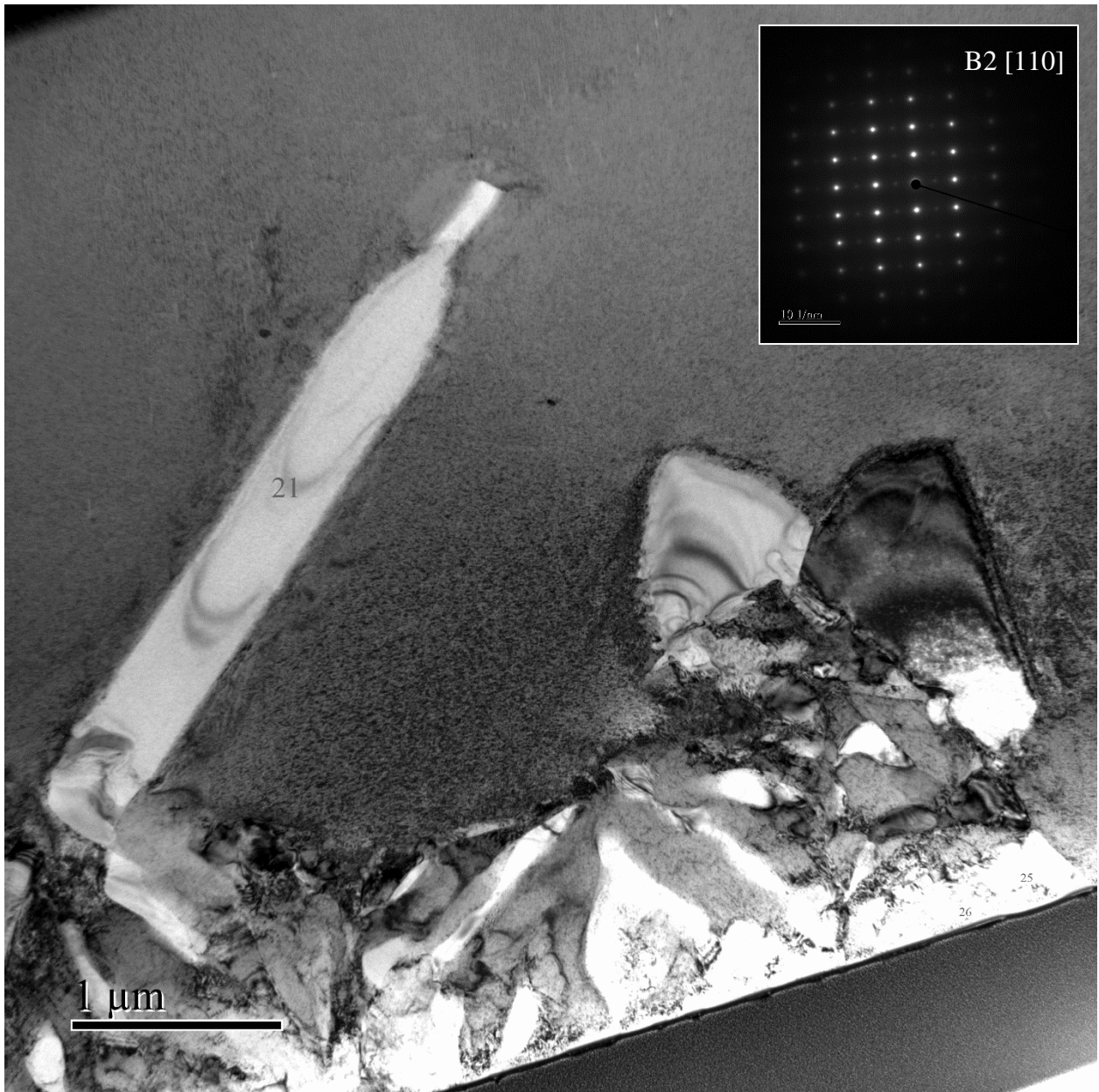


Figure 7.32 Bright field (BF) STEM image showing a section of the microstructure of the furnace cooled (FC) Al₆TiVCr sample consisting of TiN particles distributed along a grain boundary and the BCC/B2 structure. The interior of the grain was characterised by a B2 crystal structure.

As seen in Fig. 7.33, distinct regions of alternating plates corresponding to the B2 and BCC crystal structures were identified. It must be noted that, compared to the Al₉TiVCr alloy, the B2 superlattice reflections were entirely missing from regions corresponding to the BCC

crystal structure. In addition, the B2 superlattice reflections of the grain interior were rather weak, indicating that perhaps the matrix phase is instead comprised of a highly ordered BCC phase instead of a distinct B2 phase. Furthermore, by matching the explicit BCC and B2 regions to the relevant EDX quant maps (Fig. 7.34-7.35) it was verified that indeed the Cr-V-rich region corresponded to the BCC phase and the Al-Ti-rich to the B2. Therefore, the previously discussed hypothesis regarding the formation of the BCC and B2 phases is consistent with the observations from this sample. In this particular case, intergranular BCC particles were not present; the BCC-B2 phase transformation had a point of origin, that being the grain boundaries and TiN particles, and as such is not necessarily a product of a spinodal decomposition. Lastly, it needs to be mentioned that both the BCC and B2 regions contained minimal amounts of contaminants, namely N which seemed to be exclusively limited to the TiN particles.

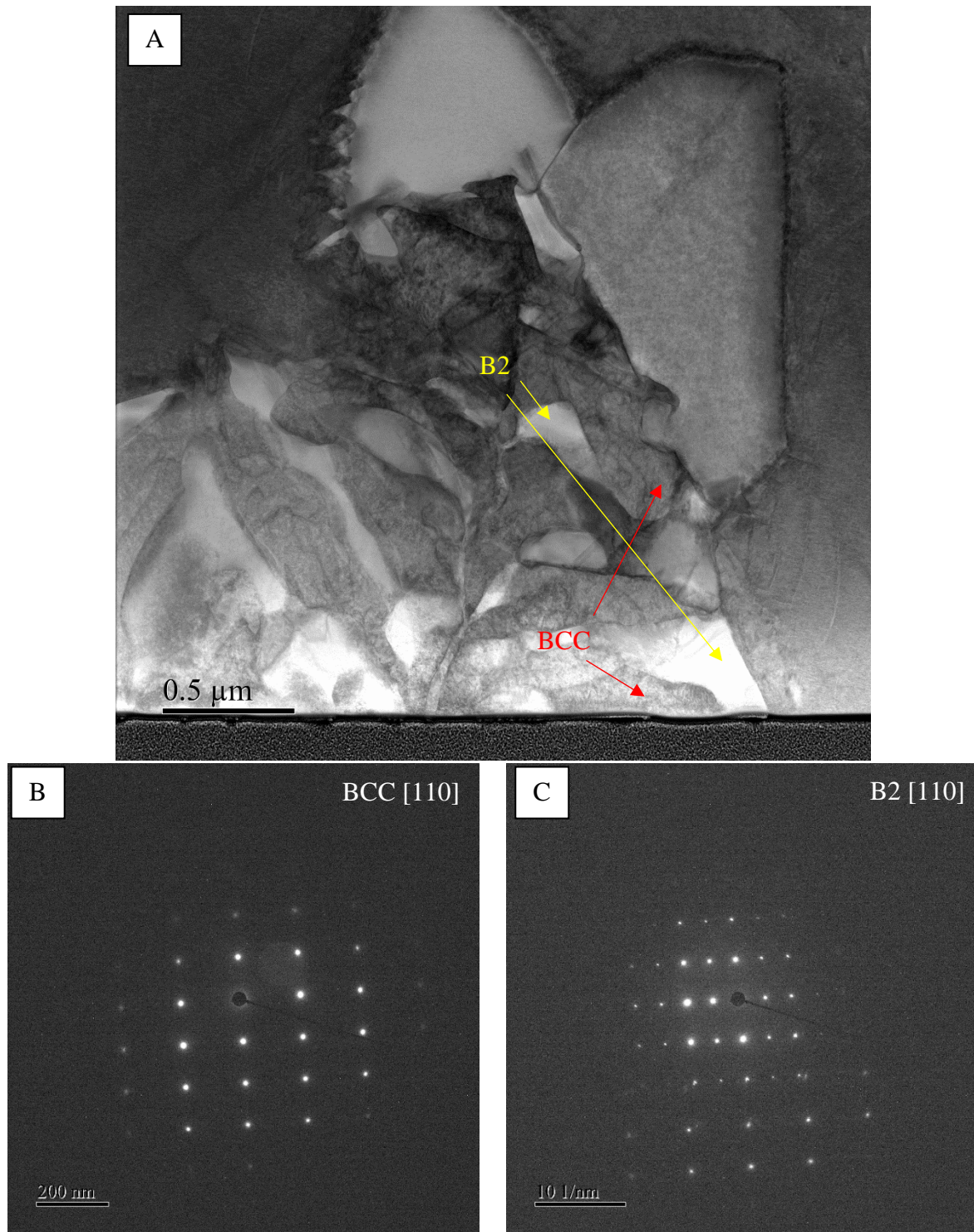


Figure 7.33 Bright field (BF) STEM image showing A) a section of the microstructure of the furnace cooled (FC) Al₆TiVCr sample consisting of a TiN particle and the BCC/B2 structure. The identification of specific regions corresponding to the B) BCC and C) B2 phase respectively was achieved.

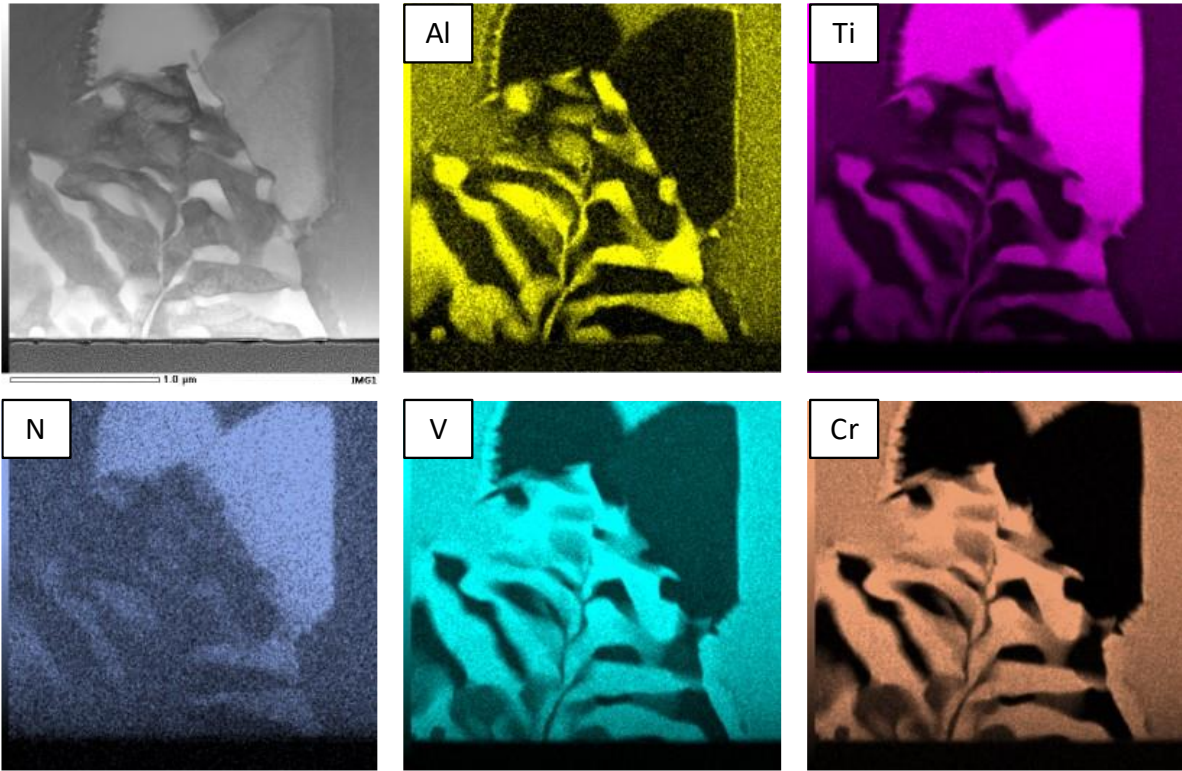


Figure 7.34 EDX quant maps illustrating the distribution of the alloying elements.

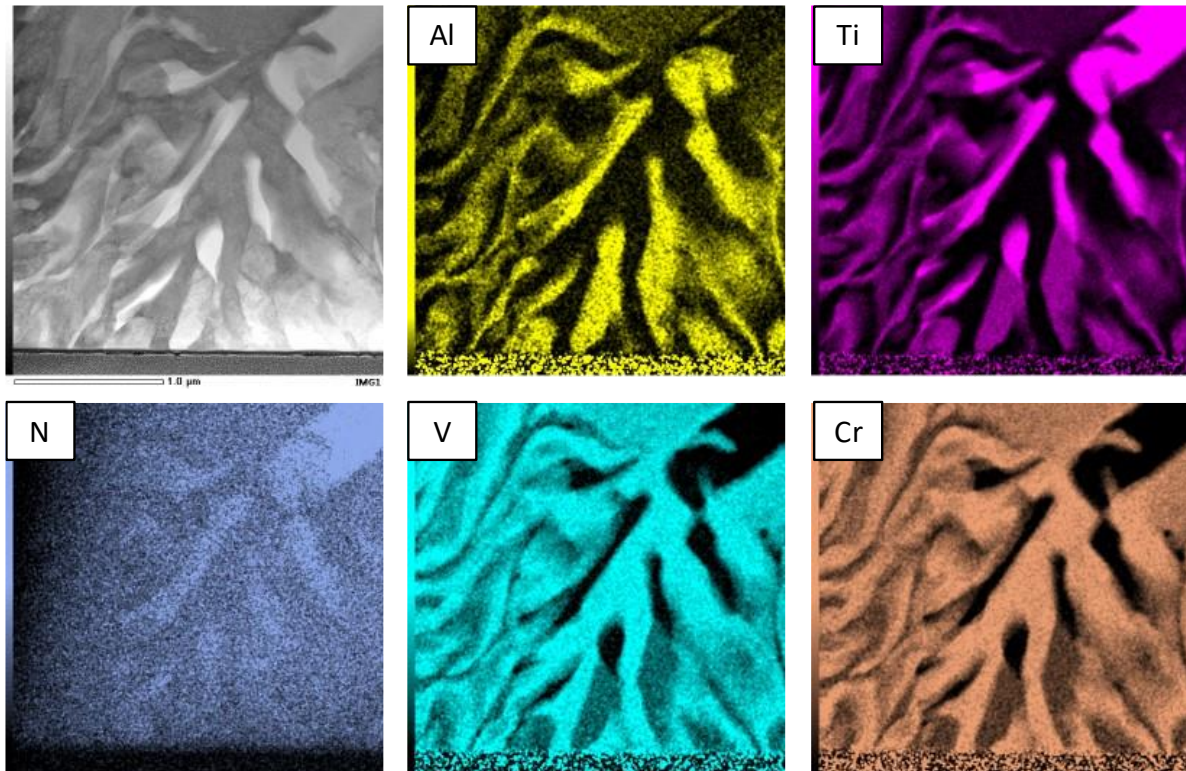


Figure 7.35 EDX quant maps illustrating the distribution of the alloying elements along the alternating plates of the BCC/B2 structure.

7.4 Implications

Thus far this research has produced significant findings regarding the formation mechanisms dictating the BCC-B2 transformation and has achieved the discovery of an alloy consisting of a single phase metastable BCC microstructure at room temperature by entirely suppressing the order-disorder transformation. Nevertheless, the findings of this work may have even greater implications. An aspect of this work that has not yet been extensively discussed is the success of the computational methods for predicting phase formation in the present system. Through the pyMPEALab toolkit, alloys forming unstable solid solutions were correctly identified, namely the $\text{Al}_{14}\text{Ti}_{26}\text{VCr}$, $\text{Al}_{20}\text{Ti}_{20}\text{VCr}$ and $\text{Al}_{17}\text{Ti}_{17}\text{VCr}$, with the $\text{Al}_{14}\text{Ti}_{20}\text{VCr}$ being considered borderline unstable. Then, with the use of DFT, this lack of stability was quantified. The $\text{Al}_{14}\text{Ti}_{26}\text{VCr}$ and $\text{Al}_{20}\text{Ti}_{20}\text{VCr}$ were found to be entirely unstable, while the $\text{Al}_{17}\text{Ti}_{17}\text{VCr}$ and $\text{Al}_{14}\text{Ti}_{20}\text{VCr}$ were more stable by comparison. Lastly, ThermoCalc was able to capture the crystal structure of the matrix phase with relatively good accuracy, that being BCC or B2, and provide some insight regarding the formation of SPPs in the unstable systems. The combination of these techniques enabled the correct prediction of all alloys that would form stable solid solutions and at the same time provide information regarding the potential microstructural constituents of unstable alloys with reasonable accuracy. The question that remains however is the performance of the model in terms of capturing the elastic properties of the investigated alloys.

By comparing the computational to the experimental results, a deviation of up to 11.2% was found in cases where the alloys were single phase or constitute of a BCC-B2 microstructure (Fig. 7.38). This level of accuracy would be considered adequate to gain a general understanding of the material behaviour, while finer trends may not be easily distinguishable. Nevertheless, the model has good predictive capability and is shown to be relatively consistent. However, it can be seen that in cases where the alloys would be considered unstable according to the DFT calculations, the predictive power diminishes greatly, with deviations from experimental values reaching up to 34.9%. Therefore, it would be advisable to thermodynamically assess compositions of interest before using DFT to avoid extracting unreliable results. As discussed previously, combining the aforementioned thermodynamic modelling techniques yields an accurate description of novel materials, acting as a precursor to the modelling of the mechanical behaviour of novel alloys.

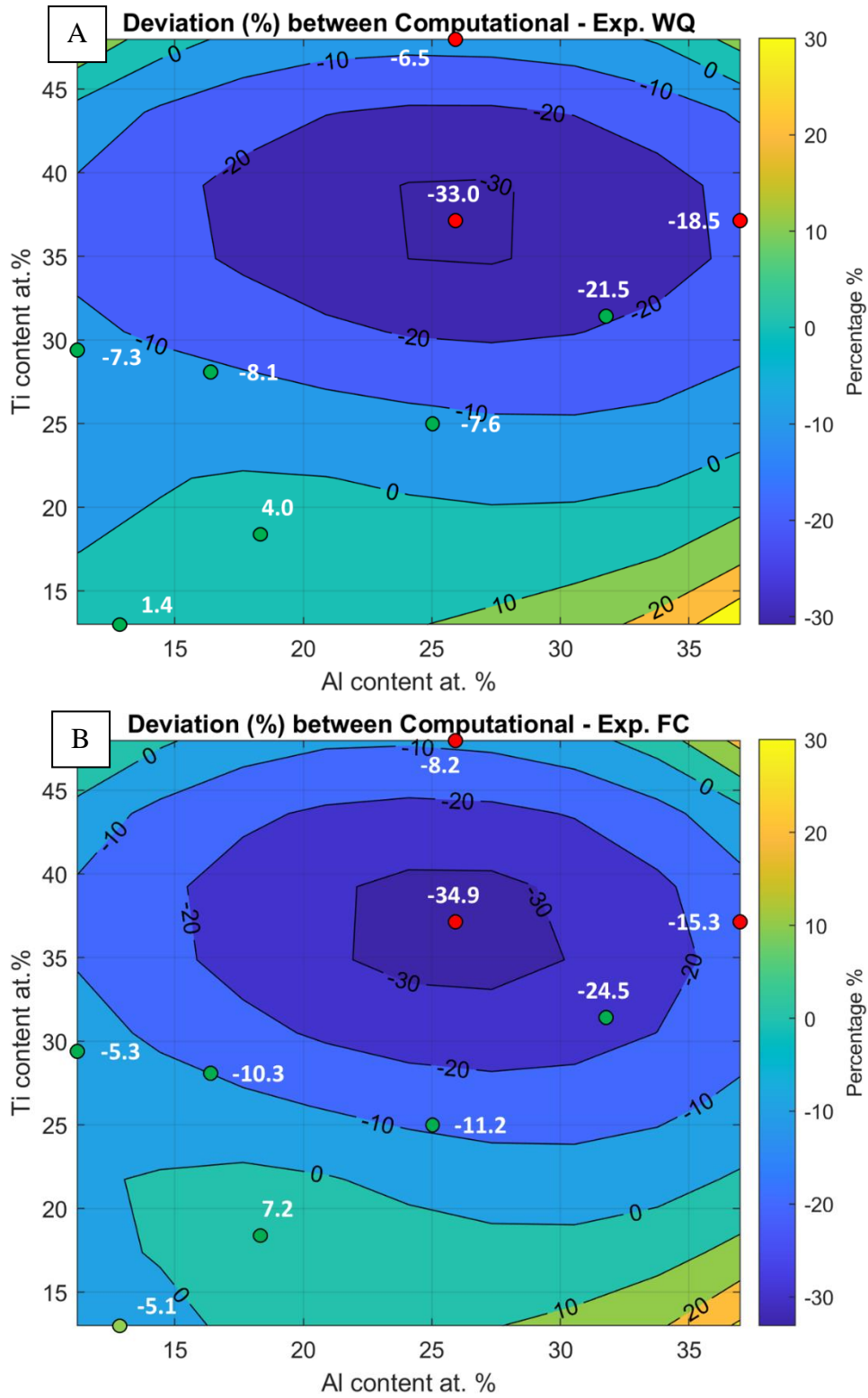


Figure 7.36 Deviation between the computationally derived compared to the experimentally measured Young's modulus in the A) water quenched (WQ) and B) furnace cooled (FC) condition of the novel AlTiVCr-based alloys in relation to the Al (at. %) and Ti (at. %) content.

The final, and perhaps grander, implication of this work lies once again in the elastic properties of the assessed systems. The rule of mixtures has been commonly used in MCAs to predict their elastic properties [265] and has been found to work generally well for most single phase alloying systems. Given that the AlTi-based SPPs found in the compositions studied within this work have an E that is similar to that of the alloy during the experimental measurement, it is expected that the E of the matrix phase and the particle would be nearly the same. As such, even multiphase materials in this work should not deviate significantly from the rule of mixtures (ROM). Nevertheless, as seen in Fig. 7.39 that is not the case. Significant deviations from the ROM are typically encountered in intermetallics such as AlTi. This may be because their bonds are partially covalent instead of metallic in character, with the greater bond stiffness resulting in elastic properties far above those predicted by the rule of mixtures. A similar effect could be taking place in this alloying system. Alloys low in Al seem to be perfectly described by the ROM; however, as the amount of Al increases their E starts to exceed that predicted by the ROM by up to 43.4% and 43.5%, as seen in the case of the FC Al₁₇Ti₁₇VCr (single phase) and FC Al₁₄Ti₂₆VCr (multiphase). As such, it is possible that in cases where the alloys remain single phase instead of forming IMs, the entire alloy becomes an IM, in the form of a highly ordered B2 structure. Subsequently, increasing amounts of Al may not only destabilise the BCC phase by promoting the formation of the B2 phase, but may also progressively transform the bond of the alloy from metallic to partially covalent or ionic. This could also provide an explanation regarding the lack of inherent ductility in Al-rich AlTiVCr since highly directional bonds are associated with poor ductility. At the same time, the partially covalent nature of the bond would be the origin of the elevated elastic properties of these alloys. If this is the case, further development of this alloying system would require an optimal Al content to be established, that combines the benefits of the covalent and metallic bond nature this alloy can attain. In turn, if found to be correct by further experimental investigation, this design principle could be a precursor for novel material design methodologies to develop and evolve.

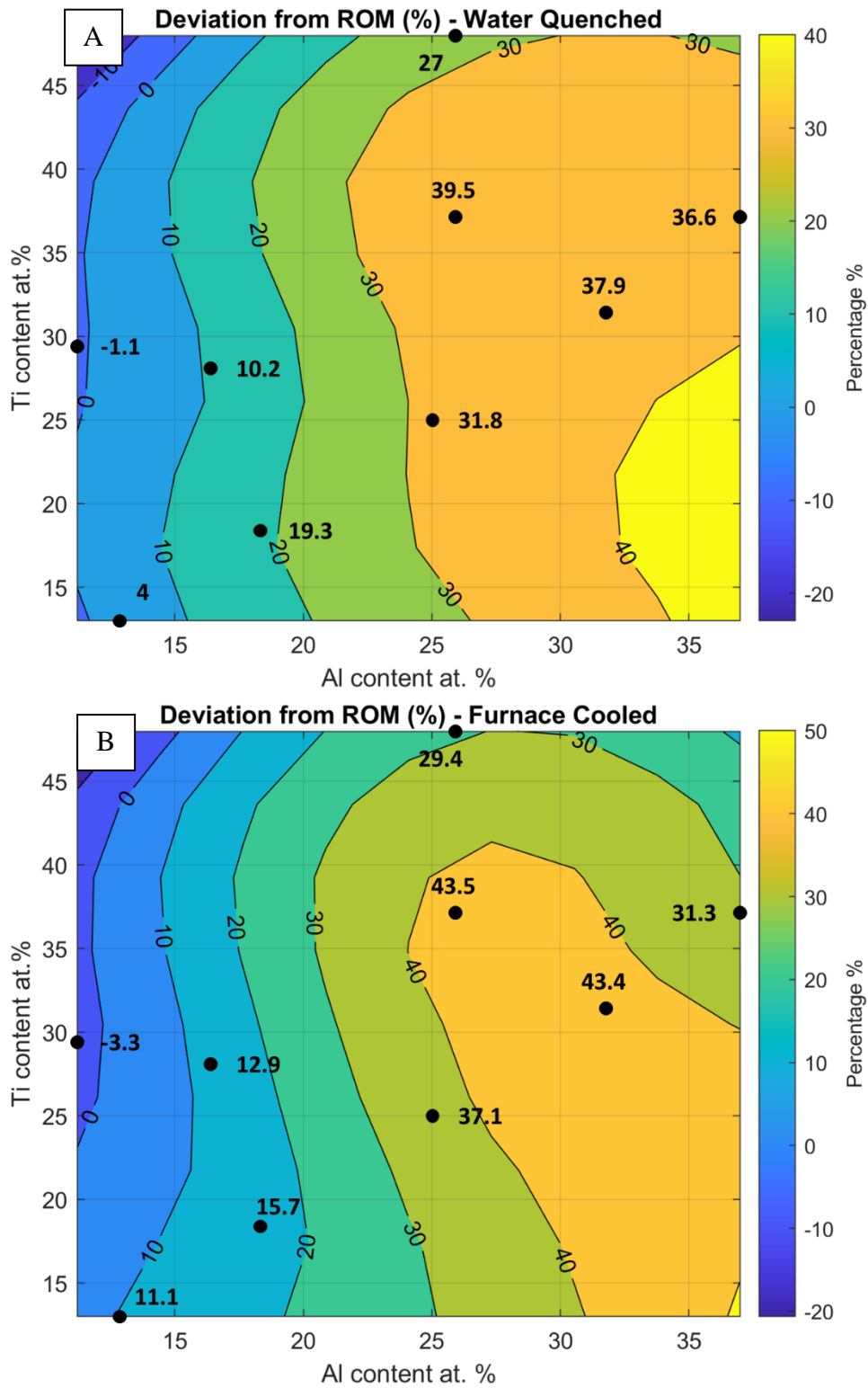


Figure 7.37 Deviation between the experimentally measured and calculated according to the Rule of Mixtures (ROM) Young's modulus of the novel AlTiVCr-based alloys in the A) water quenched (WQ) and B) furnace cooled (FC) conditions plotted in relation to the Al (at. %) and Ti (at. %) content.

7.5 Conclusions

This work concerned the development of a novel series of AlTiVCr-based alloys with the aim of retaining a single phase BCC structure at room temperature by entirely suppressing the order-disorder transformation. To do this, predictive thermodynamic modelling techniques were used to pinpoint appropriate chemical compositions. DFT calculations were additionally carried out to estimate the elastic properties of these compositions. Subsequent experimental work verified the thermodynamic and elastic properties calculations, showing that the relevant models was sufficiently accurate to aid the design of the novel compositions. The Al_{11.1}TiVCr alloy was successfully designed to fully suppress the order-disorder transformation and instead exclusively contain a metastable BCC microstructure upon WQ. In the FC condition the alloy was also characterised by a dualphase BCC-B2 microstructure. The key findings of this work are summarised below:

1. The combination of empirical rules, DFT and CALPHAD produces accurate predictions regarding phase stability in AlTiVCr-based MCAs.
2. The thermal conductivity of all compositions remained relatively constant between 3.34 – 5.52 Wm⁻¹K⁻¹.
3. The samples in the WQ condition exhibited more cracks compared to the FC ones due to the manifestation of a thermal shock effect. As such, the WQ samples which were subjected to compression testing were also characterised by inferior ductility compared to the FC ones since their structural integrity had been compromised.
4. The Al_{11.1}TiVCr alloy exhibited a single phase BCC microstructure in the WQ condition while both the Al_{11.1}TiVCr and Al_{16.7}TiVCr alloys consisted of a dualphase BCC + B2 microstructure in the FC condition.
5. The Cr-V rich phase corresponded to the BCC phase while the Al-Ti rich to the B2.
6. Minor differences were observed between the experimentally measured Young's modulus compared to the one calculated through DFT in alloys with low Al content. A progressive increase in Al did however, result in significant deviations between the model and experiment, with the computational approach underestimating the modulus by up to 34.9%. A similar trend was observed when comparing the ROM to the experimentally measured values, with the experimental values surpassing those predicted through the ROM by up to 43.5%.
7. Increasing amounts of Al may not only destabilise the BCC phase by promoting the formation of the B2 phase but may also progressively transform the bond of the alloy

from metallic to partially covalent or ionic. This could also provide an explanation regarding the lack of inherent ductility in Al-rich AlTiVCr since highly directional bonds are associated with poor ductility.

8. Conclusions

The aim of this thesis was to investigate the feasibility of the design of novel high stiffness lightweight MCAs. This was achieved through the utilisation of both experimental and computational techniques for identifying candidate systems. The path towards reaching that goal has been described across multiple chapters, each one pushing the narrative and our understanding of MCAs forward in a different manner.

The first chapter introduced a methodology for predicting the elastic properties of any single phase or multiphase alloy through ICME. The method sequentially utilised CALPHAD for predicting phase formation and stability in novel systems, followed by DFT for the individual assessment of each phase in terms of its density, crystallographic and elastic properties, and homogenisation modelling through FEM for calculating the unified elastic properties of the material. The feasibility of this methodology was experimentally confirmed through the assessment of the equiatomic AlTiVCr and AlTiVCr-Si_{7.2} alloys where a deviation of ~10% and <2% was identified between prediction and experimental verification in each case, respectively. The applicability of this methodology was deemed to be universal, with its effectiveness depending exclusively on the accuracy of each individual computational package used. Simultaneously, it was discovered that both alloys were characterised by a particularly elevated specific Young's modulus lying at 38-41 GPa·cm³g⁻¹, far surpassing advanced high modulus steels at 33-34 GPa·cm³g⁻¹.

The second chapter focused on the further assessment of both systems, leading to the identification of a distinct lack of ductility in both cases. The underlying factor for the failure of the alloys was identified to be their abnormally low thermal conductivity compared to other alloys at 4.77 Wm⁻¹K⁻¹, leading to thermal shock during exposure to rapid thermal cycles. This effect was exacerbated by the inherent lack of ductility of the alloys. This could be attributed to a high DBTT due to their increased Cr content or the formation of a B2 matrix phase manifesting through an order-disorder transformation. Neither the incorporation of Mn (aimed at reducing the DBTT) or performing low temperature heat treatments (to induce the formation of Al-based SPPs) was successful in the improvement of the ductility of the tested alloys. Furthermore, in the case of the heat treatment, no samples exhibited the formation of SPPs while heat treating at 600°C for 24h led to the disintegration of all samples. As such, the only remaining pathway for suppressing the order-disorder transformation without proceeding with compositional modifications was by heat treating at an elevated temperature followed by WQ.

This was confirmed at the third chapter where a heat treatment at 1200°C for 8h followed by WQ was demonstrated to be sufficient in partially suppressing the order-disorder transformation. This resulted in the manifestation of a dualphase microstructure consisting of alternating plates of the BCC and B2 phase. It was also noted that one of the two phases was enriched in Al-Ti and the other in Cr-V; however, it was not possible to clearly distinguish which phase corresponded to which crystal structure due to superlattice reflections. Nevertheless, it was observed that the suppression of the order-disorder transformation did not result in an increase in ductility. This is reasonable given the low thermal conductivity of the alloy, which exacerbates the thermal shock effect resulting in the extensive cracking of the sample, thus compromising its structural integrity.

The fourth and final chapter of the thesis concerned the design of novel AlTiVCr-based alloys. These compositions were tailored to suppress the order-disorder transformation while maintaining a single phase microstructure and retain the specific elastic properties exhibited by the equiatomic composition if possible. To do this, the computational principles encountered in the first chapter of the thesis were used. These also considered the empirical rules commonly utilised in HEAs for the prediction of solid solution formation. Indeed, the combination of pyMPEA (empirical rules), CALPHAD and DFT allowed for the accurate prediction of both solid solution formation and the type of intermetallics present in each composition where applicable. Furthermore, CALPHAD could identify certain compositional regions where the formation of both BCC and B2 at equilibrium would be probable. These predictions were confirmed experimentally, identifying two cases, specifically the Al_{11.1}TiVCr and Al_{16.7}TiVCr alloys where a BCC-B2 microstructural constituent was identified in the FC condition. A TEM investigation showed that the Al-Ti-rich phase corresponded to the B2 while the Cr-V-rich to the BCC. Additionally, in the case of the Al_{16.7}TiVCr alloy the intragranular formation of BCC particles was observed within a B2 matrix phase, pointing at a possible spinodal decomposition taking place, which is in line with the observations made in the field of RSAs. Nevertheless, given that the BCC-B2 structure had distinct nucleation points, namely grain boundaries and TiN particles, it is likely that its manifestation was a result of a nucleation and growth mechanism. When considering the WQ condition it was discovered that the Al_{11.1}TiVCr alloy consisted of a single BCC phase, meaning that the order-disorder transformation was fully suppressed. This was not the case for the Al_{16.7}TiVCr alloy where a single B2 phase was observed instead. This could point at an order-disorder transformation temperature lying at temperatures above 1200°C which is unlikely when considering the effect of Al and the

computational predictions. Overall, computational alloy design enabled the discovery of a composition where the microstructure would consist of a single BCC phase at the WQ condition and a dualphase BCC-B2 at the FC condition. It was also discovered that the thermal conductivity of all experimentally assessed compositions remained relatively constant and was particularly low for a metallic system.

When considering the elastic properties of the investigated compositions it was evident that the reduction of Al would drastically reduce both the density and the Young's modulus. This effect was captured through computational means and was experimentally confirmed. Progressively increasing the Al would directly increase the elastic properties until roughly the point where the alloy would decompose into multiple phases. It must be underlined that, while DFT was remarkably accurate at lower Al contents, the assessment of compositions beyond the equiatomic in terms of both the Al and Ti content would result in significant deviations from the experimental values. These would range from 21.5% to 34.9% with DFT comparably producing underestimations. This could indicate that the level of theory required to capture this phenomenon is beyond the capabilities of DFT given the parameterisation used within the context of this thesis¹. Estimating the elastic properties through the rule of mixtures (ROM) produced even greater errors reaching levels above 40%, again with the ROM underestimating the elastic properties of the investigated systems. This observation was attributed to the effect of Al, the progressive increase of which may be capable of altering the bond type from metallic to partially covalent similarly to AlTi. Therefore, it could be the case that instead of forming SPPs the entire alloy gradually transforms into an intermetallic phase with the progressive increase of Al up to a certain point. Beyond that, the formation of SPPs was observed and the elevated elastic properties also diminish.

Overall, this thesis demonstrated the feasibility of application of ICME for the discovery and design of novel MCAs. Candidate alloys for applications demanding lightweight high stiffness materials were identified acting as a solid foundation for further testing, optimisation, and development. The key findings of the thesis can be summarised in the following points:

¹ Naturally, moving at a higher level of theory or refining the simulations further would require significant computational resources which were not readily available. For context, the assessment of the multicomponent systems encountered within the thesis with the relevant parameterisation often required over 1,000 CPUs and 2 TB of RAM for a single run, with each composition requiring at least 28 runs to ensure adequate accuracy.

1. The sequential use of pyMPEA, CALPHAD, DFT and FEM through an ICME approach can predict the constituent phases and elastic properties of single phase and multiphase MCAs.
2. Heat treatments are capable of inhibiting or even fully suppressing the order-disorder transformation in AlTiVCr-based MCAs.
3. The decrease of Al results in the stabilisation of the BCC phase but also leads to an increase in density and reduction in elastic properties.
4. Most AlTiVCr-based alloys rich in Al exhibit specific elastic properties on par with or even surpassing high modulus steels. This could be attributed to the effect Al has on the bond type, resulting in the manifestation of partially covalent bonds.
5. The lack of ductility encountered in the investigated systems is predominantly attributed to their low thermal conductivity resulting in thermal shock during exposure to rapid thermal changes.

9. Future Work

The current work provided notable insights into concepts related to potential design pathways of MCAs. The ICME methodology presented here can enable an application-driven design of a new generation of MCAs aimed at tackling engineering challenges, particularly when it comes down to lightweight high stiffness design. Nevertheless, navigating the intricacies of the investigated systems gave rise to new questions and challenges.

9.1 Manufacturing

Although it was demonstrated that the low Al-containing AlTiVCr compositions could be a viable option for enabling ductility to manifest in this system this was not confirmed experimentally. Naturally, suppressing the order-disorder transformation is expected to improve the ductility. Subjecting the alloys to the rapid thermal cycles required for inhibiting the order-disorder transformation also results in compromising their structural integrity through crack formation via a thermal shock mechanism. As such, even before considering testing their mechanical properties, production routes utilising milder processes from a thermal cycling perspective are paramount. Techniques such as vacuum induction melting (VIM), spark plasma sintering (SPS) or even conventional casting, alongside hot isostatic pressing (HIP) could be used to manufacture the AlTiVCr alloy component while maintaining a sufficiently low cooling rate. This would avoid forming extensive crack networks during the process, while HIP could further aid their post-process elimination. Nevertheless, these steps alone would be inadequate for suppressing the order-disorder transformation in any of the tested compositions without significantly complicating the manufacturing process. Therefore, subjecting the alloy to a subsequent heat treatment process aimed at suppressing or controlling the order-disorder transformation is required.

To design the heat treatment, the order-disorder transformation temperature must first be accurately pinpointed and experimentally verified for each tested composition. For this, differential scanning calorimetry (DSC) or high temperature XRD (HTXRD) could be used, the latter with a well-controlled inert atmosphere or under high vacuum. Before ruling out water quenching (WQ), the following test would be advised. Conduct a heat treatment at 1200°C for 8h which has been demonstrated to be sufficient for inducing the formation of the BCC in most of the tested compositions. Then, slowly reduce the heat treatment temperature to a few degrees above the order-disorder transformation temperature. Once the desired temperature is reached, subject the alloy to a WQ process. This minimises the temperature differential and may avoid

the formation of cracks, although significant stress concentration is still expected. Should this process still lead to fracture, then redesigning the quenching process would be required. As seen in Chapter 7, in the cases where the amount of Al is reduced, a dualphase or even single phase low temperature BCC region is expected according to CALPHAD. Therefore, quenching down to a temperature corresponding to that region may reduce the driving force for the transformation sufficiently to inhibit it fully or partially. This would however require a different quenching medium. Should that still lead to crack formation, then studies on the required cooling rate for suppressing the transformation may need to be carried out. A reduction in the cooling rate should alleviate the risk of thermal shock but may induce the formation of the B2 phase. As such, this process must be diligently monitored. Although suppressing the order-disorder transformation through the above processes should result in a crack-free component with potentially high specific stiffness and reasonable ductility, the investigated alloys may hold even greater potential.

As previously mentioned during this research, the ideal goal would not be to suppress the transformation but instead control it. Subjecting the alloy to a low temperature aging treatment may enable the controlled formation of the B2 phase through the mechanisms explored in the literature review. This would lead to the manifestation of high strength through age hardening by forming an interconnected network of the BCC phase between the B2 particles, similarly to refractory (RSAs) and conventional superalloys (γ/γ'). This is expected to significantly increase both room and high temperature strength. However, it should be underlined that previous attempts at subjecting the equiatomic alloy specifically to low temperature heat treatments were unsuccessful, leading to the degradation of the tested samples. Nevertheless, confirming the age hardening hypothesis could also greatly simplify the manufacturing process by quenching to an elevated temperature instead of room temperature (Fig. 9.1). In turn, this would alleviate any issues pertaining to crack formation and the relevant thermal shock effects discussed previously.

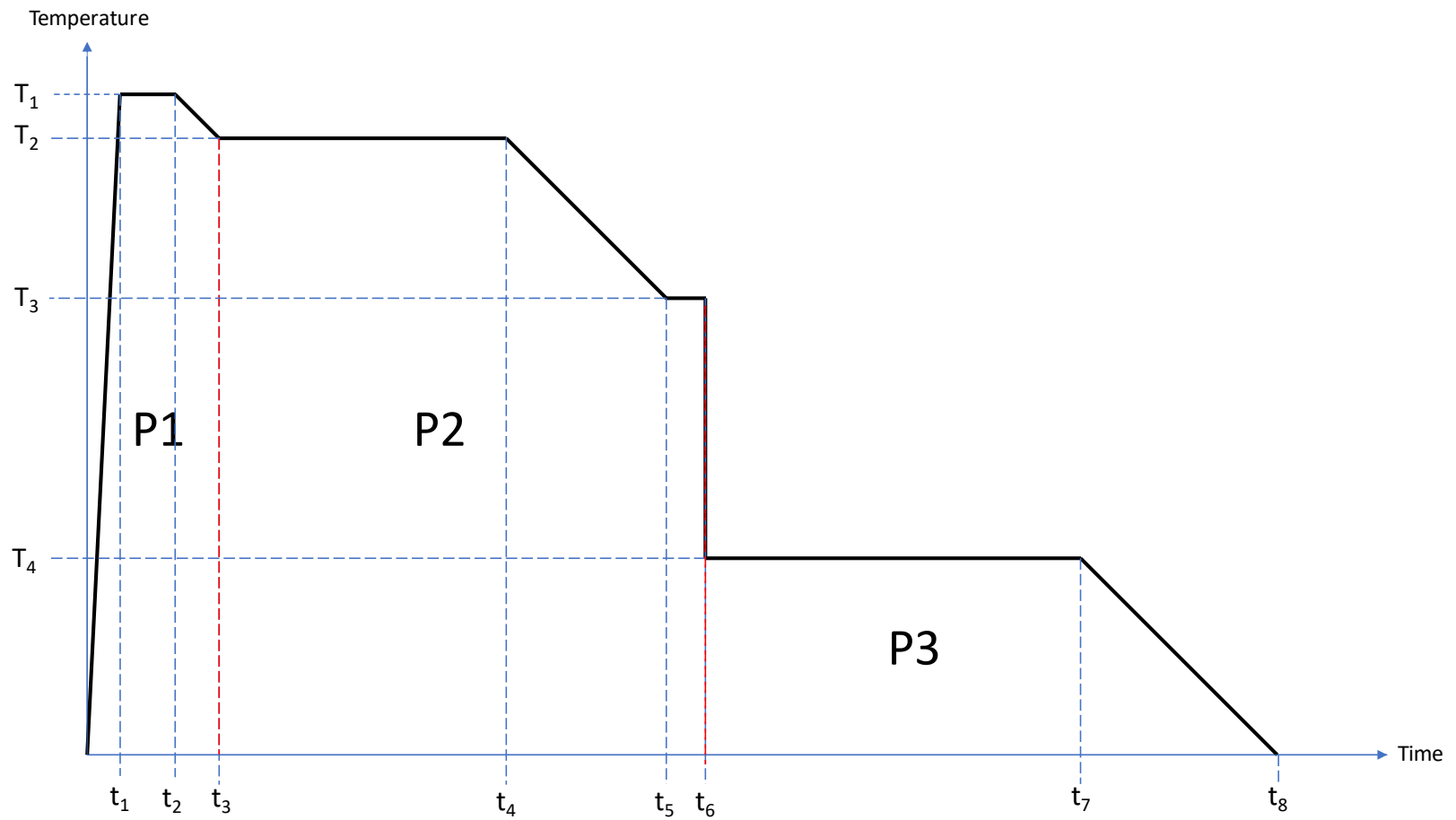


Figure 9.1 Proposed multistep manufacturing process of AlTiVCr-based alloys where P1 refers to the initial manufacturing/casting stage, P2 to the high temperature homogenisation heat treatment and P3 to the low temperature aging treatment. T_x and t_x denote the relevant points in temperature and time.

Given the control required for handling this process, the most optimal technique for this could be SPS. The powder for SPS can be manufactured through VIM/VAM and ball milling. In Figure 9.1, P1 refers to the initial sintering process, followed by a homogenisation treatment at T_2 (P2) for a defined time ($t_3 - t_4$). The alloy is then slowly cooled down to a few degrees above the order-disorder transformation temperature for the specific composition (T_3) and held there ($t_4 - t_5$) to ensure a homogeneous temperature profile across the sample. This is followed by a swift cooling or quenching process down to T_4 where the aging treatment subsequently takes place between $t_6 - t_7$ after which the sample is slow cooled to room temperature. The success of this process depends on the achievement of a sufficient cooling rate during the $T_3 - T_4$ transition to ensure a suppression of the order-disorder transformation. Assuming a reasonably low thermal expansion coefficient, this pathway may even enable the use of advanced techniques for near net shape manufacturing such as FAST forging [266].

9.2 From alloys to intermetallics

One of the key investigated phenomena within this thesis was the notable increase in the specific elastic properties of AlTiVCr-based alloys with the progressive addition of Al. This was attributed to Al transforming the bond type from metallic to partially covalent, which however has not been computationally or experimentally confirmed. Given that this effect could be key in enabling the manifestation of elevated elastic properties in a wide range of MCAs, understanding the fundamental effect of Al should be a priority. This can be done both computationally and experimentally, preferably in conjunction with one another. DFT can provide insight into the band structure and the density of states while electron energy loss spectroscopy (EELS) can be used for experimental verification. A progressive increase in the Al content also further stabilises the B2 phase against the BCC which may undermine of the ductility of the alloy. Therefore, achieving a proper balance between the elastic properties and ductility is a key challenge. Additional alloying additions capable of producing this effect may also need to be considered.

9.3 Dataset completion

Although the thesis provides a lot of insight on the behaviour of AlTiVCr-based systems the dataset has yet to be fully completed. This was intentional within the context of the thesis giving the limitations in time and resources. The more crucial experimental information to gather would be the following:

1. Compression testing data on all the novel compositions emphasising the effect of Al and suppression of the order-disorder transformation on the ductility.
2. DSC experiments to extract the order-disorder transformation temperature in each case.
3. Dilatometry experiments to gain insight regarding the thermal expansion coefficient of each composition.
4. EELS for deriving the bond type in relation to the Al addition in each case.
5. TEM on the rest of the novel compositions to verify the presence or lack of the B2 phase in both the WQ and FC condition.
6. Atom Probe Tomography (APT) to investigate the effect of the progressive increase of Al on the ordering process.
7. Investigate the elastic properties of the Mn-containing compositions.

At the same time, computational investigations may also assist in further understanding the behaviour and phenomena associated with this system. Namely:

1. Perform band structure and density of states calculations to gain insight regarding the effect of the addition of Al on the bond type.
2. Employ higher levels of DFT theory (e.g., hybrid, meta-GGA, revised PBE, PBEsol functionals) or even pure quantum-mechanical calculations to accurately predict the elastic properties of the investigated systems.
3. Utilise the improved scheme for identifying potential alloying additions capable of reproducing or improving upon the effect of Al.
4. Perform temperature-dependent DFT calculations to predict the BCC/B2 phase stability.

These recommendations may enable the identification of phenomena previously ignored while building and expanding upon the foundations lay out in this work. As a closing remark, while the field of MCAs can be challenging to navigate, expanding upon preexisting alloying systems with engineering applications in mind may help greatly reduce the number of potential candidate compositions. This can provide a direction for the employed alloying design strategies and improve the efficiency of the alloy discovery process. These design principles were paramount to the success of this work, leading to the development of a new series of alloys, the discovery of interesting effects and the development of a sound foundation for the future design and optimisation of AlTiVCr-based alloys and other MCA/RSA systems.

10. Appendix

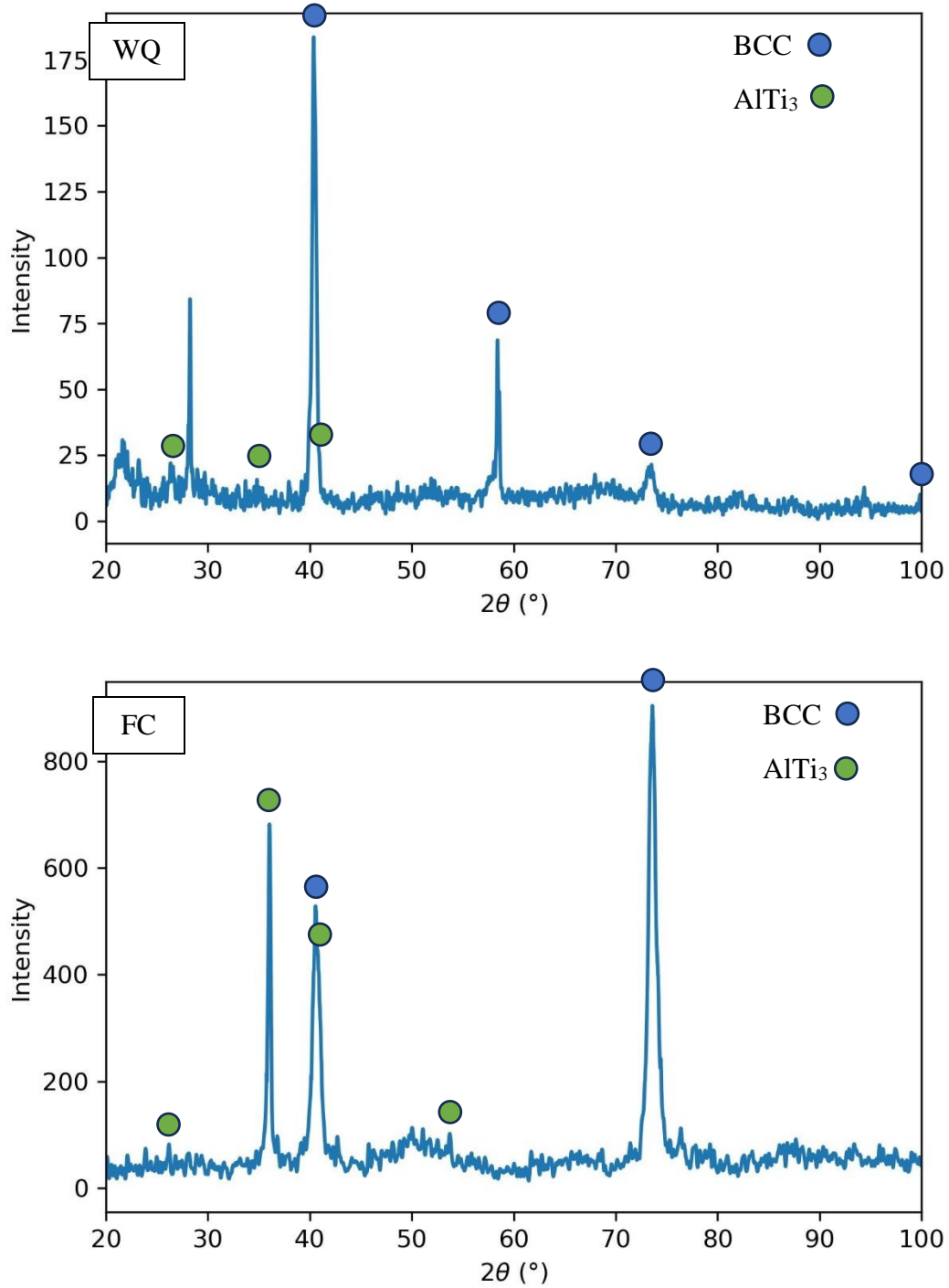


Figure 10.1 XRD pattern of the water quenched (WQ) and furnace cooled (FC) $Al_{14}Ti_{26}VCr$ alloy.

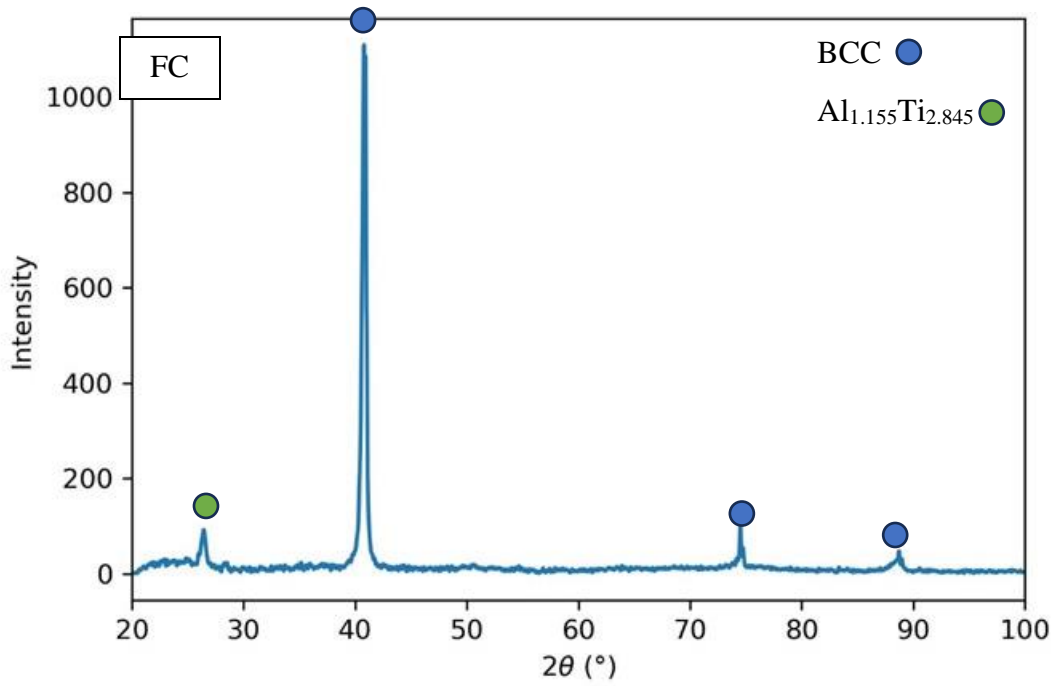
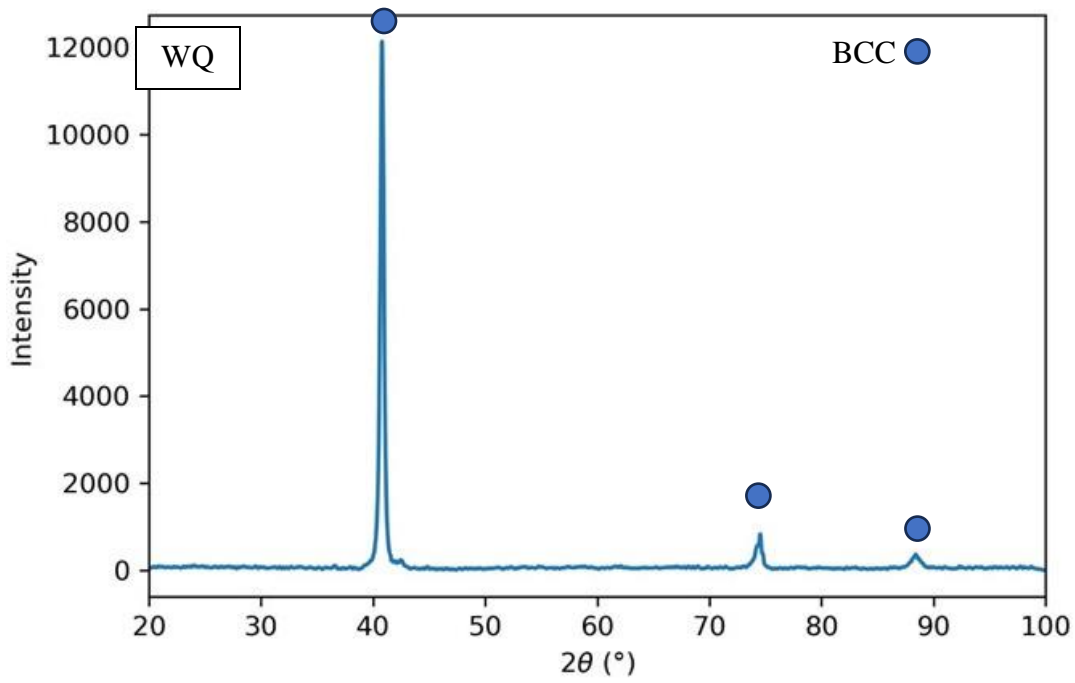


Figure 10.2 XRD pattern of the water quenched (WQ) and furnace cooled (FC) $Al_{14}Ti_{20}VCr$ alloy.

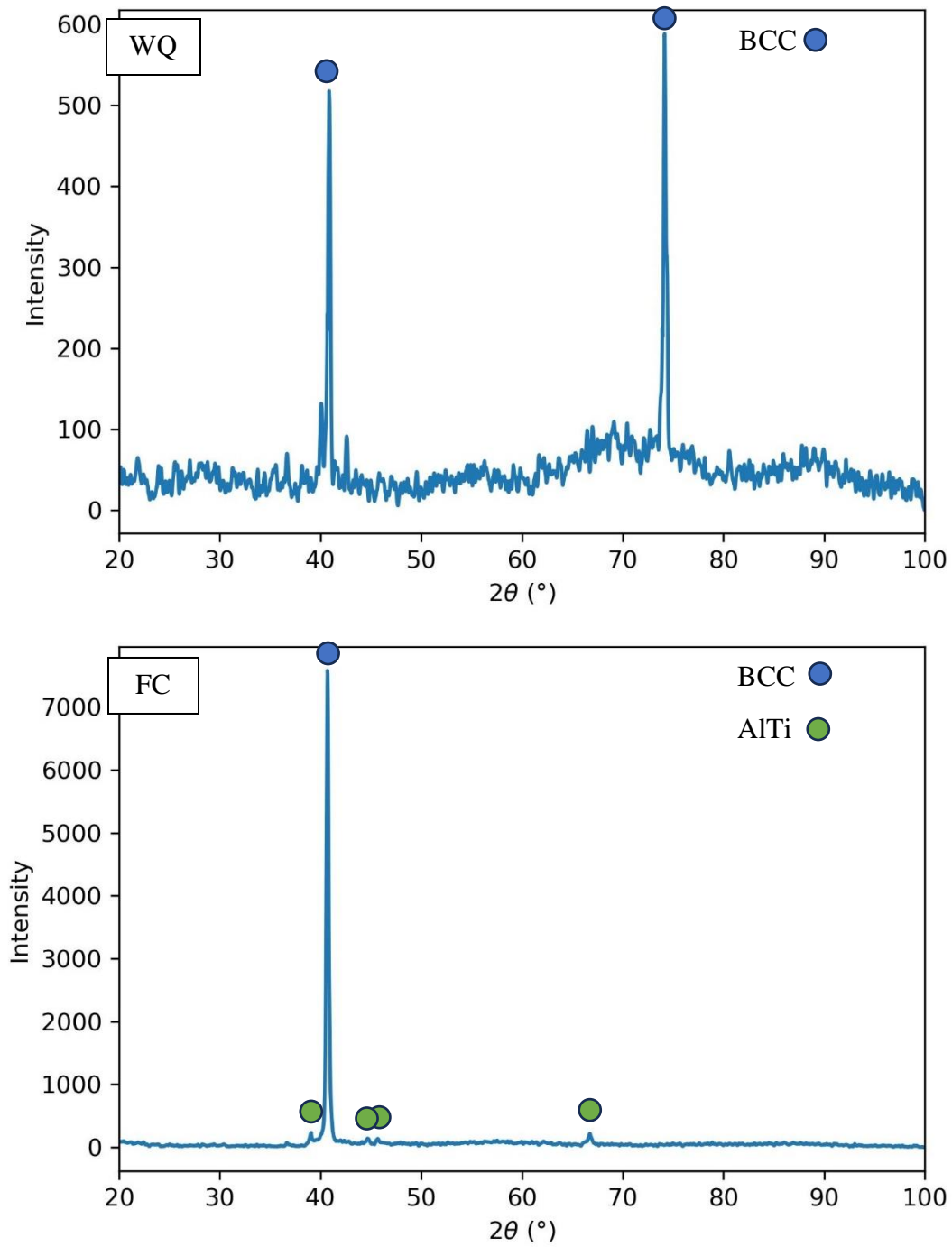


Figure 10.3 XRD pattern of the water quenched (WQ) and furnace cooled (FC) $Al_{20}Ti_{20}V_{10}Cr_{60}$ alloy.

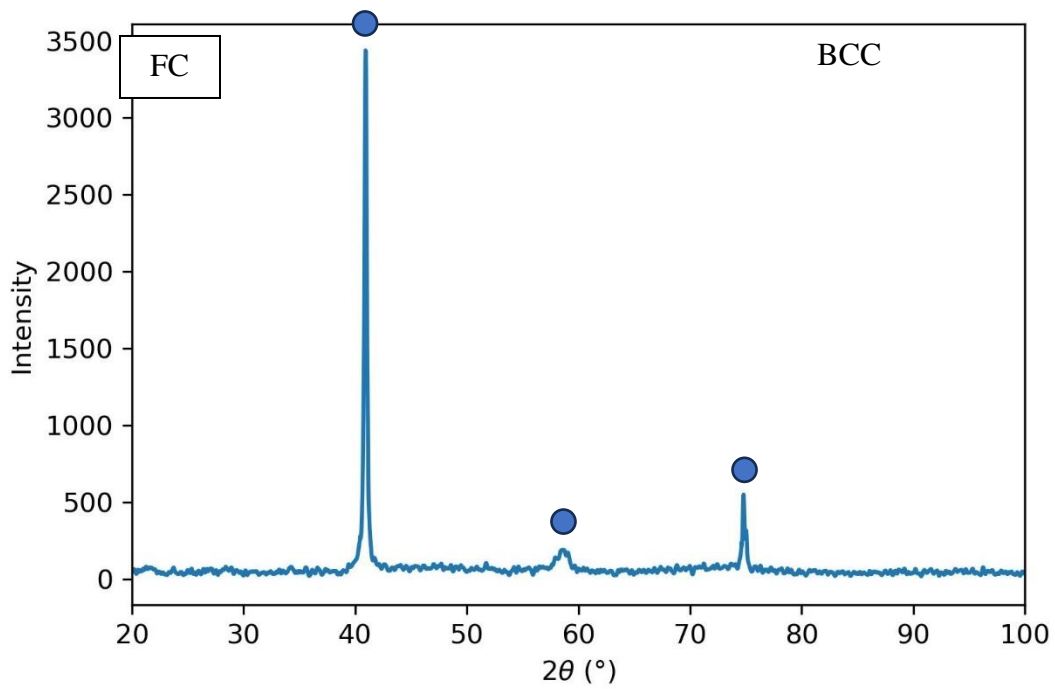
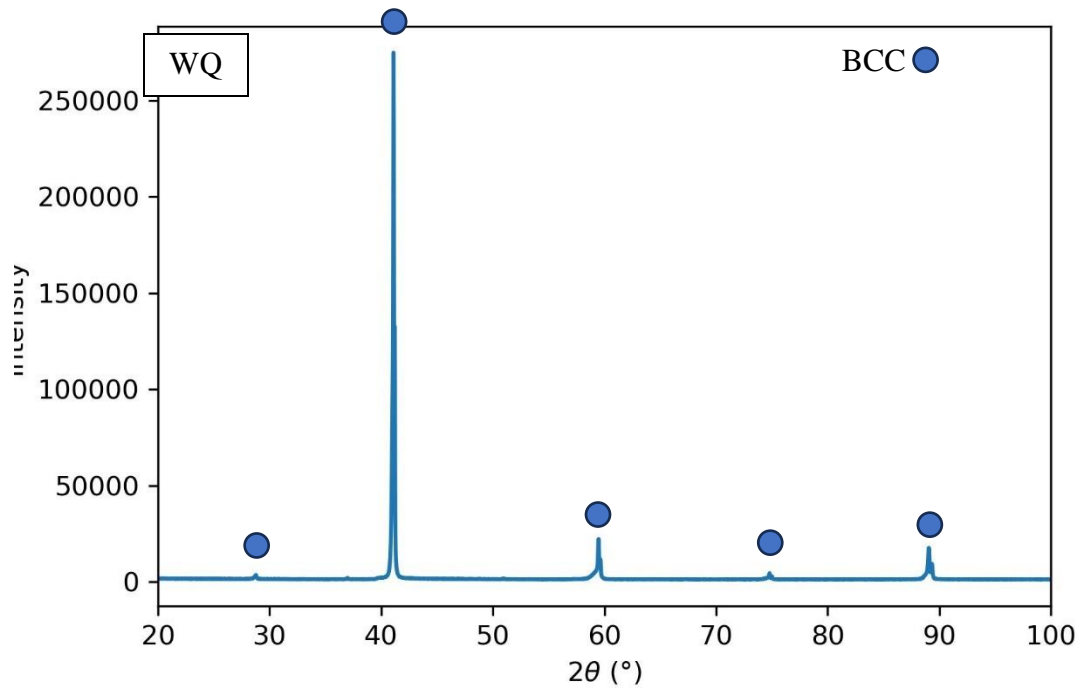


Figure 10.4 XRD pattern of the water quenched (WQ) and furnace cooled (FC) $Al_{17}Ti_{17}V$ Cr alloy.

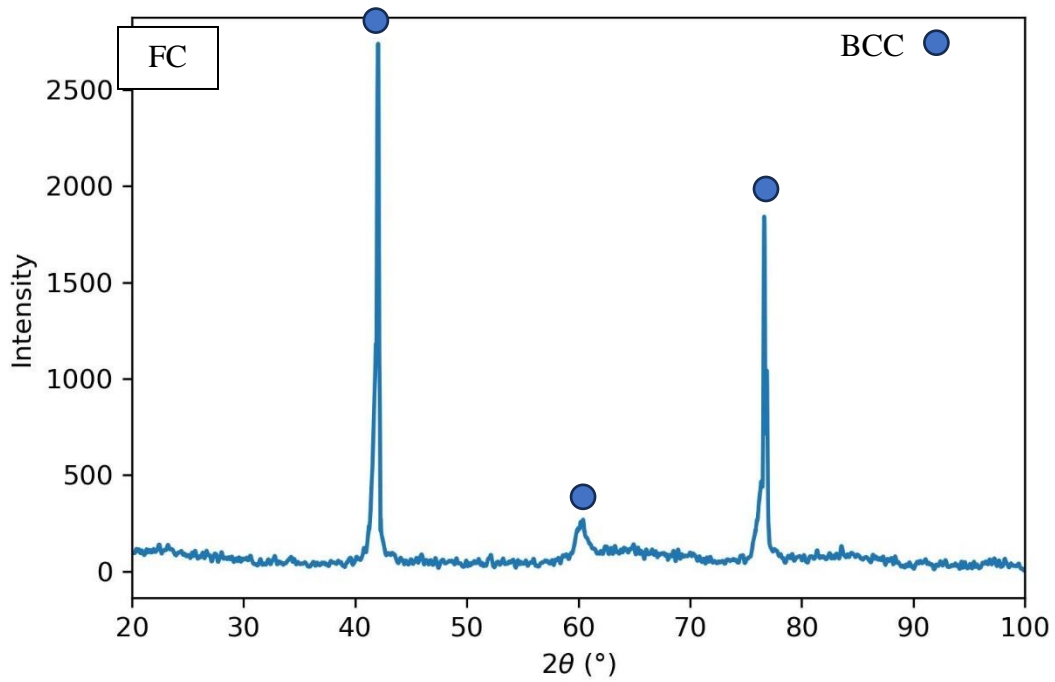
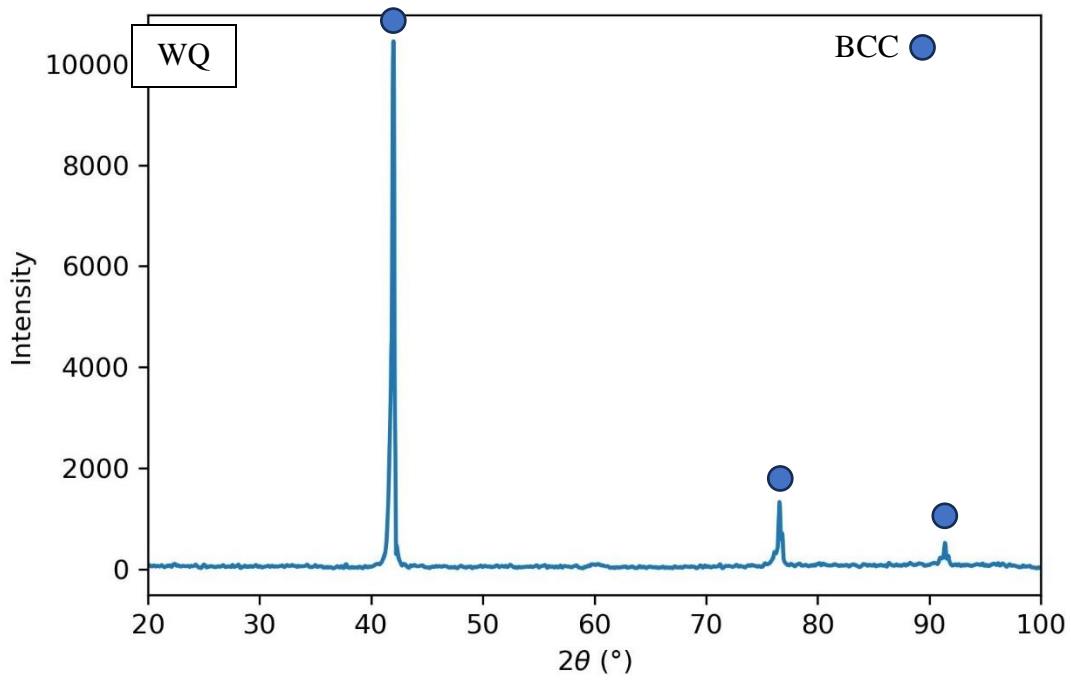


Figure 10.5 XRD pattern of the water quenched (WQ) and furnace cooled (FC) $Al_{10}Ti_{10}VCr$ alloy.

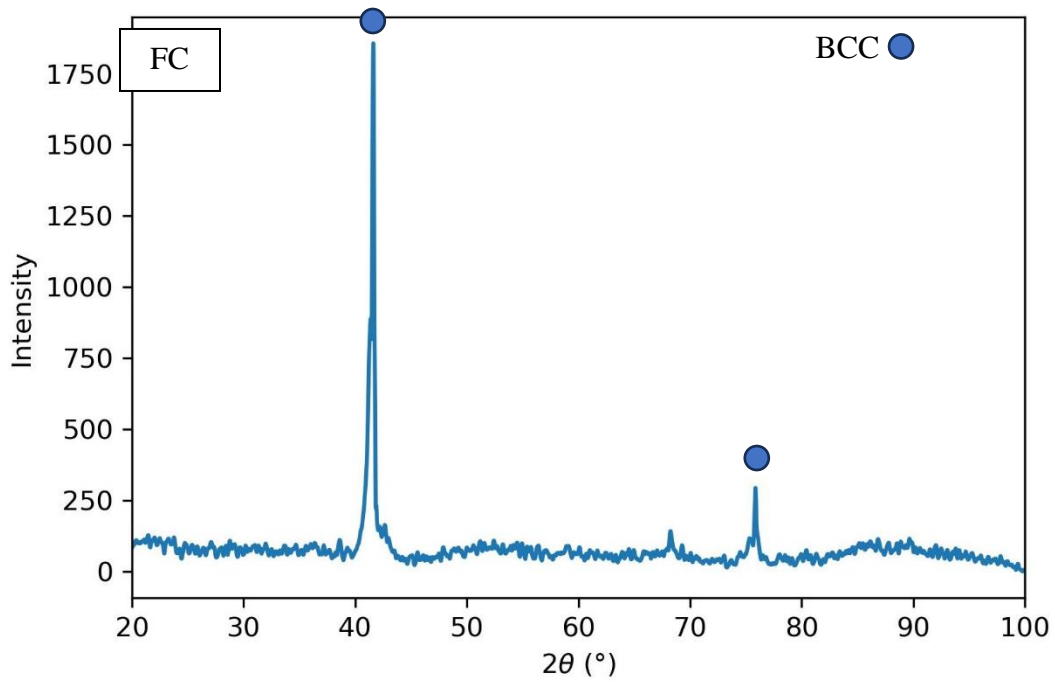
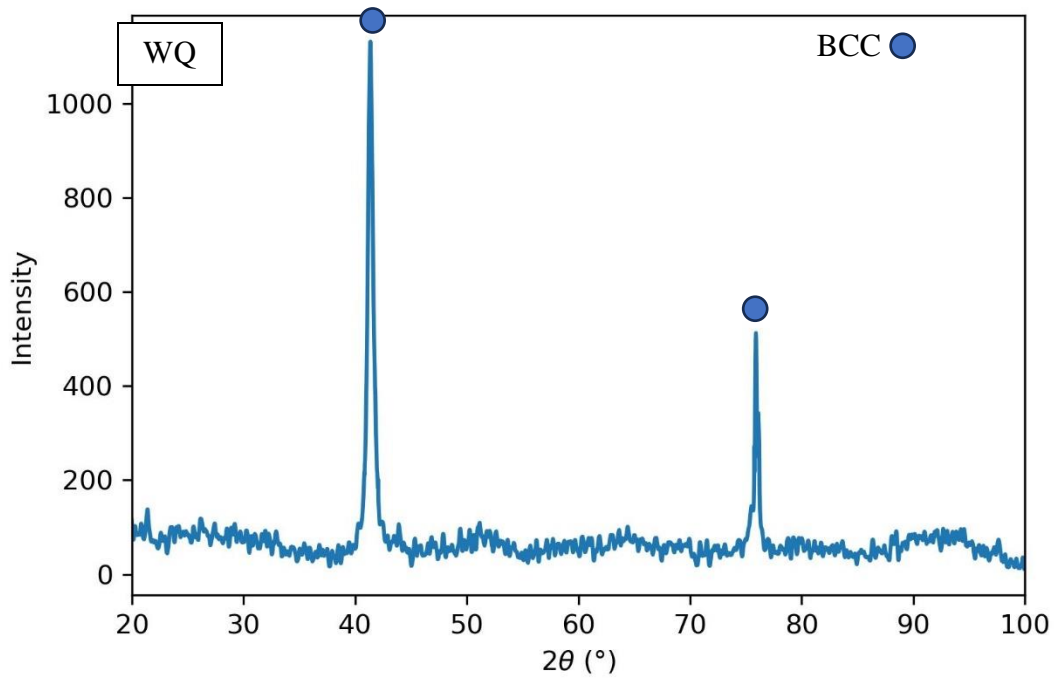


Figure 10.6 XRD pattern of the water quenched (WQ) and furnace cooled (FC) Al_7Ti_7VCr alloy.

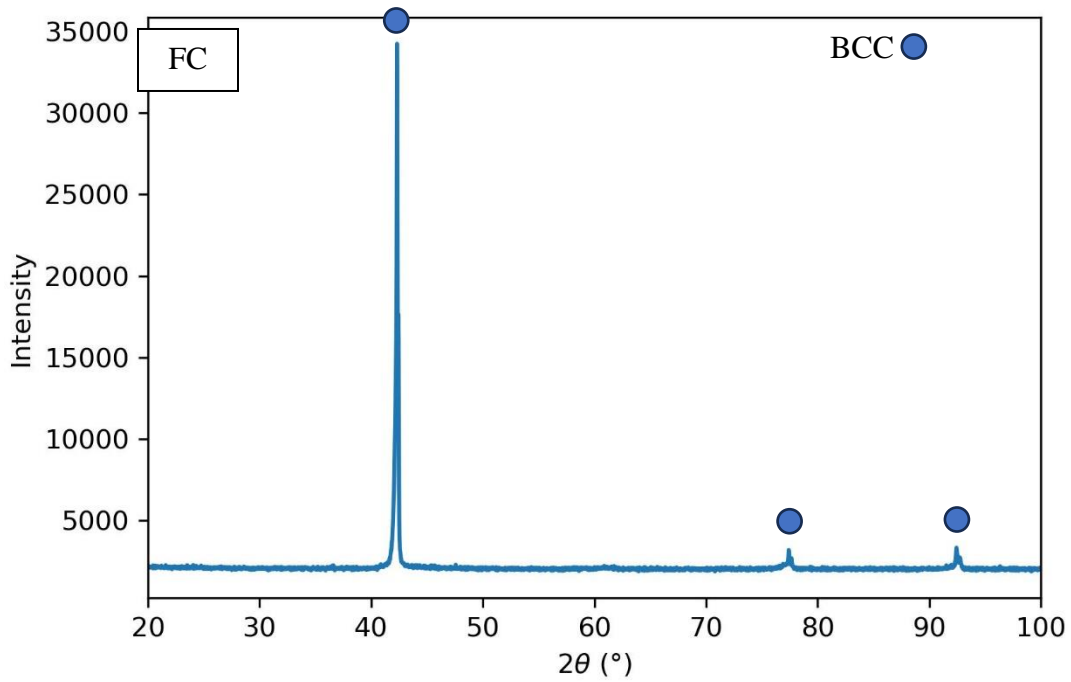
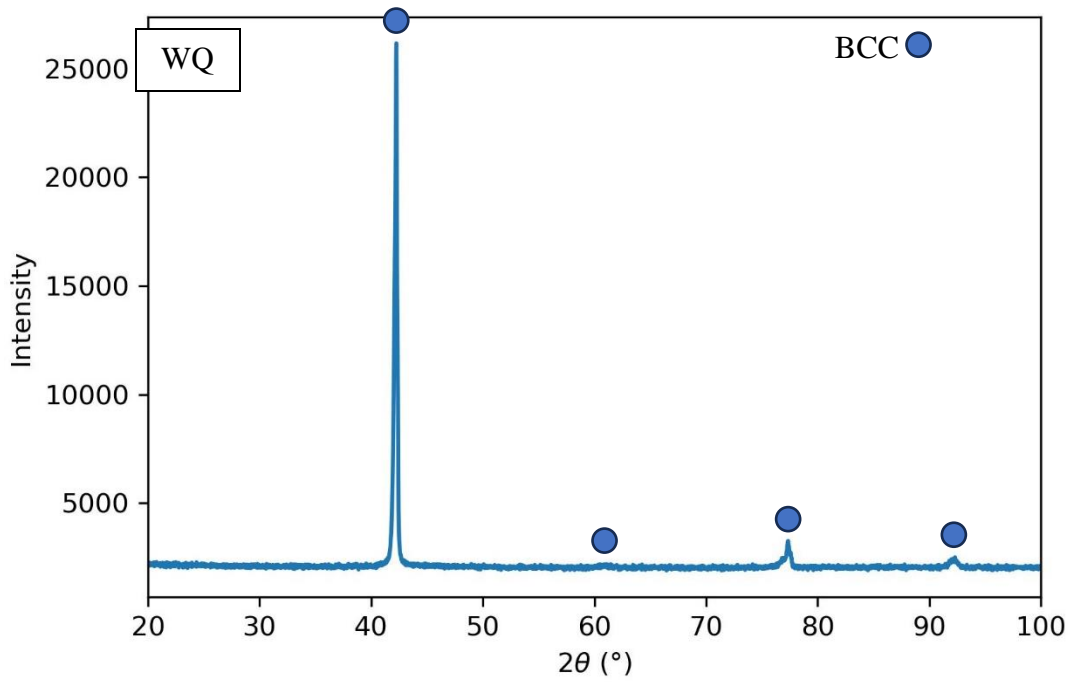


Figure 10.7 XRD pattern of the water quenched (WQ) and furnace cooled (FC) Al₅TiVCr alloy.

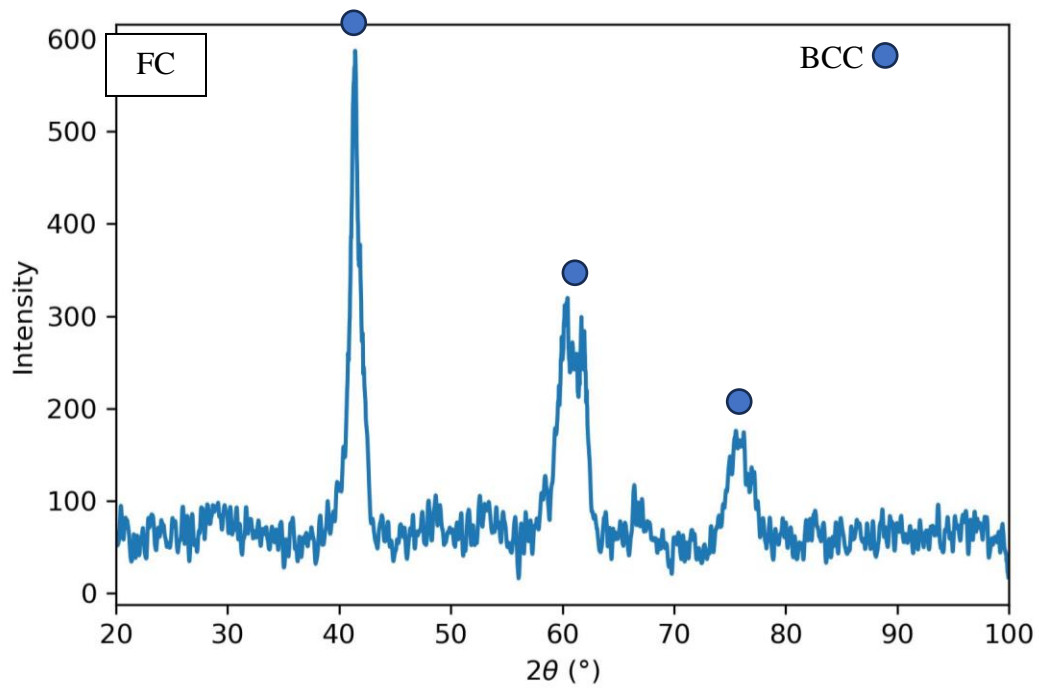
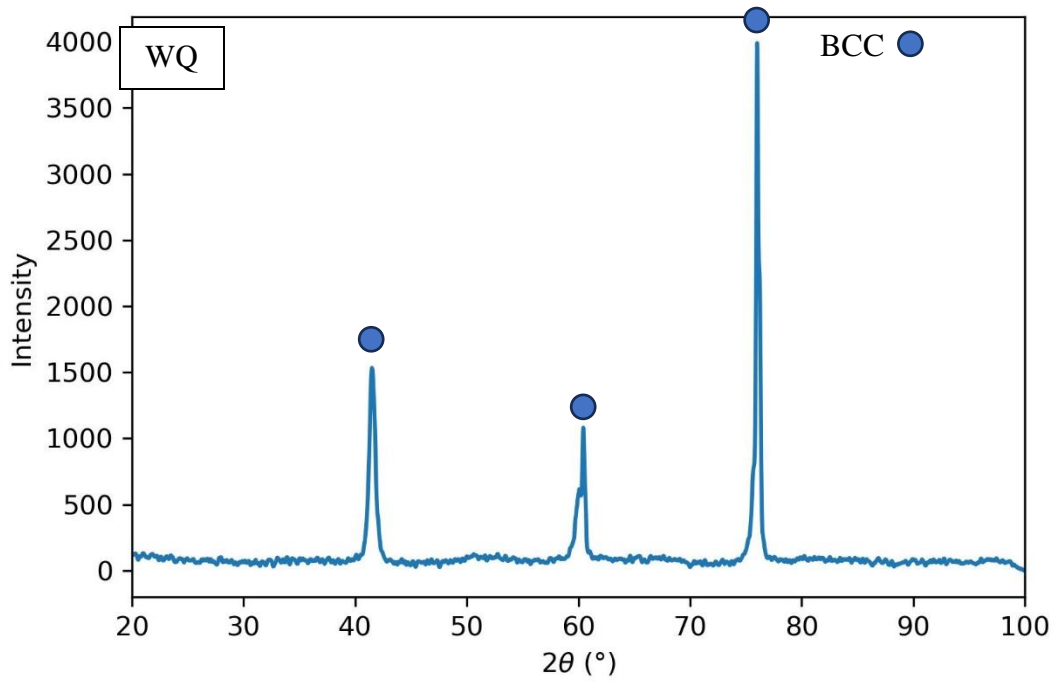


Figure 10.8 XRD pattern of the water quenched (WQ) and furnace cooled (FC) Al₆TiVCr alloy.

11. References

1. *The Oxford Handbook of the Bronze Age Aegean*, ed. E.H. Cline. 2012: Oxford University Press.
2. Sherby, O.D. and J. Wadsworth, *Ancient blacksmiths, the Iron Age, Damascus steels, and modern metallurgy*. Journal of Materials Processing Technology, 2001. **117**(3): p. 347-353.
3. Ranganathan, S., *Alloyed pleasures: Multimetallurgical cocktails*. Current science, 2003. **85**(5): p. 1404-1406.
4. Abbaschian, R. and R.E. Reed-Hill, *Physical Metallurgy Principles*. 2008: Cengage Learning.
5. Lula, R.A., *Stainless steel*. 1985, United States: American Society for Metals, Metals Park, OH.
6. Hardouin Duparc, O., *Alfred Wilm and the beginnings of Duralumin*. Rev. Met. Paris, 2004. **101**(5): p. 353-360.
7. Boyer, R.R., *An overview on the use of titanium in the aerospace industry*. Materials Science and Engineering: A, 1996. **213**(1): p. 103-114.
8. Davis, J.R., *Copper and copper alloys*. 2001: ASM international.
9. Reed, R.C., *The superalloys: fundamentals and applications*. 2008: Cambridge university press.
10. Agency, E.E. *Total greenhouse gas emission trends and projections in Europe (8th EAP)*. 2022 [cited 2023 16/07]; Available from: <https://www.eea.europa.eu/data-and-maps/indicators/greenhouse-gas-emission-trends-6/assessment-3>.
11. Commission, E. *Progress made in cutting emissions*. 2020; Available from: https://climate.ec.europa.eu/eu-action/climate-strategies-targets/progress-made-cutting-emissions_en.
12. Sun, X., et al., *Life cycle assessment-based selection of a sustainable lightweight automotive engine hood design*. The International Journal of Life Cycle Assessment, 2017. **22**(9): p. 1373-1383.
13. Raabe, D., et al., *Current Challenges and Opportunities in Microstructure-Related Properties of Advanced High-Strength Steels*. Metallurgical and Materials Transactions A, 2020. **51**(11): p. 5517-5586.
14. Miracle, D.B. and O.N. Senkov, *A critical review of high entropy alloys and related concepts*. Acta Materialia, 2017. **122**: p. 448-511.
15. Pickering, E.J. and N.G. Jones, *High-entropy alloys: a critical assessment of their founding principles and future prospects*. International Materials Reviews, 2016. **61**(3): p. 183-202.
16. Yeh, J.-W., et al., *Nanostructured High-Entropy Alloys with Multiple Principal Elements: Novel Alloy Design Concepts and Outcomes*. Advanced Engineering Materials, 2004. **6**(5): p. 299-303.
17. Yeh, J.-W., et al., *Formation of simple crystal structures in Cu-Co-Ni-Cr-Al-Fe-Ti-V alloys with multiprincipal metallic elements*. Metallurgical and Materials Transactions A, 2004. **35**: p. 2533-2536.
18. Jien-Wei, Y., *Recent progress in high entropy alloys*. Ann. Chim. Sci. Mat, 2006. **31**(6): p. 633-648.
19. Yeh, J.-W., *Alloy design strategies and future trends in high-entropy alloys*. Jom, 2013. **65**: p. 1759-1771.
20. Tsai, M.-H. and J.-W. Yeh, *High-Entropy Alloys: A Critical Review*. Materials Research Letters, 2014. **2**(3): p. 107-123.
21. Yeh, J.W., et al. *High-entropy alloys—a new era of exploitation*. in *Materials science forum*. 2007. Trans Tech Publ.
22. Yeh, J.-W., *Physical metallurgy of high-entropy alloys*. Jom, 2015. **67**(10): p. 2254-2261.
23. Michael C. Gao, J.-W.Y., Peter K. Liaw, Yong Zhang, *High-Entropy Alloys, Fundamentals and Applications*. 1 ed. 2018: Springer Cham.
24. Schuh, B., et al., *Mechanical properties, microstructure and thermal stability of a nanocrystalline CoCrFeMnNi high-entropy alloy after severe plastic deformation*. Acta Materialia, 2015. **96**: p. 258-268.

25. Otto, F., et al., *Relative effects of enthalpy and entropy on the phase stability of equiatomic high-entropy alloys*. Acta Materialia, 2013. **61**(7): p. 2628-2638.
26. Pickering, E.J., et al., *Precipitation in the equiatomic high-entropy alloy CrMnFeCoNi*. Scripta Materialia, 2016. **113**: p. 106-109.
27. Toda-Caraballo, I., et al., *Interatomic spacing distribution in multicomponent alloys*. Acta Materialia, 2015. **97**: p. 156-169.
28. Owen, L.R. and N.G. Jones, *Lattice distortions in high-entropy alloys*. Journal of Materials Research, 2018. **33**(19): p. 2954-2969.
29. Owen, L.R., et al., *An assessment of the lattice strain in the CrMnFeCoNi high-entropy alloy*. Acta Materialia, 2017. **122**: p. 11-18.
30. George, E.P., D. Raabe, and R.O. Ritchie, *High-entropy alloys*. Nature Reviews Materials, 2019. **4**(8): p. 515-534.
31. Laplanche, G., et al., *Microstructural evolution of a CoCrFeMnNi high-entropy alloy after swaging and annealing*. Journal of Alloys and Compounds, 2015. **647**: p. 548-557.
32. Abuzaid, W. and H. Sehitoglu, *Critical resolved shear stress for slip and twin nucleation in single crystalline FeNiCoCrMn high entropy alloy*. Materials Characterization, 2017. **129**: p. 288-299.
33. Varvenne, C., et al., *Solute strengthening in random alloys*. Acta Materialia, 2017. **124**: p. 660-683.
34. Senkov, O.N., et al., *Microstructure and room temperature properties of a high-entropy TaNbHfZrTi alloy*. Journal of Alloys and Compounds, 2011. **509**(20): p. 6043-6048.
35. Senkov, O.N., et al., *Microstructure and elevated temperature properties of a refractory TaNbHfZrTi alloy*. Journal of Materials Science, 2012. **47**(9): p. 4062-4074.
36. Senkov, O.N. and S.L. Semiatin, *Microstructure and properties of a refractory high-entropy alloy after cold working*. Journal of Alloys and Compounds, 2015. **649**: p. 1110-1123.
37. Schuh, B., et al., *Thermodynamic instability of a nanocrystalline, single-phase TiZrNbHfTa alloy and its impact on the mechanical properties*. Acta Materialia, 2018. **142**: p. 201-212.
38. Stepanov, N.D., et al., *Aging behavior of the HfNbTaTiZr high entropy alloy*. Materials Letters, 2018. **211**: p. 87-90.
39. Anand, G., R. Goodall, and C.L. Freeman, *Role of configurational entropy in body-centred cubic or face-centred cubic phase formation in high entropy alloys*. Scripta Materialia, 2016. **124**: p. 90-94.
40. Li, R., et al., *The effects of phase transformation on the microstructure and mechanical behavior of FeNiMnCr.75Alx high-entropy alloys*. Materials Science and Engineering: A, 2018. **725**: p. 138-147.
41. Soni, V.K. and A.K. Sinha, *Effect of Alloying Elements, Phases and Heat Treatments on Properties of High-Entropy Alloys: A Review*. Transactions of the Indian Institute of Metals, 2023. **76**(4): p. 897-914.
42. Sun, X., et al., *Phase selection rule for Al-doped CrMnFeCoNi high-entropy alloys from first-principles*. Acta Materialia, 2017. **140**: p. 366-374.
43. Kube, S.A., et al., *Phase selection motifs in High Entropy Alloys revealed through combinatorial methods: Large atomic size difference favors BCC over FCC*. Acta Materialia, 2019. **166**: p. 677-686.
44. Soni, V., et al., *Phase stability as a function of temperature in a refractory high-entropy alloy*. Journal of Materials Research, 2018. **33**(19): p. 3235-3246.
45. Tsai, M.-H., et al. *Intermetallic Phases in High-Entropy Alloys: Statistical Analysis of their Prevalence and Structural Inheritance*. Metals, 2019. **9**, DOI: 10.3390/met9020247.
46. Cantor, B., *Multicomponent and High Entropy Alloys*. Entropy, 2014. **16**(9): p. 4749-4768.
47. Zhang, H.L., et al., *Solid solution strengthening of high-entropy alloys from first-principles study*. Journal of Materials Science & Technology, 2022. **121**: p. 105-116.

48. Ali, N., et al., *Strengthening mechanisms in high entropy alloys: A review*. Materials Today Communications, 2022. **33**: p. 104686.
49. Murty, B.S., et al., *High-Entropy Alloys in High-Entropy Alloys (Second Edition)*, B.S. Murty, et al., Editors. 2019, Elsevier.
50. He, J.Y., et al., *Steady state flow of the FeCoNiCrMn high entropy alloy at elevated temperatures*. Intermetallics, 2014. **55**: p. 9-14.
51. Singh, A.K. and A. Subramaniam, *On the formation of disordered solid solutions in multi-component alloys*. Journal of Alloys and Compounds, 2014. **587**: p. 113-119.
52. Guo, S., et al., *Effect of valence electron concentration on stability of fcc or bcc phase in high entropy alloys*. Journal of Applied Physics, 2011. **109**(10): p. 103505.
53. Zhang, Y., et al., *Solid-Solution Phase Formation Rules for Multi-component Alloys*. Advanced Engineering Materials, 2008. **10**(6): p. 534-538.
54. Hume-Rothery, W., C.W. Haworth, and R.E. Smallman, *The structure of metals and alloys [by] William Hume-Rothery, R.E. Smallman and C W. Haworth*. [5th] ed. Institute of Metals. 1969, London: Institute of Metals and the Institution of Metallurgists.
55. Wang, Z., S. Guo, and C.T. Liu, *Phase Selection in High-Entropy Alloys: From Nonequilibrium to Equilibrium*. JOM, 2014. **66**(10): p. 1966-1972.
56. Yang, X. and Y. Zhang, *Prediction of high-entropy stabilized solid-solution in multi-component alloys*. Materials Chemistry and Physics, 2012. **132**(2): p. 233-238.
57. Li, Z., et al., *Interstitial atoms enable joint twinning and transformation induced plasticity in strong and ductile high-entropy alloys*. Scientific Reports, 2017. **7**(1): p. 40704.
58. Su, J., D. Raabe, and Z. Li, *Hierarchical microstructure design to tune the mechanical behavior of an interstitial TRIP-TWIP high-entropy alloy*. Acta Materialia, 2019. **163**: p. 40-54.
59. Tillmann, W., et al., *Development of high entropy alloys for brazing applications*. Welding in the World, 2020. **64**(1): p. 201-208.
60. Luo, D., et al., *High Entropy Alloys as Filler Metals for Joining*. Entropy, 2021. **23**(1): p. 78.
61. Way, M., et al., *A new high entropy alloy brazing filler metal design for joining skutterudite thermoelectrics to copper*. Journal of Alloys and Compounds, 2021. **858**: p. 157750.
62. Hardwick, L., et al., *Development of a Novel Ni-Based Multi-principal Element Alloy Filler Metal, Using an Alternative Melting Point Depressant*. Metallurgical and Materials Transactions A, 2021. **52**(6): p. 2534-2548.
63. Way, M., J. Willingham, and R. Goodall, *Brazing filler metals*. International Materials Reviews, 2020. **65**(5): p. 257-285.
64. Senkov, O.N., et al., *Refractory high-entropy alloys*. Intermetallics, 2010. **18**(9): p. 1758-1765.
65. Juan, C.-C., et al., *Simultaneously increasing the strength and ductility of a refractory high-entropy alloy via grain refining*. Materials Letters, 2016. **184**: p. 200-203.
66. Senkov, O.N., C. Woodward, and D.B. Miracle, *Microstructure and Properties of Aluminum-Containing Refractory High-Entropy Alloys*. JOM, 2014. **66**(10): p. 2030-2042.
67. Stepanov, N.D., et al., *Structure and mechanical properties of a light-weight AlNbTiV high entropy alloy*. Materials Letters, 2015. **142**: p. 153-155.
68. Senkov, O.N., et al., *Low-density, refractory multi-principal element alloys of the Cr-Nb-Ti-V-Zr system: Microstructure and phase analysis*. Acta Materialia, 2013. **61**(5): p. 1545-1557.
69. Senkov, O.N., S.V. Senkova, and C. Woodward, *Effect of aluminum on the microstructure and properties of two refractory high-entropy alloys*. Acta Materialia, 2014. **68**: p. 214-228.
70. Juan, C.-C., et al., *Enhanced mechanical properties of HfMoTaTiZr and HfMoNbTaTiZr refractory high-entropy alloys*. Intermetallics, 2015. **62**: p. 76-83.
71. Kumar, A. and M. Gupta, *An Insight into Evolution of Light Weight High Entropy Alloys: A Review*. Metals, 2016. **6**(9): p. 199.

72. Li, R., J.C. Gao, and K. Fan, *Study to Microstructure and Mechanical Properties of Mg Containing High Entropy Alloys*. Materials Science Forum, 2010. **650**: p. 265-271.
73. Li, R., J.C. Gao, and K. Fan, *Microstructure and Mechanical Properties of MgMnAlZnCu High Entropy Alloy Cooling in Three Conditions*. Materials Science Forum, 2011. **686**: p. 235-241.
74. Youssef, K.M., et al., *A Novel Low-Density, High-Hardness, High-entropy Alloy with Close-packed Single-phase Nanocrystalline Structures*. Materials Research Letters, 2015. **3**(2): p. 95-99.
75. Kozak, R., A. Sologubenko, and W. Steurer, *Single-phase high-entropy alloys – an overview*. Zeitschrift für Kristallographie - Crystalline Materials, 2015. **230**(1): p. 55-68.
76. Ye, Y.F., et al., *High-entropy alloy: challenges and prospects*. Materials Today, 2016. **19**(6): p. 349-362.
77. Lu, Z.P., et al., *An assessment on the future development of high-entropy alloys: Summary from a recent workshop*. Intermetallics, 2015. **66**: p. 67-76.
78. Gorsse, S., J.-P. Couzinié, and D.B. Miracle, *From high-entropy alloys to complex concentrated alloys*. Comptes Rendus Physique, 2018. **19**(8): p. 721-736.
79. Wang, Z., et al., *Ultrastrong lightweight compositionally complex steels via dual-nanoprecipitation*. Science Advances, 2020. **6**(46): p. eaba9543.
80. Deng, Y., et al., *Design of a twinning-induced plasticity high entropy alloy*. Acta Materialia, 2015. **94**: p. 124-133.
81. Senkov, O.N., et al., *Development of a Refractory High Entropy Superalloy*. Entropy, 2016. **18**(3): p. 102.
82. Soni, V., et al., *Microstructural Design for Improving Ductility of An Initially Brittle Refractory High Entropy Alloy*. Scientific Reports, 2018. **8**(1).
83. Senkov, O.N., et al., *Compositional variation effects on the microstructure and properties of a refractory high-entropy superalloy AlMo0.5NbTa0.5TiZr*. Materials & Design, 2018. **139**: p. 498-511.
84. Soni, V., et al., *Phase inversion in a two-phase, BCC+B2, refractory high entropy alloy*. Acta Materialia, 2020. **185**: p. 89-97.
85. Miracle, D.B., et al., *Refractory high entropy superalloys (RSAs)*. Scripta Materialia, 2020. **187**: p. 445-452.
86. Naka, S. and T. Khan, *Designing novel multiconstituent intermetallics: Contribution of modern alloy theory in developing engineered materials*. Journal of Phase Equilibria, 1997. **18**(6): p. 635.
87. Bonnet, F., V. Daeschler, and G. Petitgand, *High modulus steels: new requirement of automotive market. How to take up challenge?* Canadian Metallurgical Quarterly, 2014. **53**(3): p. 243-252.
88. Ye, Y.X., et al., *Evaluating elastic properties of a body-centered cubic NbHfZrTi high-entropy alloy – A direct comparison between experiments and ab initio calculations*. Intermetallics, 2019. **109**: p. 167-173.
89. Dirras, G., et al., *Elastic and plastic properties of as-cast equimolar TiHfZrTaNb high-entropy alloy*. Materials Science and Engineering: A, 2016. **654**: p. 30-38.
90. Cui, P., et al., *Effects of nitrogen content on microstructures and mechanical properties of (AlCrTiZrHf)N high-entropy alloy nitride films*. Journal of Alloys and Compounds, 2020. **834**: p. 155063.
91. Lee, C., et al., *Temperature dependence of elastic and plastic deformation behavior of a refractory high-entropy alloy*. Science Advances, 2020. **6**(37): p. eaaz4748.
92. Jiao, Z.M., et al., *Nanoindentation characterised plastic deformation of a Al0.5CoCrFeNi high entropy alloy*. Materials Science and Technology, 2015. **31**(10): p. 1244-1249.
93. Haglund, A., et al., *Polycrystalline elastic moduli of a high-entropy alloy at cryogenic temperatures*. Intermetallics, 2015. **58**: p. 62-64.

94. Sinha, S., et al., *Nanoindentation behavior of high entropy alloys with transformation-induced plasticity*. Scientific Reports, 2019. **9**(1): p. 6639.
95. Münstermann, S. and W. Bleck, *Einflussgrößen auf den Elastizitätsmodul von Stählen für den Karosseriebau*. Materials Testing, 2005. **47**(6): p. 337-344.
96. Springer, H., et al., *Stiff, light, strong and ductile: nano-structured High Modulus Steel*. Scientific Reports, 2017. **7**(1): p. 2757.
97. Qiu, Y., et al., *A lightweight single-phase AlTiVCr compositionally complex alloy*. Acta Materialia, 2017. **123**: p. 115-124.
98. Qiu, Y., et al., *Microstructure and corrosion properties of the low-density single-phase compositionally complex alloy AlTiVCr*. Corrosion Science, 2018. **133**: p. 386-396.
99. Esmaily, M., et al., *High-temperature oxidation behaviour of AlxFeCrCoNi and AlTiVCr compositionally complex alloys*. npj Materials Degradation, 2020. **4**(1): p. 25.
100. Huang, X., J. Miao, and A.A. Luo, *Lightweight AlCrTiV high-entropy alloys with dual-phase microstructure via microalloying*. Journal of Materials Science, 2019. **54**(3): p. 2271-2277.
101. Ma, Y., et al., *The BCC/B2 Morphologies in AlxNiCoFeCr High-Entropy Alloys*. Metals, 2017. **7**(2): p. 57.
102. Cao, P., et al., *Ordering induced transformation from high-entropy to Heusler CrVTiAl alloy*. Physics Letters A, 2019. **383**(32): p. 125934.
103. Huang, S., et al., *Chemical ordering controlled thermo-elasticity of AlTiVCr1-xNbx high-entropy alloys*. Acta Materialia, 2020. **199**: p. 53-62.
104. Sun, M., et al., *Grain boundary relaxation behavior and phase stability of AlCrTiVx (x = 0, 0.5 and 1) high-entropy alloys*. Scripta Materialia, 2021. **204**: p. 114144.
105. Huang, X., J. Miao, and A.A. Luo, *Order-disorder transition and its mechanical effects in lightweight AlCrTiV high entropy alloys*. Scripta Materialia, 2022. **210**: p. 114462.
106. Ikeda, Y., B. Grabowski, and F. Körmann, *Ab initio phase stabilities and mechanical properties of multicomponent alloys: A comprehensive review for high entropy alloys and compositionally complex alloys*. Materials Characterization, 2019. **147**: p. 464-511.
107. Wang, Z., et al., *Light-weight refractory high-entropy alloys: A comprehensive review*. Journal of Materials Science & Technology, 2023. **151**: p. 41-65.
108. Takamoto, S., et al., *Towards universal neural network interatomic potential*. Journal of Materiomics, 2023. **9**(3): p. 447-454.
109. Miracle, D.B., *High entropy alloys as a bold step forward in alloy development*. Nature Communications, 2019. **10**(1): p. 1805.
110. Lukas, H., S.G. Fries, and B. Sundman, *Computational Thermodynamics: The Calphad Method*. 2007: Cambridge University Press.
111. Chen, H.-L., H. Mao, and Q. Chen, *Database development and Calphad calculations for high entropy alloys: Challenges, strategies, and tips*. Materials Chemistry and Physics, 2018. **210**: p. 279-290.
112. Ghassemali, E. and P.L.J. Conway, *High-Throughput CALPHAD: A Powerful Tool Towards Accelerated Metallurgy*. Frontiers in Materials, 2022. **9**.
113. Yang, S., et al., *Revisit the VEC rule in high entropy alloys (HEAs) with high-throughput CALPHAD approach and its applications for material design-A case study with Al-Co-Cr-Fe-Ni system*. Acta Materialia, 2020. **192**: p. 11-19.
114. Senkov, O.N., et al., *CALPHAD-aided development of quaternary multi-principal element refractory alloys based on NbTiZr*. Journal of Alloys and Compounds, 2019. **783**: p. 729-742.
115. Raturi, A., et al., *ICME approach to explore equiatomic and non-equiatomic single phase BCC refractory high entropy alloys*. Journal of Alloys and Compounds, 2019. **806**: p. 587-595.

116. Yen, S.-y., H. Murakami, and S.-k. Lin, *Low-density CoAlTi-B2 strengthened Al-Co-Cr-Mo-Ti bcc refractory high-entropy superalloy designed with the assistance of high-throughput CALPHAD method*. Journal of Alloys and Compounds, 2023. **952**: p. 170027.
117. Müller, F., et al., *Formation of complex intermetallic phases in novel refractory high-entropy alloys NbMoCrTiAl and TaMoCrTiAl: Thermodynamic assessment and experimental validation*. Journal of Alloys and Compounds, 2020. **842**: p. 155726.
118. Feng, R., et al., *Design of Light-Weight High-Entropy Alloys*. Entropy, 2016. **18**(9): p. 333.
119. *Ground-state Properties*, in *Computational Quantum Mechanics for Materials Engineers: The EMT0 Method and Applications*, L. Vitos, Editor. 2007, Springer London: London. p. 97-123.
120. Tsai, M.-H., *Physical Properties of High Entropy Alloys*. Entropy, 2013. **15**(12): p. 5338-5345.
121. Stavroulakis, P., et al., *Successful prediction of the elastic properties of multiphase high entropy alloys in the AlTiVCr-Si system through a novel computational approach*. Materialia, 2022. **21**: p. 101365.
122. Zheng, S.-m., W.-q. Feng, and S.-q. Wang, *Elastic properties of high entropy alloys by MaxEnt approach*. Computational Materials Science, 2018. **142**: p. 332-337.
123. Giustino, F., *Materials modelling using density functional theory: properties and predictions*. 2014, Oxford, [England] ;: Oxford University Press.
124. Qiu, S., et al., *Structural stability and mechanical properties of B2 ordered refractory AlNbTiVZr high entropy alloys*. Journal of Alloys and Compounds, 2021. **886**: p. 161289.
125. Lee, C., et al., *Lattice distortion in a strong and ductile refractory high-entropy alloy*. Acta Materialia, 2018. **160**: p. 158-172.
126. Song, H., F. Tian, and D. Wang, *Thermodynamic properties of refractory high entropy alloys*. Journal of Alloys and Compounds, 2016. **682**: p. 773-777.
127. Bhandari, U., C. Zhang, and S. Yang, *Mechanical and Thermal Properties of Low-Density Al_{20+x}Cr_{20-x}Mo_{20-y}Ti₂₀V_{20+y} Alloys*. Crystals, 2020. **10**(4): p. 278.
128. Qiu, S., et al., *Local-ordering mediated configuration stability and elastic properties of aluminum-containing high entropy alloys*. Intermetallics, 2019. **110**: p. 106474.
129. Otero-de-la-Roza, A., D. Abbasi-Pérez, and V. Luaña, *Gibbs2: A new version of the quasiharmonic model code. II. Models for solid-state thermodynamics, features and implementation*. Computer Physics Communications, 2011. **182**(10): p. 2232-2248.
130. Otero-de-la-Roza, A. and V. Luaña, *Gibbs2: A new version of the quasi-harmonic model code. I. Robust treatment of the static data*. Computer Physics Communications, 2011. **182**(8): p. 1708-1720.
131. Tian, F., et al., *Ab initio investigation of high-entropy alloys of 3d elements*. Physical Review B, 2013. **87**(7): p. 075144.
132. Tian, F., et al., *Structural stability of NiCoFeCrAl_x high-entropy alloy from ab initio theory*. Physical Review B, 2013. **88**(8): p. 085128.
133. Zunger, A., et al., *Special quasirandom structures*. Physical Review Letters, 1990. **65**(3): p. 353-356.
134. Zaddach, A.J., et al., *Mechanical Properties and Stacking Fault Energies of NiFeCrCoMn High-Entropy Alloy*. JOM, 2013. **65**(12): p. 1780-1789.
135. Wang, Y., et al., *Computation of entropies and phase equilibria in refractory V-Nb-Mo-Ta-W high-entropy alloys*. Acta Materialia, 2018. **143**: p. 88-101.
136. Niu, C., et al., *First principles exploration of near-equiatomic NiFeCrCo high entropy alloys*. Journal of Alloys and Compounds, 2016. **672**: p. 510-520.
137. Huang, H., et al., *Phase-Transformation Ductilization of Brittle High-Entropy Alloys via Metastability Engineering*. Advanced Materials, 2017. **29**(30): p. 1701678.

138. Qiu, S., et al., *Strengthening mechanism of aluminum on elastic properties of NbVTiZr high-entropy alloys*. Intermetallics, 2018. **92**: p. 7-14.
139. Huang, S., F. Tian, and L. Vitos, *Elasticity of high-entropy alloys from ab initio theory*. Journal of Materials Research, 2018. **33**(19): p. 2938-2953.
140. Gschneidner, K.A., *Physical Properties and Interrelationships of Metallic and Semimetallic Elements**Work partially supported by the U.S. Atomic Energy Commission and the Advanced Research Projects Agency*, in *Solid State Physics*, F. Seitz and D. Turnbull, Editors. 1964, Academic Press. p. 275-426.
141. Agrawal, A. and A. Choudhary, *Perspective: Materials informatics and big data: Realization of the “fourth paradigm” of science in materials science*. APL Materials, 2016. **4**(5).
142. Machaka, R., *Machine learning-based prediction of phases in high-entropy alloys*. Computational Materials Science, 2021. **188**: p. 110244.
143. Yan, Y., D. Lu, and K. Wang, *Accelerated discovery of single-phase refractory high entropy alloys assisted by machine learning*. Computational Materials Science, 2021. **199**: p. 110723.
144. Guo, S. and C.T. Liu, *Phase stability in high entropy alloys: Formation of solid-solution phase or amorphous phase*. Progress in Natural Science: Materials International, 2011. **21**(6): p. 433-446.
145. Krishna, Y.V., U.K. Jaiswal, and R.M. R, *Machine learning approach to predict new multiphase high entropy alloys*. Scripta Materialia, 2021. **197**: p. 113804.
146. Huang, W., P. Martin, and H.L. Zhuang, *Machine-learning phase prediction of high-entropy alloys*. Acta Materialia, 2019. **169**: p. 225-236.
147. Islam, N., W. Huang, and H.L. Zhuang, *Machine learning for phase selection in multi-principal element alloys*. Computational Materials Science, 2018. **150**: p. 230-235.
148. Lee, S.Y., et al., *Deep learning-based phase prediction of high-entropy alloys: Optimization, generation, and explanation*. Materials & Design, 2021. **197**: p. 109260.
149. Gao, S., Z. Gao, and F. Zhao, *Machine learning and visualization assisted solid solution strengthening phase prediction of high entropy alloys*. Materials Today Communications, 2023. **35**: p. 105894.
150. Guo, Q., et al., *Predict the phase formation of high-entropy alloys by compositions*. Journal of Materials Research and Technology, 2023. **22**: p. 3331-3339.
151. Zhu, W., et al., *Phase formation prediction of high-entropy alloys: a deep learning study*. Journal of Materials Research and Technology, 2022. **18**: p. 800-809.
152. Senkov, O.N., et al., *Development and exploration of refractory high entropy alloys—A review*. Journal of Materials Research, 2018. **33**(19): p. 3092-3128.
153. Landau, L.D., et al., *Theory of elasticity: volume 7*. Vol. 7. 1986: Elsevier.
154. Wang, W.H., *The elastic properties, elastic models and elastic perspectives of metallic glasses*. Progress in Materials Science, 2012. **57**(3): p. 487-656.
155. Bragg, W.L., C. Sykes, and A.J. Bradley, *A study of the order-disorder transformation*. Proceedings of the Physical Society, 1937. **49**(4S): p. 96.
156. Sato, H. and R. Kikuchi, *Kinetics of order-disorder transformations in alloys*. Acta Metallurgica, 1976. **24**(9): p. 797-809.
157. Hull, D. and D.J. Bacon, *Chapter 6 - Dislocations in Other Crystal Structures*, in *Introduction to Dislocations (Fifth Edition)*, D. Hull and D.J. Bacon, Editors. 2011, Butterworth-Heinemann: Oxford. p. 109-136.
158. Nohara, A. and T. Imura, *Dislocation Behaviour and the Anomalous Yield-Stress Peak in a β -Brass Single Crystal*. physica status solidi (a), 1985. **91**(2): p. 559-567.
159. Broom, N., *Mechanisms of deformation in beta-brass single crystals*. 1971, ResearchSpace@ Auckland.

160. Tawancy, H.M., *Correlation between disorder-order transformations in a Ni-based alloy and its mechanical properties*. Materials Science and Engineering: A, 2018. **719**: p. 93-103.
161. Nanev, C.N., 7 - *Theory of Nucleation*, in *Handbook of Crystal Growth (Second Edition)*, T. Nishinaga, Editor. 2015, Elsevier: Boston. p. 315-358.
162. *Three-dimensional Nucleation of Crystals and Solute Solubility*, in *Nucleation and Crystal Growth*. 2018. p. 49-104.
163. *Kinetics and Mechanism of Crystallization*, in *Nucleation and Crystal Growth*. 2018. p. 105-143.
164. Uwaha, M., 8 - *Growth Kinetics: Basics of Crystal Growth Mechanisms*, in *Handbook of Crystal Growth (Second Edition)*, T. Nishinaga, Editor. 2015, Elsevier: Boston. p. 359-399.
165. Binder, K., *Theory of first-order phase transitions*. Reports on Progress in Physics, 1987. **50**(7): p. 783.
166. Soni, V., et al., *Microstructural Design for Improving Ductility of An Initially Brittle Refractory High Entropy Alloy*. Scientific Reports, 2018. **8**(1): p. 8816.
167. Whitfield, T.E., et al., *The effect of Al on the formation and stability of a BCC – B2 microstructure in a refractory metal high entropy superalloy system*. Materialia, 2020. **13**: p. 100858.
168. Whitfield, T.E., et al., *Elucidating the microstructural development of refractory metal high entropy superalloys via the Ti–Ta–Zr constituent system*. Journal of Alloys and Compounds, 2020. **818**: p. 152935.
169. Yurchenko, N., et al., *Overcoming the strength-ductility trade-off in refractory medium-entropy alloys via controlled B2 ordering*. Materials Research Letters, 2022. **10**(12): p. 813-823.
170. Qiao, D., et al., *The mechanical and oxidation properties of novel B2-ordered Ti2ZrHf0.5VNb0.5Alx refractory high-entropy alloys*. Materials Characterization, 2021. **178**: p. 111287.
171. Wang, W., et al., *Effect of Al addition on structural evolution and mechanical properties of the AlxHfNbTiZr high-entropy alloys*. Materials Today Communications, 2018. **16**: p. 242-249.
172. Nguyen-Manh, D. and D.G. Pettifor, *Electronic structure, phase stability and elastic moduli of AB transition metal aluminides*. Intermetallics, 1999. **7**(10): p. 1095-1106.
173. Tang, Z., et al., *Aluminum Alloying Effects on Lattice Types, Microstructures, and Mechanical Behavior of High-Entropy Alloys Systems*. JOM, 2013. **65**(12): p. 1848-1858.
174. Acharya, N., B. Fatima, and S.P. Sanyal, *Theoretical study of B2 type technetium AB (A=Tc, B=Ti, V, Nb and Ta) intermetallic compounds*. Journal of Physics and Chemistry of Solids, 2016. **99**: p. 25-33.
175. Dieter, G.E., D.J. Bacon, and D. Bacon, *Mechanical Metallurgy*. 1988: McGraw-Hill.
176. Pineau, A. and T. Pardoen, 2.06 - *Failure of Metals*, in *Comprehensive Structural Integrity*, I. Milne, R.O. Ritchie, and B. Karihaloo, Editors. 2007, Pergamon: Oxford. p. 684-797.
177. Armstrong, R.W., *Plasticity: Grain Size Effects II*, in *Encyclopedia of Materials: Science and Technology*, K.H.J. Buschow, et al., Editors. 2005, Elsevier: Oxford. p. 1-8.
178. Wakai, E., et al., *Radiation hardening and -embrittlement due to He production in F82H steel irradiated at 250°C in JMTR*. Journal of Nuclear Materials, 2005. **343**(1): p. 285-296.
179. 19 - *Fracture toughness properties of aerospace materials*, in *Introduction to Aerospace Materials*, A.P. Mouritz, Editor. 2012, Woodhead Publishing. p. 454-468.
180. Stewart, M., 4 - *Materials selection for pressure vessels*, in *Surface Production Operations*, M. Stewart, Editor. 2021, Gulf Professional Publishing: Boston. p. 93-116.
181. Gu, Y.F., H. Harada, and Y. Ro, *Chromium and chromium-based alloys: Problems and possibilities for high-temperature service*. JOM, 2004. **56**(9): p. 28-33.
182. Spanos, G. and W.T. Reynolds, 10 - *Microstructure of Metals and Alloys*, in *Physical Metallurgy (Fifth Edition)*, D.E. Laughlin and K. Hono, Editors. 2014, Elsevier: Oxford. p. 1073-1112.
183. *Ostwald Ripening, Crystal Size Distribution, and Polymorph Selection*, in *Nucleation and Crystal Growth*. 2018. p. 361-421.

184. Kuehmann, C.J. and P.W. Voorhees, *Ostwald ripening in ternary alloys*. Metallurgical and Materials Transactions A, 1996. **27**(4): p. 937-943.
185. Baldan, A., *Review Progress in Ostwald ripening theories and their applications to nickel-base superalloys Part I: Ostwald ripening theories*. Journal of Materials Science, 2002. **37**(11): p. 2171-2202.
186. Askeland, D.R. and W.J. Wright, *The Science and Engineering of Materials, Enhanced, SI Edition*. 2015: Cengage Learning.
187. Ashby, M.F., *Materials Selection in Mechanical Design*. 1999: Elsevier Science & Technology Books.
188. Soboyejo, W.O., *Mechanical properties of engineered materials*. Mechanical engineering (Marcel Dekker, Inc.). 2003, New York: Marcel Dekker.
189. Lu, T.J. and N.A. Fleck, *The thermal shock resistance of solids*. Acta Materialia, 1998. **46**(13): p. 4755-4768.
190. Sundman, B., H. Lukas, and S. Fries, *Computational thermodynamics: the Calphad method*. 2007: Cambridge university press Cambridge.
191. Hohenberg, P. and W. Kohn, *Inhomogeneous Electron Gas*. Physical Review, 1964. **136**(3B): p. B864-B871.
192. Kohn, W. and L.J. Sham, *Self-Consistent Equations Including Exchange and Correlation Effects*. Physical Review, 1965. **140**(4A): p. A1133-A1138.
193. Clark, S.J., et al., *First principles methods using CASTEP*. Zeitschrift für Kristallographie - Crystalline Materials, 2005. **220**(5-6): p. 567-570.
194. Francis, G.P. and M.C. Payne, *Finite basis set corrections to total energy pseudopotential calculations*. Journal of Physics: Condensed Matter, 1990. **2**(19): p. 4395.
195. Gutsev, G.L., *Numerical Pseudopotentials within DV-X α Framework*, in *Advances in Quantum Chemistry*, P.-O. Löwdin, et al., Editors. 1998, Academic Press. p. 137-157.
196. Perdew, J.P., K. Burke, and M. Ernzerhof, *Generalized Gradient Approximation Made Simple*. Physical Review Letters, 1996. **77**(18): p. 3865-3868.
197. Vanderbilt, D., *Soft self-consistent pseudopotentials in a generalized eigenvalue formalism*. Physical Review B, 1990. **41**(11): p. 7892-7895.
198. Verstraete, M. and X. Gonze, *Smearing scheme for finite-temperature electronic-structure calculations*. Physical Review B, 2001. **65**(3): p. 035111.
199. Head, J.D. and M.C. Zerner, *A Broyden—Fletcher—Goldfarb—Shanno optimization procedure for molecular geometries*. Chemical Physics Letters, 1985. **122**(3): p. 264-270.
200. Birch, F., *Finite Elastic Strain of Cubic Crystals*. Physical Review, 1947. **71**(11): p. 809-824.
201. Boehler, J.P. *Representations for Isotropic and Anisotropic Non-Polynomial Tensor Functions*. 1987.
202. de Jong, M., et al., *Charting the complete elastic properties of inorganic crystalline compounds*. Scientific Data, 2015. **2**(1): p. 150009.
203. Rassoulinejad-Mousavi, S.M., Y. Mao, and Y. Zhang, *Evaluation of copper, aluminum, and nickel interatomic potentials on predicting the elastic properties*. Journal of Applied Physics, 2016. **119**(24): p. 244304.
204. Logan, D.L., *A first course in the finite element method*. 2011: Cengage Learning.
205. Omairey, S.L., P.D. Dunning, and S. Sriramula, *Development of an ABAQUS plugin tool for periodic RVE homogenisation*. Engineering with Computers, 2019. **35**(2): p. 567-577.
206. Cheng, G.-D., Y.-W. Cai, and L. Xu, *Novel implementation of homogenization method to predict effective properties of periodic materials*. Acta Mechanica Sinica, 2013. **29**(4): p. 550-556.

207. Kanit, T., et al., *Determination of the size of the representative volume element for random composites: statistical and numerical approach*. International Journal of Solids and Structures, 2003. **40**(13): p. 3647-3679.
208. Yan, J., et al., *Comparison of prediction on effective elastic property and shape optimization of truss material with periodic microstructure*. International Journal of Mechanical Sciences, 2006. **48**(4): p. 400-413.
209. Subedi, U., et al., *pyMPEALab Toolkit for Accelerating Phase Design in Multi-principal Element Alloys*. Metals and Materials International, 2022. **28**(1): p. 269-281.
210. Daskalopoulos, I., et al., *Microstructural Characterization of AlCrTiV – Si High Entropy Alloy for advanced applications*. MATEC Web Conf., 2021. **349**: p. 02003.
211. Tukey, J.W., *Comparing Individual Means in the Analysis of Variance*. Biometrics, 1949. **5**(2): p. 99-114.
212. Wandrol, P., *Trinity Detection System for SEM and FIB/SEM*. Microscopy and Microanalysis, 2019. **25**(S2): p. 458-459.
213. Picard, Y.N., *Scanning Electron Microscopy*, in *Materials Characterization*. 2019, ASM International. p. 0.
214. Torres-Rivero, K., et al., *Chapter Ten - Metal and metal oxide nanoparticles: An integrated perspective of the green synthesis methods by natural products and waste valorization: applications and challenges*, in *Comprehensive Analytical Chemistry*, S.K. Verma and A.K. Das, Editors. 2021, Elsevier. p. 433-469.
215. Bell, D.C., *Transmission Electron Microscopy; Diffraction, Imaging, and Spectrometry C. Barry Carter and David B. Williams (Eds.)*. Springer International Publishing, Switzerland 2016, 518 pp. ISBN: 978-3-3-319-26649-7. Microscopy and Microanalysis, 2018. **24**(3): p. 324-324.
216. Jauncey, G.E., *The Scattering of X-Rays and Bragg's Law*. Proc Natl Acad Sci U S A, 1924. **10**(2): p. 57-60.
217. International, A., *ASTM E384-17-Standard Test Method for Microindentation Hardness of Materials*. 2016.
218. Oliver, W.C. and G.M. Pharr, *Measurement of hardness and elastic modulus by instrumented indentation: Advances in understanding and refinements to methodology*. Journal of Materials Research, 2004. **19**(1): p. 3.
219. International, A., *ASTM E9-09 Standard test methods of compression testing of metallic materials at room temperature*. 2018.
220. Frictioni, R.B. and L. Essig, *Inert Gas Fusion*, in *Materials Characterization*, R.E. Whan, Editor. 1986, ASM International. p. 0.
221. Daskalopoulos, I., et al., *Microstructural Characterization of AlCrTiV – Si High Entropy Alloy for advanced applications*. MATEC Web of Conferences, 2021. **349**: p. 02003.
222. Chaskis, S., et al., *Examination of Fracture Mechanisms in two Al – Ti – V – Cr – (Si) High Entropy Alloys*. MATEC Web of Conferences, 2021. **349**: p. 02002.
223. Daskalopoulos, I., *Study of thermal processes and microstructural characterization of the AlCrTiV-Si high-entropy alloy*. 2020.
224. Kiousis, D., *Αξιολόγηση της δυνατότητας παρασκευής κράματος μέσης εντροπίας TiAlCrV με μεθόδους προσθετικής κατασκευής (Additive Manufacturing)*. 2021.
225. Andersson, J.O., et al., *Thermo-Calc & DICTRA, computational tools for materials science*. Calphad, 2002. **26**(2): p. 273-312.
226. Monkhorst, H.J. and J.D. Pack, *Special points for Brillouin-zone integrations*. Physical Review B, 1976. **13**(12): p. 5188-5192.

227. Zhang, P.F., Y.X. Li, and P.K. Bai, *First principles study of Ti5Si3 intermetallic compounds with Cu additions: Elastic properties and electronic structure*. IOP Conference Series: Materials Science and Engineering, 2018. **284**(1): p. 012013.
228. Wang, H.-Y., et al., *First-principles study of the structural and elastic properties of Ti5Si3 with substitutions Zr, V, Nb, and Cr*. Journal of Materials Research, 2010. **25**(12): p. 2317-2324.
229. Lochhead, R.Y., *Chapter 3 - Basic Physical Sciences for the Formulation of Cosmetic Products*, in *Cosmetic Science and Technology*, K. Sakamoto, et al., Editors. 2017, Elsevier: Amsterdam. p. 39-76.
230. Louzguine, D.V. and A. Inoue, *Crystallization behavior of Ti50Ni25Cu25 amorphous alloy*. Journal of Materials Science, 2000. **35**(16): p. 4159-4164.
231. Anselin, F., *Etude de la decomposition de la phase γ dans le ternaire uranium-plutonium-molybdene (20)*. Proc. Int. Conf. Plutonium Metall. 2nd, 1961: p. 367-384.
232. Ray, R., B. Giessen, and N. Grant, *The constitution of metastable titanium-rich Ti-Fe alloys: An order-disorder transition*. Metallurgical and Materials Transactions B, 1972. **3**: p. 627-629.
233. (U.S.), N.B.S., *Standard X-ray diffraction powder patterns*. Circ., 1958. **539**(8): p. 64.
234. Zhang, L.-C. and L.-Y. Chen, *A Review on Biomedical Titanium Alloys: Recent Progress and Prospect*. Advanced Engineering Materials, 2019. **21**(4): p. 1801215.
235. WebElements. *The periodic table of elements*. 01/02/2023]; Available from: <https://www.webelements.com/>.
236. Lee, W.E., *4.12 - Refractories*, in *Comprehensive Composite Materials*, A. Kelly and C. Zweben, Editors. 2000, Pergamon: Oxford. p. 363-385.
237. Gao, K., et al., *Phase inversion in a lightweight high Al content refractory high-entropy alloy*. Journal of Materials Science & Technology, 2023. **150**: p. 124-137.
238. Laube, S., et al., *Controlling crystallographic ordering in Mo-Cr-Ti-Al high entropy alloys to enhance ductility*. Journal of Alloys and Compounds, 2020. **823**: p. 153805.
239. Ogura, M., et al., *Structure of the high-entropy alloy AlxCrFeCoNi: fcc versus bcc*. Journal of Alloys and Compounds, 2017. **715**: p. 454-459.
240. WebElements. [cited 2023 28 February]; Available from: <https://www.webelements.com/>.
241. H. E. Boyer, T.L.G., *Metals Handbook: Desk Edition*. 1985: ASM International.
242. Han, D. and D. Lee, *Morphology Controlled Synthesis of γ -Al₂O₃ Nano-Crystallites in Al@Al₂O₃ Core-Shell Micro-Architectures by Interfacial Hydrothermal Reactions of Al Metal Substrates*. Nanomaterials, 2021. **11**(2): p. 310.
243. Accuratus. [cited 2023 28 February]; Available from: <https://accuratus.com/alumox.html>.
244. Sun, Z., et al., *Thermal physical properties of high entropy alloy Al_{0.3}CoCrFeNi at elevated temperatures*. Journal of Alloys and Compounds, 2022. **901**: p. 163554.
245. Zhang, W.J., B.V. Reddy, and S.C. Deevi, *Physical properties of TiAl-base alloys*. Scripta Materialia, 2001. **45**(6): p. 645-651.
246. Hakeem, A.S., et al., *Comparative evaluation of thermal and mechanical properties of nickel alloy 718 prepared using selective laser melting, spark plasma sintering, and casting methods*. Journal of Materials Research and Technology, 2021. **12**: p. 870-881.
247. Rao, K.V.K., S.V.N. Naidu, and L. Iyengar, *Thermal Expansion of Rutile and Anatase*. Journal of the American Ceramic Society, 1970. **53**(3): p. 124-126.
248. Materials, A. [cited 2023 28 February]; Available from: <https://www.azom.com/properties.aspx?ArticleID=1114>.
249. Jeanne Ayache, L.B., Jacqueline Boumendil, Gabrielle Ehret, Danièle Laub, *Sample Preparation Handbook for Transmission Electron Microscopy*. 2010, New York, NY: Springer
250. Ahmed, T. and H.M. Flower, *Partial isothermal sections of Ti-Al-V ternary diagram*. Materials Science and Technology (United Kingdom), 1994. **10**(4): p. 272-288.

251. Selvaraj, S.K., et al., *Recent Advancements in the Field of Ni-Based Superalloys*. Advances in Materials Science and Engineering, 2021. **2021**: p. 9723450.
252. Joele, M. and W.R. Matizamhuka, *A Review on the High Temperature Strengthening Mechanisms of High Entropy Superalloys (HESA)*. Materials, 2021. **14**(19): p. 5835.
253. Yan, M., et al., *Review of effect of oxygen on room temperature ductility of titanium and titanium alloys*. Powder Metallurgy, 2014. **57**(4): p. 251-257.
254. Hildyard, E.M., et al., *On the role of internal stresses on the superelastic behaviour of Ti-24Nb (at.%)*. Acta Materialia, 2022. **237**: p. 118161.
255. Whitfield, T.E., et al., *An Investigation of the Miscibility Gap Controlling Phase Formation in Refractory Metal High Entropy Superalloys via the Ti-Nb-Zr Constituent System*. Metals, 2021. **11**(8): p. 1244.
256. Senkov, O.N., et al., *Microstructure, compression properties, and oxidation behavior of Hf-25Ta-5Me alloys (Me is Mo, Nb, W, 0.5Mo + 0.5 W, Cr, or Zr)*. International Journal of Refractory Metals and Hard Materials, 2022. **109**: p. 105968.
257. Butler, T.M., et al., *Oxidation behaviors of CrNb, CrNbTi, and CrNbTaTi concentrated refractory alloys*. Intermetallics, 2022. **140**: p. 107374.
258. Senkov, O.N., et al., *Effect of Fe additions on the microstructure and properties of Nb-Mo-Ti alloys*. International Journal of Refractory Metals and Hard Materials, 2020. **89**: p. 105221.
259. Liang, F., et al., *Phase Stability and Mechanical Properties Analysis of AlCo_xCrFeNi HEAs Based on First Principles*. Metals, 2022. **12**(11): p. 1860.
260. Stein, F. and A. Leineweber, *Laves phases: a review of their functional and structural applications and an improved fundamental understanding of stability and properties*. Journal of Materials Science, 2021. **56**(9): p. 5321-5427.
261. Hanna, J.A., et al., *A new high-strength spinodal alloy*. Journal of Materials Research, 2005. **20**(4): p. 791-795.
262. Dasari, S., et al., *Crystallographic and Compositional Evolution of Ordered B2 and Disordered BCC Phases During Isothermal Annealing of Refractory High-Entropy Alloys*. Microscopy and Microanalysis, 2023. **29**(1): p. 303-313.
263. Kloenne, Z.T., et al., *On the bcc/B2 interface structure in a refractory high entropy alloy*. Scripta Materialia, 2023. **223**: p. 115071.
264. Kadirvel, K., H.L. Fraser, and Y. Wang, *Microstructural design via spinodal-mediated phase transformation pathways in high-entropy alloys (HEAs) using phase-field modelling*. Acta Materialia, 2023. **243**: p. 118438.
265. Gorse, S., et al., *Database on the mechanical properties of high entropy alloys and complex concentrated alloys*. Data in Brief, 2018. **21**: p. 2664-2678.
266. Weston, N.S. and M. Jackson, *FAST-forge – A new cost-effective hybrid processing route for consolidating titanium powder into near net shape forged components*. Journal of Materials Processing Technology, 2017. **243**: p. 335-346.